

**DFT CALCULATIONS OF MAGNETIC SHIELDING AND QUADRUPOLAR  
COUPLING IN ORDERED SYSTEMS:**

**METHODS AND APPLICATIONS TO NMR CRYSTALLOGRAPHY**

by

Sean T. Holmes

A dissertation submitted to the Faculty of the University of Delaware in partial fulfillment of the requirements for the degree of Doctor of Philosophy in Chemistry and Biochemistry

Winter 2017

© 2017 Sean Holmes  
All Rights Reserved

ProQuest Number: 10256206

All rights reserved

INFORMATION TO ALL USERS

The quality of this reproduction is dependent upon the quality of the copy submitted.

In the unlikely event that the author did not send a complete manuscript and there are missing pages, these will be noted. Also, if material had to be removed, a note will indicate the deletion.



ProQuest 10256206

Published by ProQuest LLC (2017). Copyright of the Dissertation is held by the Author.

All rights reserved.

This work is protected against unauthorized copying under Title 17, United States Code  
Microform Edition © ProQuest LLC.

ProQuest LLC.  
789 East Eisenhower Parkway  
P.O. Box 1346  
Ann Arbor, MI 48106 – 1346

**DFT CALCULATIONS OF MAGNETIC SHIELDING AND QUADRUPOLAR  
COUPLING IN ORDERED SYSTEMS:**

**METHODS AND APPLICATIONS TO NMR CRYSTALLOGRAPHY**

by

Sean T. Holmes

Approved: \_\_\_\_\_  
Murray V. Johnston, Ph.D.  
Chair of the Department of Chemistry and Biochemistry

Approved: \_\_\_\_\_  
George H. Watson, Ph.D.  
Dean of the College of Arts and Sciences

Approved: \_\_\_\_\_  
Ann L. Ardis, Ph.D.  
Senior Vice Provost for Graduate and Professional Education

I certify that I have read this dissertation and that in my opinion it meets the academic and professional standard required by the University as a dissertation for the degree of Doctor of Philosophy.

Signed:

---

Cecil Dybowski, Ph.D.  
Professor in charge of dissertation

I certify that I have read this dissertation and that in my opinion it meets the academic and professional standard required by the University as a dissertation for the degree of Doctor of Philosophy.

Signed:

---

Tatyana Polenova, Ph.D.  
Member of dissertation committee

I certify that I have read this dissertation and that in my opinion it meets the academic and professional standard required by the University as a dissertation for the degree of Doctor of Philosophy.

Signed:

---

Shi Bai, Ph.D.  
Member of dissertation committee

I certify that I have read this dissertation and that in my opinion it meets the academic and professional standard required by the University as a dissertation for the degree of Doctor of Philosophy.

Signed:

---

Robbie Iulucci, Ph.D.  
Member of dissertation committee

## ACKNOWLEDGMENTS

I would like to begin by expressing my sincerest gratitude to my advisor, Professor Cecil Dybowski, for his mentorship over the past five years. I would also like to thank the other members of our research group, Dr. Fahri Alkan, Anna Murphy, and Yao Yao. I thank the members of my dissertation committee, Prof. Tatyana Polenova, Prof. Shi Bai, and Prof. Robbie Iuliucci, for their continued input throughout the completion of this work. I also thank Prof. Cynthia Jameson for helpful discussions regarding this work. Several undergraduate students, namely John Lora, Shelby Chan, and Ashley Knoerdel, have worked with me on various projects, and I would like to thank them for their contributions. Computational resources necessary for the completion of this dissertation were generously provided by Prof. Karl Mueller and Pennsylvania State University Center for Nanoscale Science.

This dissertation incorporates portions of my previously published work. Chapter 2 contains material from “Density functional investigation of intermolecular effects on  $^{13}\text{C}$  NMR chemical-shielding tensors modeled with molecular clusters”, adapted with permission from *Journal of Chemical Physics*, **2014**, *141* (16), 164121. DOI: 10.1063/1.4900158. Copyright 2014 AIP Publishing. Chapter 3 is based on “Carbon-13 chemical-shift tensors in indigo: a two-dimensional NMR-ROCSA and DFT study”, and adapted with permission from *Solid State Nuclear Magnetic Resonance*, **2015**, *72*, 90-95. DOI: 10.1016/j.ssnmr.2015.08.004. Copyright 2015 Elsevier. Chapter 4 is based on “Critical analysis of cluster models and exchange-correlation functionals for calculating magnetic shielding in molecular solids”, and

adapted with permission from *Journal of Chemical Theory and Computation*, **2015**, *11* (11), 5229-5241. DOI: 10.1021/acs.jctc.5b00752. Copyright 2016 American Chemical Society. Chapter 5 is based on “Calculations of solid-state  $^{43}\text{Ca}$  NMR parameters: a comparison of periodic and cluster approaches and an evaluation of DFT functionals”, which is under review for publication by the *Journal of Computational Chemistry*. Chapter 6 is based on “Analysis of the bond-valence method for calculating  $^{29}\text{Si}$  and  $^{31}\text{P}$  magnetic shielding in covalent network solids”, and adapted with permission from *Journal of Computational Chemistry*, **2016**, *37* (18), 1704-1710. DOI: 10.1002/jcc.24389. Copyright 2016 John Wiley and Sons. Chapter 7 is based on “Semi-empirical refinements of crystal structures using  $^{17}\text{O}$  quadrupolar-coupling tensors”, which is under review for publication by the *Journal of Chemical Physics*.

## TABLE OF CONTENTS

LIST OF TABLES .....	x
LIST OF FIGURES .....	xiv
ABSTRACT .....	xxi
Chapter	
1 INTRODUCTION .....	1
1.1 Motivation and Outline.....	1
1.2 Introduction to Nuclear Magnetic Resonance Spectroscopy.....	4
1.3 Magnetic-Shielding Tensors.....	6
1.4 Quadrupolar-Coupling Tensors .....	10
1.5 Overview of Electronic Structure Methods .....	13
1.6 Exchange-Correlation Functionals .....	18
1.6.1 The Local-Density Approximation.....	18
1.6.2 The Generalized-Gradient Approximation.....	19
1.6.3 The Meta-Generalized-Gradient Approximation .....	20
1.6.4 Hybrid Methods.....	20
1.7 Theory and Calculation of Quadrupolar-Coupling Tensors .....	21
1.8 Theory and Calculation of Magnetic-Shielding Tensors.....	22
REFERENCES .....	28
2 THE SYMMETRY-ADAPTED CLUSTER ANSATZ: CALCULATIONS OF <sup>13</sup> C MAGNETIC-SHIELDING TENSORS .....	36
2.1 Introduction .....	36
2.1.1 Models for Computing Magnetic Shielding in Solids.....	37
2.2 Materials, Computational Details, and Analysis .....	46
2.3 Results and Discussion .....	50
2.3.1 Size Requirements for Molecular Clusters.....	50
2.3.2 Symmetry Requirements for Molecular Clusters .....	52
2.3.3 Locally-Dense Basis Sets .....	55
2.3.4 Relationship between Calculated and Experimental Results .....	56
2.3.5 Analysis of Magnetic Shielding Principal Components.....	62

2.3.6	Effects of Plane-Wave Structural Refinements on Calculated Shielding.....	69
2.4	Conclusions .....	71
	REFERENCES .....	73
3	CARBON-13 CHEMICAL-SHIFT TENSORS IN INDIGO: A TWO-DIMENSIONAL NMR-ROCSA AND DFT STUDY .....	84
3.1	Introduction .....	84
3.2	Experimental Methods.....	86
3.3	Computational Methods .....	86
3.4	Results and Discussion .....	88
3.4.1	NMR Measurements and Peak Assignments .....	88
3.4.2	Discussion of $^{13}\text{C}$ Chemical-Shift Tensors of Indigo .....	89
3.4.3	Assessment of Lattice Effects .....	96
3.5	Conclusion.....	99
	REFERENCES .....	100
4	CRITICAL ANALYSIS OF CLUSTER MODELS AND EXCHANGE-CORRELATION FUNCTIONALS FOR CALCULATING MAGNETIC SHIELDING IN MOLECULAR SOLIDS.....	105
4.1	Introduction .....	105
4.2	Materials and Computational Details .....	105
4.3	Intermolecular Effects on Magnetic Shielding Revisited.....	113
4.4	Comparison of GIPAW and Cluster Models.....	117
4.5	Examination of Exchange-Correlation Functionals .....	127
4.5.1	Discussion of $^{13}\text{C}$ Results .....	130
4.5.2	Discussion of $^{15}\text{N}$ Results .....	134
4.5.3	Discussion of $^{19}\text{F}$ Results.....	137
4.5.4	Discussion of $^{31}\text{P}$ Results.....	138
4.6	Conclusion.....	138
	REFERENCES .....	141

5	CALCULATIONS OF SOLID-STATE $^{43}\text{Ca}$ NMR PARAMETERS: A COMPARISON OF PERIODIC AND CLUSTER-BASED APPROACHES AND AN EVALUATION OF DFT FUNCTIONALS .....	155
5.1	Introduction .....	155
5.2	Computational Details .....	157
5.2.1	Materials and Computational Protocols .....	157
5.2.2	Conventions for Reporting NMR Parameters .....	160
5.3	Results and Discussion .....	162
5.3.1	Comparison of GIPAW and Cluster-Based Calculations.....	162
5.3.2	Discussion of GIPAW Calculations .....	167
5.3.3	Discussion of Cluster-Based Calculations.....	168
5.4	Conclusions .....	174
	REFERENCES .....	175
6	ANALYSIS OF THE BOND-VALENCE METHOD FOR CALCULATING $^{29}\text{Si}$ AND $^{31}\text{P}$ MAGNETIC SHIELDING IN COVALENT NETWORK SOLIDS.....	182
6.1	Introduction .....	182
6.2	Computational Details and Theory.....	184
6.3	Results and Discussion .....	187
6.3.1	Cluster Size.....	187
6.3.2	Basis-Set and Pseudopotential Effects .....	190
6.3.2.1	Comparison of Periodic and Cluster Models.....	192
6.3.3	Benchmarking DFT Functionals .....	196
6.4	Conclusions .....	201
	REFERENCES .....	203
7	SEMI-EMPIRICAL REFINEMENTS OF CRYSTAL STRUCTURES USING $^{17}\text{O}$ QUADRUPOLAR-COUPLING TENSORS.....	209
7.1	Introduction .....	209
7.2	Computational Details .....	212

7.2.1	Overview and Computational Strategy .....	212
7.2.2	Semi-Empirical Geometry Optimizations .....	213
7.2.3	Conventions for Reporting NMR Parameters .....	215
7.3	Results and Discussion .....	217
7.3.1	Parameterization of Force Field Using Model Compounds .....	217
7.3.2	Changes in Bond Lengths .....	220
7.3.3	Assessment of Structural Refinements by Agreement of Calculated $^{17}\text{O}$ Quadrupolar-Coupling Tensors with Experiment .....	222
7.3.4	Additional Figures of Merit for Assessing Structural Refinements .....	225
7.3.5	Discussion of Chemical Shifts .....	227
7.3.6	Comparison to Neutron-Diffraction Structures .....	234
7.4	Conclusion .....	235
	REFERENCES .....	237
8	CONCLUSION .....	247
	REFERENCES .....	254
Appendix		
A	PERMISSION AND COPYRIGHT .....	255

## LIST OF TABLES

<b>Table 2.1.</b> Crystal structures and cluster compositions for materials examined in this study.....	47
<b>Table 2.2.</b> $^{13}\text{C}$ Principal magnetic-shielding values for oxalic acid dihydrate as a function of cluster size. The differential quantifies differences in computed principal values between different sizes of clusters. ....	51
<b>Table 2.3.</b> $^{13}\text{C}$ Principal magnetic-shielding values for squaric acid as a function of cluster size. The differential quantifies differences in computed principal values between different sizes of clusters. ....	52
<b>Table 2.4.</b> Calculated chemical-shift tensors for pentaerythritol using clusters with the experimental crystalline space group (I4) and a space group of reduced symmetry (quasi-I4). ....	54
<b>Table 2.5.</b> Comparison of locally dense and balanced basis sets for calculating the $^{13}\text{C}$ chemical shielding of oxalic acid dihydrate using the cluster $15\text{C}_2\text{O}_4\text{H}_2\cdot 20\text{H}_2\text{O}$ . ....	56
<b>Table 2.6.</b> Linear-regression parameters for $^{13}\text{C}$ principal magnetic-shielding values versus principal chemical-shift values for isolated molecules, clusters, and plane-wave optimized clusters. ....	61
<b>Table 2.7.</b> Root-mean-square deviation (RMSD) between calculated and experimental chemical shifts modeled using isolated molecules, clusters, and plane-wave optimized clusters. ....	64
<b>Table 2.8.</b> Mean-absolute deviation (MAD) between calculated magnetic shielding of cluster models and isolated-molecule models. <sup>a</sup> .....	68
<b>Table 3.1.</b> Principal components of the $^{13}\text{C}$ chemical-shift tensors of indigo, with the average of the principal components, isotropic chemical shift, span, and skew. <sup>a</sup> .....	92
<b>Table 3.2.</b> Principal components of the $^{13}\text{C}$ chemical-shift tensors of hypoxanthine, with the average of the principal components, isotropic chemical shift, span, and skew. <sup>a,b</sup> .....	93
<b>Table 3.3.</b> Principal components of the $^{13}\text{C}$ chemical-shift tensors of adenosine, with the average of the principal components, isotropic chemical shift, span, and skew. <sup>a,b,c</sup> .....	94

<b>Table 3.4.</b> Differences in calculated chemical-shift tensors between an a molecule in a cluster and a molecule in isolation. ....	97
<b>Table 4.1.</b> Crystal structures and cluster compositions for materials containing $^{13}\text{C}$ spins.....	107
<b>Table 4.2.</b> Crystal structures and cluster compositions for materials containing $^{15}\text{N}$ spins.....	108
<b>Table 4.3.</b> Crystal structures and cluster compositions for materials containing $^{19}\text{F}$ spins.....	109
<b>Table 4.4.</b> Crystal structures and cluster compositions for materials containing $^{31}\text{P}$ spins.....	110
<b>Table 4.5.</b> Linear-regression parameters for calculated principal components of $^{15}\text{N}$ magnetic-shielding tensors versus experimental principal components of chemical-shift tensors using three computational models <sup>a,b</sup> .....	117
<b>Table 4.6.</b> Linear-regression parameters obtained from correlation plots between GIPAW calculated principal magnetic-shielding values and experimental principal chemical-shift values.....	121
<b>Table 4.7.</b> Linear-regression parameters obtained from correlation plots between GIAO calculated principal magnetic-shielding values and experimental principal chemical-shift values.....	122
<b>Table 4.8.</b> T-test statistics for assessing differences between the GIPAW and GIAO/cluster methodologies for computing magnetic-shielding parameters. <sup>a</sup> .....	127
<b>Table 4.9.</b> Linear-regression parameters obtained from correlation plots between calculated principal components of magnetic-shielding tensors and experimental principal components of chemical-shift tensors obtained from the symmetry-adapted cluster approach. Calculated values were obtained using the cc-pVTZ basis set.....	129
<b>Table 4.10.</b> Linear-regression parameters and <i>T</i> -test statistics for assessing differences between $sp^3$ - and $sp^2/sp$ -hybridized carbon subpopulations. <sup>a</sup> .....	134
<b>Table 5.1.</b> Model cluster compositions for the materials used in this study.....	158

<b>Table 5.2.</b> Experimental and calculated $^{43}\text{Ca}$ NMR parameters using the cluster-based approach, with results obtained from clusters of increasing size, and MAEs <sup>a</sup> from experimental results. All results were obtained at the PBE level. ....	164
<b>Table 5.3.</b> Linear-regression parameters ( $\sigma_{ref}$ and $ m $ ) and statistical data (MAE, <sup>a</sup> Max. <sup>b</sup> ) associated with the correlations of principal values of calculated $^{43}\text{Ca}$ magnetic-shielding tensors and experimental $^{43}\text{Ca}$ chemical-shift tensors and of calculated and experimental $^{43}\text{Ca}$ quadrupolar-coupling tensors obtained from six plane-wave DFT methods. ....	167
<b>Table 5.4.</b> Linear-regression parameters ( $\sigma_{ref}$ and $ m $ ) and statistical data (MAE, <sup>a</sup> Max. <sup>b</sup> ) associated with the correlations of principal values of calculated $^{43}\text{Ca}$ magnetic-shielding tensors and experimental $^{43}\text{Ca}$ chemical-shift tensors and of calculated and experimental $^{43}\text{Ca}$ quadrupolar-coupling tensors obtained from thirteen DFT methods in cluster-based calculations. ....	169
<b>Table 5.5.</b> HF and PBE calculations of magnetic-shielding tensors in $\text{Ca}^{2+}$ , $\text{CaF}^+$ , $\text{CaOH}^+$ , and $\text{CaH}^+$ . <sup>a</sup> .....	171
<b>Table 5.6.</b> Linear-regression parameters ( $\sigma_{ref}$ and $ m $ ) and statistical data (MAE, <sup>a</sup> Max. <sup>b</sup> ) associated with the correlations of principal values of calculated $^{43}\text{Ca}$ magnetic-shielding tensors and experimental $^{43}\text{Ca}$ chemical-shift tensors and of calculated and experimental $^{43}\text{Ca}$ quadrupolar-coupling tensors obtained from Hartree-Fock theory. ....	173
<b>Table 6.1.</b> Principal components of experimental and computed magnetic-shielding tensors, isotropic magnetic shielding, and span for first, third, and fifth co-ordination-shell clusters of $\text{SiO}_2$ , $\text{Na}_2\text{SiO}_3$ , $\text{Mg}_2\text{P}_4\text{O}_{12}$ (P1), and $\text{Mg}_3(\text{PO}_4)_2$ <sup>a</sup> determined with VMTA/BV theory. .	189
<b>Table 6.2.</b> Calculated $^{29}\text{Si}$ and $^{31}\text{P}$ principal components of magnetic shielding tensors for various all-electron Slater-type and pseudopotential plane-wave basis sets. <sup>a</sup> .....	191
<b>Table 6.3.</b> Linear-regression parameters ( $m$ , $b$ ) for the relationship between experimental and calculated principal components of magnetic-shielding tensors and residuals between experimental and calculated magnetic shielding. ....	200

<b>Table 7.1.</b> Summary of linear-regression parameters describing the relationship between the principal components of calculated magnetic-shielding tensors and experimental chemical-shift tensors.....	216
<b>Table 7.2.</b> Experimental and computed $^{17}\text{O}$ quadrupolar-coupling tensors obtained from X-ray diffraction structures or from structures refined at the PW91, PW91-D2 <sup>a</sup> , or PW91-D2* <sup>b</sup> levels, and root-mean-square deviations of the sets. ....	220
<b>Table 7.3.</b> Summary of structural information and statistical data associated with the relationship between experimental and calculated NMR parameters. ....	228
<b>Table 7.4.</b> Summary of experimental and calculated $^{35}\text{Cl}$ quadrupolar-coupling tensors.....	230
<b>Table 7.5.</b> Statistical data associated with the prediction of $^{13}\text{C}$ ( $N = 21$ ), $^{15}\text{N}$ ( $N = 24$ ), and $^{17}\text{O}$ ( $N = 42$ ) chemical-shift tensors using structures obtained by X-ray diffraction, by PW91 refinement, and by PW91-D2* refinement of diffraction structures. ....	231

## LIST OF FIGURES

- Figure 1.1.** Simulated chemical-shift spectra of spin- $1/2$  nuclei in randomly oriented powders. Examples are shown for cases with axially symmetric ( $\kappa = \pm 1.0$ ) and radially symmetric ( $\kappa = 0.0$ ) chemical-shift tensors..... 11
- Figure 1.2.** Simulated spectra of spin-1 nuclei in randomly oriented powders. Examples are shown for cases with asymmetry parameters of  $\eta = 0.0$ ,  $\eta = 0.5$ , and  $\eta = 1.0$ ..... 13
- Figure 2.1.** (a) Cluster of  $\beta$ -D-fructopyranose in the space group  $P2_12_12_1$  containing fifteen molecules. (b) Cluster of methyl  $\beta$ -D-xylopyranoside in the space group  $P2_1$  containing thirteen molecules. (c) Cluster of  $\gamma$ -glycine in the space group  $P3_2$  containing fifteen molecules..... 44
- Figure 2.2.** Two orientations of a cluster of acenaphthene in the space group  $Pmc2_1$  containing fifteen molecules. .... 45
- Figure 2.3.** Cluster of  $\beta$ -D-fructopyranoside illustrating the partitioning of the basis set into locally dense (cc-pVTZ) and locally sparse (cc-pVDZ) layers. .... 49
- Figure 2.4.** Two example clusters of pentaerythritol. Cluster A is built from thirteen complete molecules and maintains all of the symmetry elements of the  $I4$  space group. Cluster B is built from nine molecules and lacks several symmetry elements of the space group..... 54
- Figure 2.5.** Correlation plots for calculated principal components of magnetic-shielding tensors versus experimental principal components of chemical-shift tensors. Aliphatic carbons principal components are in blue, aromatic principal components are in red, and carboxylic principal components are in green. Results in (a) are from the isolated-molecule models and results in (b) are from the cluster models. .... 59
- Figure 2.6.** Correlation plots for calculated isotropic magnetic shieldings versus experimental isotropic chemical shifts. Aliphatic carbons shifts are in blue, aromatic shifts are in red, and carboxylic shifts are in green. Results in (a) are from the isolated-molecule models and results in (b) are from the cluster models. .... 60

- Figure 2.7.** Correlation of errors in calculated  $^{13}\text{C}$  chemical-shift tensor principal values between cluster models and isolated-molecule models. The dotted black line represents an ideal one-to-one relationship between errors in the two methods whereas the red line represents the best-fit relationship. .... 62
- Figure 2.8.** Relationship between calculated principal components of  $^{13}\text{C}$  magnetic-shielding tensors and experimental  $^{13}\text{C}$  chemical-shift tensors of aliphatic carbon sites. The panels display values for each of the principal values: (a)  $\sigma_{11}$ , (b)  $\sigma_{22}$ , and (c)  $\sigma_{33}$ . Results obtained using cluster models are shown as solid blue points whereas results obtained using isolated-molecule models are shown as black crosses.... 65
- Figure 2.9.** Relationship between calculated principal components of  $^{13}\text{C}$  magnetic-shielding tensors and experimental  $^{13}\text{C}$  chemical-shift tensors of aromatic carbon sites. The panels display values for each of the principal values: (a)  $\sigma_{11}$ , (b)  $\sigma_{22}$ , and (c)  $\sigma_{33}$ . Results obtained using cluster models are shown as solid red points whereas results obtained using isolated-molecule models are shown as black crosses.... 66
- Figure 2.10.** Relationship between calculated principal components of  $^{13}\text{C}$  magnetic-shielding tensors and experimental  $^{13}\text{C}$  chemical-shift tensors of carboxylic carbon sites. The panels display values for each of the principal values: (a)  $\sigma_{11}$ , (b)  $\sigma_{22}$ , and (c)  $\sigma_{33}$ . Results obtained using cluster models are shown as solid red points whereas results obtained using isolated-molecule models are shown as black crosses.... 67
- Figure 3.1.** Structures of indigo (upper left), hypoxanthine (lower left), and adenosine (right). The labeling schemes for the aromatic carbon sites are shown..... 85
- Figure 3.2.** Crystal packing diagram of indigo (polymorph A,  $P2_1/c$  space group) showing the partition into two layers. The central molecule (cc-pVTZ basis set) is shown in the ball-and-stick representation and the peripheral molecules (cc-pVDZ basis set) are shown in a wireframe representation. .... 88

- Figure 3.3.** (a)  $^{13}\text{C}$  NMR-ROCSA spectrum of indigo. The chemical-shift scale in the *f1* dimension is referenced to the isotropic chemical shift of each resonance, as is customary in ROCSA spectra, whereas the *f2* dimension is referenced to TMS. (b) ROCSA chemical-shift subspectra of the eight unique  $^{13}\text{C}$  sites in indigo. The upper solid lines are the experimental spectra and the lower traces (dotted lines) are simulated spectra from fitting the chemical-shift powder patterns. ... 90
- Figure 3.4.** Correlation of calculated principal chemical-shift components and experimental principal chemical-shift components for  $^{13}\text{C}$  sites in indigo, hypoxanthine, and adenosine. Calculations were performed at the TPSSh/cc-pVTZ level. Results for the ribose carbons of adenosine are not included. Values obtained using cluster models are shown as solid orange circles whereas values obtained using isolated-molecule models are shown as black crosses. .... 95
- Figure 4.1.** A symmetry-adapted cluster model of trimethylphosphine oxide consisting of fifteen molecules in the  $C2/m$  space group. The central molecule of the cluster (ball-and-stick representation) is given the cc-pVXZ basis set ( $X = \text{D, T, Q, 5}$ ). The peripheral molecules of the cluster (wireframe representation) are given the cc-pVDZ basis set. ... 111
- Figure 4.2.** Three computational methodologies used to model the solid-state structure of uracil; isolated-molecule (IM) model, symmetry-adapted-cluster (SAC) model, and periodic-boundary-condition (PBC) model. In the PBC model, the colored lines represent the axes of the unit cell. 115
- Figure 4.3.** Principal components of  $^{15}\text{N}$  magnetic-shielding tensors in (a) isolated-molecule models, (b) symmetry-adapted cluster models, and (c) periodic GIPAW models. Shielding in the IM and SAC models is calculated at the PW91/cc-pVTZ level. Shielding in the PBC model is calculated at the PW91/600eV level. Results are shown for adenine trihydrate, guanine monohydrate, cytosine, thymine, and uracil. .... 116
- Figure 4.4.** Calculated principal components of  $^{13}\text{C}$  magnetic-shielding tensors versus experimental principal components of  $^{13}\text{C}$  chemical-shift tensors. (a) GIPAW, (b) Clusters ..... 123
- Figure 4.5.** Calculated principal components of  $^{15}\text{N}$  magnetic-shielding tensors versus experimental principal components of  $^{15}\text{N}$  chemical-shift tensors. (a) GIPAW, (b) Clusters ..... 124

- Figure 4.6.** Calculated principal components of  $^{19}\text{F}$  magnetic-shielding tensors versus experimental principal components of  $^{19}\text{F}$  chemical-shift tensors. (a) GIPAW, (b) Clusters ..... 125
- Figure 4.7.** Calculated principal components of  $^{31}\text{P}$  magnetic-shielding tensors versus experimental principal components of  $^{31}\text{P}$  chemical-shift tensors. (a) GIPAW, (b) Clusters. .... 126
- Figure 4.8.** Difference between GGA-PBE- and PBE0-calculated  $^{13}\text{C}$  principal chemical-shielding values for  $sp^3$ -hybridized (red) and  $sp^2$ - and  $sp$ -hybridized (blue) sites. The trend lines are meant to guide the eye. .... 132
- Figure 4.9** Deviation of the extrapolated magnetic shielding of the reference compound obtained with least-squares analyses for various DFT functionals from the accepted literature value. Results are shown for  $^{13}\text{C}$  (a),  $^{15}\text{N}$  (b),  $^{19}\text{F}$ (c), and  $^{31}\text{P}$  (d). The reference compounds and literature shielding values are TMS at 184.1 ppm ( $^{13}\text{C}$ ) [176],  $\text{CH}_3\text{NO}_2$  at -135.8 ppm ( $^{15}\text{N}$ ) [177],  $\text{CFCl}_3$  at 188.7 ppm ( $^{19}\text{F}$ ) [178], and 85%  $\text{H}_3\text{PO}_4$  at 328.4 ppm ( $^{31}\text{P}$ ) [179]. A finite-basis-set corrections was applied to each calculated value by subtracting 3.8 ppm ( $^{13}\text{C}$ ), 19 ppm ( $^{15}\text{N}$ ), 1 ppm ( $^{19}\text{F}$ ), and 48 ppm ( $^{31}\text{P}$ ) from calculated values of *oref*. The error bars represent both the uncertainty in the calculated and experimental values and the basis-set correction. Pure DFT functionals are shown in red and hybrid functionals are shown in blue. .... 133
- Figure 4.10.** (a) Differences in computed shielding between the GGA-PBE functional and the hybrid GGA-PBE0 functional. (b) Differences in computed shielding between the GGA-PBE functional and the meta-GGA-TPSS functional..... 136
- Figure 5.1.** Schematic drawings showing clusters of calcium formate (upper left), calcium acetate site Ca1 (lower left),  $\text{CaSO}_4 \cdot 2\text{H}_2\text{O}$  (upper right), and calcite (lower right). The cc-pVTZ region is shown in the ball-and-stick representation and the cc-pVDZ region is shown in the wireframe representation. .... 160
- Figure 5.2.** Illustration of three clusters to represent the local  $^{43}\text{Ca}$  environment in  $\text{CaCl}_2 \cdot 2\text{H}_2\text{O}$ . Upper left: 1<sup>st</sup>-co-ordination shell cluster with composition  $[\text{CaCl}_4(\text{H}_2\text{O})_2]^{2-}$ . Lower left: 3<sup>rd</sup>-co-ordination shell cluster with composition  $[\text{Ca}_5\text{Cl}_{16}(\text{H}_2\text{O})_{24}]^{6-}$ . Right: 5<sup>th</sup>-co-ordination shell cluster with composition  $[\text{Ca}_{13}\text{Cl}_{36}\text{H}_{12}(\text{H}_2\text{O})_{56}]^{2+}$  ..... 163

- Figure 5.3.** Plots illustrating the relationship between principal components of calculated  $^{43}\text{Ca}$  magnetic-shielding tensors and experimental chemical-shift tensors obtained using (a) the periodic GIPAW approach and (b) the cluster approach. Plots illustrating the relationship between principal components of calculated and experimental  $^{43}\text{Ca}$  quadrupolar-coupling tensors obtained using (c) the periodic GIPAW approach and (d) the cluster approach. Results were computed at the PBE level of theory with a plane-wave cutoff energy of 600 eV (GIPAW) or with the cc-pVTZ basis set (clusters). Best-fit lines (a,b) and ideal (c,d) relationships are shown as dotted black lines. .... 166
- Figure 5.4.** Mean absolute errors between calculated and experimental  $^{43}\text{Ca}$  chemical-shift tensors. Results obtained using GIPAW are shown in red, DFT results obtained using clusters are shown in blue, and Hartree-Fock results are shown in green. .... 172
- Figure 5.5.** Relationship between calculated principal values of  $^{43}\text{Ca}$  magnetic-shielding tensors and experimental principal values of  $^{43}\text{Ca}$  chemical-shift tensors obtained at the PBE (blue squares) and Hartree-Fock (red circles) levels. .... 173
- Figure 6.1.** Illustration of third-co-ordination-shell clusters for  $\text{Mg}_2\text{SiO}_4$  and  $\text{Mg}_3(\text{PO}_4)_2$ . The TZ2P region is shown in ball-and-stick model and the TZP region is shown as a wireframe model. .... 187
- Figure 6.2.** Clusters of  $\text{SiO}_2$  expanded around the NMR-active  $^{29}\text{Si}$  site to the first (left), third (center) and fifth (right) co-ordination shells. The TZ2P layer is shown in the ball-and-stick representation and the TZP region is shown in the wireframe representation. .... 188
- Figure 6.3.** Plots illustrating the relationship between calculated and experimental principal components of  $^{29}\text{Si}$  magnetic-shielding tensors. Values obtained using the GIPAW approach are shown in red, and results obtained using the cluster-based VMTA/BV approach are shown in blue. Results were computed at the PBE level of theory. The best-fit lines are shown in black. .... 194
- Figure 6.4.** Plots illustrating the relationship between calculated and experimental principal components of  $^{31}\text{P}$  magnetic-shielding tensors. Values obtained using the GIPAW approach are shown in red, and results obtained using the cluster-based VMTA/BV approach are shown in blue. Results were computed at the PBE level of theory. The best-fit lines are shown in black. .... 195

<b>Figure 6.5.</b> Plot illustrating the relationship between calculated and experimental principal components of $^{29}\text{Si}$ magnetic-shielding tensors. Results were computed at the PBE0 level of theory. The best-fit lines are shown in black. ....	198
<b>Figure 6.6.</b> Plot illustrating the relationship between calculated and experimental principal components of $^{31}\text{P}$ magnetic-shielding tensors. Results were computed at the PBE0 level of theory. The best-fit lines are shown in black. ....	199
<b>Figure 6.7.</b> Correlation between the linear-regression parameters $m$ and $b$ for eight DFT model chemistries. Results for $^{29}\text{Si}$ and $^{31}\text{P}$ are shown in red and blue, respectively. GIPAW results are shown as circles; cluster-based VMTA/BV results are shown as squares. ....	201
<b>Figure 7.1.</b> Mean-absolute errors (MAEs) in computed $^{17}\text{O}$ quadrupolar-coupling tensors as a function of the value of the damping parameter ( $2.5 \leq d \leq 12$ ) used in the structural refinement using PW91-D2. The minimum MAEs for the materials cluster around a value of $d = 3.5$ . ....	219
<b>Figure 7.2.</b> Changes in bond lengths in model compounds between X-ray diffraction and refined crystal structures. Black: PW91 v. X-ray; dark grey: PW91-D2* v. X-ray; light grey: PW91 v. PW91-D2*. ....	222
<b>Figure 7.3.</b> Relationship between principal components of calculated $^{17}\text{O}$ quadrupolar-coupling tensors and experimental principal components of $^{17}\text{O}$ quadrupolar-coupling tensors. Computed results were obtained from (a) X-ray diffraction structures, (b) structures obtained with refinement using PW91, and (c) structures obtained with refinement using PW91-D2*. The dashed lines represent perfect agreement between calculated and experimental values. ....	224
<b>Figure 7.4.</b> Correlation between experimental chemical-shift tensors and calculated magnetic-shielding tensors for (a) $^{13}\text{C}$ sites, (b) $^{15}\text{N}$ sites, and (c) $^{17}\text{O}$ sites. Computed magnetic-shielding constants were obtained from either unrefined X-ray diffraction structures (red crosses) or PW91-D2* refinements of diffraction structures (black circles). ....	233

**Figure 7.5.** Mean-absolute errors between calculated and experimental  $^{17}\text{O}$  quadrupolar coupling tensors in formic acid, acetic acid, oxalic acid·2H<sub>2</sub>O, urea, benzamide, L-alanine, taurine, salicylic acid, glycine·HCl, and valine·HCl. Calculated values were obtained using X-ray diffraction structures (black), neutron-diffraction structures (dark grey) or PW91-D2\*-refined X-ray diffraction structures (light grey)..... 235

## ABSTRACT

This dissertation presents quantum-mechanical calculations of nuclear magnetic resonance (NMR) parameters in crystalline solids. Several themes run through the dissertation; they all relate to aspects of the prediction of magnetic-shielding tensors and quadrupolar-coupling tensors for various light nuclides such as  $^{13}\text{C}$ ,  $^{15}\text{N}$ ,  $^{17}\text{O}$ ,  $^{19}\text{F}$ ,  $^{29}\text{Si}$ ,  $^{31}\text{P}$ ,  $^{35}\text{Cl}$ , and  $^{43}\text{Ca}$ .

A cluster-based computational protocol for modeling NMR parameters in molecular solids, referred to as the symmetry-adapted cluster *ansatz*, is discussed. This approach uses a shell of molecules to represent the local lattice environment by judiciously selecting molecules to maintain the rotational symmetry elements of the crystal space group. Chapter 2 illustrates the utility of the cluster-based approach through calculations of the principal components of the  $^{13}\text{C}$  magnetic-shielding tensors of 155 carbon sites. In Chapter 3, this analysis is applied to the assignment of the  $^{13}\text{C}$  chemical-shift tensors of the aromatic compound indigo. Chapter 4 focuses on comparison of  $^{13}\text{C}$ ,  $^{15}\text{N}$ ,  $^{19}\text{F}$ , and  $^{31}\text{P}$  magnetic-shielding tensors calculated using the cluster *ansatz* with results of using the periodic GIPAW approach. This analysis is based on calculation of the magnetic-shielding tensors of 131 NMR-active sites in 72 materials. Furthermore, benchmark calculations are provided for a large number of density functionals, including GGA, meta-GGA, and hybrid approaches.

Chapters 5 and 6 expand the focus to the calculation of NMR parameters in network solids. Chapter 5 presents  $^{43}\text{Ca}$  magnetic-shielding and quadrupolar-coupling tensors in calcium carboxylates, and Chapter 6 presents  $^{29}\text{Si}$  and  $^{31}\text{P}$  magnetic-shielding tensors in covalent network solids. In both chapters, the cluster-based approach is

benchmarked against the GIPAW approach, and various model chemistries are assessed. The calculation of  $^{29}\text{Si}$  and  $^{31}\text{P}$  magnetic-shielding tensors employs an approach in which the outermost atoms of the cluster are replaced with pseudoatoms that reduce the overall charge on the cluster to permit SCF convergence.

In addition to benchmarking cluster-based calculations of solid-state NMR parameters, applications in NMR crystallography, based on computed  $^{17}\text{O}$  quadrupolar-coupling tensors, are assessed. In particular, a method of semi-empirical geometry optimization is proposed, in which a dispersion force field is parameterized to produce structures that yield accurate predictions of  $^{17}\text{O}$  quadrupolar-coupling tensors.

# Chapter 1

## INTRODUCTION

### 1.1 Motivation and Outline

Nuclear magnetic resonance (NMR) spectroscopy is a powerful tool for the analysis of chemical structure [1, 2]. NMR parameters, such as magnetic shielding and quadrupolar coupling, provide a means of examining the structure and dynamics of solids [3]. The utility of NMR spectroscopy for structural analysis results from differences in nuclear transition energies due to variations in the local magnetic field between sites in varying chemical environments [4, 5]. The principal components of the tensors that describe the interaction of nuclei and the environment give insight into three-dimensional structure.

Computer-based numerical techniques to solve quantum-mechanical problems are a common tool to unravel the relationship between NMR parameters and structure. Modern quantum-mechanical calculations can achieve a degree of accuracy, which allows the discovery of the link between chemical environment and observed NMR parameters [6]. When dealing with solids, one must consider the local lattice structure, and this requirement necessitates significant computational resources to manage the calculations efficiently [7].

This work presents several contributions to the accurate and efficient prediction of NMR parameters in solids. In particular, a large component of this study is devoted

to demonstrating the utility of cluster-based calculations of magnetic-shielding and quadrupolar-coupling tensors in crystalline materials for a variety of light nuclides, including  $^{13}\text{C}$ ,  $^{15}\text{N}$ ,  $^{17}\text{O}$ ,  $^{19}\text{F}$ ,  $^{29}\text{Si}$ ,  $^{31}\text{P}$ ,  $^{35}\text{Cl}$ , and  $^{43}\text{Ca}$ . Further emphasis is placed on the combination of experimental NMR data with computational approaches to interpret or refine structural details in solids.

Three inter-related themes recur throughout this study, each relating to a practical aspect of the prediction and interpretation of NMR spectra. The first of these themes is the intimate relationship between solid-state structure and NMR observables. A practical difficulty in using NMR for analysis is assignment of resonance lines and bands to specific chemical structures in cases where multiple nuclear sites are present. Thus, such predictions must be robust enough to distinguish between closely-related chemical sites. The second theme concerns correct modeling of extended lattice effects on computed NMR parameters. Although it is common to model the crystalline lattice using periodic-boundary conditions (PBCs), it is also possible to account for extended effects using a cluster of atoms or molecules that represent a local portion of the lattice. The cluster *ansatz* is studied thoroughly in this work, with emphasis on the performance of this model relative to calculations employing PBCs. The third theme relates to theoretical considerations associated with the choice of model chemistry in calculations. The majority of calculations in this work are performed within the framework of density functional theory (DFT). The computational advantages associated with DFT calculations of electronic structure rely on inherent approximations, which can result in systematic errors in the prediction of NMR parameters. It is therefore necessary to study systematically the effects of different approximations on computed NMR parameters.

This dissertation is organized into four parts. The present chapter is concerned with providing necessary background information regarding the theory and calculation of NMR parameters. Chapters 2 – 6 are concerned with benchmarking the accuracy of cluster-based calculations of solid-state NMR parameters. Chapter 7 focuses on the emerging field of NMR crystallography, and illustrates a novel semi-empirical approach to refine the coordinates of atoms in crystal structures using experimental NMR constraints. Finally, Chapter 8 presents conclusions and an outlook on future work.

Chapters 2 – 6 are concerned with validating the use of cluster-based calculations for prediction of NMR parameters in solids. Chapter 2, “The Symmetry-Adapted Cluster *Ansatz*: Calculations of  $^{13}\text{C}$  Magnetic-Shielding Tensors”, provides a series of calculations of  $^{13}\text{C}$  magnetic-shielding tensors where lattice structure is described using cluster models. There I discuss criteria for selecting appropriate molecules to build adequate clusters, and electronic-structure approximations that make such calculations feasible. Chapter 3, “Carbon-13 Chemical-Shift Tensors in Indigo: A Two-Dimensional NMR-ROCSA Study”, provides measurements and assignments of the eight unique  $^{13}\text{C}$  chemical-shift tensors in the heteroatomic polycyclic aromatic dye indigo, aided by computational studies. Chapter 4, “Critical Analysis of Cluster Models and Exchange-Correlation Functionals for Calculating Magnetic Shielding in Molecular Solids”, provides a side-by-side comparison of  $^{13}\text{C}$ ,  $^{15}\text{N}$ ,  $^{19}\text{F}$ , and  $^{31}\text{P}$  magnetic-shielding tensors computed in a cluster-based framework with those computed in a periodic framework. The chapter also explores the dependence of computed magnetic-shielding tensors for these four nuclides on the choice of model chemistry, including the combination of DFT functional and basis set. General conclusions are drawn for several important classes of functionals. Chapter 5, “Calculations of Solid-State  $^{43}\text{Ca}$  NMR

Parameters: A Comparison of Periodic and Cluster Approaches and an Evaluation of DFT Functionals” expands this analysis to the prediction of  $^{43}\text{Ca}$  chemical-shift and quadrupolar-coupling tensors to extended network solids, with an emphasis on metal carboxylates. A comparison is made between periodic and cluster-based modeling techniques, and seventeen standard DFT approximations are assessed. Chapter 6, “Analysis of the of the Bond-Valence Method for Calculating  $^{29}\text{Si}$  and  $^{31}\text{P}$  Magnetic Shielding in Covalent Network Solids” expands the discussion to covalent network solids, such as silicates and phosphates, and shows that these methods are sufficient to calculate  $^{29}\text{Si}$  and  $^{31}\text{P}$  magnetic-shielding tensors in minerals. Chapter 7 focuses on the emerging field of NMR crystallography, specifically the calculation of  $^{17}\text{O}$  quadrupolar-coupling tensors and their relationship to molecular and lattice structure. In particular, a method of performing semi-empirical geometry optimization is proposed, in which experimental  $^{17}\text{O}$  quadrupolar-coupling tensors are used to parameterize a dispersion force field which results in structures that can be used consistently to predict NMR parameters in excellent agreement with experiment.

## **1.2 Introduction to Nuclear Magnetic Resonance Spectroscopy**

NMR spectroscopy is an important technique in chemical and material analysis, with applications ranging from ceramics [8-11] to semiconductors [12-14], polymers [15-18], pharmaceuticals [19-21], zeolites [22-27], metal organic frameworks [28-30], catalysis [31-34], and biomaterials [35-37]. An excellent survey of applications of NMR spectroscopy based on analyses of various nuclides is found in ref. [3].

NMR spectroscopy relies on the coupling between nuclear spins and an external magnetic field. For an ensemble of nuclear spins, transition energies between the spin states are modulated by interaction with nearby electrons and nuclei. These

perturbations, which are closely linked with chemical and material structure, are described by the following Hamiltonian:

$$\begin{aligned} \hat{\mathbf{H}}_{k,NMR} = & \hat{\mathbf{H}}_{k,Z} + \hat{\mathbf{H}}_{k,rf} + \hat{\mathbf{H}}_{k,MS} + \hat{\mathbf{H}}_{k,Q} + \hat{\mathbf{H}}_{kl,D} + \hat{\mathbf{H}}_{kl,J} \\ & + \hat{\mathbf{H}}_{k,KS} + \hat{\mathbf{H}}_{k,SR} \cdots \end{aligned} \quad (\text{Eq. 1.1})$$

In Eq. 1.1, the total NMR Hamiltonian ( $\hat{\mathbf{H}}_{k,NMR}$ ) is decomposed into many individual components, which include, but are not limited to, the nuclear Zeeman Hamiltonian ( $\hat{\mathbf{H}}_{k,Z}$ ), the radio-frequency Hamiltonian ( $\hat{\mathbf{H}}_{k,rf}$ ), the magnetic-shielding Hamiltonian ( $\hat{\mathbf{H}}_{k,MS}$ ), the quadrupolar-coupling Hamiltonian ( $\hat{\mathbf{H}}_{k,Q}$ ), the direct ( $\hat{\mathbf{H}}_{kl,D}$ ) and indirect ( $\hat{\mathbf{H}}_{kl,J}$ ) spin-spin coupling Hamiltonians, the Knight-shift Hamiltonian ( $\hat{\mathbf{H}}_{k,KS}$ ), and the spin-rotation Hamiltonian ( $\hat{\mathbf{H}}_{k,SR}$ ). In the above expression, the subscript  $k$  denotes one-spin interactions whereas the subscript  $kl$  denotes two-spin interactions.

The quintessential Hamiltonian affecting nuclear spins is the Zeeman interaction, which describes the coupling between nuclear spins and the external magnetic field. Many of the Hamiltonians in Eq. 1.1 can be described mathematically by similar forms, and this Hamiltonian is the paradigm for description of interactions affecting nuclear spins.

In the absence of a magnetic field, nuclear magnetic dipoles are oriented randomly. Under these circumstances, energies of the various spin states are degenerate, the populations of spins are equal, and there is no net magnetization. In the presence of a magnetic field, nuclear angular-momentum states become non-degenerate and are occupied according to Boltzmann statistics. The energy differences between the subpopulations depend on the strength of the applied magnetic field. The Hamiltonian for the nuclear Zeeman interaction is given by:

$$\hat{\mathbf{H}}_{k,Z} = -\gamma_k \vec{\mathbf{I}}_k \cdot \vec{\mathbf{B}}_0 \quad (\text{Eq. 1.2})$$

In the above expression,  $\gamma_k$  is the magnetogyric ratio of nucleus  $k$ ,  $\vec{\mathbf{I}}_k$  is the nuclear spin vector, and  $\vec{\mathbf{B}}_0$  is the external magnetic field. Thus, the energy of a particular state is determined by orientation of the spin vector relative to the direction of the field in space. A similar form is seen for the interaction with the oscillating field,  $\vec{\mathbf{B}}_1$ , that is at the heart of coupling to an imposed radio-frequency source. Some other Hamiltonians have a form similar to the Zeeman Hamiltonian, as if the effect of an adjacent spin could be modeled as an “effective magnetic field” to which the spin of interest is coupled. Such a model is convenient, but one must carefully examine the assumption in a quantum system. Throughout the dissertation, as these interactions are examined, these forms will be discussed. This work is devoted largely to the calculation and interpretation of the magnetic shielding and quadrupolar coupling interaction. The remaining subsections of this chapter present necessary background information for interpreting these results.

### 1.3 Magnetic-Shielding Tensors

Nuclei in atoms and molecules are subject to a secondary screening field due to interaction with electronic currents affected by an external field [38, 39]. Interaction with electron density in the vicinity of the nuclei modulate the effects of the external field, relative to the field experienced by a bare nucleus. This effect is known as magnetic shielding ( $\sigma_k$ ). Because of the inherent relationship with electronic structure, magnetic shielding is a highly sensitive structural probe [39].

NMR experiments yield a shift in the resonance frequency for a particular chemical species  $k$  relative to an arbitrary reference material, rather than the absolute shielding relative to the bare nucleus. Experimentally, one obtains the chemical shift of

species  $k$  ( $\delta_k$ ), which is the difference in resonance frequency between species  $k$  ( $\omega_k$ ) and the reference frequency ( $\omega_{ref}$ ), expressed as a fraction (in ppm) of the reference frequency:

$$\delta_k = \frac{\omega_k - \omega_{ref}}{\omega_{ref}}. \quad (\text{Eq. 1.3})$$

The relationship between the experimental chemical shift,  $\delta_k$ , and the magnetic shielding,  $\sigma_k$ , is given by the following relationship:

$$\delta_k = \frac{\sigma_{ref} - \sigma_k}{1 - \sigma_{ref}}. \quad (\text{Eq. 1.4})$$

In the above expression,  $\sigma_{ref}$  is the magnetic shielding of the reference species. Because the denominator in this expression is close to unity, the expression is often approximated as:

$$\delta_k \approx \sigma_{ref} - \sigma_k. \quad (\text{Eq. 1.5})$$

The magnetic shielding constant relates the strength of the external field ( $\vec{\mathbf{B}}_0$ ) to the effective field,  $\vec{\mathbf{B}}_{eff}$ , in the vicinity of the nucleus:

$$\vec{\mathbf{B}}_{eff} = (1 - \sigma_k)\vec{\mathbf{B}}_0 \quad (\text{Eq. 1.6})$$

Substituting this definition into the expression for the Zeeman Hamiltonian, one obtains an expression for the magnetic shielding Hamiltonian:

$$\hat{\mathbf{H}}_{k,MS} = -\gamma_k \hat{\mathbf{I}}_k \cdot (1 - \sigma_k)\vec{\mathbf{B}}_0 \quad (\text{Eq. 1.7})$$

The magnetic shielding (sometimes called ‘‘chemical shielding’’ to indicate its connection to the chemical shift) refers to the screening field experienced at a nuclear site due to interactions with induced electronic currents [40, 41]. Magnetic shielding is formally defined as a second-rank tensor of the form:

$$\sigma_{k,\alpha\beta} = \left. \frac{\partial^2 E}{\partial \mu_\alpha \partial B_\beta} \right|_{\mu_\alpha=0, B_\beta=0} \quad \alpha, \beta = x, y, z \quad (\text{Eq. 1.8})$$

In Eq. 1.8,  $\mu_\alpha$  is the component of the nuclear magnetic moment in the  $\alpha$  direction,  $B_\beta$  is the component of the external field in the  $\beta$  direction,  $E$  is the total energy of the

system derived from the full Hamiltonian including electronic and nuclear terms [42], and the subscripts  $\alpha$  and  $\beta$  denote the projections of the two vectors onto different axes of a co-ordinate system defining both the structure and the field. The Cartesian representation of the chemical-shift tensor in an arbitrary co-ordinate system is given by:

$$\sigma_{k,\alpha\beta} = \begin{pmatrix} \sigma_{k,xx} & \sigma_{k,xy} & \sigma_{k,xz} \\ \sigma_{k,yx} & \sigma_{k,yy} & \sigma_{k,yz} \\ \sigma_{k,zx} & \sigma_{k,zy} & \sigma_{k,zz} \end{pmatrix} \quad (\text{Eq. 1.9})$$

The full tensor has nine unique elements; however, if the tensor is symmetric, or the antisymmetric components are negligibly small (as is often considered to be the case, but not guaranteed), the number of unique tensor elements is reduced to six ( $\sigma_{\alpha\beta} = \sigma_{\beta\alpha}$ ). Referred to a set of coordinates called the principal-axis system (PAS), the magnetic-shielding tensor is diagonal and is characterized by the three non-vanishing principal components:

$$\sigma_{k,\alpha\beta} = \begin{pmatrix} \sigma_{k,11} & 0 & 0 \\ 0 & \sigma_{k,22} & 0 \\ 0 & 0 & \sigma_{k,33} \end{pmatrix} \quad (\text{Eq. 1.10})$$

Knowledge of the principal components of the magnetic-shielding tensor provides significant insight into the three-dimensional electronic structure. In particular, structural effects on  $^{13}\text{C}$  magnetic-shielding tensors have received considerable interest, and numerous reviews on this subject are available [43, 44].

These effects are more often specified by the so-called chemical-shift tensor, where they are described relative to those of some reference object having a specific value of the shielding. The chemical-shift tensor has a similar form to the magnetic shielding tensor:

$$\begin{aligned}
\delta_{k,\alpha\beta} &= \begin{pmatrix} \delta_{k,11} & 0 & 0 \\ 0 & \delta_{k,22} & 0 \\ 0 & 0 & \delta_{k,33} \end{pmatrix} \\
&= \begin{pmatrix} \sigma_{ref} - \sigma_{k,11} & 0 & 0 \\ 0 & \sigma_{ref} - \sigma_{k,22} & 0 \\ 0 & 0 & \sigma_{ref} - \sigma_{k,33} \end{pmatrix}
\end{aligned} \tag{Eq. 1.11}$$

The principal components of these tensors are ranked using the frequency-ordered convention, such that  $\sigma_{11} \leq \sigma_{22} \leq \sigma_{33}$ , or as  $\delta_{11} \geq \delta_{22} \geq \delta_{33}$ . The three remaining determinants of the magnetic-shielding tensor or the chemical-shift tensor are the eigenvectors that relate the PAS to the experimental co-ordinate system [45]. In principle, the full tensor, including the relative orientations of the principal components with respect to the crystal axes, is available from a study of a single-crystal sample. In contrast, only the principal components of the chemical-shift tensor are available from the analysis of a randomly oriented ensemble of microcrystallites, unless there is some special symmetry requirement that allows one to specify particular principal axes relative to known crystal axes.

In addition to the frequency-ordered convention, conventions proposed by Haeberlen [46] and by Mason [47] are commonly used to present chemical-shift tensors. Haeberlen's convention describes the chemical-shift tensor in terms of the isotropic chemical shift ( $\delta_{iso}$ ), the anisotropy ( $\Delta$ ), and the asymmetry ( $\eta$ ) parameter. The isotropic chemical shift is the average of the three principal values. The anisotropy is proportional to the difference between the most shielded principal component of the chemical-shift tensor ( $\delta_{33}$ ) and the isotropic chemical shift, and the asymmetry is a measure of deviation from axial symmetry with values in the range of  $0 \leq \eta_{CS} \leq 1$ . Definitions of  $\delta_{iso}$ ,  $\Delta$ , and  $\eta_{CS}$  are given below.

$$\delta_{iso} = \frac{1}{3}(\delta_{11} + \delta_{22} + \delta_{33}) \tag{Eq. 1.12a}$$

$$\Delta = \frac{3}{2}(\delta_{33} - \delta_{iso}) \quad (\text{Eq. 1.12b})$$

$$\eta_{CS} = \frac{\delta_{22} - \delta_{11}}{\delta_{33} - \delta_{iso}} \quad (\text{Eq. 1.12c})$$

Mason's convention, reports the chemical-shift tensor in terms of the isotropic chemical shift, the span ( $\Omega$ ), and the skew ( $\kappa$ ), as summarized in Figure 1.1. The span is the difference between the least and most shielded principal components of the chemical-shift tensor. The skew is related to the difference between  $\delta_{22}$  and  $\delta_{iso}$  relative to the span with values in the range of  $-1 \leq \kappa \leq +1$ . Definitions of  $\Omega$  and  $\kappa$  are given below.

$$\Omega = \delta_{11} - \delta_{33} \quad (\text{Eq. 1.13a})$$

$$\kappa = 3 \frac{\delta_{22} - \delta_{iso}}{\delta_{11} - \delta_{33}} \quad (\text{Eq. 1.13b})$$

#### 1.4 Quadrupolar-Coupling Tensors

Nuclei with spins greater than  $1/2$  possess a quadrupole moment ( $Q$ ) due to the asymmetric distribution of charge within the nucleus [48]. Such nuclei interact with the local electric-field gradient (EFG), as described by the following Hamiltonian bilinear in the components of the nuclear spin:

$$\hat{\mathbf{H}}_Q = \frac{eQ}{2I(2I-1)\hbar} \vec{\mathbf{I}}_k \cdot \hat{\mathbf{V}}_{k,\alpha\beta} \cdot \vec{\mathbf{I}}_k \quad (\text{Eq. 1.14})$$

In the above expression,  $e$  is the elementary charge, and  $\vec{\mathbf{I}}_k$  and  $\hat{\mathbf{V}}_{k,\alpha\beta}$  represent the nuclear spin vector and the EFG tensor, respectively. The EFG tensor represents the second spatial derivatives of the electrostatic potential,  $V$ , resulting from the distribution of electrons and nuclei, as evaluated at the nucleus:

$$\hat{\mathbf{V}}_{k,\alpha\beta} = \frac{\partial^2 V}{\partial r_\alpha \partial r_\beta} \quad \alpha, \beta = x, y, z \quad (\text{Eq. 1.15})$$

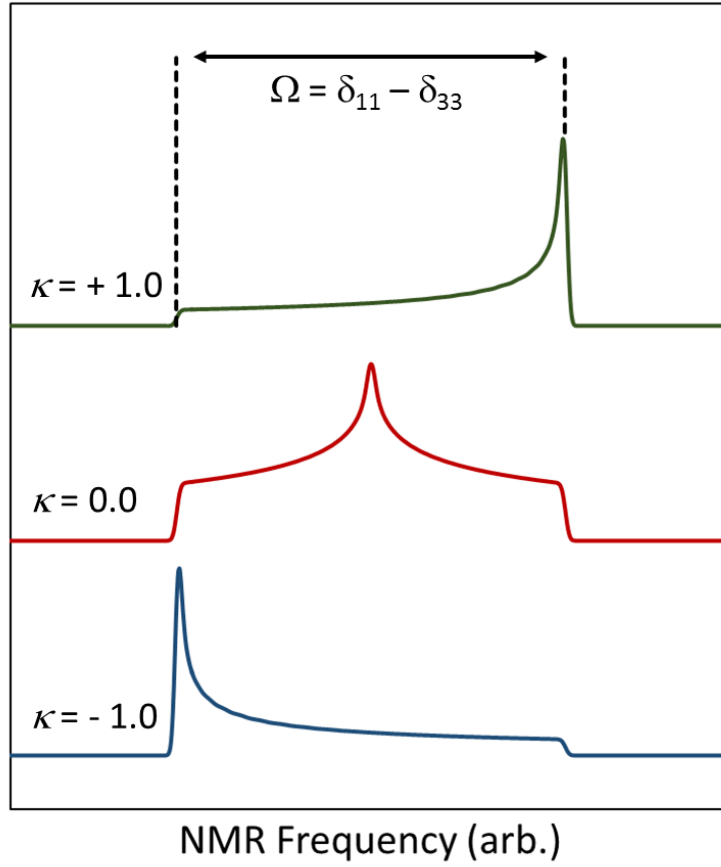


**Figure 1.1.** Simulated chemical-shift spectra of spin- $1/2$  nuclei in randomly oriented powders. Examples are shown for cases with axially symmetric ( $\kappa = \pm 1.0$ ) and radially symmetric ( $\kappa = 0.0$ ) chemical-shift tensors.

The EFG tensor can be represented as a  $3 \times 3$  matrix:

$$\hat{V}_{k,\alpha\beta} = \begin{pmatrix} V_{k,xx} & V_{k,xy} & V_{k,xz} \\ V_{k,yx} & V_{k,yy} & V_{k,yz} \\ V_{k,zx} & V_{k,zy} & V_{k,zz} \end{pmatrix} \quad (\text{Eq. 1.16})$$

As is the case with the magnetic-shielding tensor, the EFG tensor is diagonal in its PAS:

$$\hat{V}_{k,\alpha\beta} = \begin{pmatrix} V_{k,11} & 0 & 0 \\ 0 & V_{k,22} & 0 \\ 0 & 0 & V_{k,33} \end{pmatrix} \quad (\text{Eq. 1.17})$$

The principal components of this tensor are ranked such that  $|V_{k,33}| \geq |V_{k,22}| \geq |V_{k,11}|$ . Furthermore, the EFG tensor obeys Laplace's equation ( $\nabla^2 V = 0$ ), and is therefore traceless. Thus, there are only two independent parameters that describe the electric-field-gradient tensor.

The quadrupole interaction, as defined in Eq. 1.14, is therefore also described by two parameters, rather than three. It is typical to report these interaction parameters as the quadrupolar-coupling constant ( $C_Q$ ) and the asymmetry parameter ( $\eta$ ), of which, the latter is a measure of deviation from axial symmetry with values in the range of  $0 \leq \eta \leq 1$ :

$$C_Q = \frac{eQ}{h} V_{k,33} \quad (\text{Eq. 1.18})$$

$$\eta = \frac{V_{k,11} - V_{k,22}}{V_{k,33}} \quad (\text{Eq. 1.19})$$

Figure 1.2. illustrates several examples of simulated spectra for spin-1 nuclei in a randomly oriented powder, for which there are only two transitions. For spins with higher spin quantum numbers, the number of transitions increases, and therefore the appearance of the spectrum becomes considerably more complex.

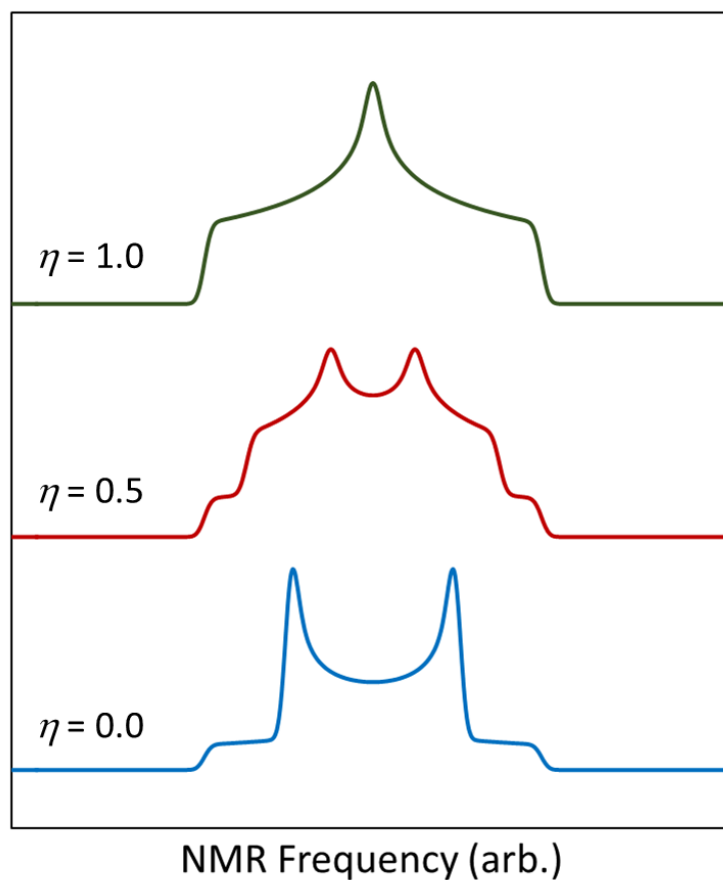


**Figure 1.2.** Simulated spectra of spin-1 nuclei in randomly oriented powders. Examples are shown for cases with asymmetry parameters of  $\eta = 0.0$ ,  $\eta = 0.5$ , and  $\eta = 1.0$

### 1.5 Overview of Electronic Structure Methods

With the advent of numerical techniques using computers to solve quantum-mechanical problems, predictions of NMR properties have become relatively routine for molecules containing light nuclei. In the non-relativistic limit, magnetic-shielding tensors and quadrupolar-coupling tensors are calculated as response properties from knowledge of the ground-state or excited-state wave functions. The remaining sections of this chapter are devoted to describing the calculation of such parameters.

Within the Born-Oppenheimer approximation, and in natural units, the time-independent Schrödinger equation is given by the following [49]:

$$\left( -\frac{1}{2} \sum_i^N \vec{\nabla}_i^2 - \sum_i^N \sum_A^M \frac{Z_A}{|\vec{\mathbf{r}}_i - \vec{\mathbf{R}}_A|} + \sum_i^N \sum_{j>1}^N \frac{1}{|\vec{\mathbf{r}}_i - \vec{\mathbf{r}}_j|} \right) \psi = E\psi \quad (\text{Eq. 1.20})$$

In this expression,  $\psi$  is the electronic wave function and  $E$  is the total electronic energy. The three terms in the Hamiltonian correspond to the total electron kinetic energy, electron-nucleus potential, and the inter-electronic potential. The summations in these terms are over the  $N$  electrons and  $M$  nuclei. Eq. 1.20 is often expressed in the shorthand notation as

$$(\hat{\mathbf{T}} + \hat{\mathbf{V}} + \hat{\mathbf{U}})\psi = E\psi \quad (\text{Eq. 1.21})$$

It is worth noting that the set of eigenvalues derived from evaluating this equation are the solutions associated with a particular set of nuclear coordinates, i.e.,  $E_{elec} = E_{elec}(\{\mathbf{R}_A\})$ . This fact suggests that computed energies vary according to nuclear-imposed geometry, a consideration that will be revisited throughout this work.

Schrödinger's equation cannot be solved exactly for a many-electron system due to the inter-electronic term, so approximate methods are necessary to obtain the wave function, a complex function of the  $3N$  spatial variables and  $N$  spin variables. Some of the more popular methods to solve Eq. 1.20 include Hartree-Fock theory [50-53], Møller-Plesset perturbation theory [54], and coupled-cluster theory [55, 56]. A comprehensive introduction to electronic structure calculation by Hartree-Fock and post Hartree-Fock methods is provided by Szabo and Ostlund [57].

The majority of calculations in this dissertation are performed within the formalism of density-functional theory (DFT), a popular quantum-mechanical technique in electronic-structure modeling [58, 59]. DFT allows chemical properties to

be calculated in a fashion that typically scales better with the number of electrons in the system than do calculations based on Hartree-Fock and post Hartree-Fock methods, and is therefore appropriate for modeling properties of materials. A general overview of DFT is available from Koch and Holthausen [59] and a more comprehensive treatment is available from Parr and Yang [60].

As the name implies, the central quantity in DFT is the electron density,  $\rho(\vec{\mathbf{r}})$ , which is given by:

$$\rho(\vec{\mathbf{r}}) = N \int \dots \int |\Psi(\vec{\mathbf{x}}_1 \vec{\mathbf{x}}_2 \dots \vec{\mathbf{x}}_N)|^2 d\vec{\mathbf{s}}_1 \vec{\mathbf{x}}_2 \dots \vec{\mathbf{x}}_N \quad (\text{Eq. 1.22})$$

Unlike the wave function, the electron density is a physical observable. Modern DFT derives from two theorems proposed by Hohenberg and Kohn [61]. These theorems illustrate that the  $3N$  variational degrees of freedom in Eq. 1.20 can be reduced to the 3 spatial coordinates of the density by reformulating the intractable many-body problem as a fictitious system composed of non-interacting electrons in an effective potential. The first Hohenberg-Kohn theorem demonstrates that two electrons experiencing external potentials  $v_1(\vec{\mathbf{r}})$  and  $v_2(\vec{\mathbf{r}})$  have the same ground-state energy if  $v_1(\vec{\mathbf{r}}) - v_2(\vec{\mathbf{r}}) = c$ , where  $c$  is a constant. The second Hohenberg-Kohn theorem defines the energy functional,  $E[\rho(\vec{\mathbf{r}})]$ , and illustrates that the ground-state electron density,  $\rho_0(\vec{\mathbf{r}})$ , minimizes the energy functional. It is therefore possible to obtain the ground-state density variationally. Furthermore, the ground-state wave function is a unique functional of the ground-state density:

$$\psi_0 = \psi[\rho_0(\vec{\mathbf{r}})] \quad (\text{Eq. 1.23})$$

Similarly, the expectation values ( $O$ ) of operations ( $\hat{\mathbf{O}}$ ) on the ground-state wave function are also functionals of the ground-state density:

$$O[\rho_0(\vec{\mathbf{r}})] = \langle \psi[\rho_0(\vec{\mathbf{r}})] | \hat{\mathbf{O}} | \psi[\rho_0(\vec{\mathbf{r}})] \rangle \quad (\text{Eq. 1.24})$$

In the Kohn-Sham formalism of DFT [62], the expression for the total energy is:

$$E[\rho(\vec{\mathbf{r}})] = T[\rho(\vec{\mathbf{r}})] + \int v_{ext}(\vec{\mathbf{r}}) \rho(\vec{\mathbf{r}}) d\vec{\mathbf{r}} + J[\rho(\vec{\mathbf{r}})] + E_{xc}[\rho(\vec{\mathbf{r}})] \quad (\text{Eq. 1.25})$$

This expression presents the kinetic energy,  $T[\rho(\vec{\mathbf{r}})]$ , the classical inter-electronic Coulombic potential,  $J[\rho(\vec{\mathbf{r}})]$ , and the non-classical exchange-correlation potential,  $E_{xc}[\rho(\vec{\mathbf{r}})]$ , as functionals of the electron density. The integral represents the interaction between the nuclei and the electron density. The final term,  $E_{xc}[\rho(\vec{\mathbf{r}})]$ , accounts for non-classical interactions between electrons. The form of the exchange-correlation energy is unknown and must be approximated. The kinetic energy is given by:

$$T[\rho(\vec{\mathbf{r}})] = -\frac{1}{2} \sum_i^N \int \langle \phi_i | \hat{\nabla}_i^2 | \phi_i \rangle d\vec{\mathbf{r}} \quad (\text{Eq. 1.26})$$

Here,  $\phi_i$  represents a one-electron Kohn-Sham orbital for the fictitious system with non-interacting electrons.

Implementation of the concepts behind this discussion leads to the integro-differential Kohn-Sham equation [62] for the one-electron orbitals:

$$\left( -\frac{1}{2} \nabla_i^2 + v_{ext}(\vec{\mathbf{r}}) + \int \frac{\rho(\vec{\mathbf{r}}')}{|\vec{\mathbf{r}} - \vec{\mathbf{r}}'|} d\vec{\mathbf{r}}' + v_{xc}(\vec{\mathbf{r}}) \right) \phi_i = \varepsilon \phi_i \quad (\text{Eq. 1.27})$$

The exchange-correlation functional in Eq. 1.27 is given by the following derivative:

$$v_{xc}(\vec{\mathbf{r}}) = \frac{\partial E_{xc}[\rho(\vec{\mathbf{r}})]}{\partial \rho(\vec{\mathbf{r}})} \quad (\text{Eq. 1.28})$$

Several of the potentials in Eq. 1.27, specifically the inter-electronic Coulomb potential and the exchange-correlation potential, depend on the density, and can only be solved through self-consistent-field (SCF) procedures. The first step in the SCF procedure is to introduce a basis-set expansion of the one-electron Kohn-Sham orbitals, thereby rendering Eq. 1.27 in a matrix form that can be solved computationally. The basis set describes the set of vectors which span the space in which the Kohn-Sham

equation is solved. Basis functions ( $\chi_r$ ) are used to construct molecular orbitals according to the linear combination of atomic orbitals (LCAO) scheme [63-65]:

$$\phi_\mu = \sum_r c_{\mu r} \chi_r \quad (\text{Eq. 1.29})$$

Eq. 1.27 is solved by introducing an initial guess for the expansion coefficients,  $c_{ri}$ , and iterating these values until a convergence threshold is reached.

At this stage, a few comments about DFT in a periodic framework are necessary. Electrons in systems containing periodic environments, such as a crystalline solid, are subject to periodic potentials, and the electron density is periodic with respect to translations along integral multiples of the lattice vectors,  $\vec{\mathbf{R}}_m$ :

$$\rho(\vec{\mathbf{r}}) = \rho(\vec{\mathbf{r}} + \vec{\mathbf{R}}_m) \quad (\text{Eq. 1.30})$$

By Bloch's theorem, the wave function is periodic with respect to translations along the lattice vectors:

$$\psi_{\mathbf{k}}(\vec{\mathbf{r}} + \vec{\mathbf{R}}_m) = e^{i\vec{\mathbf{k}} \cdot \vec{\mathbf{R}}_m} u_{\mathbf{k}}(\vec{\mathbf{r}}) \quad (\text{Eq. 1.31})$$

In Eq. 1.31,  $u_{\mathbf{k}}(\vec{\mathbf{r}}) = u_{\mathbf{k}}(\vec{\mathbf{r}} + \vec{\mathbf{R}}_m)$  is a periodic function of the unit cell's structural parameters. A plane-wave basis function is described by:

$$\psi_{\mathbf{k}}(\vec{\mathbf{r}}) = \sum_{\vec{\mathbf{G}}_m} c_{\mathbf{k}}(\vec{\mathbf{G}}_m) e^{i(\vec{\mathbf{k}} + \vec{\mathbf{G}}_m) \cdot \vec{\mathbf{r}}} \quad (\text{Eq. 1.32})$$

In Eq.1.32, the summation is over the lattice vectors in reciprocal space,  $\vec{\mathbf{G}}_m$ . The Coulomb, Hartree, and exchange-correlation (XC) potentials are computed in terms of their Fourier transforms by sampling the first Brillouin zone of the crystal's reciprocal lattice over a set of  $k$ -points. The size of the plane-wave basis set is governed by a plane-wave cutoff energy such that all plane waves with a kinetic energy under a defined threshold are included:

$$\frac{1}{2} |\vec{\mathbf{k}} + \vec{\mathbf{G}}_m|^2 \leq E \quad (\text{Eq. 1.33})$$

In practice, plane-wave basis sets are often paired with effective core potentials, or pseudopotentials, to describe the density of the core electrons. Common pseudopotential schemes include norm-conserving potentials [66] and ultrasoft potentials [67].

## 1.6 Exchange-Correlation Functionals

The Kohn-Sham formalism is, in principle, exact, provided the form of the exchange-correlation functional is known. However, because the form of the exchange-correlation functional is not known, there is a significant number of approximate models in the literature, but none of those models can be applied universally to arbitrary chemical systems [68, 69]. Almost all functionals are determined in some manner by arbitrary fitting parameters to give agreement either with empirical data or the results of earlier post Hartree-Fock calculations. The types of approximations can be sorted into classes of models, as described below.

### 1.6.1 The Local-Density Approximation

The local-density approximation (LDA) to the exchange-correlation energy was proposed by Kohn and Sham [62]. In the LDA,  $E_{XC}^{LDA}[\rho(\vec{\mathbf{r}})]$  is approximated by the energy of a homogeneous electron gas (HEG). This approach uses an exchange-correlation functional that is dependent only on the value of  $\rho(\vec{\mathbf{r}})$  at each point in space, and is therefore a local functional. The HEG model is a limit in which the atomic nuclear potentials, and therefore the electron density, are distributed uniformly in space. This simple model is sometimes used to model delocalized conduction-band electrons [70], but is generally insufficient for accurately modeling of systems, such as molecules, in which the density varies rapidly from point to point.

The general expression for the LDA exchange-correlation energy is:

$$E_{XC}^{LDA}[\rho(\vec{r})] = \int \rho(\vec{r})\epsilon_{XC}(\rho(\vec{r}))d\vec{r} \quad (\text{Eq. 1.34})$$

where  $\epsilon_{XC}$  is the exchange-correlation energy per electron of a HEG.  $E_{XC}^{LDA}$  can be linearly decomposed into the sum of exchange and correlation terms:

$$E_{XC}^{LDA} = E_X^{LDA} + E_C^{LDA} \quad (\text{Eq. 1.35})$$

This decomposition allows independent solutions to be derived for each term. The exchange energy ( $E_X^{LDA}$ ) of a HEG has a known analytic solution, as proposed by Dirac [71]:

$$E_X^{LDA}[\rho(\vec{r})] = -\frac{3}{4}\left(\frac{3}{\pi}\right)^{1/3} \int \rho^{4/3}(\vec{r})d\vec{r} \quad (\text{Eq. 1.36})$$

The correlation energy ( $E_C^{LDA}$ ) does not have an exact analytic form. Instead, approximate solutions for  $E_C^{LDA}$  are obtained through quantum Monte Carlo simulations [72-79]. Substitution of Eq. 1.34 into 1.28, one obtains the LDA exchange-correlation potential:

$$v_{XC}^{LDA} = \epsilon_{XC}(\rho(\vec{r})) + \frac{\partial\epsilon_{XC}(\rho(\vec{r}))}{\partial\rho(\vec{r})} \quad (\text{Eq. 1.37})$$

## 1.6.2 The Generalized-Gradient Approximation

The generalized-gradient approximation (GGA) improves upon the LDA by introducing a dependence in  $E_{XC}^{GGA}[\rho(\vec{r})]$  on the gradient of the density,  $\nabla\rho(\vec{r})$ , at each point in space (in addition to the density), as given by:

$$E_{XC}^{GGA}[\rho(\vec{r})] = \int \rho(\vec{r})\epsilon_{XC}(\rho(\vec{r}), \nabla\rho(\vec{r}))d\vec{r} \quad (\text{Eq. 1.38})$$

This generalized-gradient-approximation approach often results in improvement in the prediction of chemical properties relative to the LDA approach, particularly in cases where the density varies rapidly, and is therefore one of the most widely used DFT approximations. Many examples of GGA functionals are in the literature [80-82],

including the common functionals proposed by Perdew, Burke, and Ernzerhof (PBE) [83], and by Perdew and Wang (PW91) [84]. There also exist many modifications of the PBE functional such as the revised PBE (denoted rPBE throughout this dissertation) [85], which has been re-parameterized using a more comprehensive training set of thermochemical quantities.

### 1.6.3 The Meta-Generalized-Gradient Approximation

Further improvement in the prediction of chemical properties is possible through the use of the meta-generalized-gradient approximation, which incorporates a dependence in  $E_{CX}^{MGGGA}[\rho(\vec{r})]$  on the Laplacian of the density,  $\nabla^2\rho(\vec{r})$ , at each point in space (in addition to the density and the gradient of the density), yielding:

$$E_{XC}^{MGGGA}[\rho(\vec{r})] = \int \rho(\vec{r})\epsilon_{XC}(\rho(\vec{r}), \nabla\rho(\vec{r}), \nabla^2\rho(\vec{r}))d\vec{r} \quad (\text{Eq. 1.39})$$

In this dissertation, I shall use the meta-GGA functional of Tao, Perdew, Staroverov, and Scuseria (TPSS) [86] frequently, although other useful approximations could be used [87-89].

### 1.6.4 Hybrid Methods

Hybrid functionals are used evaluate  $E_{XC}[\rho(\vec{r})]$  in some cases. Hybrid functionals generally involve an admixture of non-local exact exchange from Hartree-Fock theory with DFT exchange-correlation. This approach, introduced by Becke [90], often leads to improvement of the prediction of thermochemical parameters, bond lengths, vibrational frequencies, and other measurable parameters, relative to pure DFT approaches [91]. For example, the PBE0 functional [92] is given by:

$$E_{XC}^{PBE0} = \frac{1}{4}E_X^{HF} + \frac{3}{4}E_X^{PBE} + E_C^{PBE} \quad (\text{Eq. 1.40})$$

The parameters in this expression, or the expression for other hybrid functionals, are generally obtained using a training set of thermochemical quantities for gas-phase systems. It is therefore necessary to point out that, because of the inclusion of experimental data in the construction of these functionals, the application of hybrid functionals to systems that are not chemically similar to the training set should be systematically benchmarked to understand the accuracy for such systems. It is possible, for example, that the proper admixture of Hartree-Fock exchange necessary to obtain agreement with experiment differs significantly from one type of material to another.

With hybrid functionals, the calculation of  $E_{XC}^{Hybrid}[\rho(\vec{\mathbf{r}})]$  requires an evaluation of the Hartree-Fock exchange energy. As discussed in section 1.5, evaluation of two-electron integrals in Hartree-Fock theory is computationally demanding. Thus, the increased accuracy in computed chemical quantities that is sometimes possible with hybrid DFT comes with the tradeoff of a significant increase in computational cost.

### 1.7 Theory and Calculation of Quadrupolar-Coupling Tensors

As given in Eq. 1.15, the EFG tensor represents the second spatial derivative of the electrostatic potential resulting from the distribution of electrons and nuclei, as evaluated at the nucleus. The electrostatic potential is a scalar quantity that defines the electric energy of a unit charge at a point in space. The total electrostatic potential at position  $\vec{\mathbf{r}}$  results from the superposition of the classical Coulombic potential of the nuclei and the quantum-mechanical potential of the electrons [93]:

$$V(\vec{\mathbf{r}}) = \sum_A \frac{Z_A}{|\vec{\mathbf{r}} - \vec{\mathbf{R}}_A|} - \int \frac{\rho(\vec{\mathbf{r}}')}{|\vec{\mathbf{r}} - \vec{\mathbf{r}}'|} d\vec{\mathbf{r}}' \quad (\text{Eq. 1.41})$$

The summation in Eq. 1.41 represents the interaction between the nucleus at position  $\vec{\mathbf{r}}$  and additional nuclei at positions  $\vec{\mathbf{R}}_A$ , whereas the integral represents the

interaction with electron density at position  $\vec{r}'$ . The second term in the electrostatic potential can be rewritten such that the total electrostatic potential is an expectation value [94]:

$$V(\vec{r}) = \sum_A \frac{Z_A}{|\vec{r} - \vec{R}_A|} - \sum_r \sum_s P_{rs} \left\langle \chi_r \left| \frac{1}{|\vec{r} - \vec{r}'|} \right| \chi_s \right\rangle \quad (\text{Eq. 1.42})$$

Here, the summation is over all pairs of basis functions  $\chi_r$  and  $\chi_s$ , and  $P_{rs}$  is an element of the density matrix between the basis functions. Substitution of the above expression into Eq. 1.15 results in the following definition of the EFG tensor:

$$\begin{aligned} \hat{V}_{k,\alpha\beta} &= \frac{\partial^2 V}{\partial r_\alpha \partial r_\beta} \\ &= \sum_A \frac{3(r_\alpha - R_{A,\alpha})(r_\beta - R_{A,\beta}) - \delta_{\alpha\beta}^K (\vec{r} - \vec{R}_A)^2}{|\vec{r} - \vec{R}_A|^5} \\ &+ \sum_r \sum_s P_{rs} \left\langle \chi_r \left| \frac{3(r_\alpha - r'_\alpha)(r_\beta - r'_\beta) - \delta_{\alpha\beta}^K (\vec{r} - \vec{r}')^2}{|\vec{r} - \vec{r}'|^5} \right| \chi_s \right\rangle \end{aligned} \quad (\text{Eq. 1.43})$$

$\delta_{\alpha\beta}^K$  is the Krönecker delta function. As Eq. 1.43 demonstrates, the EFG tensor has a classical component that depends only on the positions of the nuclei, and a quantum-mechanical component that depends on the electronic structure, and indirectly on the nuclear coordinates.

## 1.8 Theory and Calculation of Magnetic-Shielding Tensors

The formal definition of the magnetic-shielding tensor is given by Eq. 1.8, in which the shielding tensor is expressed as a mixed partial derivative of the total energy with respect to the magnetic dipole moment component,  $\mu_\alpha$ , and the magnetic field component,  $B_\beta$ . As proposed by Ramsey [39], and as utilized in subsequent implementations [95-101], an explicit expression for the shielding tensor is obtained from as a sum over states through use of a perturbation expansion.

Generic double perturbation theory uses a Taylor series to expand the Hamiltonian with the arbitrary expansion parameters  $\kappa$  and  $\lambda$ :

$$H = H^{(0)} + \kappa H^{(1,0)} + \lambda H^{(0,1)} + \kappa\lambda H^{(1,1)} + \dots \quad (\text{Eq. 1.44})$$

The total energy of the perturbed system is given by:

$$E = E^{(0)} + \kappa E^{(1,0)} + \lambda E^{(0,1)} + \kappa\lambda E^{(1,1)} + \dots \quad (\text{Eq. 1.45})$$

In non-degenerate time-independent perturbation theory, generic second-order expansion coefficients are given by the following expression [102]:

$$\begin{aligned} E_{11} &= \left. \frac{\partial^2 E}{\partial \lambda \partial \kappa} \right|_{\lambda=0, \kappa=0} \\ &= \langle \Psi_0 | \hat{\mathbf{H}}^{(1,1)} | \Psi_0 \rangle + 2Re \left[ \sum_{n \neq 0} \frac{\langle \Psi_0 | \hat{\mathbf{H}}^{(1,0)} | \Psi_p \rangle \langle \Psi_p | \hat{\mathbf{H}}^{(0,1)} | \Psi_0 \rangle}{E_p - E_0} \right] \\ &= \left\langle \Psi_0 \left| \frac{\partial^2 \hat{\mathbf{H}}}{\partial \mu_\alpha \partial B_\beta} \right| \Psi_0 \right\rangle + 2Re \left[ \sum_{n \neq 0} \frac{\langle \Psi_0 | \frac{\partial \hat{\mathbf{H}}}{\partial \mu_\alpha} | \Psi_p \rangle \langle \Psi_p | \frac{\partial \hat{\mathbf{H}}}{\partial B_\beta} | \Psi_0 \rangle}{E_p - E_0} \right] \end{aligned} \quad (\text{Eq. 1.46})$$

In the above expression, the subscripts 0 and  $p$  denote ground-state and excited-state wave functions, respectively.

The generic expression in Eq. 1.46 for second-order properties is related to the magnetic-shielding tensor by defining the Hamiltonian in the presence of an external magnetic field. This is done by substituting the angular momentum ( $\vec{\mathbf{p}}$ ) with the following expression [103]:

$$\vec{\mathbf{p}} \xrightarrow{sub.} \vec{\mathbf{p}} + \vec{\mathbf{A}}_i(\vec{\mathbf{r}}) \quad (\text{Eq. 1.47})$$

In the above expression,  $\vec{\mathbf{A}}_i(\vec{\mathbf{r}})$  is the total vector potential at the position of the  $i^{th}$  electron resulting from the sum of the vector potentials for the external magnetic field and the nuclear magnetic dipole field [104], given by:

$$\vec{\mathbf{A}}_i(\vec{\mathbf{r}}) = \frac{1}{2} \vec{\mathbf{B}}_0 \times \vec{\mathbf{r}}_{i0} + \frac{\vec{\boldsymbol{\mu}}_n \times \vec{\mathbf{r}}_{in}}{\mathbf{r}_{in}^3} \quad (\text{Eq. 1.48})$$

The second term in the above expression is irrelevant for the calculation of magnetic shielding, but is necessary for calculation of scalar-coupling constants. The subscripts  $0$  and  $n$  are used to denote the gauge-origin and nuclear-magnetic-moment position vectors, respectively. The expression for the Hamiltonian in the presence of an external magnetic field is [40]:

$$\hat{\mathbf{H}} = -\frac{1}{2} \sum_i^N [\vec{\nabla}_i + \vec{\mathbf{A}}_i(\vec{\mathbf{r}})]^2 - \sum_i^N \sum_A^M \frac{Z_A}{|\vec{\mathbf{r}}_i - \vec{\mathbf{R}}_A|} + \sum_i^N \sum_{j>1}^N \frac{1}{|\vec{\mathbf{r}}_i - \vec{\mathbf{r}}_j|} \quad (\text{Eq. 1.49})$$

The expansion of this Hamiltonian around  $\vec{\mathbf{B}}_0$  and  $\vec{\boldsymbol{\mu}}_n$  yields the following terms relevant to the calculation of magnetic-shielding tensors:

$$\hat{\mathbf{H}}^{(1,1)} = \frac{1}{2c^2} \sum_i^N \frac{\vec{\mathbf{r}}_{i0} \cdot \vec{\mathbf{r}}_{in} \delta_{\alpha\beta}^K - r_{i0,\alpha} r_{in,\beta}}{\vec{\mathbf{r}}_{in}^3} \quad (\text{Eq. 1.50a})$$

$$\hat{\mathbf{H}}^{(1,0)} = \frac{1}{c^2} \sum_i^N \frac{\hat{\mathbf{L}}_{in}}{\vec{\mathbf{r}}_{in}^3} \quad (\text{Eq. 1.50b})$$

$$\hat{\mathbf{H}}^{(0,1)} = \frac{1}{2} \sum_i^N \hat{\mathbf{L}}_{i0} \quad (\text{Eq. 1.50c})$$

In the above expressions,  $\hat{\mathbf{L}}_{in}$  and  $\hat{\mathbf{L}}_{i0}$  are angular-momentum operators with respect to the nuclear origin and gauge origin, respectively.

Insertion of the terms in Eq. 1.50 into Eq. 1.46 gives the following expression for the magnetic-shielding tensor:

$$\sigma_{\alpha\beta} = \frac{\partial^2 E}{\partial \mu_\alpha \partial B_\beta} = \langle \Psi_0 | \hat{\mathbf{H}}^{(1,1)} | \Psi_0 \rangle + 2Re \left[ \sum_{p \neq 0} \frac{\langle \Psi_0 | \hat{\mathbf{H}}^{(1,0)} | \Psi_p \rangle \langle \Psi_p | \hat{\mathbf{H}}^{(0,1)} | \Psi_0 \rangle}{E_p - E_0} \right] \quad (\text{Eq. 1.51})$$

This expression for the magnetic-shielding tensor is exact in the non-relativistic limit because the perturbation expansion includes all terms relevant to the magnetic shielding. In practice, the accuracy of such calculations depend on the accuracy of the computed ground-state and excited state densities.

As is evident in the previous discussion, there are two contributions to the shielding tensor, denoted the diamagnetic and paramagnetic contributions, i.e.,

$$\sigma_{\alpha\beta} = \sigma_{\alpha\beta}^d + \sigma_{\alpha\beta}^p \quad (\text{Eq. 1.52})$$

The diamagnetic term is calculated as an integral over the ground electronic state; as such, it depends on the mixing coefficients that describe the ground state [38]. The ground-state electronic wave function is a linear combination of products of atomic orbitals, and the integral becomes a sum of integrals over these one-electron orbitals. The paramagnetic contribution depends on the ground state as well as all excited electronic states. Because the diamagnetic contribution is mostly dependent on core electrons, the differences in magnetic shieldings between nuclei of the same type, but in different chemical environments, are mostly due to differences in paramagnetic contributions. It should be noted that only the total shielding is a physical observable; thus, decomposing the shielding into a sum of terms is done for purely mathematical reasons.

As implied by Eq. 1.48, calculations of magnetic-shielding tensors depend on the choice of gauge origin of the vector potential. The gauge-dependent terms cancel perfectly in the limit of a complete basis set; however, this is not the case in practical calculations. The most common solution to the gauge-origin problem in the framework of atomic orbital basis functions is referred to as the gauge-including atomic orbital (GIAO) method. The method is derived from the early work of London, who employed

this method for the calculation of electronic energies in the presence of an external magnetic field [105]. The use of GIAOs in the calculation of magnetic shielding was first illustrated in two landmark papers by Pople [40, 41]. The implementation of the GIAO method in SCF calculations originated with Ditchfield [96] and in DFT with Schreckenbach and Ziegler [100]. In the GIAO formalism, basis functions (Eq. 1.29) are augmented with a gauge-dependent phase factor:

$$\chi_{\mu}^{GIAO}(\vec{\mathbf{B}}_0) = \exp\left[-\frac{i}{2c}(\vec{\mathbf{B}}_0 \times \vec{\mathbf{R}}_{\mu}) \cdot \vec{\mathbf{r}}\right] \chi_{\mu} \quad (\text{Eq. 1.53})$$

In this expression,  $\vec{\mathbf{R}}_{\mu}$  is the position vector of basis function  $\chi_{\mu}$ .

The gauge-including projector-augmented wave (GIPAW) approach of Pickard and Mauri addresses the gauge problem with plane wave DFT [106]. As discussed previously (Section 1.5), plane-wave calculations are typically paired with pseudopotential approximations of the core electrons. However, this approximation results in an insufficient treatment of the interaction between core and valence electrons. Although this consideration is not critical for many properties, a proper description of core-valence interactions is essential for the prediction of magnetic shielding. The projector-augmented-wave (PAW) method of van de Walle and Blöchl allows the all-electron wave function to be reconstructed [107]. In essence, this linear transformation,

$$T_{PAW} = 1 + \sum_i (|\phi_i\rangle - |\tilde{\phi}_i\rangle) \langle \tilde{P}_i| \quad (\text{Eq. 1.54})$$

allows one to obtain the expectation value of an all-electron operator acting on the all-electron wave function,  $|\phi_i\rangle$ , in terms of the expectation value of a pseudopotential operator acting on a pseudo-partial wave function,  $|\tilde{\phi}_i\rangle$ . In the above expression,  $\tilde{P}_i$  refers to the set of projector functions. Although plane wave do not suffer from gauge dependence, the PAW transformation reintroduces this dependence. GIPAW augments

the PAW linear-transformation operators by introducing a phase factor to overcome the gauge problem:

$$T_{GIPAW} = 1 + \sum_i \exp \left[ -\frac{i}{2c} (\vec{\mathbf{B}}_0 \times \vec{\mathbf{R}}) \cdot \vec{\mathbf{r}} \right] (|\phi_i\rangle - |\tilde{\phi}_i\rangle) \langle \tilde{p}_i | \exp \left[ -\frac{i}{2c} (\vec{\mathbf{B}}_0 \times \vec{\mathbf{R}}) \cdot \vec{\mathbf{r}} \right] \quad (\text{Eq. 1.55})$$

The discussion in this chapter focused on the background theory necessary to understand DFT calculations of NMR parameters. Chapters 2 - 7 are devoted to the implementation of these methods for the prediction of magnetic-shielding and quadrupolar-coupling tensors in chemically-interesting solid-state materials.

## REFERENCES

- [1] E.M. Purcell, H.C. Torrey, R.V. Pound, Resonance absorption by nuclear magnetic moments in a solid, *Phys. Rev.*, 69 (1946) 37-38.
- [2] F. Bloch, W.W. Hansen, M. Packard, Nuclear induction, *Phys. Rev.*, 69 (1946) 127-127.
- [3] K.J.D. MacKenzie, M.E. Smith, *Multinuclear Solid-State NMR of Inorganic Materials*, Pergamon, Amsterdam, 2002.
- [4] C.P. Slichter, *Principles of Magnetic Resonance*, 3rd ed., Springer-Verlag, Heidelberg, 1992.
- [5] J.A. Pople, W.G. Schneider, H.J. Bernstein, *High-Resolution Nuclear Magnetic Resonance*, McGraw-Hill, New York, 1959.
- [6] J.C. Facelli, Chemical shift tensors: theory and application to molecular structural problems, *Prog. Nucl. Magn. Reson. Spectrosc.*, 58 (2011) 176-201.
- [7] C. Bonhomme, C. Gervais, F. Babonneau, C. Coelho, F. Pourpoint, T. Azais, S.E. Ashbrook, J.M. Griffin, J.R. Yates, F. Mauri, C.J. Pickard, First-principles calculation of NMR parameters using the gauge including projector augmented wave method: a chemist's point of view, *Chem. Rev.*, 112 (2012) 5733-5779.
- [8] M.R. Mitchell, D. Carnevale, R. Orr, K.R. Whittle, S.E. Ashbrook, Exploiting the chemical shielding anisotropy to probe structure and disorder in ceramics:  $^{89}\text{Y}$  MAS NMR and first-principles calculations, *J. Phys. Chem. C*, 116 (2012) 4273-4286.
- [9] K.J.D. MacKenzie, R.H. Meinhold, Prospects for  $^{137}\text{Ba}$  MAS NMR spectroscopy of ceramics and related inorganic materials, *Ceram. Int.*, 26 (2000) 87-92.
- [10] J. Emery, T. Šalkus, A. Abramova, M. Barré, A.F. Orliukas, NMR investigations in  $\text{Li}_{1.3}\text{Al}_{0.3}\text{Ti}_{1.7}(\text{PO}_4)_3$  ceramics. part I: structural aspect, *J. Phys. Chem. C*, 120 (2016) 26173-26186.
- [11] J. Emery, T. Šalkus, M. Barré, NMR investigations in  $\text{Li}_{1.3}\text{Al}_{0.3}\text{Ti}_{1.7}(\text{PO}_4)_3$  ceramics. part II: lithium dynamics, experiments, and model, *J. Phys. Chem. C*, 120 (2016) 26235-26243.
- [12] R.E. Taylor, F. Alkan, D. Koumoulis, M.P. Lake, D. King, C. Dybowski, L.S. Bouchard, A Combined NMR and DFT Study of Narrow Gap Semiconductors: The Case of PbTe, *J. Phys. Chem. C*, 117 (2013) 8959-8967.
- [13] R.E. Taylor, P.A. Beckmann, S. Bai, C. Dybowski,  $^{127}\text{I}$  and  $^{207}\text{Pb}$  solid-state NMR spectroscopy and nuclear spin relaxation in  $\text{PbI}_2$ : A preliminary study, *J. Phys. Chem. C*, 118 (2014) 9143-9153.
- [14] D. Koumoulis, R.E. Taylor, D. King, L.S. Bouchard, NMR study of native defects in PbSe, *Phys. Rev. B*, 90 (2014) 125201.

- [15] A.J. Brandolini, K.J. Rocco, C.R. Dybowski, Solid-state fluorine-19 NMR investigations of annealed poly(tetrafluoroethylene), *Macromolecules*, 17 (1984) 1455-1458.
- [16] P. Wormald, D.C. Apperley, F. Beaume, R.K. Harris, Fluorine-19 solid-state NMR investigation of regiodefective semicrystalline  $\alpha$ -poly(vinylidene fluoride), *Polymer*, 44 (2003) 643-651.
- [17] P. Wormald, B. Ameduri, R.K. Harris, P. Hazendonk, Fluorine-19 solid state NMR study of vinylidene fluoride polymers using selective relaxation filters, *Solid State Nucl. Magn. Reson.*, 30 (2006) 114-123.
- [18] P. Wormald, B. Ameduri, R.K. Harris, P. Hazendonk, High-resolution  $^{19}\text{F}$  and  $^1\text{H}$  NMR of a vinylidene fluoride telomer, *Polymer*, 49 (2008) 3629-3638.
- [19] H. Hamaed, J.M. Pawlowski, B.F.T. Cooper, R. Fu, S.H. Eichhorn, R.W. Schurko, Application of solid-state  $^{35}\text{Cl}$  NMR to the structural characterization of hydrochloride pharmaceuticals and their polymorphs, *J. Am. Chem. Soc.*, 130 (2008) 11056-11065.
- [20] M. Hildebrand, H. Hamaed, A.M. Namespetra, J.M. Donohue, R. Fu, I. Hung, Z. Gan, R.W. Schurko,  $^{35}\text{Cl}$  solid-state NMR of HCl salts of active pharmaceutical ingredients: structural prediction, spectral fingerprinting and polymorph recognition, *CrystEngComm*, 16 (2014) 7334-7356.
- [21] W.D. Wang, X.D. Gao, M. Strohmeier, W. Wang, S. Bai, C. Dybowski, Solid-state NMR studies of form I of atorvastatin calcium, *J. Phys. Chem. B*, 116 (2012) 3641-3649.
- [22] G.E. Pavlovskaya, C.D. Ren, M. Van Buskirk, C. Dybowski, D.R. Corbin, J.A. Reimer, A.T. Bell, Cadmium solid state NMR studies of cadmium-exchanged zeolites, *Cat. Lett.*, 80 (2002) 19-24.
- [23] G.E. Pavlovskaya, C.F. Horton-Garcia, C. Dybowski, D.R. Corbin, T. Meersmann, Metallic clusters and color changes in silver-exchanged zeolites:  $^{109}\text{Ag}$  solid state NMR and optical studies, *J. Phys. Chem. B*, 108 (2004) 1584-1589.
- [24] Q. Chen, M.A. Springuel-Huet, J. Fraissard, M.L. Smith, D.R. Corbin, C. Dybowski, Study of ZSM-5 and ZSM-11 zeolites by xenon-129 NMR: effect of silicon/aluminum ratio, *J. Phys. Chem.*, 96 (1992) 10914-10917.
- [25] H.G. Niessen, M. Van Buskirk, C. Dybowski, D.R. Corbin, J.A. Reimer, A.T. Bell, Solid-state NMR studies of lead-containing zeolites, *J. Phys. Chem. B*, 105 (2001) 2945-2950.
- [26] M.L. Smith, D.R. Corbin, C. Dybowski, Effects of temperature on  $^{129}\text{Xe}$  NMR spectroscopy of xenon in zeolite rho, *J. Phys. Chem.*, 97 (1993) 9045-9047.
- [27] W. Morris, C.J. Stevens, R.E. Taylor, C. Dybowski, O.M. Yaghi, M.A. Garcia-Garibay, NMR and X-ray study revealing the rigidity of zeolitic imidazolate frameworks, *J. Phys. Chem. C*, 116 (2012) 13307-13312.
- [28] V.N. Vukotic, K.J. Harris, K. Zhu, R.W. Schurko, S.J. Loeb, Metal-organic frameworks with dynamic interlocked components, *Nat. Chem.*, 4 (2012) 456-460.

- [29] K. Zhu, V.N. Vukotic, C.A. O'Keefe, R.W. Schurko, S.J. Loeb, Metal-organic frameworks with mechanically interlocked pillars: controlling ring dynamics in the solid-state via a reversible phase change, *J. Am. Chem. Soc.*, 136 (2014) 7403-7409.
- [30] K. Zhu, C.A. O'Keefe, V.N. Vukotic, R.W. Schurko, S.J. Loeb, A molecular shuttle that operates inside a metal-organic framework, *Nat. Chem.*, 7 (2015) 514-519.
- [31] M. Engelsberg, C.S. Yannoni, M.A. Jacintha, C. Dybowski, R.E. de Souza,  $^{13}\text{C}$  dipolar NMR study of benzene chemisorbed on high-surface alumina-supported platinum, *J. Phys. Chem.*, 98 (1994) 2397-2402.
- [32] N.D. Triantafillou, M.L. Smith, M.A. Hepp, C.R. Dybowski, B.C. Gates, Deuterium adsorbed on MgO-supported iridium clusters: characterization by infrared and deuterium NMR spectroscopies, *Langmuir*, 10 (1994) 1793-1795.
- [33] M. Engelsberg, C.S. Yannoni, M.A. Jacintha, C. Dybowski, Geometry and dynamics of benzene chemisorbed on a Pt/ $\eta\text{-Al}_2\text{O}_3$  catalyst: a  $^{13}\text{C}$  dipolar NMR study, *J. Am. Chem. Soc.*, 114 (1992) 8319-8320.
- [34] C.F. Tirendi, G.A. Mills, C. Dybowski, G. Neue, Platinum-proton coupling in the NMR spectrum of benzene on an alumina-supported platinum catalyst, *J. Phys. Chem.*, 96 (1992) 5045-5048.
- [35] M.P. Bhate, A.E. McDermott, Protonation state of E71 in KcsA and its role for channel collapse and inactivation, *Proc. Natl. Acad. Sci. USA*, 109 (2012) 15265-15270.
- [36] B.J. Wylie, L.J. Sperling, A.J. Nieuwkoop, W.T. Franks, E. Oldfield, C.M. Rienstra, Ultrahigh resolution protein structures using NMR chemical shift tensors, *Proc. Natl. Acad. Sci. USA*, 108 (2011) 16974-16979.
- [37] G. Hou, S. Paramasivam, S. Yan, T. Polenova, A.J. Vega, Multidimensional magic angle spinning NMR spectroscopy for site-resolved measurement of proton chemical shift anisotropy in biological solids, *J. Am. Chem. Soc.*, 135 (2013) 1358-1368.
- [38] N.F. Ramsey, The internal diamagnetic field correction in measurements of the proton magnetic moment, *Phys. Rev.*, 77 (1950) 567-567.
- [39] N.F. Ramsey, Magnetic shielding of nuclei in molecules, *Phys. Rev.*, 78 (1950) 699-703.
- [40] J.A. Pople, The theory of chemical shifts in nuclear magnetic resonance. I. induced current densities, *Proc. R. Soc. London, Ser. A*, 239 (1957) 541-549.
- [41] J.A. Pople, The theory of chemical shifts in nuclear magnetic resonance. II. interpretation of proton shifts, *Proc. R. Soc. London, Ser. A*, 239 (1957) 550-556.
- [42] J. Autschbach, The calculation of NMR parameters in transition metal complexes, *Struct. Bond.*, 112 (2004) 1-48.
- [43] J.C. Facelli, D.M. Grant, J. Michl, Carbon-13 shielding tensors: experimental and theoretical determination, *Acc. Chem. Res.*, 20 (1987) 152-158.

- [44] D.M. Grant, F. Liu, R.J. Iulucci, C.G. Phung, J.C. Facelli, D.W. Alderman, Relationship of  $^{13}\text{C}$  NMR chemical shift tensors to diffraction structures, *Acta Crystallogr., Sect. B*, B51 (1995) 540-546.
- [45] D.W. Alderman, M.H. Sherwood, D.M. Grant, Comparing, modeling, and assigning chemical-shift tensors in the cartesian, irreducible spherical, and icosahedral representations, *J. Magn. Reson.*, 101 (1993) 188-197.
- [46] U. Haeberlen, *High Resolution NMR in Solids*, Academic Press, New York, 1976.
- [47] J. Mason, Conventions for the reporting of nuclear magnetic shielding (or shift) tensors suggested by participants in the NATO ARW on NMR shielding constants at the University of Maryland, College-Park, July 1992, *Solid State Nucl. Magn. Reson.*, 2 (1993) 285-288.
- [48] P.P. Man, Quadrupole Couplings in Nuclear Magnetic Resonance, General, *Encyclopedia of Analytical Chemistry*, John Wiley & Sons, Ltd 2006.
- [49] E. Schrödinger, An undulatory theory of the mechanics of atoms and molecules, *Phys. Rev.*, 28 (1926) 1049-1070.
- [50] D.R. Hartree, The wave mechanics of an atom with a non-Coulomb central field. part I. theory and methods, *Proc. Cambridge Philos. Soc.*, 24 (1928) 89-110.
- [51] D.R. Hartree, The wave mechanics of an atom with a non-Coulomb central field. part II. some results and discussion, *Proc. Cambridge Philos. Soc.*, 24 (1928) 111-132.
- [52] D.R. Hartree, The wave mechanics of an atom with a non-Coulomb central field. part III. term values and intensities in series an optical spectra, *Proc. Cambridge Philos. Soc.*, 24 (1928) 426-437.
- [53] A. Fock, Näherungsmethode zur lösung des quantenmechanischen mehrkörperproblems, *Z. Physik.*, 61 (1930) 126.
- [54] C. Møller, M.S. Plesset, Note on an approximation treatment for many-electron systems, *Phys. Rev.*, 46 (1934) 618-622.
- [55] F. Coester, H. Kümmel, Short-range correlations in nuclear wave functions, *Nucl. Phys.*, 17 (1960) 477-485.
- [56] J. Čížek, On the correlation problem in atomic and molecular systems. calculation of wavefunction components in Ursell-type expansion using quantum-field theoretical methods, *J. Chem. Phys.*, 45 (1966) 4256-4266.
- [57] A. Szabo, N.S. Ostlund, *Modern Quantum Chemistry: Introduction to Advanced Electronic Structure Theory*, First Edition, Revised ed., McGraw-Hill Publishing Company, New York, 1989.
- [58] W. Kohn, C.D. Sherrill, Editorial: Reflections on fifty years of density functional theory, *J. Chem. Phys.*, 140 (2014).

- [59] W. Koch, M.C. Holthausen, *A Chemist's Guide to Density Functional Theory*, 2<sup>nd</sup> Edition ed., Wiley-VHC, Weinheim, 2001.
- [60] R.G. Parr, W. Yang, *Density-Functional Theory of Atoms and Molecules*, Oxford University Press, Oxford, 1994.
- [61] P. Hohenberg, W. Kohn, Inhomogeneous electron gas, *Phys. Rev.*, 136 (1964) B864.
- [62] W. Kohn, L.J. Sham, Self-consistent equations including exchange and correlation effects, *Phys. Rev.*, 140 (1965) 1133-&.
- [63] S.F. Boys, Electronic wave functions. I. a general method of calculation for the stationary states of any molecular system, *Proc. R. Soc. London, Ser. A*, 200 (1950) 542-554.
- [64] J.C. Slater, Atomic shielding constants, *Phys. Rev.*, 36 (1930) 57-64.
- [65] J.A. Pople, P.M.W. Gill, B.G. Johnson, Kohn-Sham density-functional theory within a finite basis set, *Chem. Phys. Lett.*, 199 (1992) 557-560.
- [66] N. Troullier, J.L. Martins, Efficient pseudopotentials for plane-wave calculations, *Phys. Rev. B*, 43 (1991) 1993-2006.
- [67] D. Vanderbilt, Soft self-consistent pseudopotentials in a generalized eigenvalue formalism, *Phys. Rev. B*, 41 (1990) 7892-7895.
- [68] R. Peverati, D.G. Truhlar, Quest for a universal density functional: the accuracy of density functionals across a broad spectrum of databases in chemistry and physics, *Philos. Trans. R. Soc. London, Ser. A*, 372 (2014).
- [69] X. Xu, W.A. Goddard, Assessment of Handy–Cohen optimized exchange density functional (OPTX), *J. Phys. Chem. A*, 108 (2004) 8495-8504.
- [70] M.D. Segall, J.D.L. Philip, M.J. Probert, C.J. Pickard, P.J. Hasnip, S.J. Clark, M.C. Payne, First-principles simulation: ideas, illustrations and the CASTEP code, *J. Phys.: Condens. Matter*, 14 (2002) 2717.
- [71] P.A.M. Dirac, Note on exchange phenomena in the Thomas atom, *Proc. Cambridge Philos. Soc.*, 26 (1930) 376-385.
- [72] D.M. Ceperley, B.J. Alder, Ground state of the electron gas by a stochastic method, *Phys. Rev. Lett.*, 45 (1980) 566-569.
- [73] S.H. Vosko, L. Wilk, M. Nusair, Accurate spin-dependent electron liquid correlation energies for local spin density calculations: a critical analysis, *Can. J. Phys.*, 58 (1980) 1200-1211.
- [74] J.P. Perdew, A. Zunger, Self-interaction correction to density-functional approximations for many-electron systems, *Phys. Rev. B*, 23 (1981) 5048-5079.
- [75] L.A. Cole, J.P. Perdew, Calculated electron affinities of the elements, *Phys. Rev. A*, 25 (1982) 1265-1271.

- [76] J.P. Perdew, Density-functional approximation for the correlation-energy of the inhomogeneous electron-gas, *Phys. Rev. B*, 33 (1986) 8822-8824.
- [77] J.P. Perdew, J.A. Chevary, S.H. Vosko, K.A. Jackson, M.R. Pederson, D.J. Singh, C. Fiolhais, Atoms, molecules, solids, and surfaces: Applications of the generalized gradient approximation for exchange and correlation, *Phys. Rev. B*, 46 (1992) 6671-6687.
- [78] D.C. Langreth, M.J. Mehl, Beyond the local-density approximation in calculations of ground-state electronic properties, *Phys. Rev. B*, 28 (1983) 1809-1834.
- [79] T. Chachiyo, Communication: simple and accurate uniform electron gas correlation energy for the full range of densities, *J. Chem. Phys.*, 145 (2016) 021101.
- [80] C. Lee, W. Yang, R.G. Parr, Development of the Colle-Salvetti correlation-energy formula into a functional of the electron density, *Phys. Rev. B*, 37 (1988) 785-789.
- [81] A.D. Becke, Density-functional exchange-energy approximation with correct asymptotic behavior, *Phys. Rev. A*, 38 (1988) 3098-3100.
- [82] C. Adamo, V. Barone, Exchange functionals with improved long-range behavior and adiabatic connection methods without adjustable parameters: the mPW and mPW1PW models, *J. Chem. Phys.*, 108 (1998) 664-675.
- [83] J.P. Perdew, K. Burke, M. Ernzerhof, Generalized gradient approximation made simple, *Phys. Rev. Lett.*, 77 (1996) 3865-3868.
- [84] J.P. Perdew, Y. Wang, Accurate and simple analytic representation of the electron-gas correlation energy, *Phys. Rev. B*, 45 (1992) 13244.
- [85] B. Hammer, L.B. Hansen, J.K. Nørskov, Improved adsorption energetics within density-functional theory using revised Perdew-Burke-Ernzerhof functionals, *Phys. Rev. B*, 59 (1999) 7413-7421.
- [86] J.M. Tao, J.P. Perdew, V.N. Staroverov, G.E. Scuseria, Climbing the density functional ladder: nonempirical meta-generalized gradient approximation designed for molecules and solids, *Phys. Rev. Lett.*, 91 (2003) 146401.
- [87] J.P. Perdew, S. Kurth, A. Zupan, P. Blaha, Accurate density functional with correct formal properties: a step beyond the generalized gradient approximation, *Phys. Rev. Lett.*, 82 (1999) 2544-2547.
- [88] A.D. Boese, J.M.L. Martin, Development of density functionals for thermochemical kinetics, *J. Chem. Phys.*, 121 (2004) 3405-3416.
- [89] Y. Zhao, D.G. Truhlar, A new local density functional for main-group thermochemistry, transition metal bonding, thermochemical kinetics, and noncovalent interactions, *J. Chem. Phys.*, 125 (2006) 194101.
- [90] A.D. Becke, A new mixing of Hartree-Fock and local density-functional theories, *J. Chem. Phys.*, 98 (1993) 1372-1377.

- [91] J.P. Perdew, M. Ernzerhof, K. Burke, Rationale for mixing exact exchange with density functional approximations, *J. Chem. Phys.*, 105 (1996) 9982-9985.
- [92] C. Adamo, V. Barone, Toward reliable density functional methods without adjustable parameters: the PBE0 model, *J. Chem. Phys.*, 110 (1999) 6158-6170.
- [93] J.S. Murray, *Molecular Electrostatic Potentials: Concepts and Applications*, Elsevier, New York, 1996.
- [94] M. Kaupp, M. Buhl, V.G. Malkin, *Calculation of NMR and EPR Parameters: Theory and Applications*, WILEY-VCH Verlag GmbH & Co. KGaA, Weinheim, 2004.
- [95] R.M. Stevens, W.N. Lipscomb, R.M. Pitzer, Perturbed Hartree-Fock calculations. 1. magnetic susceptibility and shielding in the LiH molecule, *J. Chem. Phys.*, 38 (1963) 550-&.
- [96] R. Ditchfield, Self-consistent perturbation theory of diamagnetism, *Mol. Phys.*, 27 (1974) 789-807.
- [97] K. Wolinski, J.F. Hinton, P. Pulay, Efficient implementation of the gauge-independent atomic orbital method for NMR chemical shift calculations, *J. Am. Chem. Soc.*, 112 (1990) 8251-8260.
- [98] V.G. Malkin, O.L. Malkina, M.E. Casida, D.R. Salahub, Nuclear magnetic resonance shielding tensors calculated with a sum-over-states density functional perturbation theory, *J. Am. Chem. Soc.*, 116 (1994) 5898-5908.
- [99] P. Pulay, J.F. Hinton, K. Wolinski, Efficient Implementation of the GIAO Method for Magnetic Properties: Theory and Application, in: J.A. Tossell (Ed.) *Nuclear Magnetic Shieldings and Molecular Structure*, Springer Netherlands, Dordrecht, 1993, pp. 243-262.
- [100] G. Schreckenbach, T. Ziegler, Calculation of NMR shielding tensors using gauge-including atomic orbitals and modern density functional theory, *J. Phys. Chem.*, 99 (1995) 606-611.
- [101] J.R. Cheeseman, G.W. Trucks, T.A. Keith, M.J. Frisch, A comparison of models for calculating nuclear magnetic resonance shielding tensors, *J. Chem. Phys.*, 104 (1996) 5497-5509.
- [102] T. Helgaker, M. Jaszuński, K. Ruud, Ab initio methods for the calculation of NMR shielding and indirect spin-spin coupling constants, *Chem. Rev.*, 99 (1999) 293-352.
- [103] R. McWeeny, *Methods of Molecular Quantum Mechanics*, 2nd Ed., Academic Press, London, New York, 1989.
- [104] J.C. Facelli, Chemical shift tensors: theory and application to molecular structural problems, *Prog. Nucl. Magn. Reson. Spectrosc.*, 58 (2010) 176-201.
- [105] F. London, The quantum theory of inter-atomic currents in aromatic combinations, *J. Phys. Radium*, 8 (1937) 397.

[106] C.J. Pickard, F. Mauri, All-electron magnetic response with pseudopotentials: NMR chemical shifts, Phys. Rev. B, 63 (2001) 245101.

[107] C.G. Van de Walle, P.E. Blöchl, First-principles calculations of hyperfine parameters, Phys. Rev. B, 47 (1993) 4244-4255.

## Chapter 2

### THE SYMMETRY-ADAPTED CLUSTER ANSATZ: CALCULATIONS OF $^{13}\text{C}$ MAGNETIC-SHIELDING TENSORS

#### 2.1 Introduction

Chemical-shift tensors are a powerful gauge of local electronic geometry [1-4]. A variety of one- and two-dimensional methods for obtaining  $^{13}\text{C}$  chemical-shift tensors from the spectra of solids can be found in the literature [5-8]. It has become routine to acquire these data with accuracies as high as  $\pm 1$  ppm [9]. Despite the strong dependence on structure, it remains difficult to interpret chemical shifts in terms of local structure without quantum-chemical modeling [10-12]. Experimental chemical shifts are often correlated with calculated magnetic shieldings to gain a deeper insight into a material's local structure. The ever-increasing number of published solid-state  $^{13}\text{C}$  chemical-shift measurements has been met with a corresponding demand for highly accurate computational models for calculating magnetic shielding in solids [1].

In this chapter, I discuss specific challenges associated with calculations of magnetic-shielding tensors in molecular crystals. A survey of modern computational methodologies, including their shortcomings, is provided. In particular, a distinction is drawn between periodic calculations based on the GIPAW approach (discussed in the previous chapter) and calculations in which a cluster of molecules is employed to represent a local portion of the lattice. A generalized quantum-mechanical model to account for intermolecular contributions to the magnetic-shielding tensor using cluster models is proposed, and several of the inherent limitations are discussed, in particular, the requirements of size and symmetry adaptation.

I provide benchmark calculations of a wide variety of  $^{13}\text{C}$  magnetic-shielding tensors in organic solids, where the crystalline lattice is modeled according to the symmetry-adapted cluster method. Results are provided for 155 carbon sites from 24 materials. These materials, which include saccharides, aromatic rings, amino acids, nucleosides, active pharmaceutical ingredients, etc., were chosen to represent a wide variety of local electronic environments. Altogether, 465 chemical-shift principal components have been considered. Of these, 258 are from nuclei in aliphatic environments, 165 are from nuclei in aromatic environments, and 42 are from nuclei in carboxylic environments. Cluster models are shown to be appropriate for modeling magnetic-shielding tensors in a wide array of systems with a level of accuracy that matches, and sometimes surpasses, the GIPAW method. It is important to emphasize that the systematic use of clusters allows magnetic shielding to be calculated using model chemistries that are more advanced than those typically accessible in plane-wave codes such as GIPAW. The cluster-based method illustrated here opens the possibility of benchmarking a wide variety of model chemistries that have not been sufficiently studied for the prediction of magnetic-shielding tensors.

### **2.1.1 Models for Computing Magnetic Shielding in Solids**

Several effects are important when calculating magnetic shielding in a crystalline solid, which can largely be ignored in gas-phase systems [13]. Molecules maintain long-range spatial relationships with other molecules in the crystal lattice that are not averaged out by thermal motion. Individual molecules in a solid are often distorted from their idealized gas-phase structures by dispersion interactions, hydrogen bonding, and steric interactions with adjacent molecules. These effects may be observed as changes of bond lengths and angles, as bending in planar compounds, as locking the

orientation of a pendant group, or as any number of other differences from gas-phase structures. More than one unique molecule may be present in the asymmetric unit of a solid, giving rise to more nuclear sites than otherwise would be predicted on the basis of a unique molecule considered in isolation. Structural polymorphism may exist, in which the material has multiple stable crystalline phases that depend on the history of the sample, each polymorph having a unique set of magnetic-shielding parameters due to differences in local structure.

For a molecular solid, the shielding experienced at a nuclear site may be assumed to be due to internal currents in the molecule or to the effects of currents external to the molecule. Historically, many studies have focused solely on internal currents due to the cost of modeling the lattice in calculations of magnetic shielding. This simple approximation is referred to here as the isolated-molecule model. Studies examining intermolecular effects in heavy-nucleus-containing compounds, where the range of possible chemical shifts is much larger than that of  $^{13}\text{C}$ , illustrate how important intermolecular and lattice effects can be [14]. For example, the  $^{199}\text{Hg}$  chemical-shift tensor in  $\text{Hg}(\text{CN})_2$  is reported to differ from experiment by 1005 ppm when the lattice is modeled with a simple  $\text{Hg}(\text{CN})_2$  unit, whereas models that account for lattice effects decrease this error to only 285 ppm [14]. In cases where intermolecular effects are expected to be small, their contributions must still be considered to ensure that the model is an accurate representation of the material. The following subsections discuss several historical and contemporary methods that have been employed to model magnetic-shielding tensors.

The most direct method for modeling lattice effects of magnetic-shielding tensors is to use a cluster of atoms or molecules to represent the local electronic structure

around the NMR-active nuclei. Pioneering work on cluster-based calculations of magnetic shielding was performed by Tossell, who was interested in second-nearest neighbor effects on  $^{15}\text{N}$  chemical shifts in  $\text{Si}_3\text{N}_4$ ,  $\text{C}_3\text{N}_4$ ,  $\text{P}_3\text{N}_5$ , and hexagonal BN [15, 16], and on  $^{23}\text{Na}$  shielding in silicates and aluminosilicates [17]. Around the same time, Valero and co-workers calculated  $^{27}\text{Al}$  and  $^{29}\text{Si}$  shieldings in zeolites [18, 19]. Another early study examined  $^{23}\text{Na}$  isotropic shifts in several sodium oxides [20]. Cluster methods were employed more recently in a study of  $^{19}\text{F}$  magnetic shielding in inorganic fluorides [21, 22]. Alkan and Dybowski have examined the use of clusters for calculating  $^{119}\text{Sn}$ ,  $^{199}\text{Hg}$ , and  $^{207}\text{Pb}$  shifts in a large variety of materials [14, 23-27]. Burgess *et al.* have used cluster-based approaches to model  $^{25}\text{Mg}$  NMR parameters in magnesium carboxylates [28], and Chapman and Bryce have applied similar techniques to the prediction of  $^{35}\text{Cl}$  NMR parameters in amino acid hydrochlorides [29]. Orendt *et al.* have calculated  $^{13}\text{C}$  magnetic shielding of an acetate adduct of cadmium [30].

However, the study of structural effects on NMR parameters of molecular organic solids has been confined largely to materials of biological importance. In a survey of crystalline amino acids, Zheng *et al.* calculated the effects of hydrogen bonding on magnetic shielding [31]. In their study, the two nearest amino acid molecules were replaced by  $\text{NH}_3$  groups to reduce computational cost. Substitution of ammonia in the place of a larger ligand has been used in numerous studies [32]. The calculation of properties of small clusters, sometimes employing molecular fragments, also has been applied to determine  $^{15}\text{N}$  magnetic shielding [33-35]. In general, the effects of nearest neighbors have been explored in cases where neighboring molecules are involved in hydrogen-bonding or  $\pi$ -stacking interactions. Chen and Zhan performed calculations which included between six and nine complete molecules to represent the

local structure of a solid. With these models they were able to achieve better agreement with experiment than was possible with earlier small-cluster methods [36]. Cluster models have associated problems, the most prominent being the size of the cluster and the termination scheme. Furthermore, the computational cost associated with such calculations increases exponentially with the size of the cluster.

A second approach for modeling magnetic shielding in solid-state systems is provided by the embedded-ion method (EIM). A generalized EIM procedure, appropriate calculations of magnetic-shielding tensors in materials containing molecular ions, was proposed by Grant and co-workers [37]. A review of this method has been provided by Steuber [38]. The embedded ion method models extended solid-state effects by embedding a central molecule in an array of classical point charges centered on the crystallographic nuclear origins. The values of the point charges are chosen in an iterative, self-consistent manner based on natural-bond order (NBO) analysis. Such calculations lead to significant improvement in computed magnetic-shielding tensors relative to values obtained from isolated molecules. For example, the embedded-ion method has been applied successfully to calculations  $^{13}\text{C}$  magnetic shielding in ionic compounds such as  $\text{S}_2\text{CSCH}_3^-$  [37], to  $^{13}\text{C}$  and  $^{15}\text{N}$  magnetic shielding in nucleic acid bases [39], and the magnetic shielding in many other materials [40, 41]. Unfortunately, several problems with this method exist. Most importantly, non-Coulombic interactions that contribute to the intermolecular component of the magnetic shielding are ignored. Furthermore, SCF convergence is sometimes difficult due to difficulties associated with the interface of the classical and quantum-mechanical regions. To highlight the inherent errors associated with electrostatic embedding models, Ferrero compared calculations of  $^{15}\text{N}$  magnetic shielding using EIM with

calculations in which molecular fragments were used to model neighboring molecules, and found that the latter model resulted in superior agreement with experiment.

However, EIM is inherently complementary with cluster-based approaches. A study by Weber and Schmedt auf der Günne has applied the EIM to the prediction of  $^{31}\text{P}$  magnetic shielding in inorganic phosphates, including  $\text{Mg}_2\text{P}_2\text{O}_{12}$ ,  $\alpha\text{-Mg}_3(\text{PO}_4)_2$ ,  $\alpha\text{-Mg}_2\text{P}_2\text{O}_7$ , and  $\text{MgP}_4\text{O}_{11}$  [42]. A notable feature of this work is that the local structure around the NMR-active  $^{31}\text{P}$  sites were modeled with a small cluster of atoms. This method appears to alleviate, but not remove, some of the difficulties mentioned above. Strohmeier *et al.* applied a similar technique to modeling  $^{13}\text{C}$  and  $^{15}\text{N}$  magnetic-shielding tensors, and  $^{14}\text{N}$  quadrupolar-coupling tensors in amino acid crystals [43].

Another common approach to calculation of magnetic shielding in a solid is to use periodic-boundary conditions (PBCs), as is done in the GIPAW method. A review of applications of the GIPAW method has recently been presented [44], and a general outline of this computational approach has been discussed in Chapter 1. One particular study by Johnston *et al.* applied the GIPAW approach to the prediction of the complete chemical-shift tensors for the  $^{13}\text{C}$  sites in 14 materials [9]. The results concluded that GIPAW calculations are demonstrably superior to isolated-molecule models for predicting  $^{13}\text{C}$  NMR magnetic-shielding tensors. Isotropic chemical shifts were predicted with an accuracy of  $\pm 1$  ppm when systematic flaws in the calculations were removed through careful modeling of the results [9].

Despite the significant advances that have been made from GIPAW calculations of magnetic shielding, this approach has inherent limitations. For example, the majority of calculations based on the GIPAW approach have been performed within the formalism of the generalized-gradient approximation (GGA). Modern hybrid

functionals, which incorporate a portion of Hartree-Fock exchange, are known to improve calculations of atomization energies, ionization energies, and many other thermochemical properties [45]. Inclusion of this term also improves the quality of computed spectroscopic properties, including NMR parameters, due to the treatment of the band-gap problem [46-48]. However, Hartree-Fock exchange is difficult to implement in plane-wave calculations due to the appearance of a singularity that slows convergence [49]. Furthermore, GIPAW calculations of magnetic shielding are limited to lighter nuclei due to the inherent treatment of relativistic effects [27]. Thus, studies in the literature employing GIPAW are restricted to a limited range of model chemistries.

A set of computational protocols that allows the implementation of modern model chemistries in the prediction of solid-state NMR parameters is, therefore, inherently valuable. As discussed previously, a possible alternative to the GIPAW approach for modeling solid-state NMR parameters is to employ a cluster of molecules that sufficiently accounts for intermolecular interactions. Cluster-based calculations have the advantage that they are not limited to periodic systems and can be applied to amorphous solids, nanostructures, surfaces, biological systems, and gas-phase aggregations of molecules [50]. Furthermore, cluster-based calculations can be implemented in many standard quantum-mechanical software packages where a wide array of model chemistries are available. All of these considerations make an exploration of the advantages and limitations of cluster methodologies of fundamental importance.

Despite the successes of early cluster-based calculations of chemical shifts, the selection of nearby molecules (or molecular fragments) that contribute substantially to

predicted magnetic shielding long appeared somewhat arbitrary, and depended, to a large extent, on chemical intuition for the judicious choice of which molecules to include in the cluster. Clusters should be designed to reflect the lattice structure around the NMR-active nucleus. For a molecular solid, a cluster can be defined by a shell of adjacent molecules around one central molecule.

Calculations of magnetic shielding involves the evaluation of three-centered integrals of the general form:

$$\langle \phi_a | \hat{L}_k | \phi_b \rangle \neq 0 \quad (\text{Eq. 2.1})$$

Here,  $\phi_a$  and  $\phi_b$  are one-electron orbitals and  $\hat{L}_k$  is an angular-momentum operator with respect to either the magnetic field or the nuclear origin [51, 52]. The angular momentum operators belong to the same irreducible representations as the rotational operators of group theory ( $\hat{R}_k$ ) [53]:

$$\Gamma(\hat{L}_k) = \Gamma(\hat{R}_k) \quad (\text{Eq. 2.2})$$

The effect of  $\hat{L}_k$  operating on an orbital can be visualized as the rotation of the orbital around a particular axis. Qualitatively, the point group of a molecule can be used to predict the symmetry-allowed mixing of orbitals that contribute to the calculated shielding. When applied to crystalline systems, this fact suggests a strong dependence on both localized and extended rotational symmetry operations, which must be considered when designing a cluster to represent the solid-state environment. In a crystalline solid, the space group gives the symmetry elements of the simplest repeating unit. In analogy to the symmetry arguments for predicting magnetic shielding in isolated molecules, it is proposed that, for a cluster to represent the solid-state environment sufficiently well, all rotational symmetry elements of the space group must

be present in the cluster. This approach is hereafter referred to as the symmetry-adapted cluster (SAC) *ansatz*.

The simplest method to maintain space-group symmetry in a cluster model is to preserve all symmetry requirements from the perspective of a single molecule located at the center of the cluster. Thus, a material belonging to a spherical space group would be represented by a cluster belonging to a spherical point group, where the central molecule is surrounded by a spherical shell of peripheral molecules.

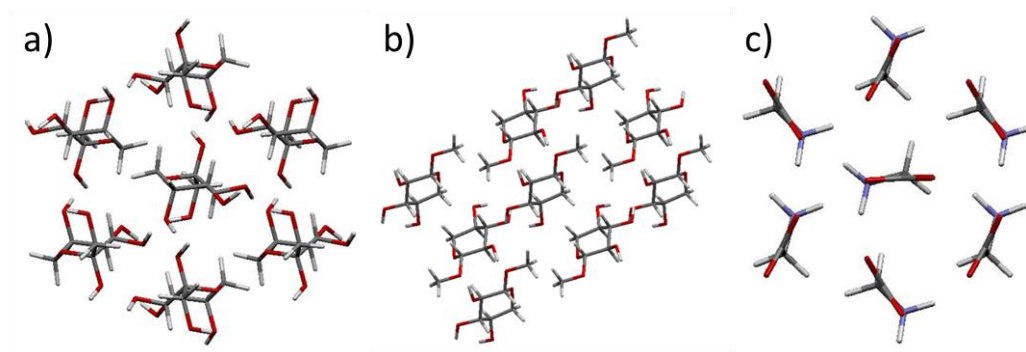


**Figure 2.1.** (a) Cluster of  $\beta$ -D-fructopyranose in the space group  $P2_12_12_1$  containing fifteen molecules. (b) Cluster of methyl  $\beta$ -D-xylopyranoside in the space group  $P2_1$  containing thirteen molecules. (c) Cluster of  $\gamma$ -glycine in the space group  $P3_2$  containing fifteen molecules.

The simplest cluster that can sufficiently account for all lattice effects must have a unique constitution that depends on the space group of the material. For example, the  $P2_12_12_1$  space group maintains spherical symmetry around the central molecule. The elimination of any of the three  $C_2$  rotational axes in the cluster reduces the symmetry to oblate or prolate spheroidal symmetry. All example clusters from the  $P2_12_12_1$  space

group in this study contain between thirteen and fifteen complete molecules that maintain the symmetry. A cluster of  $\beta$ -D-fructopyranose molecules is shown in Figure 2.1(a) as a representation of this space group. The  $P2_1$  space group is a subgroup of  $P2_12_12_1$ , which has only one  $C_2$  axis and no other rotational symmetry elements. Shown in Figure 2.1(b) is a cluster built from thirteen molecules of methyl  $\beta$ -D-xylopyranoside that maintains the symmetry. The  $P3_2$  space group contains  $C_3$  and  $C_3^2$  elements as shown in Figure 2.1(c) for  $\alpha$ -glycine. The cluster is built from fifteen complete molecules and maintains the proper symmetry. As a final example, acenaphthene belongs to the space group  $Pmc2_1$ , which has a single  $C_2$  rotational axis and two mirror planes. Figure 2.2 shows two orientations of a model cluster that contains fifteen complete acenaphthene molecules and maintains the symmetry. A different  $\sigma_v$  plane is apparent in each panel and the  $C_2$  axis can be seen in both.

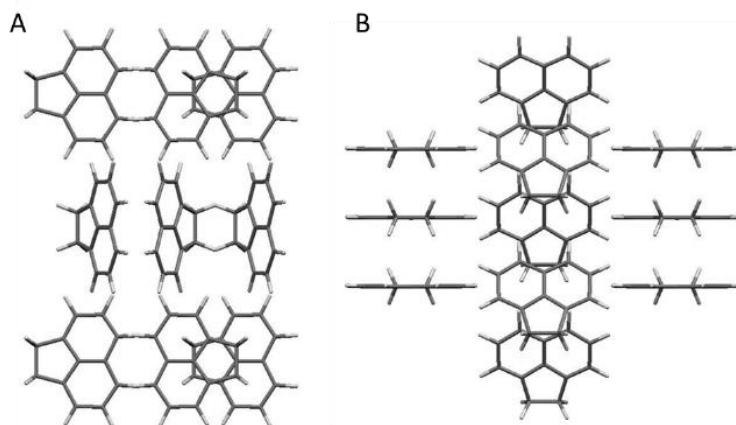


**Figure 2.2.** Two orientations of a cluster of acenaphthene in the space group  $Pmc2_1$  containing fifteen molecules.

## 2.2 Materials, Computational Details, and Analysis

In this study, twenty-four organic materials were selected that have both accepted single-crystal neutron diffraction structures and measurements of the principal components of the  $^{13}\text{C}$  chemical-shift tensors with small associated uncertainties. The majority of chemical-shift principal components in this study have been measured to within  $\pm 1.0$  ppm and the maximum quoted uncertainty of any single value is  $\pm 4.1$  ppm. The specific materials investigated in this study are methyl  $\alpha$ -D-glucopyranoside [54, 55], methyl  $\alpha$ -D-mannopyranoside [54, 55], methyl  $\alpha$ -D-galactopyranoside monohydrate [54, 56], methyl  $\beta$ -D-galactopyranoside [54, 57], methyl  $\beta$ -D-xylopyranoside [54, 58], sucrose [59, 60],  $\alpha$ -L-rhamnose monohydrate [61, 62],  $\beta$ -D-fructopyranose [63, 64],  $\alpha$ -glycine [65, 66],  $\gamma$ -glycine [67, 68], L-alanine [69, 70], L-serine monohydrate [71, 72], L-asparagine monohydrate [73, 74], L-threonine [75, 76], oxalic acid dihydrate [77, 78], squaric acid [79, 80], naphthalene [81, 82], durene [83, 84], triphenylene [85, 86], acenaphthene [87, 88], pentaerythritol [89, 90], adenosine [39, 91], acetaminophen (form I) [92, 93], and ibuprofen (form I) [94, 95]. Descriptions of the model clusters are provided in Table 2.1.

**Table 2.1.** Crystal structures and cluster compositions for materials examined in this study.

Compound	Space Group	Cluster Composition
L-alanine	P2 <sub>1</sub> 2 <sub>1</sub> 2 <sub>1</sub>	13C <sub>3</sub> H <sub>7</sub> NO <sub>2</sub>
L-asparagine monohydrate	P2 <sub>1</sub> 2 <sub>1</sub> 2 <sub>1</sub>	15C <sub>4</sub> H <sub>8</sub> N <sub>2</sub> O <sub>3</sub> ·6H <sub>2</sub> O
L-serine monohydrate	P2 <sub>1</sub> 2 <sub>1</sub> 2 <sub>1</sub>	11C <sub>3</sub> H <sub>7</sub> NO <sub>3</sub> ·8H <sub>2</sub> O
L-threonine	P2 <sub>1</sub> 2 <sub>1</sub> 2 <sub>1</sub>	15C <sub>4</sub> H <sub>9</sub> NO <sub>3</sub>
Methyl $\alpha$ -D-galactopyranoside monohydrate	P2 <sub>1</sub> 2 <sub>1</sub> 2 <sub>1</sub>	15C <sub>7</sub> H <sub>14</sub> O <sub>6</sub> ·6H <sub>2</sub> O
Methyl $\alpha$ -D-glucopyranoside	P2 <sub>1</sub> 2 <sub>1</sub> 2 <sub>1</sub>	15C <sub>7</sub> H <sub>14</sub> O <sub>6</sub>
Methyl $\alpha$ -D-mannopyranoside	P2 <sub>1</sub> 2 <sub>1</sub> 2 <sub>1</sub>	13C <sub>7</sub> H <sub>14</sub> O <sub>6</sub>
Methyl $\beta$ -D-galactopyranoside	P2 <sub>1</sub> 2 <sub>1</sub> 2 <sub>1</sub>	15C <sub>7</sub> H <sub>14</sub> O <sub>6</sub>
Triphenylene	P2 <sub>1</sub> 2 <sub>1</sub> 2 <sub>1</sub>	15C <sub>18</sub> H <sub>12</sub>
$\beta$ -D-fructopyranose	P2 <sub>1</sub> 2 <sub>1</sub> 2 <sub>1</sub>	15C <sub>6</sub> H <sub>12</sub> O <sub>6</sub>
Acenaphthene	Pcm2 <sub>1</sub>	15C <sub>12</sub> H <sub>10</sub>
Adenosine	P2 <sub>1</sub>	15C <sub>10</sub> H <sub>13</sub> N <sub>5</sub> O <sub>4</sub>
Methyl $\beta$ -D-xylopyranoside	P2 <sub>1</sub>	13C <sub>6</sub> H <sub>11</sub> O <sub>5</sub>
Sucrose	P2 <sub>1</sub>	13C <sub>12</sub> H <sub>22</sub> O <sub>11</sub>
$\alpha$ -L-rhamnose monohydrate	P2 <sub>1</sub>	15C <sub>6</sub> H <sub>12</sub> O <sub>5</sub> ·6H <sub>2</sub> O
Acetaminophen	P2 <sub>1</sub> /a	15C <sub>8</sub> H <sub>9</sub> NO <sub>2</sub>
Durene	P2 <sub>1</sub> /a	15C <sub>10</sub> H <sub>14</sub>
Naphthalene	P2 <sub>1</sub> /a	13C <sub>10</sub> H <sub>8</sub>
Ibuprofen	P2 <sub>1</sub> /c	15C <sub>13</sub> H <sub>18</sub> O <sub>2</sub>
Squaric acid	P2 <sub>1</sub> /c	17C <sub>4</sub> H <sub>2</sub> O <sub>4</sub>
Oxalic acid dihydrate	P2 <sub>1</sub> /n	15C <sub>2</sub> O <sub>4</sub> H <sub>2</sub> ·20H <sub>2</sub> O
$\alpha$ -glycine	P2 <sub>1</sub> /n	15C <sub>2</sub> H <sub>5</sub> NO <sub>2</sub>
$\gamma$ -glycine	P3 <sub>2</sub>	15C <sub>2</sub> H <sub>5</sub> NO <sub>2</sub>
Pentaerythritol	I $\bar{4}$	13C <sub>5</sub> H <sub>12</sub> O <sub>4</sub>

Beginning with neutron-diffraction structures, proton positions were optimized on an isolated molecule at the B3LYP level of theory using the 6-31G(d) basis set [96-

98]. In the partial geometry optimizations, all heavy atoms remained frozen in their experimental positions, as did all hydrogen atoms participating in intermolecular hydrogen bonding. This feature of the optimization was especially important for saccharides, which are distorted from the ideal staggered conformation. Optimizing these sites would have eliminated this important structural feature. Periodic plane-wave geometry optimizations were performed on adenosine, acetaminophen, ibuprofen, and  $\alpha$ -glycine using the energy-minimization method of Broyden, Fletcher, Goldfarb, and Shanno, as implemented in the CASTEP module of MATERIALS STUDIO 6.1 by Accelrys Software, Inc [99]. Optimizations were performed at the PBE/ultra-fine level of theory with a plane-wave cutoff energy of 610 eV and a  $k$ -point spacing of  $0.07 \text{ \AA}^{-1}$  [100]. The unit cell dimensions remained fixed during the structural refinements because these parameters are well-known from experiment.

Magnetic-shielding tensors were computed using the GIAO method with the B3PW91 functional, Becke's three-parameter hybrid functional where the non-local correlation is provided by the PW91 gradient-corrected functional [101]. Calculations were performed using a two-layer approach, in which a more flexible basis set was given to the molecule of interest (the central molecule of the cluster) than was given to the neighboring molecules in the cluster. Dunning's correlation-consistent basis set cc-pVTZ was used for the central molecule and cc-pVDZ was used for peripheral molecules (Figure 2.3) [102].  $^{13}\text{C}$  magnetic-shielding calculations were also performed on single refined molecules taken in isolation, as a means to examine intermolecular effects on the magnetic shielding. All calculations of  $^{13}\text{C}$  magnetic-shielding tensors were performed using GAUSSIAN 09 [103].

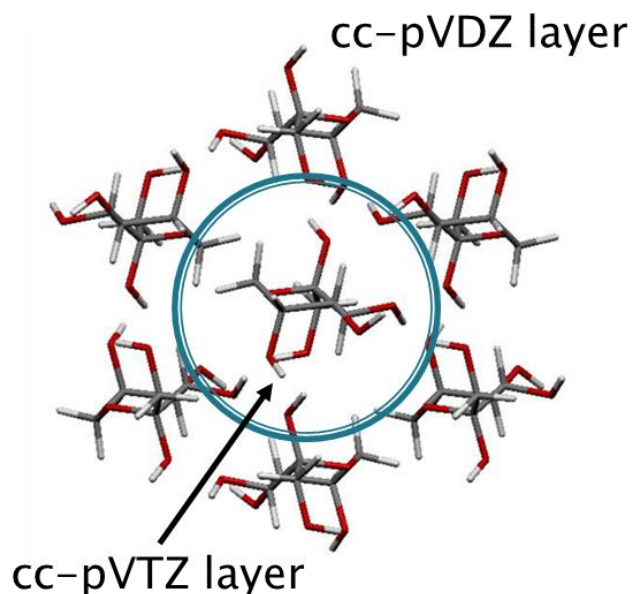


**Figure 2.3.** Cluster of  $\beta$ -D-fructopyranoside illustrating the partitioning of the basis set into locally dense (cc-pVTZ) and locally sparse (cc-pVDZ) layers.

NMR experiments yield a shift in the frequency of the resonance of a particular chemical species relative to an arbitrary reference material, rather than the absolute shielding relative to the bare nucleus. For  $^{13}\text{C}$ , chemical shifts are typically referenced to the resonance position of tetramethylsilane (TMS), whose principal components are all the same in solution because of the effective symmetry caused by rapid motional averaging. The correlation between experimental chemical shifts ( $\delta_{ii}^{exp}$ ) and calculated magnetic shieldings ( $\sigma_{ii}$ ) is linear with a proportionality constant  $m$ , and an intercept that is the absolute chemical shielding of TMS:

$$\sigma_{ii} = m\delta_{ii}^{exp} + \sigma_{\text{TMS}} \quad (\text{Eq. 2.3})$$

I use as a reference in our calculations the intercept derived from the linear regression of a correlation plot. Ideally,  $|m|$  should be 1.00, with deviations reflecting

systematic flaws in the method of calculating the shielding tensor [11]. With knowledge of the reference shielding and slope, all magnetic-shielding components can be expressed as their equivalents on the chemical-shift scale ( $\delta_{ii}^{calc}$ ), for comparison to experiment:

$$\delta_{ii}^{calc} = \frac{\sigma_{ii} - \sigma_{TMS}}{m} \quad (\text{Eq. 2.4})$$

In addition, to quantify the data scatter of the set of calculations, we use the root-mean-square deviation (RMSD) of the set:

$$RMSD = \sqrt{\frac{1}{N-2} \sum_{n=1}^N (\delta_{ii}^{calc} - \delta_{ii}^{exp})^2} \quad (\text{Eq. 2.5})$$

where N is the total number of chemical-shift-tensor components.

## 2.3 Results and Discussion

### 2.3.1 Size Requirements for Molecular Clusters

This section explores variations in computed magnetic-shielding parameters with cluster size. To assess this effect,  $^{13}\text{C}$  magnetic-shielding tensors of nuclei in isolated molecules, and that of molecules in clusters, have been calculated as a function of cluster size to demonstrate that the calculated shielding parameters tend to converge to a constant set of values. At this limit, the cluster model can be said to represent the lattice structure sufficiently. It should be noted that the purpose of this discussion is to illustrate the convergence of computed NMR parameters with respect to cluster size, not to illustrate the size of cluster yields the best agreement with experiment.

**Table 2.2.**  $^{13}\text{C}$  Principal magnetic-shielding values for oxalic acid dihydrate as a function of cluster size. The differential quantifies differences in computed principal values between different sizes of clusters.

Cluster Composition	$\sigma_{11}$ (ppm)	$\sigma_{22}$ (ppm)	$\sigma_{33}$ (ppm)	$\sigma_{iso}$ (ppm)	Differential (ppm)
$\text{C}_2\text{O}_4\text{H}_2$	-80.3	75.9	84.7	26.8	-
$3\text{C}_2\text{O}_4\text{H}_2 \cdot 6\text{H}_2\text{O}$	-72.8	56.8	78.4	20.8	12.4
$11\text{C}_2\text{O}_4\text{H}_2 \cdot 12\text{H}_2\text{O}$	-70.9	54.7	77.6	20.4	1.7
$15\text{C}_2\text{O}_4\text{H}_2 \cdot 20\text{H}_2\text{O}$	-69.4	51.9	77.0	19.8	1.9
$21\text{C}_2\text{O}_4\text{H}_2 \cdot 26\text{H}_2\text{O}$	-70.3	52.3	77.9	19.9	0.8

Tables 2.2 and 2.3 show the effect of cluster size on the computed principal components of  $^{13}\text{C}$  magnetic-shielding tensors in oxalic acid dihydrate and squaric acid, respectively. Differences in shielding between each subsequent size of cluster are quantified by the differentials displayed in these tables. Shielding constants tends to converge smoothly. In the case of oxalic acid dihydrate, convergence appears to be achieved with the two largest clusters, as the differential for the single carbon site is only 0.8 ppm. For squaric acid, the differentials between the two largest clusters range between 1.3 ppm and 0.8 ppm for the four carbon sites. From these observations, it is clear that clusters must be large to account for intermolecular effects properly.

**Table 2.3.**  $^{13}\text{C}$  Principal magnetic-shielding values for squaric acid as a function of cluster size. The differential quantifies differences in computed principal values between different sizes of clusters.

Cluster Composition	Site	$\sigma_{11}$ (ppm)	$\sigma_{22}$ (ppm)	$\sigma_{33}$ (ppm)	$\sigma_{iso}$ (ppm)	Differential (ppm)
$\text{C}_4\text{H}_2\text{O}_4$	C1	-68.4	-34.8	103	-0.1	-
	C2	-66.9	-30.7	98.3	0.2	-
	C3	-97.7	15.9	66.4	-5.1	-
	C4	-97.2	1.3	69.6	-8.8	-
$9\text{C}_4\text{H}_2\text{O}_4$	C1	-74.4	-51.3	100.4	-8.4	10.2
	C2	-65.8	-44.7	99.6	-3.6	8.1
	C3	-93.3	-12.2	71.8	-11.2	16.7
	C4	-97.1	-9.6	72.8	-11.3	6.6
$13\text{C}_4\text{H}_2\text{O}_4$	C1	-69.1	-50.8	94.2	-8.6	4.7
	C2	-64.2	-54.8	96.8	-7.4	6.1
	C3	-83.6	-29.3	80.4	-10.8	12.4
	C4	-86.8	-25.1	78.6	-11.1	11.3
$17\text{C}_4\text{H}_2\text{O}_4$	C1	-67.0	-51.5	93.7	-8.3	1.3
	C2	-63.1	-54.1	96.3	-7.0	0.8
	C3	-84.5	-27.9	79.3	-11.0	1.2
	C4	-87.6	-24.4	77.6	-11.5	0.8

### 2.3.2 Symmetry Requirements for Molecular Clusters

Another aspect of solid-state magnetic-shielding calculations is the difficulty of ensuring that the cluster reflects all symmetry elements associated with the space group of the material. Artifacts may be introduced into a computational result by designing a cluster that does not maintain the symmetry elements of the crystalline space. To

illustrate this point, we present calculated magnetic-shielding principal components for the carbon sites of pentaerythritol. Pentaerythritol belongs to the  $I\bar{4}$  space group, which contains  $C_2$ ,  $S_4$ , and  $S_4^3$  symmetry elements. The magnetic shielding from a model having the appropriate symmetry exhibits axial symmetry at the quaternary carbon site. When the symmetry is not fully realized, the principal components differ by a sizable amount (Table 2.4).

The two clusters for which the data in Table 2.4 were calculated were designed from the diffraction structure (Figure 2.4). The first cluster contained thirteen molecules in a manner that preserved all symmetry elements of the crystalline space group. The second cluster was designed from only nine molecules, with the effect of removing the inversion center inherent in the crystalline space group. This smaller cluster is labeled as a quasi- $I\bar{4}$  cluster, reflecting the difference from the actual crystalline symmetry. As is clearly evident in Table 2.4, calculations on the first ( $I\bar{4}$ ) cluster predict the axial symmetry of the quaternary carbon (site A), whereas calculations on the second cluster do not. In particular, the quasi- $I\bar{4}$  cluster predicts a skew of  $\kappa = -0.71$ , whereas the  $I\bar{4}$  cluster predicts  $\kappa = -1.00$ . The latter value is in agreement with experiment.

**Table 2.4.** Calculated chemical-shift tensors for pentaerythritol using clusters with the experimental crystalline space group ( $I\bar{4}$ ) and a space group of reduced symmetry (quasi- $I\bar{4}$ ).

Model		$\sigma_{11}$ (ppm)	$\sigma_{22}$ (ppm)	$\sigma_{33}$ (ppm)	$\Omega$ (ppm)	$\kappa$
Site A	Exp.	-	-	-	14.6	-1.00
	Quasi- $I\bar{4}$	123.9	141.2	144.1	20.2	-0.71
	$I\bar{4}$	126.0	140.5	140.5	14.5	-1.00
Site B	Exp.	-	-	-	76.9	0.37
	Quasi- $I\bar{4}$	92.5	114.6	172.7	80.5	0.45
	$I\bar{4}$	89.3	116.6	170.0	80.7	0.32

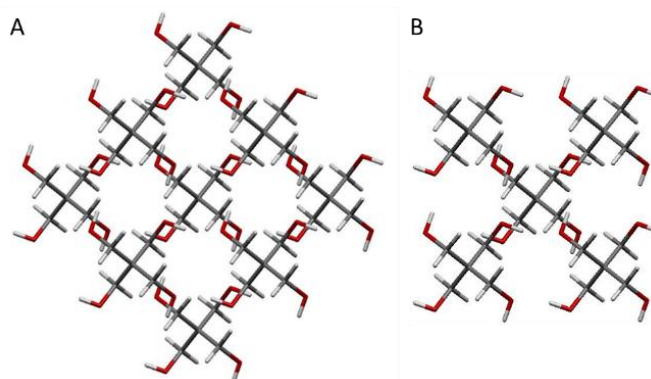


**Figure 2.4.** Two example clusters of pentaerythritol. Cluster A is built from thirteen complete molecules and maintains all of the symmetry elements of the  $I\bar{4}$  space group. Cluster B is built from nine molecules and lacks several symmetry elements of the space group.

### 2.3.3 Locally-Dense Basis Sets

The use of locally dense, rather than balanced, basis functions allows calculations to be performed on large clusters, which otherwise would be prohibitively expensive. The use of locally dense basis functions in magnetic-shielding calculations has been surveyed by Chesnut and co-workers [104, 105]. A more comprehensive modern survey of the subject has been provided by Reid [106]. These studies demonstrate that only small discrepancies appear between locally dense and balanced basis sets for  $^{13}\text{C}$ , provided a sufficiently large basis set is employed in the dense region.

Some of the largest clusters in this study contain up to seven thousand Cartesian basis functions, although a smaller basis set (cc-pVDZ) is used for peripheral molecules. The  $^{13}\text{C}$  magnetic shielding of oxalic acid dihydrate, the smallest molecule in this study, serves as a basis for comparison because the magnetic shielding of the carbon site can be calculated using the large basis set (cc-pVTZ) for all atoms. Differences in magnetic-shielding principal components between balanced and locally-dense basis functions are given in Table 2.5. The differences in computed magnetic shielding between the two basis-set partitioning schemes are under 1.5 ppm, and the overall residual between the two schemes is only 1.1 ppm. This indicates that the increase in computational efficiency outweighs the loss of accuracy associated with the smaller basis set.

**Table 2.5.** Comparison of locally dense and balanced basis sets for calculating the  $^{13}\text{C}$  chemical shielding of oxalic acid dihydrate using the cluster  $15\text{C}_2\text{O}_4\text{H}_2\cdot 20\text{H}_2\text{O}$ .

Method	$\sigma_{11}$ (ppm)	$\sigma_{22}$ (ppm)	$\sigma_{33}$ (ppm)	$\sigma_{iso}$ (ppm)
Locally Dense	-69.4	51.9	77.0	19.8
Balanced	-67.9	50.9	77.8	20.3
Difference <sup>a</sup>	-1.5	1.0	-0.7	-0.5

<sup>a</sup>Locally dense shielding minus balanced shielding.

#### 2.3.4 Relationship between Calculated and Experimental Results

Figure 2.5 shows correlation plots for the calculated magnetic-shielding principal components versus experimental chemical-shift principal components for 155 unique  $^{13}\text{C}$  lattice sites. Figures 2.5(a) and 2.5(b) show results for the isolated-molecule model and the cluster model, respectively. Figure 2.6 provides the relationship between the isotropic magnetic shieldings and isotropic chemical shifts. A summary of linear-regression parameters and statistical data associated with the relationship of the principal components of magnetic-shielding tensors and the principal components of chemical-shift tensors is provided in Table 2.6. The RMSDs for these two models of 9.5 ppm (isolated-molecule model) and 3.4 ppm (cluster model) indicate that the cluster model is significantly superior to the isolated-molecule model. The deviation from the ideal slope in the cluster model ( $1.035 \pm 0.002$ ) may reflect the choice of exchange-correlation functional and basis set employed in the calculation. The RMSD of the cluster model (3.4 ppm) represents less than 1% of the possible  $^{13}\text{C}$  chemical-shift dispersion (approximately 500 ppm), indicating that this method is a powerful,

quantitative predictor of chemical-shift values. Every calculated value obtained by the cluster method agrees with experiment to within 5% of the possible chemical-shift range. Figure 2.7. shows the correlation in errors associated with chemical shifts calculated with the two methods. As is evident in the figure, errors in the isolated-molecules model tend to be more widely distributed.

It is sometimes assumed that one should correlate various subpopulations of carbons separately [107]. The set in this study consists of subpopulations of aliphatic, aromatic and carboxylic carbon sites. In particular, it is assumed that different kinds of intermolecular interactions affect the magnetic shielding at these sites differently. Table 3.6 presents linear-regression parameters and statistical data for the relationship between calculated magnetic-shielding tensor principal values and experimental chemical-shift tensor principal values for these three subpopulations. For aliphatic carbons, comparison of the RMSDs of the two models (3.2 ppm and 2.2 ppm, respectively) suggests that the cluster model is superior for the prediction of aliphatic chemical shifts. This change of 1.0 ppm is more impressive when one considers that it represents an average change of the calculated values in the correct direction for 258 principal components. The single largest deviation between the cluster model and isolated-molecule models for an aliphatic principal component is 13.6 ppm.

As with the aliphatic carbons, the comparison of the RMSDs (5.1 ppm and 4.3 ppm, respectively) for the aromatic carbons shows that a cluster model is slightly better than the isolated-molecule model. As in the previous case, the decrease in the RMSD of 0.8 ppm reflects an average change over 165 principal components. Many individual values are relatively unchanged by the inclusion of intermolecular effects, whereas

others, such as a  $\sigma_{22}$  value in the heterocyclic ring of adenosine, are changed up to 18.5 ppm.

Finally, the results for carboxylic carbons again demonstrate that the cluster model improves the predictive capability over the isolated-molecule model. The isolated-molecule model's RMSD of 25.9 ppm is substantially larger than the RMSD of 4.5 ppm for the cluster model. Additionally, the projected shielding of the reference compound of  $202 \pm 13$  ppm predicted by the isolated-molecule model is substantially different from the  $187 \pm 2$  ppm predicted by the cluster model. This latter value is more in line with reference shieldings derived from the cluster model for the other two carbon subpopulations ( $186.0 \pm 0.3$  and  $187.3 \pm 0.6$  predicted for the aliphatic and aromatic subpopulations, respectively).

The correlations for aliphatic, aromatic, and carboxylic carbons in the cluster model are sufficiently close that one may consider, within uncertainty, that they all follow a single correlation, with a low RMSD of 3.4 ppm. Perhaps this is the strongest indicator of the importance of incorporating the extended local structure into any calculations of the magnetic-shielding tensor of a carbon site in the solid state. In contrast, it has been noted in studies employing GIPAW calculations that distinct carbon species belong to separate subpopulations with statistically-different sets of linear-regression parameters [107]. This trend is notably absent in the results presented here, suggesting that symmetry-adapted cluster models, combined with a suitable model chemistry, are able to correct systematic errors that sometimes appear in GIPAW calculations of magnetic-shielding tensors. This observation is discussed in further detail in Chapter 4.

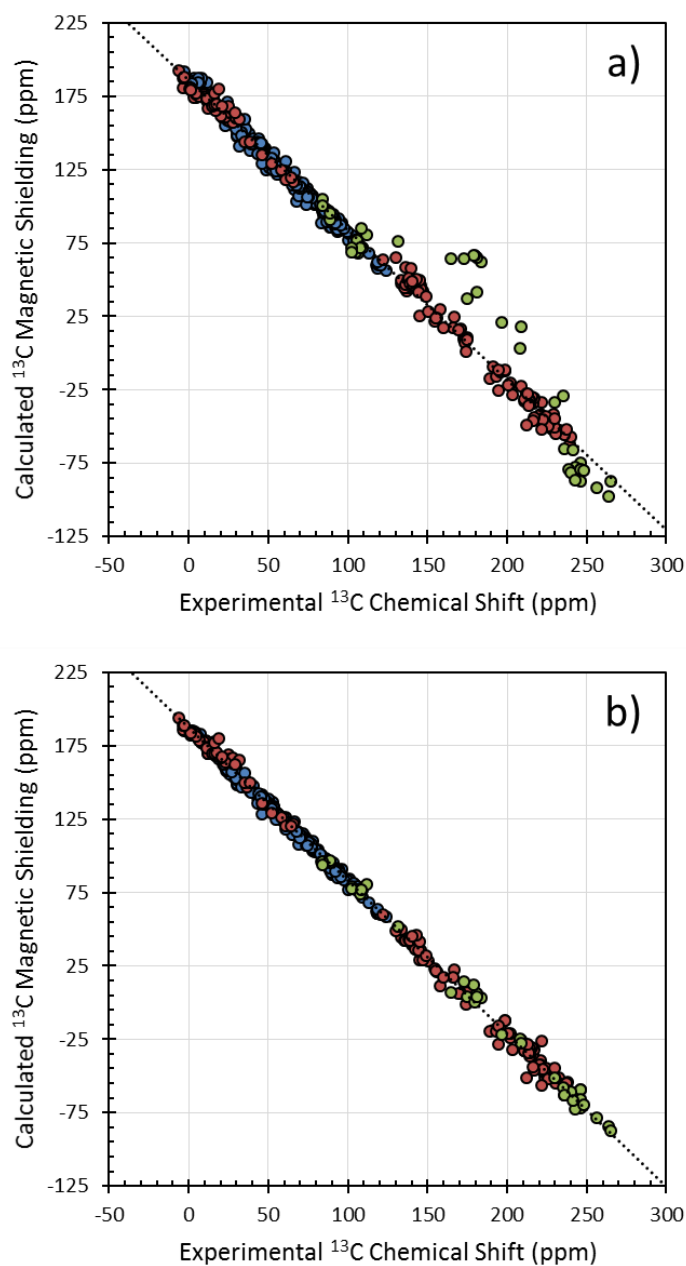


**Figure 2.5.** Correlation plots for calculated principal components of magnetic-shielding tensors versus experimental principal components of chemical-shift tensors. Aliphatic carbons principal components are in blue, aromatic principal components are in red, and carboxylic principal components are in green. Results in (a) are from the isolated-molecule models and results in (b) are from the cluster models.

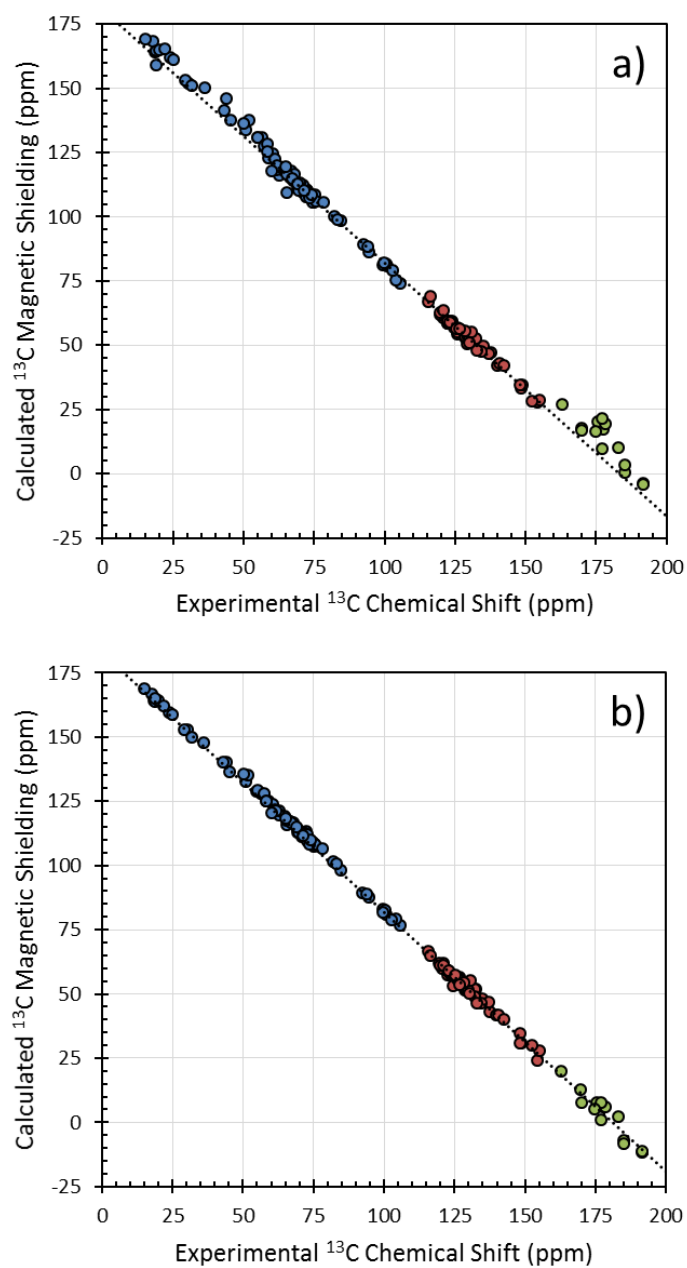


**Figure 2.6.** Correlation plots for calculated isotropic magnetic shieldings versus experimental isotropic chemical shifts. Aliphatic carbons shifts are in blue, aromatic shifts are in red, and carboxylic shifts are in green. Results in (a) are from the isolated-molecule models and results in (b) are from the cluster models.

**Table 2.6.** Linear-regression parameters for  $^{13}\text{C}$  principal magnetic-shielding values versus principal chemical-shift values for isolated molecules, clusters, and plane-wave optimized clusters.

Model	N-2	$ m $	$\sigma_{TMS}$ (ppm)	RMSD (ppm)	Max. <sup>a</sup> (ppm)
<b><u>All Carbons</u></b>					
Isolated		$1.010 \pm 0.006$	$184.5 \pm 0.8$	9.5	62.6
Cluster	463	$1.035 \pm 0.002$	$186.1 \pm 0.3$	3.4	17.2
Cluster, Opt.		$1.039 \pm 0.002$	$186.4 \pm 0.3$	3.5	18.1
<b><u>Aliphatic Carbons</u></b>					
Isolated		$1.069 \pm 0.007$	$187.2 \pm 0.5$	3.2	11.2
Cluster	256	$1.040 \pm 0.005$	$186.0 \pm 0.3$	2.2	9.3
Cluster, Opt.		$1.052 \pm 0.005$	$186.9 \pm 0.4$	2.3	9.0
<b><u>Aromatic Carbons</u></b>					
Isolated		$1.020 \pm 0.005$	$185.3 \pm 0.7$	5.1	17.5
Cluster	163	$1.042 \pm 0.004$	$187.3 \pm 0.6$	4.3	17.0
Cluster, Opt.		$1.043 \pm 0.007$	$187.3 \pm 0.7$	4.6	18.3
<b><u>Carboxylic Carbons</u></b>					
Isolated		$1.06 \pm 0.07$	$202 \pm 13$	25.9	52.0
Cluster	40	$1.03 \pm 0.01$	$187 \pm 2$	4.5	9.2
Cluster, Opt.		$1.03 \pm 0.01$	$186 \pm 2$	4.3	9.4

<sup>a</sup>Maximum error in any principal value.

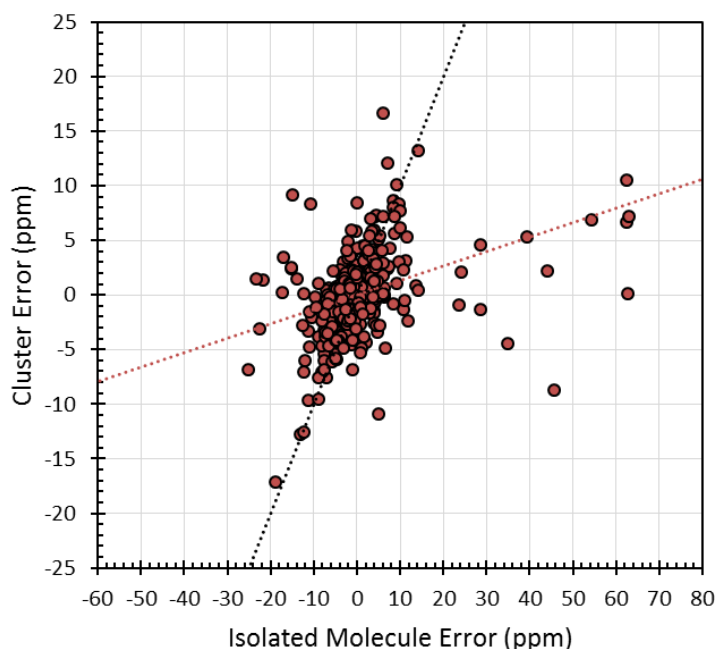


**Figure 2.7.** Correlation of errors in calculated  $^{13}\text{C}$  chemical-shift tensor principal values between cluster models and isolated-molecule models. The dotted black line represents an ideal one-to-one relationship between errors in the two methods whereas the red line represents the best-fit relationship.

### 2.3.5 Analysis of Magnetic Shielding Principal Components

Table 2.7 summarizes RMSDs associated with the prediction of each principal component of the aliphatic, aromatic, and carboxylic  $^{13}\text{C}$  chemical-shift tensors. In every case, the RMSDs of each principal component of each type of carbon demonstrate that the cluster model is closer to the experimental value than the corresponding component calculated with the isolated-molecule model, except for the  $\sigma_{11}$  values of the aromatic sites. A more detailed summary of this analysis is found in Figures 2.8 – 2.10, which provides a comparison of calculations of shielding for each of the principal components for the three carbon subpopulations, as obtained by the two models.

For aliphatic species, deviations fall between 2.0 ppm ( $\sigma_{22}$ ) and 2.3 ppm ( $\sigma_{11}$  and  $\sigma_{33}$ ) for cluster models. However, the RMSDs vary for the principal components of the aromatic and carboxylic sites. For aromatic carbons, the principal components are generally aligned such that  $\sigma_{11}$  is along the C-H bonding axis,  $\sigma_{22}$  is perpendicular to the bonding axis and in the plane of the ring, and  $\sigma_{33}$  is perpendicular to the plane of the ring. Of these values,  $\sigma_{22}$  seems to be most strongly influenced by intermolecular effects. For each carboxylic principal component, the disagreement between experiment and calculation is greatly reduced by the inclusion of intermolecular effects, with RMSDs ranging between 4.2 ppm ( $\sigma_{33}$ ) and 5.4 ppm ( $\sigma_{22}$ ). The principal axes at carboxylic sites generally do not align with the bonding axes, leading to large changes for each principal component when intermolecular effects are incorporated. The most shielded element is generally aligned approximately perpendicular to the bonding axis, resulting in substantial differences for  $\sigma_{11}$  and  $\sigma_{22}$  and relatively small changes for  $\sigma_{33}$ .

The most significant discrepancies between isolated-molecule models and cluster models are seen for  $\sigma_{22}$  values of carboxylic carbons. For example,  $\sigma_{22}$  of L-alanine differs from experiment by 62.6 ppm in the isolated-molecule model, but only by 6.7 ppm in the cluster model.  $\sigma_{11}$  and  $\sigma_{33}$  also differ from experiment for L-alanine by 17.0 ppm and 7.1 ppm in the isolated-molecule model, respectively, whereas in the cluster model there are deviations of only 3.5 ppm and 1.0 ppm, respectively. This fact further indicates that the isolated-molecule model does not give an accurate approximation of magnetic shielding caused by the local structure of a carboxyl group in the solid state. For all cases where intermolecular hydrogen bonding is present, we find the same effects as are observed for L-alanine. Calculations on the amino acids employing isolated molecules predict that the  $^{13}\text{C}$  magnetic-shielding tensor for the

carboxylic sites have nearly axial symmetry, whereas in cluster models, the carboxylic sites have nearly radial symmetry. The observed experimental results suggest that the radial symmetry is more appropriate.

**Table 2.7.** Root-mean-square deviation (RMSD) between calculated and experimental chemical shifts modeled using isolated molecules, clusters, and plane-wave optimized clusters.

Model	All (ppm)	$\sigma_{11}$ (ppm)	$\sigma_{22}$ (ppm)	$\sigma_{33}$ (ppm)	$\sigma_{iso}$ (ppm)
<b><u>All Carbons</u></b>					
Isolated	9.5	7.0	14.2	4.6	3.6
Cluster	3.4	4.0	3.1	3.1	1.6
Cluster, Opt.	3.5	3.9	3.2	3.4	1.7
<b><u>Aliphatic Carbons</u></b>					
Isolated	3.2	3.4	2.9	3.3	3.2
Cluster	2.2	2.3	2.0	2.3	1.4
Cluster, Opt.	2.3	2.3	2.0	2.3	1.6
<b><u>Aromatic Carbons</u></b>					
Isolated	5.1	5.3	5.6	4.5	1.4
Cluster	4.3	5.6	3.6	3.8	1.5
Cluster, Opt.	4.6	5.4	3.8	4.5	1.6
<b><u>Carboxylic Carbons</u></b>					
Isolated	25.9	21.6	38.9	16.1	4.3
Cluster	4.6	4.8	5.5	3.8	3.0
Cluster, Opt.	4.5	4.6	4.9	3.8	3.0

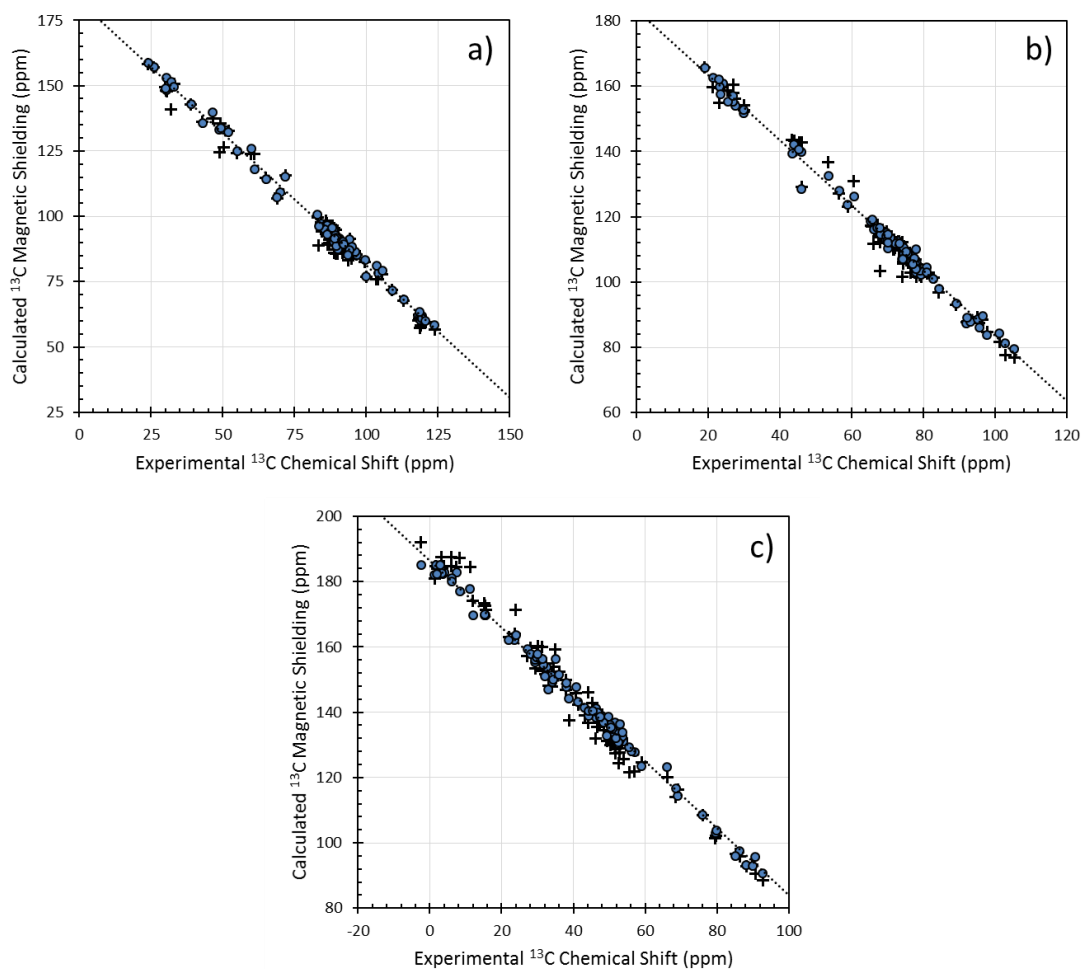


**Figure 2.8.** Relationship between calculated principal components of  $^{13}\text{C}$  magnetic-shielding tensors and experimental  $^{13}\text{C}$  chemical-shift tensors of aliphatic carbon sites. The panels display values for each of the principal values: (a)  $\sigma_{11}$ , (b)  $\sigma_{22}$ , and (c)  $\sigma_{33}$ . Results obtained using cluster models are shown as solid blue points whereas results obtained using isolated-molecule models are shown as black crosses.

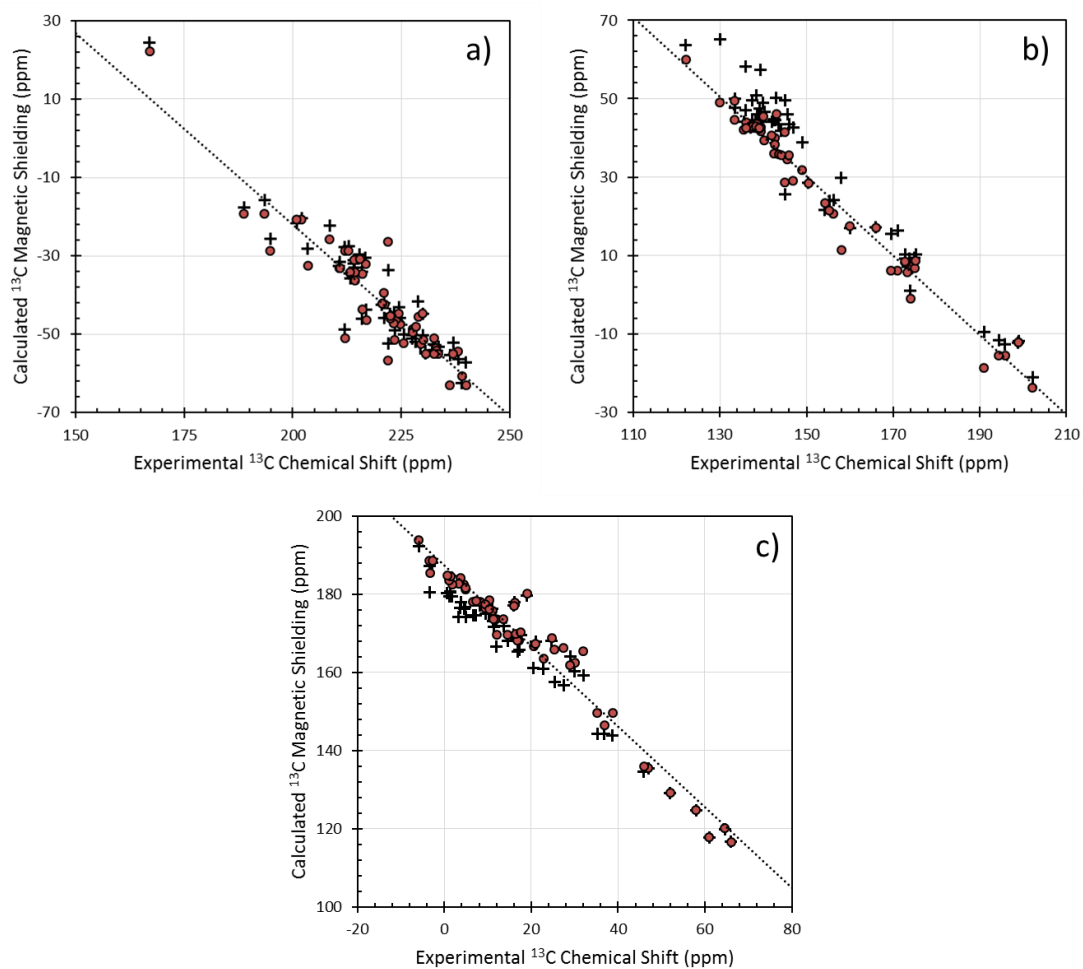


**Figure 2.9.** Relationship between calculated principal components of  $^{13}\text{C}$  magnetic-shielding tensors and experimental  $^{13}\text{C}$  chemical-shift tensors of aromatic carbon sites. The panels display values for each of the principal values: (a)  $\sigma_{11}$ , (b)  $\sigma_{22}$ , and (c)  $\sigma_{33}$ . Results obtained using cluster models are shown as solid red points whereas results obtained using isolated-molecule models are shown as black crosses.

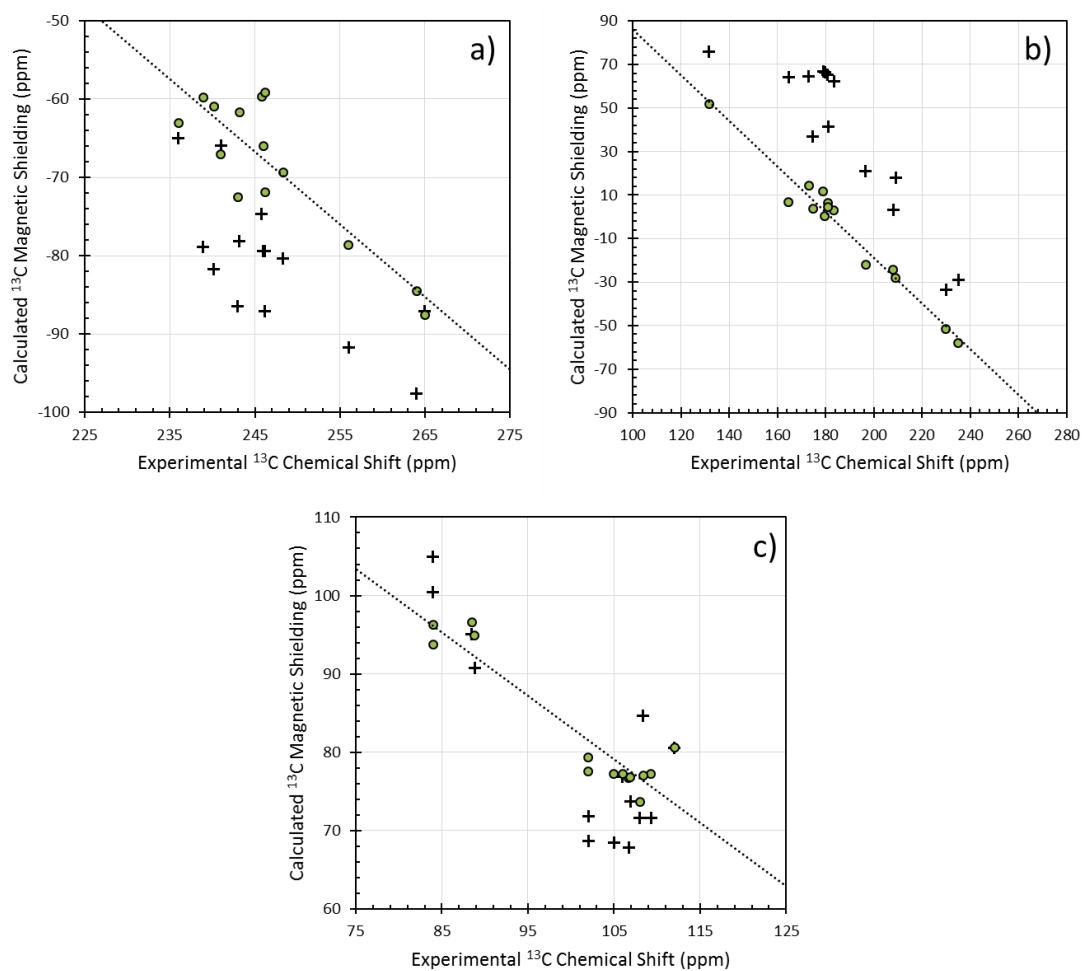


**Figure 2.10.** Relationship between calculated principal components of  $^{13}\text{C}$  magnetic-shielding tensors and experimental  $^{13}\text{C}$  chemical-shift tensors of carboxylic carbon sites. The panels display values for each of the principal values: (a)  $\sigma_{11}$ , (b)  $\sigma_{22}$ , and (c)  $\sigma_{33}$ . Results obtained using cluster models are shown as solid red points whereas results obtained using isolated-molecule models are shown as black crosses.

The mean absolute deviations (MADs) between computed magnetic-shielding values for isolated-molecule models and cluster models are given in Table 2.8. Deviations are given for each principal component of the magnetic-shielding tensor. For aliphatic species, the three principal components deviate between 1.9 ppm and 2.3 ppm, indicating that no single direction is significantly more influence by neighboring molecules than the others, on average. All calculated principal components agree equally well with experimental values. For the aromatic species, both  $\sigma_{11}$  and  $\sigma_{33}$  deviate by approximately the same amount (2.0 ppm to 2.8 ppm); however,  $\sigma_{22}$  deviates by 5.0 ppm, demonstrating that intermolecular effects tend to affect this particular principal component more than the others. For carboxylic carbons, the deviations are much larger, with the largest differences associated with  $\sigma_{22}$ . For this principal component, the principal axis for which lies near the intermolecular hydrogen-bonding axis, the MAD is 42.6 ppm. A much smaller MAD is seen for  $\sigma_{33}$  (4.4 ppm), the principal axis for which lies perpendicular to the bonding plane.

**Table 2.8.** Mean-absolute deviation (MAD) between calculated magnetic shielding of cluster models and isolated-molecule models.<sup>a</sup>

	All (ppm)	$\sigma_{11}$ (ppm)	$\sigma_{22}$ (ppm)	$\sigma_{33}$ (ppm)	$\sigma_{iso}$ (ppm)
All Carbons	4.2	3.1	6.7	2.9	2.2
Aliphatic Carbons	2.3	2.0	1.9	2.8	1.7
Aromatic Carbons	3.3	2.0	5.0	2.8	1.4
Carboxylic Carbons	20.3	12.5	42.6	5.3	9.6

$$^aMAD = \sqrt{(\sigma_{ii}^{cluster} - \sigma_{ii}^{isolated})^2}$$

### 2.3.6 Effects of Plane-Wave Structural Refinements on Calculated Shielding

The largest residuals calculated in this study are observed for acetaminophen, adenosine, ibuprofen, and  $\alpha$ -glycine. Most anomalous results arise for the principal components in the planes of aromatic rings (when present in the structure). Several residuals are greater than 10 ppm. Because these residuals are much larger than those for other materials examined, we hypothesize that they may have arisen from rovibrational effects in the structures of molecules obtained through neutron diffraction.

Crystal-structure refinements have been monitored through agreement between calculated and experimental  $^{13}\text{C}$  chemical-shift tensors [9, 92]. Studies have shown that plane-wave DFT structural refinements can produce modest improvements in predicted magnetic shieldings over results obtained from unrefined coordinates determined by neutron diffraction, in some cases. To examine if these effects are significant in the present cases, we determined the effects of plane-wave optimizations on computed  $^{13}\text{C}$  magnetic-shielding principal components of acetaminophen, adenosine, ibuprofen, and  $\alpha$ -glycine. The linear-regression results incorporating the optimized structures are included in Tables 2.6 and 2.7. Optimized and un-optimized linear-regression parameters are essentially in agreement.

The RMSDs associated with the structures where all atomic positions were refined are slightly higher than that of the structures where only the hydrogen positions were refined, except for carboxylic sites, which were modestly improved. The RMSD of  $\sigma_{22}$  values of carboxylic sites decreases from 5.5 ppm to 4.9 ppm when optimization is performed. The improvement is attributed to a better representation of the hydrogen bonds. We conclude that the positions of hydrogen sites that do not participate in hydrogen bonds can be refined using partial optimizations involving isolated molecules and that introducing repositionings of the structure around the heavy atoms sometimes

degrades the quality of the structural data, except in cases where intermolecular hydrogen-bonding is present.

Some of the largest differences between calculated and experimental chemical-shift values can be attributed to motional averaging of experimental chemical shifts that are not accounted for in static computational models. Rovibrational effects tend to reduce calculated magnetic-shift anisotropies by averaging over many possible orientations [108]. In the majority of cases where large residuals were encountered in this study, the calculated residuals for  $\sigma_{11}$  and  $\sigma_{33}$  had opposite signs. It is possible to address internal rotations by averaging over a series of single-point magnetic-shielding calculations for structures derived from either classical or *ab initio* molecular dynamics (MD) simulations. The former method has been employed to study the effects of solvation on the magnetic shielding of ions, whereas the latter has been used to account for motion in crystalline systems or proteins [109-114]. In the case of ibuprofen, multi-point studies have been used to improve the correlation with experiment by introducing thermal motion in the form of librations in the phenyl ring and bending modes for the C-H bonds [94].

The largest discrepancies between experimental principal components and calculated principal components using cluster models for carboxylic sites are for the components whose principal axes lie nearest to the hydrogen bonding axis. These large deviations can be explained by assuming a dynamic effect involving the hydrogen atoms [115].

As another example,  $\sigma_{22}$  for aromatic carbons were not calculated as accurately as the other two principal components. It has previously been suggested that large residuals associated with  $\sigma_{22}$  may result from motion of the C-H bond [116]. In nearly

every case, the calculated values of  $\sigma_{22}$  are slightly smaller than the experimental value. Furthermore, the agreement of calculated  $\sigma_{11}$  values for aromatic carbons with experimental chemical shifts is generally worse when one includes intermolecular effects, and is only marginally improved following geometry optimizations. This observation suggests that rovibrational effects influence this principal component at least as strongly as intermolecular effects, and that the two contributions may partially cancel one another in static, isolated-molecule models.

## 2.4 Conclusions

The inclusion of intermolecular effects on calculated  $^{13}\text{C}$  magnetic shielding has been evaluated using density-functional theory for a representative set of organic materials having well-defined atomic coordinates and experimental chemical-shift-tensor components. Molecular clusters and isolated molecules were used to model the solid materials. A comparison of the calculations for the two models shows that cluster models, when properly chosen to take into account the properties of the material, provide systematic improvement over the results of the isolated-molecule model.

One aspect of the problem which this investigation emphasizes is that, with cluster models, one can partition the model structure into regions with locally-dense basis sets and regions with sparse basis sets. This approximation greatly reduces the computational cost without a significant effect on the calculated magnetic shielding. Such a method allows calculations to be performed on larger clusters, which would otherwise be prohibitively expensive. Magnetic shielding is strongly influenced by cluster size, but shielding tends to converge smoothly when the number of molecules in the cluster is increased. Clusters that provide converged, or nearly converged, results can be handled with current software capabilities.

This analysis demonstrates the importance of size and symmetry considerations when defining a molecular cluster. Clusters should not be defined arbitrarily so that, for instance, only molecules participating in direct hydrogen bonds are included, because this may exclude other important intermolecular interactions. Instead, clusters should be defined so as to reflect the symmetry of the crystalline space group. Judicious placement of molecules in a cluster to represent the solid state seems to be of considerable importance in obtaining quantitative results.

The results here strongly suggest that modeling the solid state with extended molecular clusters is a viable alternative to the use of PBCs. Cluster models have several inherent advantages over the latter, including the ability to compare results to isolated-molecule calculations, the possibility of simplification of calculation by using lower basis sets in regions removed from the molecule of interest, general applicability to non-periodic systems, and the ability to exploit additional model chemistries such as hybrid exchange-correlation functionals and *ab initio* methods.

## REFERENCES

- [1] J.C. Facelli, Calculations of chemical shieldings: theory and applications, *Concepts Magn. Reson., Part A*, 20A (2004) 42-69.
- [2] J.C. Facelli, Chemical shift tensors: theory and application to molecular structural problems, *Prog. Nucl. Magn. Reson. Spectrosc.*, 58 (2011) 176-201.
- [3] C.J. Jameson, Understanding NMR chemical shifts, *Annu. Rev. Phys. Chem.*, 47 (1996) 135-169.
- [4] G. Hou, I.-J.L. Byeon, J. Ahn, A.M. Gronenborn, T. Polenova, Recoupling of chemical shift anisotropy by R-symmetry sequences in magic angle spinning NMR spectroscopy, *J. Chem. Phys.*, 137 (2012) 134201.
- [5] J. Kempf, H.W. Spiess, U. Haeberlen, H. Zimmermann, Carbon-13 anisotropic chemical shift in a single crystal of benzophenone, *Chem. Phys. Lett.*, 17 (1972) 39-42.
- [6] J. Herzfeld, A.E. Berger, Sideband intensities in NMR spectra of sample spinning at the magic angle, *J. Chem. Phys.*, 73 (1980) 6021-6030.
- [7] D.W. Alderman, G. McGeorge, J.Z. Hu, R.J. Pugmire, D.M. Grant, A sensitive, high resolution magic angle turning experiment for measuring chemical shift tensor principal values, *Mol. Phys.*, 95 (1998) 1113-1126.
- [8] J.C.C. Chan, R. Tycko, Recoupling of chemical shift anisotropies in solid-state NMR under high-speed magic-angle spinning and in uniformly  $^{13}\text{C}$ -labeled systems, *J. Chem. Phys.*, 118 (2003) 8378-8389.
- [9] J.C. Johnston, R.J. Iulucci, J.C. Facelli, G. Fitzgerald, K.T. Mueller, Intermolecular shielding contributions studied by modeling the  $^{13}\text{C}$  chemical-shift tensors of organic single crystals with plane waves, *J. Chem. Phys.*, 131 (2009) 144503.
- [10] J.C. Facelli, D.M. Grant, J. Michl, Carbon-13 shielding tensors: experimental and theoretical determination, *Acc. Chem. Res.*, 20 (1987) 152-158.
- [11] M. Kaupp, M. Bühl, V.G. Malkin, *Calculation of NMR and EPR Parameters: Theory and Applications*, Wiley 2006.

- [12] J. Vaara, Theory and computation of nuclear magnetic resonance parameters, *Phys. Chem. Chem. Phys.*, 9 (2007) 5399-5418.
- [13] A.M. Orendt, J.C. Facelli, Solid-state effects on NMR chemical shifts, in: G.A. Webb (Ed.) *Annual Reports on NMR Spectroscopy*, Vol 62, Elsevier Academic Press Inc, San Diego, 2007, pp. 115-178.
- [14] F. Alkan, C. Dybowski, Calculation of chemical-shift tensors of heavy nuclei: a DFT/ZORA investigation of  $^{199}\text{Hg}$  chemical-shift tensors in solids, and the effects of cluster size and electronic-state approximations, *Phys. Chem. Chem. Phys.*, 16 (2014) 14298-14308.
- [15] J.A. Tossell, Second-nearest-neighbor effects upon N NMR shieldings in models for solid  $\text{Si}_3\text{N}_4$  and  $\text{C}_3\text{N}_4$ , *J. Magn. Reson.*, 127 (1997) 49-53.
- [16] J.A. Tossell, Second-nearest-neighbor effects on the NMR shielding of N in  $\text{P}_3\text{N}_5$  and hexagonal BN, *Chem. Phys. Lett.*, 303 (1999) 435-440.
- [17] J.A. Tossell, Quantum mechanical calculation of  $^{23}\text{Na}$  NMR shieldings in silicates and aluminosilicates, *Phys. Chem. Miner.*, 27 (1999) 70-80.
- [18] G. Valerio, A. Goursot, R. Vetrivel, O. Malkina, V. Malkin, D.R. Salahub, Calculation of  $^{29}\text{Si}$  and  $^{27}\text{Al}$  MAS NMR chemical shifts in zeolite- $\beta$  using density functional theory: correlation with lattice structure, *J. Am. Chem. Soc.*, 120 (1998) 11426-11431.
- [19] G. Valerio, A. Goursot, Density functional calculations of the  $^{29}\text{Si}$  and  $^{27}\text{Al}$  MAS NMR spectra of the zeolite mazzite: analysis of geometrical and electronic effects, *J. Phys. Chem. B*, 103 (1999) 51-58.
- [20] H. Koller, G. Engelhardt, A.P.M. Kentgens, J. Sauer,  $^{23}\text{Na}$  NMR spectroscopy of solids: interpretation of quadrupole interaction parameters and chemical shifts, *J. Phys. Chem.*, 98 (1994) 1544-1551.
- [21] S.-H. Cai, Z. Chen, H.-L. Wan, Theoretical investigation of  $^{19}\text{F}$  NMR chemical shielding of alkaline-earth-metal and alkali-metal fluorides, *J. Phys. Chem. A*, 106 (2002) 1060-1066.
- [22] M. Body, G. Silly, C. Legein, J.-Y. Buzare, Cluster models and ab initio calculations of  $^{19}\text{F}$  NMR isotropic chemical shifts for inorganic fluorides, *J. Phys. Chem. B*, 109 (2005) 10270-10278.
- [23] O. Dmitrenko, S. Bai, P.A. Beckmann, S. van Bramer, A.J. Vega, C. Dybowski, The relationship between  $^{207}\text{Pb}$  NMR chemical shift and solid-state structure in Pb(II) compounds, *J. Phys. Chem. A*, 112 (2008) 3046-3052.

- [24] O. Dmitrenko, S. Bai, C. Dybowski, Prediction of  $^{207}\text{Pb}$  NMR parameters for the solid ionic lead(II) halides using the relativistic ZORA-DFT formalism: comparison with the lead-containing molecular systems, *Solid State Nucl. Magn. Reson.*, 34 (2008) 186-190.
- [25] F. Alkan, C. Dybowski, Chemical-shift tensors of heavy nuclei in network solids: a DFT/ZORA investigation of  $^{207}\text{Pb}$  chemical-shift tensors using the bond-valence method, *Phys. Chem. Chem. Phys.*, 17 (2015) 25014-25026.
- [26] F. Alkan, C. Dybowski, Effect of co-ordination chemistry and oxidation state on  $^{207}\text{Pb}$  magnetic-shielding tensor: a DFT/ZORA investigation. , *J. Phys. Chem. A*, 120 (2016) 161-168.
- [27] F. Alkan, S.T. Holmes, R.J. Iulicci, K.T. Mueller, C. Dybowski, Spin-orbit effects on the  $^{119}\text{Sn}$  magnetic-shielding tensor in solids: a ZORA/DFT investigation, *Phys. Chem. Chem. Phys.*, 18 (2016) 18914-18922.
- [28] K.M.N. Burgess, Y. Xu, M.C. Leclerc, D.L. Bryce, Insight into magnesium coordination environments in benzoate and salicylate complexes through  $^{25}\text{Mg}$  solid-state NMR spectroscopy, *J. Phys. Chem. A*, 117 (2013) 6561-6570.
- [29] R.P. Chapman, D.L. Bryce, A high-field solid-state  $^{35/37}\text{Cl}$  NMR and quantum chemical investigation of the chlorine quadrupolar and chemical shift tensors in amino acid hydrochlorides, *Phys. Chem. Chem. Phys.*, 9 (2007) 6219-6230.
- [30] A.M. Orendt, J.C. Facelli, D.M. Grant, A theoretical study of the acetate  $^{13}\text{C}$  chemical shift tensor in cadmium acetate dihydrate, *Chem. Phys. Lett.*, 302 (1999) 499-504.
- [31] G. Zheng, L. Wang, J. Hu, X. Zhang, L. Shen, C. Ye, G.A. Webb, Hydrogen bonding effects on the  $^{13}\text{C}$  NMR chemical shift tensors of some amino acids in the solid state, *Magn. Reson. Chem.*, 35 (1997) 606-608.
- [32] K.M.N. Burgess, Y. Xu, M.C. Leclerc, D.L. Bryce, Alkaline-earth metal carboxylates characterized by  $^{43}\text{Ca}$  and  $^{87}\text{Sr}$  solid-state NMR: impact of metal-amine bonding, *Inorg. Chem.*, 53 (2014) 552-561.
- [33] J.Z. Hu, J.C. Facelli, D.W. Alderman, R.J. Pugmire, D.M. Grant,  $^{15}\text{N}$  chemical shift tensors in nucleic acid bases, *J. Am. Chem. Soc.*, 120 (1998) 9863-9869.
- [34] M.S. Solum, K.L. Altman, M. Strohmeier, D.A. Berges, Y. Zhang, J.C. Facelli, R.J. Pugmire, D.M. Grant,  $^{15}\text{N}$  chemical shift principal values in nitrogen heterocycles, *J. Am. Chem. Soc.*, 119 (1997) 9804-9809.

- [35] J.C. Facelli, R.J. Pugmire, D.M. Grant, Effects of hydrogen bonding in the calculation of  $^{15}\text{N}$  chemical shift tensors: benzamide, *J. Am. Chem. Soc.*, 118 (1996) 5488-5489.
- [36] X. Chen, C.-G. Zhan, First-principles studies of C-13 NMR chemical shift tensors of amino acids in crystal state, *J. Mol. Struct.*, 682 (2004) 73-82.
- [37] D. Stueber, F.N. Guenneau, D.M. Grant, The calculation of  $^{13}\text{C}$  chemical shielding tensors in ionic compounds utilizing point charge arrays obtained from Ewald lattice sums, *J. Chem. Phys.*, 114 (2001) 9236-9243.
- [38] D. Stueber, The embedded ion method: a new approach to the electrostatic description of crystal lattice effects in chemical shielding calculations, *Concepts Magn. Reson.*, Part A, 28A (2006) 347-368.
- [39] D. Stueber, D.M. Grant,  $^{13}\text{C}$  and  $^{15}\text{N}$  chemical shift tensors in adenosine, guanosine dihydrate, 2'-deoxythymidine, and cytidine, *J. Am. Chem. Soc.*, 124 (2002) 10539-10551.
- [40] M.B. Ferraro, V. Repetto, J.C. Facelli, Modeling NMR chemical shifts: a comparison of charge models for solid state effects on  $^{15}\text{N}$  chemical shift tensors, *Solid State Nucl. Magn. Reson.*, 10 (1998) 185-189.
- [41] D. Solís, M.B. Ferraro, J.C. Facelli, Modeling NMR chemical shifts: surface charge representation of the electrostatic embedding potential modeling of crystalline intermolecular effects in  $^{19}\text{F}$  solid state NMR chemical shifts, *J. Mol. Struct.*, 602-603 (2002) 159-164.
- [42] J. Weber, J. Schmedt auf der Gunne, Calculation of NMR parameters in ionic solids by an improved self-consistent embedded cluster method, *Phys. Chem. Chem. Phys.*, 12 (2010) 583-603.
- [43] M. Strohmeier, D. Stueber, D.M. Grant, Accurate  $^{13}\text{C}$  and  $^{15}\text{N}$  chemical shift and  $^{14}\text{N}$  quadrupolar coupling constant calculations in amino acid crystals: zwitterionic, hydrogen-bonded systems, *J. Phys. Chem. A*, 107 (2003) 7629-7642.
- [44] C. Bonhomme, C. Gervais, F. Babonneau, C. Coelho, F. Pourpoint, T. Azais, S.E. Ashbrook, J.M. Griffin, J.R. Yates, F. Mauri, C.J. Pickard, First-Principles Calculation of NMR Parameters Using the Gauge Including Projector Augmented Wave Method: A Chemist's Point of View, *Chem. Rev.*, 112 (2012) 5733-5779.
- [45] A.D. Becke, Density-functional thermochemistry. 3. The role of exact exchange, *J. Chem. Phys.*, 98 (1993) 5648-5652.

- [46] R. Laskowski, P. Blaha, F. Tran, Assessment of DFT functionals with NMR chemical shifts, *Phys. Rev. B*, 87 (2013).
- [47] A.V. Arbuznikov, M. Kaupp, Advances in local hybrid exchange-correlation functionals: From thermochemistry to magnetic-resonance parameters and hyperpolarizabilities, *Int. J. Quant. Chem.*, 111 (2011) 2625-2638.
- [48] R. Suardiaz, C. Perez, R. Crespo-Otero, J.M.G. de la Vega, J.S. Fabian, Influence of density functionals and basis sets on one-bond carbon-carbon NMR spin-spin coupling constants, *J. Chem. Theory Comput.*, 4 (2008) 448-456.
- [49] P. Broqvist, A. Alkauskas, A. Pasquarello, Hybrid-functional calculations with plane-wave basis sets: effect of singularity correction on total energies, energy eigenvalues, and defect energy levels, *Phys. Rev. B*, 80 (2009) 085114.
- [50] C.J. Jameson, A.C. de Dios, Ab initio calculations of the intermolecular chemical shift in nuclear magnetic resonance in the gas phase and for adsorbed species, *J. Chem. Phys.*, 97 (1992) 417-434.
- [51] N.F. Ramsey, The internal diamagnetic field correction in measurements of the proton magnetic moment, *Phys. Rev.*, 77 (1950) 567-567.
- [52] J.A. Pople, Molecular-orbital theory of diamagnetism. I. an approximate LCAO scheme, *J. Chem. Phys.*, 37 (1962) 53-59.
- [53] C.M. Widdifield, R.W. Schurko, Understanding chemical shielding tensors using group theory, MO analysis, and modern density-functional theory, *Concepts Magn. Reson., Part A*, 34A (2009) 91-123.
- [54] F. Liu, C.G. Phung, D.W. Alderman, D.M. Grant, Carbon-13 chemical shift tensors in methyl glycosides, comparing diffraction and optimized structures with single-crystal NMR, *J. Am. Chem. Soc.*, 118 (1996) 10629-10634.
- [55] G.A. Jeffrey, R.K. McMullan, S. Takagi, A neutron diffraction study of the hydrogen bonding in the crystal structures of methyl  $\alpha$ -D-mannopyranoside and methyl  $\alpha$ -D-glucopyranoside, *Acta Crystallogr., Sect. B*, B33 (1977) 728-737.
- [56] S. Takagi, G.A. Jeffrey, Neutron diffraction refinement of the crystal structures of methyl  $\alpha$ -D-galactopyranoside monohydrate and methyl  $\beta$ -D-galactopyranoside, *Acta Crystallogr., Sect. B*, B35 (1979) 902-906.
- [57] S. Takagi, G.A. Jeffrey, Methyl  $\beta$ -D-galactopyranoside, *Acta Crystallogr., Sect. B*, B34 (1978) 2006-2010.

- [58] S. Takagi, G.A. Jeffrey, A neutron diffraction refinement of the crystal structures of  $\beta$ -L-arabinose and methyl  $\beta$ -D-xylopyranoside, *Acta Crystallogr., Sect. B*, B33 (1977) 3033-3040.
- [59] M.H. Sherwood, D.W. Alderman, D.M. Grant, Assignment of carbon-13 chemical-shift tensors in single-crystal sucrose, *J. Magn. Reson., Ser A*, 104 (1993) 132-145.
- [60] G.M. Brown, H.A. Levy, Further refinement of the structure of sucrose based on neutron-diffraction data, *Acta Crystallogr., Sect. B*, 29 (1973) 790-797.
- [61] F. Liu, C.G. Phung, D.W. Alderman, D.M. Grant, Analyzing and assigning carbon-13 chemical-shift tensors in  $\alpha$ -L-rhamnose monohydrate single crystals, *J. Magn. Reson., Ser A*, 120 (1996) 242-248.
- [62] S. Takagi, G.A. Jeffrey, A neutron diffraction refinement of the crystal structure of  $\alpha$ -L-rhamnose monohydrate, *Acta Crystallogr., Sect. B*, B34 (1978) 2551-2555.
- [63] F. Liu, C.G. Phung, D.W. Alderman, D.M. Grant, Analyzing and assigning carbon-13 chemical-shift tensors in fructose, sorbose, and xylose single crystals, *J. Magn. Reson., Ser A*, 120 (1996) 11-11.
- [64] S. Takagi, G.A. Jeffrey, A neutron diffraction study of the crystal structure of  $\beta$ -D-fructopyranose, *Acta Crystallogr., Sect. B*, B33 (1977) 3510-3515.
- [65] V.G. Malkin, O.L. Malkina, D.R. Salahub, Influence of intermolecular interactions on the  $^{13}\text{C}$  NMR shielding tensor in solid  $\alpha$ -glycine, *J. Am. Chem. Soc.*, 117 (1995) 3294-3295.
- [66] P.G. Jonsson, A. Kvik, Precision neutron diffraction structure determination of protein and nucleic acid components. III. Crystal and molecular structure of the amino acid  $\alpha$ -glycine, *Acta Crystallogr., Sect. B*, 28 (1972) 1827-1833.
- [67] M.J. Potrzebowski, P. Tekely, Y. Dusauroy, Comment to  $^{13}\text{C}$ -NMR studies of  $\alpha$  and  $\gamma$  polymorphs of glycine, *Solid State Nucl. Magn. Reson.*, 11 (1998) 253-257.
- [68] A. Kvik, W.M. Canning, T.F. Koetzle, G.J.B. Williams, An experimental study of the influence of temperature on a hydrogen-bonded system: the crystal structure of  $\gamma$ -glycine at 83 K and 298 K by neutron diffraction, *Acta Crystallogr., Sect. B*, 36 (1980) 115-120.
- [69] A. Naito, S. Ganapathy, K. Akasaka, C.A. McDowell, Chemical shielding tensor and  $^{13}\text{C}$ - $^{14}\text{N}$  dipolar splitting in single crystals of L-alanine, *J. Chem. Phys.*, 74 (1981) 3190-3197.

- [70] C.C. Wilson, D. Myles, M. Ghosh, L.N. Johnson, W. Wang, Neutron diffraction investigations of L- and D-alanine at different temperatures: the search for structural evidence for parity violation, *New J. Chem.*, 29 (2005) 1318-1322.
- [71] A. Naito, S. Ganapathy, P. Raghunathan, C.A. McDowell, Determination of the nitrogen-14 quadrupole coupling tensor and the carbon-13 chemical shielding tensors in a single crystal of L-serine monohydrate, *J. Chem. Phys.*, 79 (1983) 4173-4182.
- [72] M.N. Frey, M.S. Lehmann, T.F. Koetzle, W.C. Hamilton, Precision neutron diffraction structure determination of protein and nucleic acid components. XI. Molecular configuration and hydrogen bonding of serine in the crystalline amino acids L-serine monohydrate and DL-serine, *Acta Crystallogr., Sect. B*, 29 (1973) 876-884.
- [73] A. Naito, C.A. McDowell, Determination of the nitrogen-14 quadrupole coupling tensors and the carbon-13 chemical shielding tensors in a single crystal of L-asparagine monohydrate, *J. Chem. Phys.*, 81 (1984) 4795-4803.
- [74] M. Ramanadham, S.K. Sikka, R. Chidambaram, Structure of L-asparagine monohydrate by neutron diffraction, *Acta Crystallogr., Sect. B*, 28 (1972) 3000-3005.
- [75] N. Janes, S. Ganapathy, E. Oldfield, Carbon-13 chemical shielding tensors in L-threonine, *J. Magn. Reson.*, 54 (1983) 111-121.
- [76] M. Ramanadham, S.K. Sikka, R. Chidambaram, Structure determination of L<sub>s</sub>-threonine by neutron diffraction, *Pramana*, 1 (1973) 247-259.
- [77] R.G. Griffin, A. Pines, S. Pausak, J.S. Waugh, Carbon-13 chemical shielding in oxalic acid, oxalic acid dihydrate, and diammonium oxalate, *J. Chem. Phys.*, 63 (1975) 1267-1271.
- [78] T.M. Sabine, G.W. Cox, B.M. Craven, Neutron-diffraction study of  $\alpha$ -oxalic acid dihydrate, *Acta Crystallogr., Sect. B*, 25 (1969) 2437-2441.
- [79] M. Mehring, J.D. Becker, Observation of electronic structure change at the first-order phase transition in quasi-two-dimensional squaric acid, *Phys. Rev. Lett.*, 47 (1981) 366-370.
- [80] D. Semmingsen, F.J. Hollander, T.F. Koetzle, A neutron diffraction study of squaric acid (3,4-dihydroxy-3-cyclobutene-1,2-dione), *J. Chem. Phys.*, 66 (1977) 4405-4412.
- [81] M.H. Sherwood, J.C. Facelli, D.W. Alderman, D.M. Grant, Carbon-13 chemical shift tensors in polycyclic aromatic compounds. 2. single-crystal study of naphthalene, *J. Am. Chem. Soc.*, 113 (1991) 750-753.

- [82] S.C. Capelli, A. Albinati, S.A. Mason, B.T.M. Willis, Molecular motion in crystalline naphthalene: analysis of multi-temperature X-Ray and neutron diffraction data, *J. Phys. Chem. A*, 110 (2006) 11695-11703.
- [83] S. Pausak, A. Pines, J.S. Waugh, Carbon-13 chemical shielding tensors in single-crystal durene, *J. Chem. Phys.*, 59 (1973) 591-595.
- [84] E. Prince, L.W. Schroeder, J.J. Rush, Constrained refinement of the structure of durene, *Acta Crystallogr., Sect. B*, 29 (1973) 184-191.
- [85] R.J. Iulucci, C.G. Phung, J.C. Facelli, D.M. Grant, Carbon-13 chemical shift tensors in polycyclic aromatic compounds. 7. Symmetry augmented chemical shift-chemical shift correlation spectroscopy and single crystal study of triphenylene, *J. Am. Chem. Soc.*, 120 (1998) 9305-9311.
- [86] G. Ferraris, D.W. Jones, J. Yerkess, A neutron-diffraction study of the crystal and molecular structure of triphenylene, *Z. Kristallogr.*, 138 (1973) 113-128.
- [87] R.J. Iulucci, J.C. Facelli, D.W. Alderman, D.M. Grant, Carbon-13 chemical shift tensors in polycyclic aromatic compounds. 5. single-crystal study of acenaphthene, *J. Am. Chem. Soc.*, 117 (1995) 2336-2343.
- [88] A.C. Hazell, R.G. Hazell, L. Noerskov-Lauritsen, C.E. Briant, D.W. Jones, A neutron diffraction study of the crystal and molecular structure of acenaphthene, *Acta Crystallogr., Sect. C*, C42 (1986) 690-693.
- [89] F. Liu, A.M. Orendt, D.W. Alderman, D.M. Grant, Carbon-13 chemical shift tensors in pentaerythritol, *J. Am. Chem. Soc.*, 119 (1997) 8981-8984.
- [90] D. Semmingsen, Neutron diffraction refinement of the structure of pentaerythritol, *Acta Chem. Scand., Ser. A*, A42 (1988) 279-283.
- [91] W.T. Klooster, J.R. Ruble, B.M. Craven, R.K. McMullan, Structure and thermal vibrations of adenosine from neutron diffraction data at 123 K, *Acta Crystallogr., Sect. B*, B47 (1991) 376-383.
- [92] J.K. Harper, R. Iulucci, M. Gruber, K. Kalakewich, Refining crystal structures with experimental <sup>13</sup>C NMR shift tensors and lattice-including electronic structure methods, *CrystEngComm*, 15 (2013) 8693-8704.
- [93] C.C. Wilson, Neutron diffraction of p-hydroxyacetanilide (paracetamol): Libration or disorder of the methyl group at 100 K, *J. Mol. Struct.*, 405 (1997) 207-217.

- [94] E. Carignani, S. Borsacchi, A. Marini, B. Mennucci, M. Geppi,  $^{13}\text{C}$  chemical shielding tensors: A combined solid-state NMR and DFT study of the role of small-amplitude motions, *J. Phys. Chem. C*, 115 (2011) 25023-25029.
- [95] N. Shankland, C.C. Wilson, A.J. Florence, P.J. Cox, Refinement of ibuprofen at 100 K by single-crystal pulsed neutron diffraction, *Acta Crystallogr., Sect. C*, C53 (1997) 951-954.
- [96] A.D. Becke, A new mixing of Hartree–Fock and local density-functional theories, *J. Chem. Phys.*, 98 (1993) 1372-1377.
- [97] C. Lee, W. Yang, R.G. Parr, Development of the Colle-Salvetti correlation-energy formula into a functional of the electron density, *Phys. Rev. B*, 37 (1988) 785-789.
- [98] P.C. Hariharan, J.A. Pople, The effect of d-functions on molecular orbital energies for hydrocarbons, *Chem. Phys. Lett.*, 16 (1972) 217-219.
- [99] S.J. Clark, M.D. Segall, C.J. Pickard, P.J. Hasnip, M.J. Probert, K. Refson, M.C. Payne, S.J. Clark, M.D. Segall, C.J. Pickard, P.J. Hasnip, M.J. Probert, K. Refson, M.C. Payne, First principles methods using CASTEP, *Z. Kristallogr.*, 220 (2005) 567-570.
- [100] J.P. Perdew, K. Burke, M. Ernzerhof, Generalized gradient approximation made simple, *Phys. Rev. Lett.*, 77 (1996) 3865-3868.
- [101] J.P. Perdew, Y. Wang, Accurate and simple analytic representation of the electron-gas correlation energy, *Physical Review B*, 45 (1992) 13244.
- [102] T.H. Dunning, Gaussian basis sets for use in correlated molecular calculations. I. the atoms boron through neon and hydrogen, *J. Chem. Phys.*, 90 (1989) 1007-1023.
- [103] M.J. Frisch, G.W. Trucks, H.B. Schlegel, G.E. Scuseria, M.A. Robb, J.R. Cheeseman, G. Scalmani, V. Barone, B. Mennucci, G.A. Petersson, H. Nakatsuji, M. Caricato, X. Li, H.P. Hratchian, A.F. Izmaylov, J. Bloino, G. Zheng, J.L. Sonnenberg, M. Hada, M. Ehara, K. Toyota, R. Fukuda, J. Hasegawa, M. Ishida, T. Nakajima, Y. Honda, O. Kitao, H. Nakai, T. Vreven, J.A. Montgomery, J.E. Peralta, F. Ogliaro, M. Bearpark, J.J. Heyd, E. Brothers, K.N. Kudin, V.N. Staroverov, R. Kobayashi, J. Normand, K. Raghavachari, A. Rendell, J.C. Burant, S.S. Iyengar, J. Tomasi, M. Cossi, N. Rega, J.M. Millam, M. Klene, J.E. Knox, J.B. Cross, V. Bakken, C. Adamo, J. Jaramillo, R. Gomperts, R.E. Stratmann, O. Yazyev, A.J. Austin, R. Cammi, C. Pomelli, J.W. Ochterski, R.L. Martin, K. Morokuma, V.G. Zakrzewski, G.A. Voth, P. Salvador, J.J. Dannenberg, S. Dapprich, A.D. Daniels, Farkas, J.B. Foresman, J.V. Ortiz, J. Cioslowski, D.J. Fox, *Gaussian 09, Revision B.01*, Wallingford CT, 2009.

- [104] D.B. Chesnut, K.D. Moore, Locally dense basis sets for chemical shift calculations, *J. Comput. Chem.*, 10 (1989) 648-659.
- [105] D.B. Chesnut, B.E. Rusiloski, K.D. Moore, D.A. Egolf, Use of locally dense basis sets for nuclear magnetic resonance shielding calculations, *J. Comput. Chem.*, 14 (1993) 1364-1375.
- [106] D.M. Reid, R. Kobayashi, M.A. Collins, Systematic study of locally dense basis sets for NMR shielding constants, *J. Chem. Theory Comput.*, 10 (2014) 146-152.
- [107] J.C. Johnston, R.J. Iuliucci, J.C. Facelli, G. Fitzgerald, K.T. Mueller, Intermolecular shielding contributions studied by modeling the  $^{13}\text{C}$  chemical-shift tensors of organic single crystals with plane waves, *J. Chem. Phys.*, 131 (2009) 144501-144511.
- [108] M. Dracinsky, H.M. Moller, T.E. Exner, Conformational sampling by ab initio molecular dynamics simulations improves NMR chemical shift predictions, *J. Chem. Theory Comput.*, 9 (2013) 3806-3815.
- [109] L.A. Truflandier, J. Autschbach, Probing the solvent shell with  $^{195}\text{Pt}$  chemical shifts: Density functional theory molecular dynamics study of  $\text{Pt}^{\text{II}}$  and  $\text{Pt}^{\text{IV}}$  anionic complexes in aqueous solution, *J. Am. Chem. Soc.*, 132 (2010) 3472-3483.
- [110] M. Dracinsky, P. Hodgkinson, A molecular dynamics study of the effects of fast molecular motions on solid-state NMR parameters, *CrystEngComm*, 15 (2013) 8705-8712.
- [111] C. Scheurer, N.R. Skrynnikov, S.F. Lienin, S.K. Straus, R. Bruschweiler, R.R. Ernst, Effects of dynamics and environment on  $^{15}\text{N}$  chemical shielding anisotropy in proteins. A combination of density functional theory, molecular dynamics simulation, and NMR relaxation, *J. Am. Chem. Soc.*, 121 (1999) 4242-4251.
- [112] M. Dracinsky, P. Hodgkinson, Effects of quantum nuclear delocalisation on NMR parameters from path integral molecular dynamics, *Chem. Eur. J.*, 20 (2014) 2201-2207.
- [113] M. Dračinský, P. Bouř, P. Hodgkinson, Temperature dependence of NMR parameters calculated from path integral molecular dynamics simulations, *J. Chem. Theory Comput.*, (2016).
- [114] D.H. Barich, R.J. Pugmire, D.M. Grant, R.J. Iuliucci, Investigation of the structural conformation of biphenyl by solid state C-13 NMR and quantum chemical NMR shift calculations, *J. Phys. Chem. A*, 105 (2001) 6780-6784.

[115] J. Powell, K. Kalakewich, F.J. Uribe-Romo, J.K. Harper, Solid-state NMR and DFT predictions of differences in COOH hydrogen bonding in odd and even numbered n-alkyl fatty acids, *Phys. Chem. Chem. Phys.*, 18 (2016) 12541-12549.

[116] T.H. Sefzik, D. Turco, R.J. Iuliucci, J.C. Facelli, Modeling NMR chemical shift: a survey of density functional theory approaches for calculating tensor properties, *J. Phys. Chem. A*, 109 (2005) 1180-1187.

## Chapter 3

### CARBON-13 CHEMICAL-SHIFT TENSORS IN INDIGO: A TWO-DIMENSIONAL NMR-ROCSA AND DFT STUDY

#### 3.1 Introduction

Indigo, 2,2'-bis(2,3-dihydro-3-oxoindolyliden), is a blue dye with technological, industrial, cultural, and biological significance [1]. The molecular structure and atom-labeling scheme of indigo are given in Figure 3.1. Traditionally, indigo has been obtained as a tryptophan-derived natural product extracted from tropical plants. The synthesis of indigo has been important in the history of industrial chemistry through processes such as those developed by Baeyer [2-4], including the Baeyer-Drewson reaction [5], and later synthetic routes appropriate to large-scale production by Heumann [6] and by Pflieger [7]. Other than its use as a textile dye, indigo and its derivatives have been used as components of organic semiconductors [8-10].

NMR spectroscopy has been used in combination with computational chemistry to study the interaction between indigo molecules and porous clays [11-16]. Complexation of indigo derivatives with model fibers has been the subject of investigation by NMR spectroscopy [17, 18]. Chemical analyses of cultural heritage objects with NMR spectroscopy have detected indigo [18, 19]. NMR has been used to study the biodegradation of indigo dye and its derivatives [20, 21], as well as the biosynthesis of indigo and indigo precursors in plants [22] and bacteria [23].

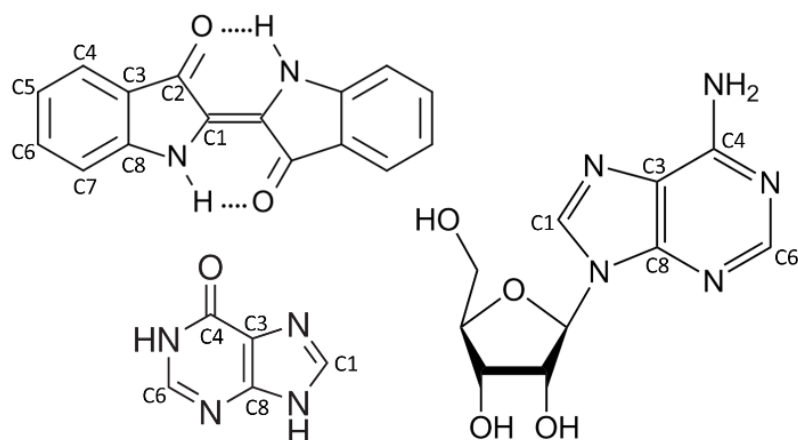


**Figure 3.1.** Structures of indigo (upper left), hypoxanthine (lower left), and adenosine (right). The labeling schemes for the aromatic carbon sites are shown.

The ubiquity of indigo makes it an excellent model for the study of indole rings, which are found in such places as the amino acid tryptophan and its derivatives. Carbon-13 chemical-shift tensors have not been reported for carbons in indole rings in any material containing such rings. Careful measurements of the  $^{13}\text{C}$  chemical-shift parameters of crystalline indigo are important in understanding the crystalline structure, the molecular structure, and the electronic state of the solid. An analysis of structural effects on the  $^{13}\text{C}$  chemical shifts of indigo may be of significance in the interpretation of NMR data on indole-containing materials like tryptophan.

The link between chemical shifts and crystal structure is established through quantum-chemical calculations. In this chapter, experimental  $^{13}\text{C}$  chemical-shift tensors for all sites in indigo are assigned to their respective lattice sites by comparison to calculated values. Calculations are also performed on the purine derivative hypoxanthine, and the purine nucleoside adenosine, both of which are structurally similar to indigo (Figure 3.1).

### 3.2 Experimental Methods

Measurements of the  $^{13}\text{C}$  chemical-shift tensors in indigo employed the recoupling-of-chemical-shift-anisotropy (ROCSA) sequence, a two-dimensional magic-angle-spinning (MAS) technique in which rotor-synchronized pulse sequences are used to obtain the recoupled powder patterns [24]. The ROCSA sequence is amenable to high-frequency MAS because the recoupling field is required to be only about four times the MAS frequency. The technique was originally developed for the study of isotopically labeled proteins; however, ROCSA and related sequences have been applied in the analysis of organic systems other than peptides [25-28]. High-power decoupling of  $^1\text{H}$  spins used a sequence of  $^1\text{H}$   $90^\circ$  pulses of  $2.97\ \mu\text{s}$  (SPINAL-64 at 100 kHz). The ROCSA sequence was rotor-synchronized with a MAS frequency of 10.0 kHz. 32  $t_1$  points, with 544 scans each, were collected with a 6.0 s recycle delay. The isotropic chemical shifts were externally referenced to tetramethylsilane (TMS) using the amide carbon in  $\alpha$ -glycine (176.5 ppm) as a secondary reference [29].

Principal components of the  $^{13}\text{C}$  chemical-shift tensors were extracted from the recoupled chemical-shift powder patterns using a numerical simulation with WSOLIDS [30], which identified the principal components of the chemical-shift tensors by searching for singularities in the derivative spectra. The numerical simulations introduced an expansion factor of 0.272, as suggested by Chan and Tycko [24].

### 3.3 Computational Methods

Predicted chemical-shift tensors were derived from DFT calculations on molecular clusters representing structures of the three solids. The models of indigo, hypoxanthine, and adenosine were built from thirteen, eleven, and fifteen molecules, respectively (see Figure 3.2 for an illustration of the indigo cluster), to represent the

local lattice structure around a single molecule, in accordance with the symmetry-adapted-cluster ansatz discussed in the preceding chapter. The cluster models were based on single-crystal diffraction parameters [31-33]. Geometry optimizations to refine the atomic coordinates were performed using the cluster model with the PBE functional [34] and the cc-pVDZ basis set [35]. For adenosine, the positions of only the hydrogen atoms were refined, as the structure was obtained from neutron diffraction. For indigo and hypoxanthine, the optimizations were performed in two steps where the first optimization allowed only the positions of hydrogen atoms to relax and the second optimization allowed the entire molecule to relax. The optimization procedure did not alter the structure of the molecule significantly, with changes in bond lengths limited to ranges found in previous studies [36].

Magnetic shielding was calculated with the GIAO formalism [37-39] using the  $\tau$ -dependent hybrid exchange-correlation functional TPSSh [40]. This model chemistry was selected to provide a rigorous description of electron correlation in the heteroatomic ring. The basis-set-partitioning scheme discussed in Chapter 2 was employed, with the more flexible basis set cc-pVTZ used for the central molecules and cc-pVDZ used for peripheral molecules (Figure 3.2). Calculations were also performed on single refined molecules in isolation, as a means to examine intermolecular effects on the magnetic shielding. All calculations in this study were performed using GAUSSIAN 09 [41].

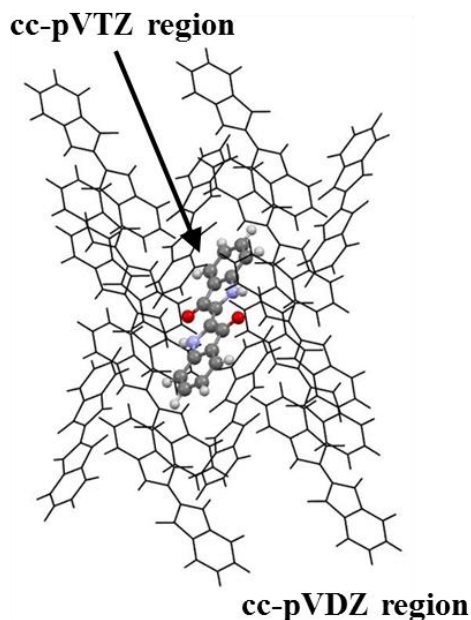


**Figure 3.2.** Crystal packing diagram of indigo (polymorph A,  $P2_1/c$  space group) showing the partition into two layers. The central molecule (cc-pVTZ basis set) is shown in the ball-and-stick representation and the peripheral molecules (cc-pVDZ basis set) are shown in a wireframe representation.

### 3.4 Results and Discussion

#### 3.4.1 NMR Measurements and Peak Assignments

Indigo belongs to the  $P2_1/c$  space group with an asymmetric unit composed of half a molecule. The experimental MAS NMR spectrum consists of eight unique resonances located between 112.5 ppm and 187.8 ppm, in agreement with expectation based on the crystal structure. Three peaks fall between 118.6 ppm and 121.0 ppm but are resolvable, as shown in the 2D ROCSA spectrum in Figure 3.3(a). Subspectra from the ROCSA experiment are shown in Figure 3.3(b) and a summary of the  $^{13}\text{C}$  chemical-shift tensors extracted from the powder patterns is given in Table 3.1. Each site exhibits

considerable chemical-shift anisotropy with the narrowest powder pattern having a span of 124 ppm and the widest, 200 ppm.

An assignment of the resonances is accomplished by correlating the experimental principal components of the  $^{13}\text{C}$  chemical-shift tensors with those obtained from DFT calculations (Figure 3.4). On this plot are shown the results for indigo, as well as those for hypoxanthine and adenosine (Tables 3.2 and 3.3). Large deviations between experiment and calculation (up to 13 ppm for an individual principal component in indigo) are observed for some sites (Table 3.1). However, these deviations are well within the range of errors typically reported for aromatic systems containing heteroatoms, as is supported by the calculations on hypoxanthine and adenosine, as well as previous work [36]. This overall assignment yields a root-mean-square deviation (RMSD) between calculation and experiment of 7.1 ppm.

### 3.4.2 Discussion of $^{13}\text{C}$ Chemical-Shift Tensors of Indigo

Several aromatic  $^{13}\text{C}$  chemical-shift tensors of indigo are very different from the tensors of other polycyclic ring systems such as naphthalene [42], indicating the significant effect of incorporating heteroatoms. In six-membered rings containing a heteroatom,  $\pi$ -deficient nitrogens have been found to stabilize positive charge at positions *ortho* and *para* to the nitrogen [43]. The result of this charge stabilization is that carbons *meta* to the nitrogen center are more isotropically shielded than carbons *ortho* and *para* to the nitrogen. In five-membered heteroatomic rings, carbons one bond from the nitrogen center are typically deshielded relative to carbons two bonds from the nitrogen center [43]. C8 of indigo, which resides adjacent to the nitrogen, is the most strongly deshielded carbon site, with  $\delta_{iso} = 152.3$  ppm. C6, three bonds from the nitrogen, is also isotropically deshielded, with  $\delta_{iso} = 134.0$  ppm, as compared to C7,

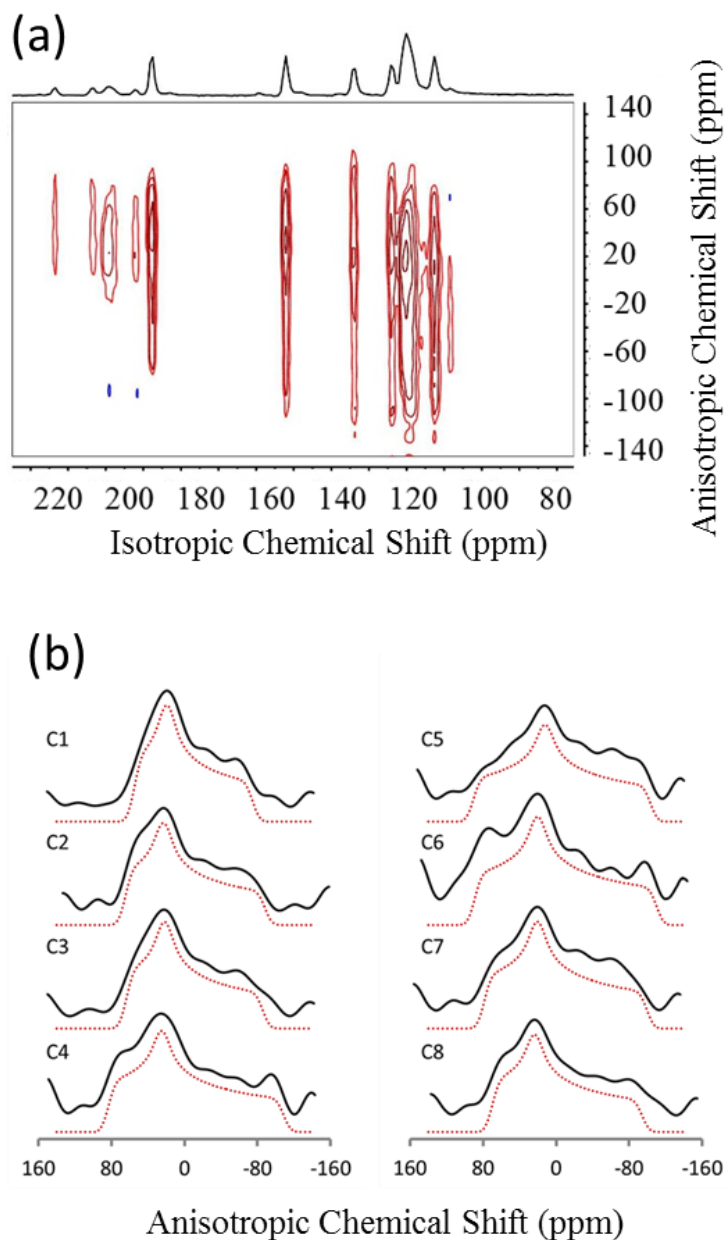


**Figure 3.3.** (a)  $^{13}\text{C}$  NMR-ROCSA spectrum of indigo. The chemical-shift scale in the  $f1$  dimension is referenced to the isotropic chemical shift of each resonance, as is customary in ROCSA spectra, whereas the  $f2$  dimension is referenced to TMS. (b) ROCSA chemical-shift subspectra of the eight unique  $^{13}\text{C}$  sites in indigo. The upper solid lines are the experimental spectra and the lower traces (dotted lines) are simulated spectra from fitting the chemical-shift powder patterns.

with  $\delta_{iso} = 112.5$  ppm, which is two bonds from nitrogen. C5, four bonds from the nitrogen has an intermediate shift of  $\delta_{iso} = 118.6$  ppm. Although C1 is one bond away from the nitrogen,  $\delta_{iso} = 120.7$  ppm, which suggests that its involvement in the double bond compensates the deshielding effects of the adjacent nitrogen.

The aromatic carbon sites in indigo can be parsed into classes based on similarities between the principal components of the  $^{13}\text{C}$  chemical-shift tensors. The first major aromatic class is represented by C8, the carbon site one bond from the nitrogen center. For C8 uniquely, significant deshielding is observed in  $\delta_{22}$  and  $\delta_{33}$  (176 ppm and 58 ppm from TMS, respectively) relative to the other aromatic carbon sites. The remaining aromatic sites (C3 – C7) can be parsed into classes according to the number of bonds separating them from nitrogen. C3 and C7, each two bonds from the nitrogen center, have similar tensors. C4 and C6, each three bonds from nitrogen, form another class. C5, four bonds from the nitrogen site, is the final class. The principal components of the  $^{13}\text{C}$  chemical-shift tensor for C5 fall within the tolerances of polycyclic-aromatic hydrocarbons (PAH) reported by Facelli [44]. However, the remaining carbon sites do not fall within the tolerances provided in reference 44, indicating the substantial role of the nitrogen heteroatom on the observed chemical-shift tensors of carbons in the ring.

The class comprised of carbons two bonds from nitrogen can be subdivided into carbons bonded directly to a hydrogen and those which have no directly bonded hydrogen. This difference appears most strongly in the value of  $\delta_{33}$ . For example, C3, a bridgehead site, is strongly deshielded ( $\delta_{33} = 34$  ppm) relative to the same principal component of C7 ( $\delta_{33} = 13$  ppm), the latter being bonded to a hydrogen. The remaining

**Table 3.1.** Principal components of the  $^{13}\text{C}$  chemical-shift tensors of indigo, with the average of the principal components, isotropic chemical shift, span, and skew.<sup>a</sup>

Site	$\delta_{11}$ (ppm) <sup>b</sup>	$\delta_{22}$ (ppm) <sup>b</sup>	$\delta_{33}$ (ppm) <sup>b</sup>	$\delta_{ave}$ (ppm) <sup>b</sup>	$\delta_{iso}$ (ppm) <sup>b</sup>	$\Omega$ (ppm)	$\kappa$
C1	<b>173</b> <i>177.1</i>	<b>140</b> <i>144.2</i>	<b>49</b> <i>48.7</i>	<b>120.7</b> -	<b>121.0</b> <i>123.3</i>	<b>124</b> <i>128.4</i>	<b><math>0.46 \pm 0.06</math></b> <i>0.488</i>
C2	<b>253</b> <i>255.6</i>	<b>211</b> <i>202.9</i>	<b>100</b> <i>102.6</i>	<b>188.0</b> -	<b>187.8</b> <i>187.0</i>	<b>153</b> <i>153.0</i>	<b><math>0.45 \pm 0.05</math></b> <i>0.312</i>
C3	<b>184</b> <i>192.1</i>	<b>142</b> <i>153.7</i>	<b>34</b> <i>23.6</i>	<b>120.0</b> -	<b>119.9</b> <i>123.2</i>	<b>150</b> <i>168.5</i>	<b><math>0.44 \pm 0.05</math></b> <i>0.543</i>
C4	<b>208</b> <i>218.0</i>	<b>149</b> <i>162.0</i>	<b>16</b> <i>4.4</i>	<b>124.3</b> -	<b>124.1</b> <i>128.1</i>	<b>192</b> <i>213.6</i>	<b><math>0.39 \pm 0.04</math></b> <i>0.476</i>
C5	<b>210</b> <i>214.4</i>	<b>131</b> <i>128.4</i>	<b>15</b> <i>11.1</i>	<b>118.7</b> -	<b>118.6</b> <i>117.9</i>	<b>194</b> <i>203.3</i>	<b><math>0.22 \pm 0.02</math></b> <i>0.155</i>
C6	<b>224</b> <i>236.5</i>	<b>154</b> <i>143.9</i>	<b>24</b> <i>13.4</i>	<b>134.0</b> -	<b>134.1</b> <i>131.3</i>	<b>200</b> <i>223.1</i>	<b><math>0.30 \pm 0.04</math></b> <i>0.169</i>
C7	<b>191</b> <i>193.4</i>	<b>133</b> <i>143.1</i>	<b>13</b> <i>14.7</i>	<b>112.3</b> -	<b>112.5</b> <i>117.1</i>	<b>178</b> <i>178.7</i>	<b><math>0.35 \pm 0.04</math></b> <i>0.436</i>
C8	<b>223</b> <i>222.2</i>	<b>176</b> <i>182.8</i>	<b>58</b> <i>50.0</i>	<b>152.3</b> -	<b>152.3</b> <i>151.7</i>	<b>165</b> <i>172.2</i>	<b><math>0.43 \pm 0.04</math></b> <i>0.542</i>

<sup>a</sup>Experimental values are shown in bold; calculated values are shown in italics. Calculated magnetic-shielding parameters were converted to chemical shifts using least-squares linear-regression parameters  $\sigma_{ref} = 185.4$  ppm and  $m = -1.012$ . <sup>b</sup>The uncertainty in experimental principal components is  $\pm 2$  ppm; uncertainty in  $\delta_{ave}$  and  $\delta_{iso}$  is  $\pm 0.5$  ppm and  $\pm 1.2$  ppm, respectively; uncertainty in the span is  $\pm 3$  ppm.

**Table 3.2.** Principal components of the  $^{13}\text{C}$  chemical-shift tensors of hypoxanthine, with the average of the principal components, isotropic chemical shift, span, and skew.<sup>a,b</sup>

Site	$\delta_{11}$ (ppm)	$\delta_{22}$ (ppm)	$\delta_{33}$ (ppm)	$\delta_{ave}$ (ppm)	$\delta_{iso}$ (ppm)	$\Omega$ (ppm)	$\kappa$
C1	<b>218</b>	<b>150</b>	<b>57</b>	<b>141.7</b>	<b>141.8</b>	<b>161</b>	<b>0.15</b>
	<i>212.9</i>	<i>151.2</i>	<i>62.6</i>	-	<i>142.2</i>	<i>150.3</i>	<i>0.180</i>
C3	<b>167</b>	<b>155</b>	<b>45</b>	<b>122.3</b>	<b>122.4</b>	<b>122</b>	<b>0.80</b>
	<i>165.6</i>	<i>157.7</i>	<i>51.4</i>	-	<i>124.9</i>	<i>114.2</i>	<i>0.862</i>
C4	<b>239</b>	<b>156</b>	<b>82</b>	<b>159.0</b>	<b>159.2</b>	<b>157</b>	<b>-0.06</b>
	<i>233.8</i>	<i>156.7</i>	<i>88.8</i>	-	<i>159.7</i>	<i>145.0</i>	<i>-0.062</i>
C6	<b>231</b>	<b>149</b>	<b>56</b>	<b>145.3</b>	<b>145.3</b>	<b>175</b>	<b>0.06</b>
	<i>229.7</i>	<i>153.8</i>	<i>60.8</i>	-	<i>148.1</i>	<i>168.9</i>	<i>0.101</i>
C8	<b>225</b>	<b>163</b>	<b>60</b>	<b>149.3</b>	<b>149.4</b>	<b>165</b>	<b>0.25</b>
	<i>217.8</i>	<i>167.2</i>	<i>64.6</i>	-	<i>149.9</i>	<i>153.2</i>	<i>0.339</i>

<sup>a</sup>Experimental values are taken from Maliňáková *et al.* [45]. NMR parameters were obtained from Herzfeld-Berger analysis of the manifold of spinning side bands.

<sup>b</sup>Experimental values are shown in bold; calculated values are shown in italics.

**Table 3.3.** Principal components of the  $^{13}\text{C}$  chemical-shift tensors of adenosine, with the average of the principal components, isotropic chemical shift, span, and skew.<sup>a,b,c</sup>

Site	$\delta_{11}$ (ppm)	$\delta_{22}$ (ppm)	$\delta_{33}$ (ppm)	$\delta_{ave}$ (ppm)	$\delta_{iso}$ (ppm)	$\Omega$ (ppm)	$\kappa$
C1	<b>216</b>	<b>136</b>	<b>61</b>	<b>137.7</b>	<b>137.8</b>	<b>155</b>	<b>-0.03</b>
	<i>208.7</i>	<i>133.4</i>	<i>63.5</i>	-	<i>135.2</i>	<i>145.2</i>	<i>-0.037</i>
C3	<b>167</b>	<b>145</b>	<b>47</b>	<b>119.7</b>	<b>119.7</b>	<b>120</b>	<b>0.63</b>
	<i>154.0</i>	<i>149.6</i>	<i>48.3</i>	-	<i>117.3</i>	<i>105.7</i>	<i>0.917</i>
C4	<b>222</b>	<b>191</b>	<b>52</b>	<b>155.0</b>	<b>155.2</b>	<b>170</b>	<b>0.63</b>
	<i>201.6</i>	<i>194.0</i>	<i>56.4</i>	-	<i>150.7</i>	<i>145.2</i>	<i>0.895</i>
C6	<b>239</b>	<b>158</b>	<b>66</b>	<b>154.3</b>	<b>154.8</b>	<b>173</b>	<b>0.06</b>
	<i>234.5</i>	<i>162.7</i>	<i>62.5</i>	-	<i>153.2</i>	<i>172.0</i>	<i>0.166</i>
C8	<b>221</b>	<b>166</b>	<b>58</b>	<b>148.3</b>	<b>148.5</b>	<b>163</b>	<b>0.32</b>
	<i>213.7</i>	<i>161.2</i>	<i>57.8</i>	-	<i>144.2</i>	<i>155.9</i>	<i>0.327</i>

<sup>a</sup>Experimental values are taken from Steuber *et al.* [46]. NMR parameters were measured with the FIREMAT sequence. <sup>b</sup>Experimental values are shown in bold; calculated values are shown in italics. <sup>c</sup>Results are not reported for the ribose carbons.

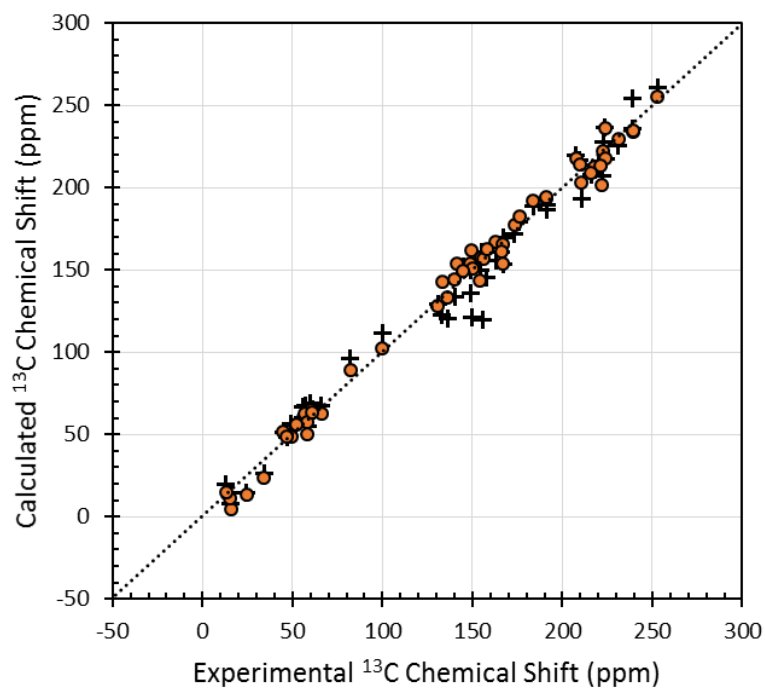


**Figure 3.4.** Correlation of calculated principal chemical-shift components and experimental principal chemical-shift components for  $^{13}\text{C}$  sites in indigo, hypoxanthine, and adenosine. Calculations were performed at the TPSSh/cc-pVTZ level. Results for the ribose carbons of adenosine are not included. Values obtained using cluster models are shown as solid orange circles whereas values obtained using isolated-molecule models are shown as black crosses.

aromatic sites in indigo (C4 – C6) are bonded to hydrogens and have  $\delta_{33}$  between 15 ppm and 24 ppm, similar to that of C7.

Comparison of measured and calculated chemical-shift principal components of indigo to those of hypoxanthine [45] and adenosine [46] gives further insight into the effect of heteroatoms on the carbon chemical-shift tensor. The position of the nitrogen atom in the ring is important to the extended lattice structure because it determines the geometry of intermolecular hydrogen bonds. Of particular interest are C3, C6, and C8, as these sites are unsubstituted aromatic or bridgehead carbons in all three molecules.

The most similar feature of these three molecules is the chemical-shift tensor of C8. In all three molecules, C8 is a bridgehead carbon linking a six-membered ring with a five-membered ring one bond from a nitrogen center. In all cases, the principal components fall in the ranges of  $223 \pm 2$  ppm,  $168 \pm 7$  ppm, and  $59 \pm 1$  ppm for  $\delta_{11}$ ,  $\delta_{22}$ , and  $\delta_{33}$ , respectively. C3 in indigo is bound to three neighboring carbon atoms, whereas in the purine rings of hypoxanthine and adenosine, C3 is bonded to two carbon sites and a nitrogen site. For all three molecules,  $\delta_{22}$  and  $\delta_{33}$  fall in the ranges of  $147 \pm 8$  ppm and  $42 \pm 7$  ppm, respectively. For indigo,  $\delta_{11}$  of C3 is 184 ppm whereas this value is  $167 \pm 3$  ppm in the purine rings, suggesting that the adjacency to the nitrogen produces shielding of this component. For C6,  $\delta_{11}$  and  $\delta_{22}$  fall in the ranges of  $231 \pm 8$  ppm and  $154 \pm 5$  ppm, respectively, for all three materials. However,  $\delta_{33}$  is 24 ppm for indigo, but  $61 \pm 5$  ppm in the purine rings. It appears that an indole derivative can be distinguished readily from a derivative of purine through analysis of the principal components of the  $^{13}\text{C}$  chemical-shift tensors, particularly the  $\delta_{33}$  component.

### 3.4.3 Assessment of Lattice Effects

The effect of the crystalline lattice on the calculated chemical-shift tensors in indigo can be assessed by comparison of calculations including the effects of the lattice (as done above) with the results of calculations where lattice effects are ignored, specifically calculations on an isolated indigo molecule, as if it were in the gas phase. The differences in the computed principal components between the two models are given in Table 3.4.

In indigo, intermolecular interactions result in increased shielding of the  $^{13}\text{C}$  principal component  $\delta_{33}$  at each carbon site. The average increase is 4.7 ppm, with a maximum of 9.2 ppm observed for the keto carbon (C2). The largest effect for any

principal component is seen for  $\delta_{22}$  of C7, which is deshielded by 20.2 ppm relative to the isolated molecule. Significant deshielding is seen in the  $\delta_{22}$  principal components of C1 (10.7 ppm) and C4 (11.8 ppm).

**Table 3.4.** Differences in calculated chemical-shift tensors between an a molecule in a cluster and a molecule in isolation.

Site	<u>Indigo</u>			<u>Hypoxanthine</u>			<u>Adenosine</u>		
	$\Delta\delta_{11}$ (ppm)	$\Delta\delta_{22}$ (ppm)	$\Delta\delta_{33}$ (ppm)	$\Delta\delta_{11}$ (ppm)	$\Delta\delta_{22}$ (ppm)	$\Delta\delta_{33}$ (ppm)	$\Delta\delta_{11}$ (ppm)	$\Delta\delta_{22}$ (ppm)	$\Delta\delta_{33}$ (ppm)
C1	5.4	10.7	-7.8	2.2	30.4	-5.0	0.8	13.2	-1.9
C2	-5.4	9.8	-9.2	-	-	-	-	-	-
C3	3.2	7.8	-2.7	-4.2	-3.1	0.5	0.2	-2.1	-0.1
C4	-1.7	12.1	-3.9	-20.4	37.4	-7.0	-5.5	7.5	0.6
C5	-2.5	-1.2	-3.2	-	-	-	-	-	-
C6	-0.2	-6.0	-1.1	4.1	18.1	-5.6	-1.6	17.3	-4.9
C7	3.9	20.2	-4.9	-	-	-	-	-	-
C8	-5.5	4.0	-5.0	0.5	11.8	-4.6	-2.6	0.2	-2.2

A simple explanation for the differences in chemical shifts between the cluster models and the isolated-molecule models is the existence of weak intermolecular interactions such as N-H $\cdots$ O and C-H $\cdots$ O hydrogen bonding that would not be present in an isolated molecule. Süsse suggests that indigo contains a bifurcated N-H $\cdots$ O hydrogen bond where the position of the amine hydrogen is stabilized through intramolecular and intermolecular interactions with nearby keto oxygens [31]. The importance of this interaction is evidenced by the large change in all three principal components of the  $^{13}\text{C}$  chemical-shift tensor of C2 (the keto carbon). The C-H $\cdots$ O

interaction is known to be important in the crystal packing of purines [47], and appears to be present in indigo as well. For C7 of indigo, the nearest-neighbor atom in the crystal lattice is a keto oxygen site, which resides only 2.39 Å from the hydrogen site of C7, a distance less than the sum of the van der Waals radii of the atoms (2.6 Å). For C4, the nearest neighbor is also a keto oxygen at a distance of only 2.41 Å from the bonded hydrogen. The difference in the calculated chemical-shift components is an indication of these weak intermolecular C-H···O hydrogen bonds.

The intermolecular contributions to  $^{13}\text{C}$  magnetic shielding in the purine rings is very different from that observed in indigo, reflecting the different lattice environments arising from hydrogen bonding. In hypoxanthine, the largest difference is again observed for the keto carbon, C4, where  $\delta_{11}$  of the site in the cluster is strongly shielded by 20.4 ppm relative to the isolated molecule and  $\delta_{22}$  is deshielded by 37.4 ppm. These values are consistent with strong intermolecular N-H···O hydrogen bonding in the crystalline material [48].  $\delta_{22}$  for aromatic carbons C1 and C6 in the cluster are deshielded by 30.4 ppm and 18.1 ppm, respectively, relative to the isolated molecule. The effect of intermolecular hydrogen bonding on computed  $^{13}\text{C}$  NMR parameters in hypoxanthine, again, is consistent with previous studies [45]. In adenosine, the largest difference in calculated  $^{13}\text{C}$  chemical shifts for  $\delta_{22}$  of C6, which is deshielded by 17.3 ppm relative to the same site in an isolated molecule. Earlier computational studies have ascribed the large differences in adenosine to the effects of hydrogen bonding [46].

The RMSD between values calculated for an isolated molecule and the experimental results is 10.6 ppm. When the model includes intermolecular effects, as for the cluster calculations, this RMSD between calculated and experimental values is 7.1 ppm. This difference indicates that the inclusion of intermolecular interactions in

magnetic-shielding calculations clearly improves the agreement between calculated and experimental results.

### 3.5 Conclusion

The  $^{13}\text{C}$  NMR chemical-shift tensors of the eight carbons of crystalline indigo have been measured with a recoupling-of-chemical-shift-anisotropy (ROCSA) experiment. Theoretical NMR parameters derived from a refined diffraction structure were used as an aid to assign the experimental measurements to their respective sites. Comparison of the principal components of the chemical-shift tensors was necessary, in some cases, to complete the assignments. The assignment is unambiguous and results in an average error of 7.1 ppm, a value consistent with materials containing heteroatomic aromatic rings. The principal components of the chemical-shift tensors of the aromatic sites in indigo deviate substantially from those reported for aromatic hydrocarbons such as naphthalene, indicating the significant effect of heteroatoms on the magnetic shielding at carbon sites.

A comparison of the principal components of the  $^{13}\text{C}$  chemical-shift tensors of indigo with those of two purine derivatives confirms that magnetic shielding is very sensitive to the position of nitrogen in the ring. To explain the effects on chemical shifts due to the presence of other molecules, we posit that the presence of a heteroatom allows indigo to form hydrogen bonds with adjacent molecules in the crystal lattice. Ignoring these intermolecular effects in calculations shows substantial disagreement of the calculated chemical-shift principal components with experiment, with deviations between the computational models as high as 20.2 ppm for some principal components. Inclusion of these effects through a cluster model brings the experimental and calculated values of principal components into good agreement.

## REFERENCES

- [1] J.M. Matthews, The industrial development of indigo, *J. Frankl. Inst.*, 154 (1902) 423-429.
- [2] A. Baeyer, Synthese des isatins und des indigblaus, *Chem. Ber.*, 11 (1878) 1228.
- [3] A. Baeyer, Synthese des indigblaus, *Chem. Ber.*, 11 (1878) 1296-1297.
- [4] A. Baeyer, Ueber die beziehungen der zimmtsäure zu der indigogruppe, *Chem. Ber.*, 13 (1880) 2254-2263.
- [5] A. Baeyer, V. Drewsen, Darstellung von indigblau aus orthonitrobenzaldehyd, *Chem. Ber.*, 15 (1882) 2856-2864.
- [6] K. Heumann, Neue synthesen des indigos und verwandter farbstoffe, *Chem. Ber.*, 23 (1890) 3043-3045.
- [7] J. Pfleger, Process of Making Indoxyl Derivatives, Deutsche Gold & Silber Scheide Anstalt Vorm. Roessler, Germany . 1901.
- [8] M. Irimia-Vladu, E.D. Głowacki, P.A. Troshin, G. Schwabegger, L. Leonat, D.K. Susarova, O. Krystal, M. Ullah, Y. Kanbur, M.A. Bodea, V.F. Razumov, H. Sitter, S. Bauer, N.S. Sariciftci, Indigo - A natural pigment for high performance ambipolar organic field effect transistors and circuits, *Adv. Mater.*, 24 (2012) 375-380.
- [9] B. He, A.B. Pun, D. Zherebetsky, Y. Liu, F. Liu, L.M. Klivansky, A.M. McGough, B.A. Zhang, K. Lo, T.P. Russell, L.W. Wang, New form of an old natural dye: Bay-annulated indigo (BAI) as an excellent electron accepting unit for high performance organic semiconductors, *J. Am. Chem. Soc.*, 136 (2014) 15093-15101.
- [10] O. Pitayatanakul, T. Higashino, T. Kadoya, M. Tanaka, H. Kojima, M. Ashizawa, T. Kawamoto, H. Matsumoto, K. Ishikawa, T. Mori, High performance ambipolar organic field-effect transistors based on indigo derivatives, *J. Mater. Chem. C*, 2 (2014) 9311-9317.
- [11] S. Ovarlez, F. Giulieri, A.M. Chaze, F. Delamare, J. Raya, J. Hirschinger, The incorporation of indigo molecules in sepiolite tunnels, *Chem. Eur. J.*, 15 (2009) 11326-11332.

- [12] R. Giustetto, F. Xamena, G. Ricchiardi, S. Bordiga, A. Damin, R. Gobetto, M.R. Chierotti, Maya blue: A computational and spectroscopic study, *J. Phys. Chem. B*, 109 (2005) 19360-19368.
- [13] E. Lima, A. Guzman, M. Vera, J.L. Rivera, J. Fraissard, Aged natural and synthetic Maya blue-like pigments: What difference does it make?, *J. Phys. Chem. C*, 116 (2012) 4556-4563.
- [14] J. Raya, J. Hirschinger, S. Ovarlez, F. Giulieri, A.M. Chaze, F. Delamare, Insertion of indigo molecules in the sepiolite structure as evidenced by  $^1\text{H}$ - $^{29}\text{Si}$  heteronuclear correlation spectroscopy, *Phys. Chem. Chem. Phys.*, 12 (2010) 14508-14514.
- [15] A. Domenech, M.T. Domenech-Carbo, M.S. del Rio, S. Goberna, E. Lima, Evidence of topological indigo/dehydroindigo isomers in Maya blue-like complexes prepared from palygorskite and sepiolite, *J. Phys. Chem. C*, 113 (2009) 12118-12131.
- [16] B. Hubbard, W.X. Kuang, A. Moser, G.A. Facey, C. Detellier, Structural study of Maya Blue: Textural, thermal and solid-state multinuclear magnetic resonance characterization of the palygorskite-indigo and sepiolite-indigo adducts, *Clays Clay Miner.*, 51 (2003) 318-326.
- [17] C. Bonechi, S. Martini, C. Rossi, Interaction study of indigo carmine with albumin and dextran by NMR relaxation, *Journal of Materials Science*, 46 (2011) 2541-2547.
- [18] R.C. Hoffman, R.C. Zilber, R.E. Hoffman, NMR spectroscopic study of the Murex trunculus dyeing process, *Magn. Reson. Chem.*, 48 (2010) 892-895.
- [19] N. Proietti, F. Presciutti, V. Di Tullio, B. Doherty, A.M. Marinelli, B. Provinciali, N. Macchioni, D. Capitani, C. Miliani, Unilateral NMR,  $^{13}\text{C}$  CPMAS NMR spectroscopy and micro-analytical techniques for studying the materials and state of conservation of an ancient Egyptian wooden sarcophagus, *Anal. Bioanal. Chem.*, 399 (2011) 3117-3131.
- [20] M. Ramya, B. Anusha, S. Kalavathy, Decolorization and biodegradation of indigo carmine by a textile soil isolate *Paenibacillus* larvae, *Biodegradation*, 19 (2008) 283-291.
- [21] H. Podgornik, I. Poljansek, A. Perdih, Transformation of indigo carmine by *Phanerochaete chrysosporium* ligninolytic enzymes, *Enzyme Microb. Technol.*, 29 (2001) 166-172.
- [22] Z.Q. Xia, M.H. Zenk, Biosynthesis of indigo precursors in higher plants, *Phytochemistry*, 31 (1992) 2695-2697.

- [23] S. Hart, K.R. Koch, D.R. Woods, Identification of indigo-related pigments produced by *Escherichia coli* containing a cloned rhodococcus gene, *J. Gen. Microbiol.*, 138 (1992) 211-216.
- [24] J.C.C. Chan, R. Tycko, Recoupling of chemical shift anisotropies in solid-state NMR under high-speed magic-angle spinning and in uniformly  $^{13}\text{C}$ -labeled systems, *J. Chem. Phys.*, 118 (2003) 8378-8389.
- [25] S. Paramasivam, A. Balakrishnan, O. Dmitrenko, A. Godert, T.P. Begley, F. Jordan, T. Polenova, Solid-state NMR and density functional theory studies of ionization states of thiamin, *J. Phys. Chem. B*, 115 (2011) 730-736.
- [26] L.B. Casabianca, M.A. Shaibat, W.W.W. Cai, S. Park, R. Piner, R.S. Ruoff, Y. Ishii, NMR-based structural modeling of graphite oxide using multidimensional  $^{13}\text{C}$  solid-state NMR and ab initio chemical shift calculations, *J. Am. Chem. Soc.*, 132 (2010) 5672-5676.
- [27] G. Hou, I.-J.L. Byeon, J. Ahn, A.M. Gronenborn, T. Polenova, Recoupling of chemical shift anisotropy by R-symmetry sequences in magic angle spinning NMR spectroscopy, *J. Chem. Phys.*, 137 (2012) 134201.
- [28] R.M. Orr, M.J. Duer, Recoupling of chemical-shift anisotropy powder patterns in MAS NMR, *J. Magn. Reson.*, 181 (2006) 1-8.
- [29] V.G. Malkin, O.L. Malkina, D.R. Salahub, Influence of intermolecular interactions on the  $^{13}\text{C}$  NMR shielding tensor in solid  $\alpha$ -glycine, *J. Am. Chem. Soc.*, 117 (1995) 3294-3295.
- [30] K. Eichele, HBA 3.1 and WSOLIDS, University of Tübingen, Tübingen, 2013.
- [31] P. Susse, M. Steins, V. Kupcik, Indigo: Crystal structure refinement based on synchrotron data, *Z. Kristallogr.*, 184 (1988) 269-273.
- [32] H.W. Schmalle, G. Hanggi, E. Dubler, Structure of hypoxanthine, *Acta Crystallogr., Sect. C*, 44 (1988) 732-736.
- [33] W.T. Klooster, J.R. Ruble, B.M. Craven, R.K. McMullan, Structure and thermal vibrations of adenosine from neutron diffraction data at 123 K, *Acta Crystallogr., Sect. B*, B47 (1991) 376-383.
- [34] J.P. Perdew, K. Burke, M. Ernzerhof, Generalized gradient approximation made simple, *Phys. Rev. Lett.*, 77 (1996) 3865-3868.

- [35] T.H. Dunning, Gaussian basis sets for use in correlated molecular calculations. I. the atoms boron through neon and hydrogen, *J. Chem. Phys.*, 90 (1989) 1007-1023.
- [36] J.K. Harper, R. Iulucci, M. Gruber, K. Kalakewich, Refining crystal structures with experimental  $^{13}\text{C}$  NMR shift tensors and lattice-including electronic structure methods, *CrystEngComm*, 15 (2013) 8693-8704.
- [37] J.R. Cheeseman, G.W. Trucks, T.A. Keith, M.J. Frisch, A comparison of models for calculating nuclear magnetic resonance shielding tensors, *J. Chem. Phys.*, 104 (1996) 5497-5509.
- [38] G. Schreckenbach, T. Ziegler, Calculation of NMR shielding tensors using gauge-including atomic orbitals and modern density functional theory, *J. Phys. Chem.*, 99 (1995) 606-611.
- [39] R. Ditchfield, Self-consistent perturbation theory of diamagnetism, *Mol. Phys.*, 27 (1974) 789-807.
- [40] J.M. Tao, J.P. Perdew, V.N. Staroverov, G.E. Scuseria, Climbing the density functional ladder: nonempirical meta-generalized gradient approximation designed for molecules and solids, *Phys. Rev. Lett.*, 91 (2003) 146401.
- [41] M.J. Frisch, G.W. Trucks, H.B. Schlegel, G.E. Scuseria, M.A. Robb, J.R. Cheeseman, G. Scalmani, V. Barone, B. Mennucci, G.A. Petersson, H. Nakatsuji, M. Caricato, X. Li, H.P. Hratchian, A.F. Izmaylov, J. Bloino, G. Zheng, J.L. Sonnenberg, M. Hada, M. Ehara, K. Toyota, R. Fukuda, J. Hasegawa, M. Ishida, T. Nakajima, Y. Honda, O. Kitao, H. Nakai, T. Vreven, J.A. Montgomery, J.E. Peralta, F. Ogliaro, M. Bearpark, J.J. Heyd, E. Brothers, K.N. Kudin, V.N. Staroverov, R. Kobayashi, J. Normand, K. Raghavachari, A. Rendell, J.C. Burant, S.S. Iyengar, J. Tomasi, M. Cossi, N. Rega, J.M. Millam, M. Klene, J.E. Knox, J.B. Cross, V. Bakken, C. Adamo, J. Jaramillo, R. Gomperts, R.E. Stratmann, O. Yazyev, A.J. Austin, R. Cammi, C. Pomelli, J.W. Ochterski, R.L. Martin, K. Morokuma, V.G. Zakrzewski, G.A. Voth, P. Salvador, J.J. Dannenberg, S. Dapprich, A.D. Daniels, Farkas, J.B. Foresman, J.V. Ortiz, J. Cioslowski, D.J. Fox, *Gaussian 09, Revision B.01*, Wallingford CT, 2009.
- [42] M.H. Sherwood, J.C. Facelli, D.W. Alderman, D.M. Grant, Carbon-13 chemical shift tensors in polycyclic aromatic compounds. 2. single-crystal study of naphthalene, *J. Am. Chem. Soc.*, 113 (1991) 750-753.
- [43] W.W. Paudler, *Nuclear Magnetic Resonance: General Concepts and Applications*, John Wiley & Sons, Ltd., New York, 1988.

- [44] J.C. Facelli, B.K. Nakagawa, A.M. Orendt, R.J. Pugmire, Cluster analysis of  $^{13}\text{C}$  chemical shift tensor principal values in polycyclic aromatic hydrocarbons, *J. Phys. Chem. A*, 105 (2001) 7468-7472.
- [45] K. Maliňáková, L. Novosadová, M. Lahtinen, E. Kolehmainen, J. Brus, R. Marek,  $^{13}\text{C}$  chemical shift tensors in hypoxanthine and 6-mercaptopurine: effects of substitution, tautomerism, and intermolecular interactions, *J. Phys. Chem. A*, 114 (2010) 1985-1995.
- [46] D. Stueber, D.M. Grant,  $^{13}\text{C}$  and  $^{15}\text{N}$  chemical shift tensors in adenosine, guanosine dihydrate, 2'-deoxythymidine, and cytidine, *J. Am. Chem. Soc.*, 124 (2002) 10539-10551.
- [47] D.J. Sutor, C-H $\cdots$ O hydrogen bonds in crystals, *Nature*, 195 (1962) 68-&.
- [48] S.T. Holmes, R.J. Iulucci, K.T. Mueller, C. Dybowski, Density functional investigation of intermolecular effects on  $^{13}\text{C}$  NMR chemical-shielding tensors modeled with molecular clusters, *J. Chem. Phys.*, 141 (2014) 164121.

## Chapter 4

# CRITICAL ANALYSIS OF CLUSTER MODELS AND EXCHANGE-CORRELATION FUNCTIONALS FOR CALCULATING MAGNETIC SHIELDING IN MOLECULAR SOLIDS

### 4.1 Introduction

Chapter 2 demonstrated that calculations of  $^{13}\text{C}$  magnetic-shielding tensors, where symmetry-adapted clusters (SACs) are employed to represent a local portion of the lattice structure, and are combined with modern DFT methods, result in significant agreement with experimental  $^{13}\text{C}$  chemical-shift tensors. This chapter has two goals. First, this chapter demonstrates that the symmetry-adapted cluster *ansatz* can be employed successfully for the prediction of magnetic-shielding tensors in a variety of nuclides, including  $^{13}\text{C}$ ,  $^{15}\text{N}$ ,  $^{19}\text{F}$  and  $^{31}\text{P}$ . To illustrate this, the results of calculations on a wide variety of molecular solids, which contain these nuclides, are presented. Furthermore, the magnetic-shielding tensors obtained from the cluster approach are compared to the magnetic-shielding tensors from GIPAW calculations. Second, calculations performed using more advanced computational models available with the cluster approach are explored. It is demonstrated that the use of modern DFT functionals based on hybrid DFT or on the meta-generalized-gradient approximation (meta-GGA) improve agreement between calculation and experiment for the four nuclides.

### 4.2 Materials and Computational Details

A large series of model compounds was examined. To ensure that sample set did not unnecessarily introduce uncertainty, only compounds that met the following

criteria were included: (1) the structure of the material had to be known from high-quality single-crystal diffraction studies, (2) high-resolution measurements of the NMR chemical-shift tensors had to be available for the compound in the same solid phase, and (3) the chemical shifts must have been assigned unambiguously to their respective nuclear sites in the crystalline lattice.

Materials were selected to encompass a large variety of chemical environments for  $^{13}\text{C}$ ,  $^{15}\text{N}$ ,  $^{19}\text{F}$ , and  $^{31}\text{P}$  nuclides. Whenever available, neutron-diffraction structures were used to define the structure; otherwise, single-crystal X-ray diffraction provided the structural information. Altogether, this database contains 393 principal components of NMR chemical-shift tensors taken from 72 materials. The subset of  $^{13}\text{C}$  NMR measurements consists of 177 principal components, of which 96 are  $sp^3$ -hybridized, 75 are  $sp^2$ -hybridized, and 6 are  $sp$ -hybridized. The subsets of  $^{15}\text{N}$ ,  $^{19}\text{F}$ , and  $^{31}\text{P}$  NMR measurements consist of 99, 60, and 57 principal components, respectively.

The database of  $^{13}\text{C}$ -containing materials (Table 4.1) includes naphthalene [1, 2], durene [3, 4], hypoxanthine [5, 6], sucrose [7, 8],  $\alpha$ -oxalic acid [9, 10], oxalic acid dihydrate [9, 11], L-threonine [12, 13], squaric acid [14, 15], cyclopropane [16, 17], ethylene [18, 19], nitromethane [20, 21], acetylene [22, 23], carbon disulfide [24, 25], dimethoxymethane [26, 27], pentaerythritol [28, 29], dimedone [30, 31], norbornadiene [32, 33], and [1.1.1]propellane [34, 35].

The database of  $^{15}\text{N}$ -containing materials (Table 4.2) includes adenine trihydrate [36, 37], cytosine [36, 38], guanine monohydrate [36, 39], thymine [36, 40], uracil [36, 41], pyrrole [42, 43], imidazole [42, 44], benzamide [45, 46], benzimidazole [42, 47], nitrobenzene [48, 49], (*E*)-acetophenone oxime [50, 51], pyridine [42, 52], pyridine *N*-

oxide [42, 53], acetonitrile [54, 55], 1,4-dicyanobenzene [56, 57], *cis*-azobenzene [58, 59], *trans*-azobenzene [60, 61], and sulfamic acid [62, 63].

**Table 4.1.** Crystal structures and cluster compositions for materials containing  $^{13}\text{C}$  spins.

Compound	Space Group	Cluster Composition
Naphthalene	$P2_1/a$	$13\text{C}_{10}\text{H}_8$
Durene	$P2_1/a$	$15\text{C}_{10}\text{H}_{14}$
Hypoxanthine	$P\bar{1}$	$11\text{C}_5\text{H}_4\text{N}_4\text{O}$
Oxalic acid	$Pbca$	$15\text{C}_2\text{H}_2\text{O}_4$
Oxalic acid dihydrate	$P2_1/n$	$15\text{C}_2\text{H}_2\text{O}_4 \cdot 20\text{H}_2\text{O}$
Sucrose	$P2_1$	$13\text{C}_{12}\text{H}_{22}\text{O}_{11}$
L-threonine	$P2_12_12_1$	$15\text{C}_4\text{H}_9\text{NO}_3$
Squaric acid	$P2_1/c$	$17\text{C}_4\text{H}_2\text{O}_4$
Pentaerythritol	$I\bar{4}$	$13\text{C}_5\text{H}_{12}\text{O}_4$
Cyclopropane	$P1$	$13\text{C}_3\text{H}_6$
Norbornadiene	$P2_1/c$	$15\text{C}_7\text{H}_8$
[1.1.1]propellane	$C2$	$13\text{C}_5\text{H}_6$
Ethylene	$P2_1/n$	$13\text{C}_2\text{H}_4$
Nitromethane	$P2_12_12_1$	$13\text{CH}_3\text{NO}_2$
Dimethoxymethane	$P2_1/n$	$15\text{C}_3\text{H}_8\text{O}_2$
Dimedone	$P2_1/n$	$13\text{C}_8\text{H}_{10}\text{O}_2$
Acetylene	$Pa\bar{3}$	$13\text{C}_2\text{H}_2$
Carbon disulfide	$P1$	$15\text{CS}_2$

The database of  $^{19}\text{F}$ -containing materials (Table 4.3) includes fluorobenzene [64, 65], 1,2-difluorobenzene [64, 65], 1,3-difluorobenzene [64, 66], 1,4-difluorobenzene [64, 65], 1,3,5-trifluorobenzene [64, 65], 1,2,4,5-tetrafluorobenzene [64, 67], perfluorobenzene [68, 69], perfluoronaphthalene [70, 71], 2-fluorobenzoic acid [64, 72], 4-fluorobenzoic acid [64, 73], 4,4'-difluorobiphenyl [74, 75], 3-fluorophenol [64, 76], 4-fluorophenol [64, 76], 2-fluorotoluene [64, 77], 3-fluorotoluene [64, 77], 4-fluorotoluene [64, 77], *p*-fluoranil [64, 78], and trichlorofluoromethane [79, 80].

**Table 4.2.** Crystal structures and cluster compositions for materials containing  $^{15}\text{N}$  spins.

Adenine trihydrate	$P\bar{1}$	$7\text{C}_5\text{H}_5\text{N}_5 \cdot 12\text{H}_2\text{O}$
Cytosine	$P2_12_12_1$	$15\text{C}_4\text{H}_5\text{N}_3\text{O}$
Guanine monohydrate	$P2_1/n$	$12\text{C}_5\text{H}_5\text{N}_5\text{O} \cdot 10\text{H}_2\text{O}$
Thymine	$P2_1/c$	$15\text{C}_5\text{H}_6\text{N}_2\text{O}_2$
Uracil	$P2_1/a$	$15\text{C}_4\text{H}_4\text{N}_2\text{O}_2$
Imidazole	$P2_1/c$	$13\text{C}_3\text{H}_4\text{N}_2$
Benzamide	$P2_1/c$	$15\text{C}_7\text{H}_7\text{NO}$
<i>cis</i> -azobenzene	$Pbcn$	$15\text{C}_{12}\text{H}_{10}\text{N}_2$
<i>trans</i> -azobenzene <sup>a</sup>	$P2_1/a$	$15\text{C}_{12}\text{H}_{10}\text{N}_3$
Sulfamic acid	$Pbca$	$13\text{SO}_3\text{NH}_3$
Pyridine	$P2_12_12_1$	$15\text{C}_5\text{H}_5\text{N}$
Pyridine <i>N</i> -oxide	$P4_12_12$	$13\text{C}_5\text{H}_5\text{NO}$
Benzimidazole	$Pna2_1$	$15\text{C}_7\text{H}_6\text{N}_2$
Acetanilide	$Pbca$	$13\text{C}_8\text{H}_9\text{NO}$
<i>N</i> -methylacetanilide	$Pnma$	$13\text{C}_9\text{H}_{11}\text{NO}$
Pyrrrole	$Pnma$	$13\text{C}_4\text{H}_5\text{N}$
1,4-dicyanobenzene	$P\bar{1}$	$13\text{C}_8\text{H}_4\text{O}_2$
Nitrobenzene	$P2_1/c$	$15\text{C}_6\text{H}_5\text{NO}_2$

<sup>a</sup>Structure comprised of two unique molecules. Separate clusters were built to represent the local structure of each unique site.

The database of  $^{31}\text{P}$ -containing materials (Table 4.4) includes trimethylphosphine oxide [81, 82], triphenylphosphine oxide [81, 83], trichlorophosphine oxide [84, 85], methyldiphenylphosphine oxide [86, 87], trimethylphosphine sulfide [81, 88], tetramethyldiphosphine disulfide [89, 90], tetraethyldiphosphine disulfide [91], trimethylphosphine selenide [81, 92], urea phosphoric acid [93, 94], methylphosphonic acid [86, 95], 5-phenyl-5*H*-dibenzophosphole 5-oxide [96, 97], 2,4-bis(methylthio)-1,3-dithia-2,4-diphosphetane-

2,4-disulfide [98, 99], 2,4-bis(4-methoxyphenyl)-1,3-dithia-2,4-diphosphetane-2,4-disulfide [98, 100], *cis*-(diphenylimido-2,4,6-tri-*t*-butylphenyl)iminophosphine [101, 102], chloro-(2,4,6-tri-*t*-butylphenyl)iminophosphine [101, 103], tricyclohexylphosphine [104, 105], 1,2,3-triphenylphosphirene [106, 107], and 1,2,2-triphenyl-3,3-bis(trimethylsilyl)phosphirane [108, 109].

**Table 4.3.** Crystal structures and cluster compositions for materials containing  $^{19}\text{F}$  spins.

Compound	Space Group	Cluster Composition
2-fluorobenzoic acid	$P2_1/n$	$15\text{C}_7\text{H}_4\text{O}_2\text{F}$
4-fluorobenzoic acid	$P2_1/n$	$15\text{C}_7\text{H}_4\text{O}_2\text{F}$
4,4'-difluorobiphenyl	$P2_1/a$	$11\text{C}_{12}\text{H}_8\text{F}_2$
Fluorobenzene	$P4_32_12$	$15\text{C}_6\text{H}_5\text{F}$
1,2-difluorobenzene	$P2_1/n$	$15\text{C}_6\text{F}_2\text{H}_4$
1,3-difluorobenzene	$C2/c$	$15\text{C}_6\text{F}_2\text{H}_4$
1,4-difluorobenzene	$P2_1/c$	$15\text{C}_6\text{F}_2\text{H}_4$
1,3,5-trifluorobenzene	$I2/a$	$15\text{C}_6\text{H}_3\text{F}_3$
1,2,4,5-tetrafluorobenzene	$P2_1/c$	$15\text{C}_6\text{H}_2\text{F}_4$
Perfluorobenzene	$P2_1/n$	$15\text{C}_6\text{F}_6$
Perfluoronaphthalene	$P2_1/c$	$13\text{C}_{10}\text{F}_8$
3-fluorophenol	$P2_1$	$15\text{C}_6\text{H}_5\text{OF}$
4-fluorophenol	$R\bar{3}$	$13\text{C}_6\text{H}_5\text{OF}$
2-fluorotouene	$P2_1/n$	$15\text{C}_7\text{H}_7\text{F}$
3-fluorotoluene	$Pbca$	$15\text{C}_7\text{H}_7\text{F}$
4-fluorotoluene	$Pna2_1$	$15\text{C}_7\text{H}_7\text{F}$
<i>p</i> -Fluoranyl	$P2_1/c$	$15\text{C}_6\text{O}_2\text{F}_4$
Trichlorofluoromethane	$Pbca$	$15\text{CFCl}_3$

Periodic all-atom plane-wave geometry optimizations were performed on each of the structures of the 72 crystalline materials. Optimizations were performed using fixed lattice parameters because they are generally well-established from experiment.

Refined structures produced by the geometry optimizations were used in all subsequent magnetic-shielding calculations. Geometry optimizations were specifically performed

**Table 4.4.** Crystal structures and cluster compositions for materials containing  $^{31}\text{P}$  spins.

Compound	Space Group	Cluster Composition
Trimethylphosphine oxide	$C2/m$	13OPMe <sub>3</sub>
Triphenylphosphine oxide	$Pbca$	13OPPh <sub>3</sub>
Trichlorophosphine oxide	$Pn21a$	15OPCl <sub>3</sub>
Methyldiphenylphosphine oxide	$P2_1/c$	15OPMePh <sub>3</sub>
Trimethylphosphine sulfide	$P2_1/m$	13SPMe <sub>3</sub>
Tetramethyldiphosphine disulfide	$C2/m$	13C <sub>4</sub> H <sub>12</sub> S <sub>2</sub> P <sub>2</sub>
Tetraethyldiphosphine disulfide	$P\bar{1}$	15C <sub>8</sub> H <sub>20</sub> S <sub>2</sub> P <sub>2</sub>
2,4-bis(methylthio)-1,3-dithia-2,4-diphosphetane-2,4-disulfide	$P2_1/a$	13C <sub>2</sub> H <sub>6</sub> S <sub>6</sub> P <sub>2</sub>
2,4-bis(4-methoxyphenyl)-1,3-dithia-2,4-diphosphetane-2,4-disulfide	$P2_1/c$	11C <sub>12</sub> H <sub>14</sub> O <sub>2</sub> S <sub>4</sub> P <sub>3</sub>
Trimethylphosphine selenide	$P2_1/m$	13SePMe <sub>3</sub>
Tricyclohexylphosphine	$P3_1$	15C <sub>15</sub> H <sub>33</sub> P
<i>cis</i> -(diphenylimido-2,4,6-tri- <i>t</i> -butylphenyl)iminophosphine	$P2_1/c$	13C <sub>30</sub> H <sub>37</sub> N <sub>2</sub> P
Chloro-(2,4,6-tri- <i>t</i> -butylphenyl)iminophosphine	$P2_1/n$	13C <sub>15</sub> H <sub>29</sub> NPCl
Urea phosphoric acid	$Pbca$	9PO <sub>4</sub> H <sub>2</sub> ·9CH <sub>4</sub> N <sub>2</sub> O
Methylphosphonic acid	$P2_1/c$	15MeH <sub>2</sub> PO <sub>4</sub>
5-phenyl-5H-dibenzophosphole 5-oxide	$P2_1/c$	13C <sub>18</sub> H <sub>12</sub> OP
1,2,3-triphenylphosphirene	$P\bar{1}$	13C <sub>20</sub> H <sub>15</sub> P
1,2,2-triphenyl-3,3-bis(trimethylsilyl)phosphirane	$Pna2_1$	11C <sub>24</sub> H <sub>33</sub> Si <sub>2</sub> P

with the CASTEP module of MATERIALS STUDIO 7.0 by Accelrys Software, Inc [110]. The optimizations were carried out at the PW91/ultra-fine level of theory using ultrasoft pseudopotentials (USPP) generated *on the fly*. At the ultra-fine level, the plane-wave

cutoff varied between 390 eV and 610 eV, depending on the types of atoms in the lattice. The Brillouin zone was sampled with a  $k$ -point spacing of  $0.07 \text{ \AA}^{-1}$ . The thresholds for structural convergence were a maximum change in energy of  $5 \times 10^{-6} \text{ eV}$  per atom, a maximum displacement of  $5 \times 10^{-4} \text{ \AA}$  per atom, and a maximum Cartesian force of  $0.01 \text{ eV \AA}^{-1}$ . For diffraction structures where the hydrogen positions were not published, or where the hydrogen sites were disordered, a preliminary optimization was performed using loosened SCF-convergence criteria to obtain an initial guess for the full geometry optimization.

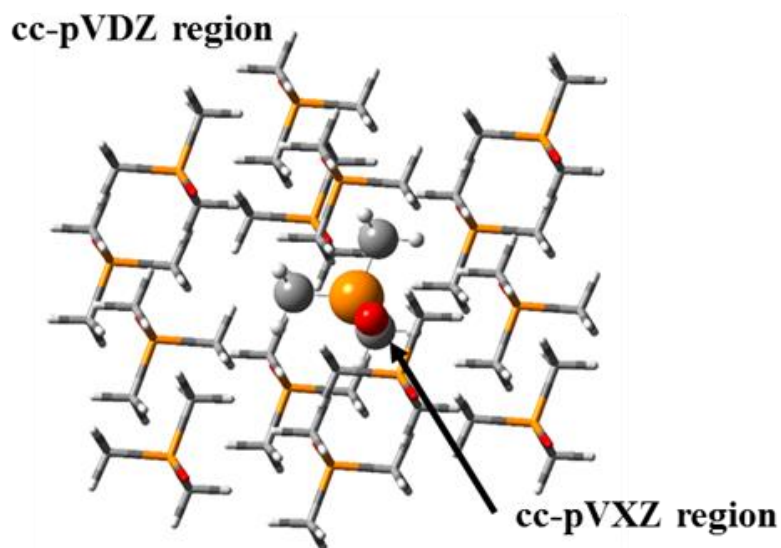


**Figure 4.1.** A symmetry-adapted cluster model of trimethylphosphine oxide consisting of fifteen molecules in the  $C2/m$  space group. The central molecule of the cluster (ball-and-stick representation) is given the cc-pVXZ basis set ( $X = D, T, Q, 5$ ). The peripheral molecules of the cluster (wireframe representation) are given the cc-pVDZ basis set.

Magnetic-shielding constants for the plane-wave-optimized structures were generated using the GIPAW procedure, as implemented in the CASTEP module of MATERIALS STUDIO 7.0 [110]. Plane-wave cutoff energies of 200 eV, 300 eV, 400 eV, 500 eV, and 600 eV were examined. Convergence of computed magnetic-shielding constants was verified with respect to plane-wave cutoff energy and  $k$ -point spacing. The calculations were performed at the PW91 level of theory. Ultra-fine SCF convergence criteria were used in all calculations, independent of the plane-wave cutoff energy. Core orbitals were replaced by USPPs generated *on the fly*.

Magnetic-shielding calculations on symmetry-adapted clusters of molecules, that replicated a portion of the crystalline lattice, were performed using the GIAO method [111-113], as implemented in GAUSSIAN 09 [114]. An example cluster of trimethylphosphine oxide is given in Figure 4.1. The results presented in sections 4.3 and 4.4 were obtained with the PW91 functional. Results in section 4.5 were obtained using various DFT methodologies. Our method for calculating magnetic-shielding constants partitioned the cluster into two layers, corresponding to the central molecule and to all peripheral molecules (Figure 4.1). The low layer (peripheral molecules) was given a less flexible basis set than the high layer (central molecule) to decrease the computational cost. For the central molecule, the basis set cc-pVXZ (X = D, T, Q, 5) was used [115, 116]. For the peripheral molecules, cc-pVDZ was used. The effects of this approximation were discussed in Chapter 2.

Calculations of magnetic-shielding tensors using the cluster model were also performed using several other DFT functionals. We selected the PW91 [117] and PBE [118] functionals as representative examples of the GGA class. The hybrid equivalents of these are B3PW91 [119] and PBE0 [120], respectively. The meta-GGA functional

TPSS [121] was used in this analysis with the hybrid analog being labeled TPSSh [121]. The functionals PBE0, TPSS, and TPSSh are related, in that they are modifications of the PBE functional. The TPSS and TPSSh functionals have not been studied rigorously for their ability to predict principal components of magnetic-shielding tensors in solids.

### **4.3 Intermolecular Effects on Magnetic Shielding Revisited**

The importance of intermolecular interactions on computed NMR parameters can be assessed by examining a set of materials where the structure is simplified by considering only a single molecule taken in isolation, as if it were in the gas phase. Such calculations based on isolated-molecule (IM) models ignore all intermolecular contributions to the magnetic shielding. Intermolecular effects on computed NMR parameters can be assessed through calculations using the same plane-wave or atomic-orbital basis set by calculations with and without PBCs, as has been done, for example, in calculations of quadrupole coupling in titanocene complexes [122]. Here, the results obtained from the IM model are compared with calculations where lattice effects are taken into account using (1) the SAC method or (2) the PBC method (Figure 4.2).

Chapter 2 presented similar calculations for a set of  $^{13}\text{C}$ -containing materials and provided found results as are shown for the several  $^{15}\text{N}$ -containing materials. All calculations herein were performed using the same plane-wave optimized structures. A summary of the linear-regression parameters for the three computational methodologies is given in Table 4.5, with computational details provided as a footnote. Correlation plots of calculated principal components of  $^{15}\text{N}$  magnetic-shielding tensors versus experimental principal components of  $^{15}\text{N}$  chemical-shift tensors illustrating these results are shown in Figure 4.3.

The scatter in these plots is significantly higher for the IM models (RMSD = 28.5 ppm) than is observed for either the SAC (RMSD = 10.8 ppm) or PBC model (RMSD = 11.4 ppm). Of the 51 magnetic-shielding values included here, all but eight values are improved over the isolated-molecule model by the SAC model and all but twelve are improved by the PBC model. Of the sites not improved by incorporation of lattice effects, none are significantly worsened. Furthermore, the slope of  $-1.15 \pm 0.02$  in the IM model deviates from unity much more than for the two models that incorporate intermolecular effects ( $-1.03 \pm 0.01$  for the SAC model and  $-1.06 \pm 0.02$  for the PBC model). There are also significant differences between the extrapolated reference shieldings. Only the IM and SAC models can be compared directly because the PBC model uses a different type of basis set. The reference of the SAC model is predicted to be more shielded than the isolated-molecule model by  $23 \pm 10$  ppm.

The similarity in the scatter of the SAC and PBC models suggests that NMR magnetic-shielding values are most sensitive to the immediately-surrounding molecules in the crystal lattice and that sufficient agreement with experiment is obtained when representing solid-state effects with a finite cluster, provided that the cluster model satisfies the symmetry requirements of the crystalline space group.

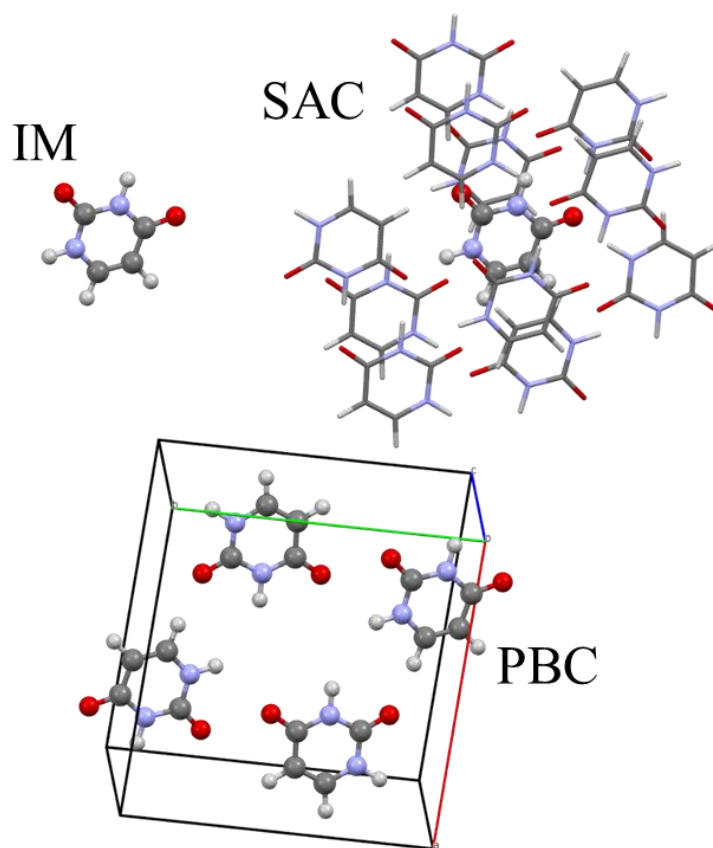


**Figure 4.2.** Three computational methodologies used to model the solid-state structure of uracil; isolated-molecule (IM) model, symmetry-adapted-cluster (SAC) model, and periodic-boundary-condition (PBC) model. In the PBC model, the colored lines represent the axes of the unit cell.

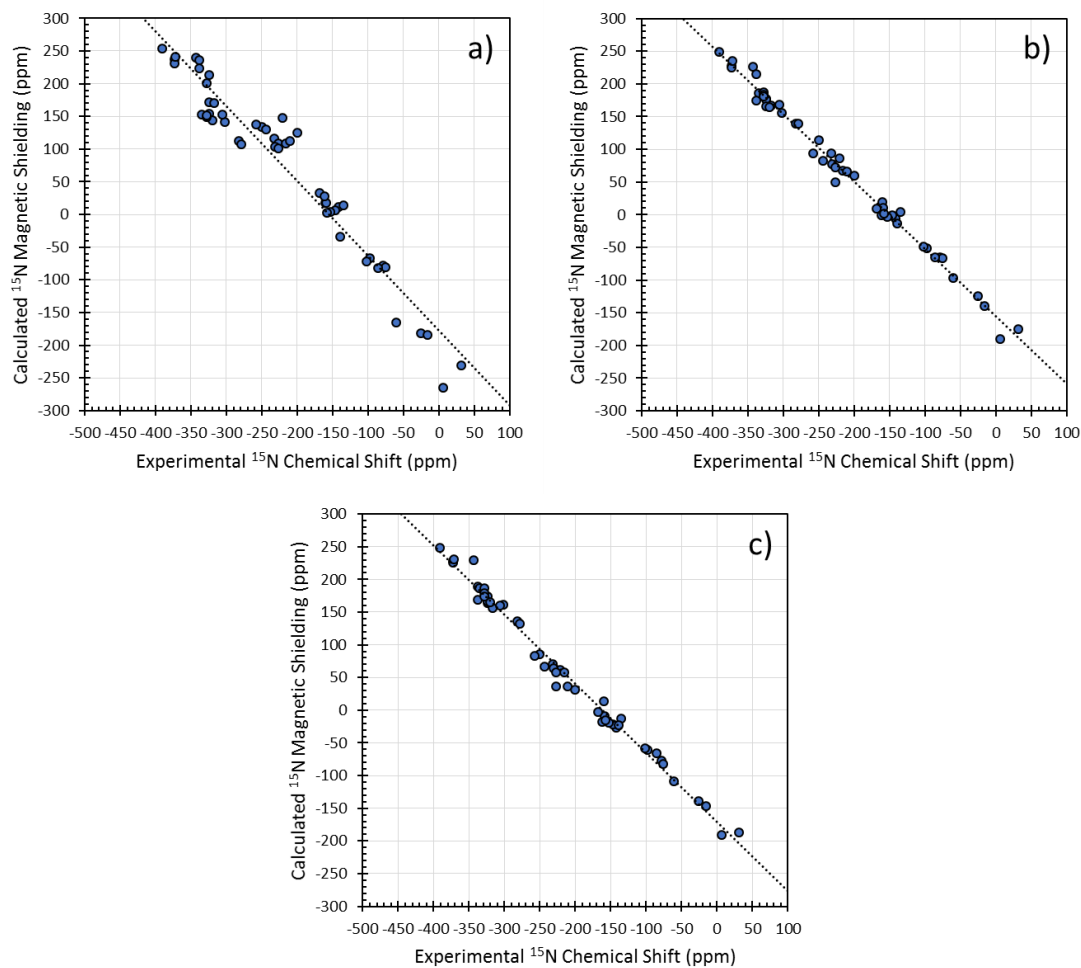


**Figure 4.3.** Principal components of  $^{15}\text{N}$  magnetic-shielding tensors in (a) isolated-molecule models, (b) symmetry-adapted cluster models, and (c) periodic GIPAW models. Shielding in the IM and SAC models is calculated at the PW91/cc-pVTZ level. Shielding in the PBC model is calculated at the PW91/600eV level. Results are shown for adenine trihydrate, guanine monohydrate, cytosine, thymine, and uracil.

**Table 4.5.** Linear-regression parameters for calculated principal components of  $^{15}\text{N}$  magnetic-shielding tensors versus experimental principal components of chemical-shift tensors using three computational models<sup>a,b</sup>

Model	$ m $	$\sigma_{\text{CH}_3\text{NO}_2}$ (ppm)	RMSD (ppm)
IM	$1.15 \pm 0.04$	$-178 \pm 10$	28.5
SAC	$1.03 \pm 0.01$	$-155 \pm 3$	10.8
PBC	$1.06 \pm 0.02$	$-172 \pm 4$	11.4

<sup>a</sup>GIAO calculations for the IM and SAC models were performed at the PW91/cc-pVTZ level; GIPAW calculations for the PBC model were performed at the PW91/600 eV level. <sup>b</sup>Materials are adenine trihydrate, guanine monohydrate, cytosine, thymine, and uracil with a total of 51 principal components.

#### 4.4 Comparison of GIPAW and Cluster Models

Direct comparison of methods based on different computational methodologies is difficult. The GIPAW technique expands the wave function in a plane-wave basis whereas the GIAO method expands the wave function in atom-centered functions. Additionally, each basis is generally truncated, which may lead to errors that affect the quality of the method. The effects of finite basis sets on computed magnetic-shielding parameters have been discussed in numerous articles [123-130]. For example, Kupka *et al.* have noted that increasing the number of basis functions tends to decrease magnetic-shielding parameters obtained by density-functional calculations [125, 126]. One method to deal with this problem involves calculating the magnetic shielding of a suitable reference compound according to both computational procedures and presenting the results as a shift relative to the reference [131, 132]. Another approach is to converge both calculations to the basis set limit. This method has been employed

in calculations of, for example,  $^{14}\text{N}$  quadrupolar couplings [133]. The latter method has been employed here.

Using a class of basis sets such as cc-pVXZ ( $X = \text{D, T, Q, 5, . . .}$ ) allows the basis-set limit to be reached in a systematic manner for the GIAO approach. GIPAW and GIAO/SAC methodologies can be compared meaningfully using NMR parameters extrapolated to the basis-set limit. Calculations were performed by incrementally increasing the plane-wave cutoff energy (PBC method) or the number of Cartesian basis functions (SAC method), while maintaining the SCF convergence criteria. For the PBC calculations, the basis-set limit seems to be approached for a cutoff energy of 600 eV. Calculations on several systems using higher cutoff energies did not substantially alter the computed values found using a cutoff energy of 600 eV. For SACs, the basis-set limit is given by an extrapolated value obtained by modeling the change in magnetic-shielding with basis-set size [125, 126].

Linear-regression parameters for the correlation between calculated principal components of magnetic-shielding tensors and experimental principal components of chemical-shift tensors are presented in Table 4.6 for the PBC method and in Table 4.7 for the SAC method. An evaluation of the data presented in these tables reveals several important trends that are generally consistent among the nuclei. For the first-row nuclei ( $^{13}\text{C}$ ,  $^{15}\text{N}$ ,  $^{19}\text{F}$ ), individual principal components exponentially approach the basis-set limit. For  $^{31}\text{P}$ , individual principal components approach the basis-set limit either exponentially or in a damped-oscillatory fashion. Importantly, both the PBC and SAC methods approach the same reference shielding within experimental uncertainty at the basis-set limit for all nuclei except  $^{19}\text{F}$ . The linear-regression parameters vary in a

manner that reflects the changes in the individual principal components. Each increase in the number of basis functions leads to deshielding of the reference compound.

Plots comparing calculated principal components of magnetic-shielding tensors with experimental principal components of chemical-shift tensors are shown in Figures 4.4 – 4.7. These correlation plots demonstrate the equivalence of GIPAW and GIAO for all nuclides but  $^{19}\text{F}$ . At the basis-set limit, in every case, the slope of the correlation line has a magnitude greater than unity, indicating that calculations performed at the PW91 level of theory overestimate differences in chemical shifts between nuclear sites and overestimate the anisotropies of individual sites. It is notable that the data set yielding a slope closest to -1 is the set of  $^{13}\text{C}$  shifts, with the GIPAW method predicting a slope of  $-1.043 \pm 0.005$  and the GIAO method predicting a slope of  $-1.056 \pm 0.005$ .  $^{15}\text{N}$  yields a slope of  $-1.09 \pm 0.01$  and  $^{31}\text{P}$  yields a slope of  $-1.09 \pm 0.02$  for both computational methodologies. The slope of the  $^{19}\text{F}$  linear-regression line depends on the computational methodology, with the GIPAW method having a slope of  $-1.22 \pm 0.02$  and the GIAO method having a slope of  $-1.17 \pm 0.02$ .

For calculations of  $^{15}\text{N}$  and  $^{31}\text{P}$  shieldings, there is no statistical difference in linear-regression parameters between the two computational methodologies. Similarly, the differences observed for  $^{13}\text{C}$  are small, with a difference in  $\sigma_{TMS}$  of  $1.9 \pm 0.8$  ppm and a difference in slope of  $0.013 \pm 0.007$ . For  $^{19}\text{F}$ , the reference shielding for the GIAO value is shielded relative to the GIPAW value by  $17 \pm 4$  ppm. In addition, the slopes of the lines differ by  $0.05 \pm 0.03$ , with the GIAO method yielding a result closer to unity.

The *T*-test was used to determine whether these differences observed in the trend lines represent a significant difference between the two computational models. This question is equivalent to asking if the computed results from the cluster method can be

modeled using the trend line obtained by analyzing the GIPAW results. This can be evaluated by tabulating the RMSDs according to the two modeling techniques and defining a threshold for significance. These results are shown in Table 4.8. At the 95% level, there is no significant difference between the computed magnetic-shielding parameters for  $^{13}\text{C}$ ,  $^{15}\text{N}$ , or  $^{31}\text{P}$ . However, there is a statistical difference between the GIPAW and GIAO cluster methods for computed magnetic shielding of  $^{19}\text{F}$  sites.

To explore this deviation further, the  $^{19}\text{F}$  magnetic-shielding constants were calculated using Jensen's segmented polarization-consistent basis set, pcSseg-3, which is optimized for calculations of magnetic-shielding constants [158]. Similar results were obtained using both the correlation-consistent (cc-pVTZ) and polarization-consistent (pcSseg-3) basis sets, with the equations of the correlations lines given by:

$$\sigma_{ii}^{cc-pVTZ} = (-1.18 \pm 0.02)\delta_{ii} + (132 \pm 3) \text{ ppm}, \quad (\text{Eq. 4.1})$$

$$\sigma_{ii}^{pcSseg-3} = (-1.18 \pm 0.02)\delta_{ii} + (129 \pm 3) \text{ ppm}. \quad (\text{Eq. 4.1})$$

Augmented basis sets such as aug-cc-pVTZ and aug-pcSseg-3 typically altered  $^{19}\text{F}$  magnetic shielding no more than 1 ppm.

**Table 4.6.** Linear-regression parameters obtained from correlation plots between GIPAW calculated principal magnetic-shielding values and experimental principal chemical-shift values.

Nucleus	Cutoff Energy (eV)	Slope	$\sigma_{\text{Ref}}$ (ppm)	RMSD (ppm)
<b>Carbon-13</b> N = 177	200	$-0.833 \pm 0.006$	$188.3 \pm 0.8$	8.2
	300	$-1.009 \pm 0.005$	$175.8 \pm 0.6$	5.0
	400	$-1.040 \pm 0.005$	$172.5 \pm 0.6$	4.9
	500	$-1.042 \pm 0.005$	$172.4 \pm 0.6$	4.9
	600	$-1.043 \pm 0.005$	$172.5 \pm 0.6$	4.9
<b>Nitrogen-15</b> N = 99	200	$-0.61 \pm 0.01$	$41 \pm 2$	22.8
	300	$-1.01 \pm 0.01$	$-142 \pm 2$	17.1
	400	$-1.08 \pm 0.01$	$-175 \pm 3$	17.3
	500	$-1.09 \pm 0.01$	$-178 \pm 3$	17.1
	600	$-1.09 \pm 0.01$	$-178 \pm 3$	17.2
<b>Fluorine-19</b> N = 60	200	$-0.71 \pm 0.01$	$301 \pm 2$	8.1
	300	$-1.03 \pm 0.02$	$179 \pm 2$	8.6
	400	$-1.17 \pm 0.02$	$129 \pm 3$	8.3
	500	$-1.21 \pm 0.02$	$116 \pm 3$	8.3
	600	$-1.22 \pm 0.02$	$114 \pm 3$	8.3
<b>Phosphorus-31</b> N = 57	200	$-1.05 \pm 0.03$	$284 \pm 5$	29.9
	300	$-1.11 \pm 0.03$	$268 \pm 5$	29.2
	400	$-1.08 \pm 0.02$	$270 \pm 4$	23.7
	500	$-1.11 \pm 0.03$	$269 \pm 5$	28.5
	600	$-1.09 \pm 0.02$	$271 \pm 4$	22.0

<sup>a</sup>All calculations were performed at the PW91 level. <sup>b</sup>Linear-regression parameters are given for the correlation line  $\sigma_{ii}^{calc} = m\delta_{ii}^{exp} + \sigma_{\text{ref}}$ , where ( $\sigma_{ii}^{calc}$ ) represents the calculated principal components of magnetic-shielding tensors, ( $\delta_{ii}^{exp}$ ) represents experimental principal components of chemical-shift tensors,  $\sigma_{\text{ref}}$  is the shielding of the reference compound, and  $m$  is the slope of a correlation plot of calculated shielding versus experimental shift. <sup>c</sup>The RMSD is defined by  $RMSD = [(N - 2)^{-1} \sum_{n=1}^N (\delta_{ii}^{calc} - \delta_{ii}^{exp})^2]^{1/2}$ . Calculated magnetic shielding is converted to the chemical-shift scale ( $\delta_{ii}^{calc}$ ) using the relationship  $\delta_{ii}^{calc} = (\sigma_{ii}^{calc} - \sigma_{\text{ref}})/m$ .

**Table 4.7.** Linear-regression parameters obtained from correlation plots between GIAO calculated principal magnetic-shielding values and experimental principal chemical-shift values.

Nucleus	Basis Set	Slope	$\sigma_{\text{Ref}}$ (ppm)	RMSD (ppm)
<b>Carbon-13</b> N = 177	cc-pVDZ	$-0.948 \pm 0.005$	$186.4 \pm 0.7$	5.5
	cc-pVTZ	$-1.004 \pm 0.005$	$178.2 \pm 0.6$	5.0
	cc-pVQZ	$-1.031 \pm 0.005$	$175.9 \pm 0.6$	5.0
	cc-pV5Z	$-1.047 \pm 0.005$	$175.0 \pm 0.6$	5.0
	CBS	$-1.056 \pm 0.005$	$174.4 \pm 0.6$	4.9
<b>Nitrogen-15</b> N = 99	cc-pVDZ	$-1.01 \pm 0.01$	$-131 \pm 2$	17.4
	cc-pVTZ	$-1.05 \pm 0.01$	$-158 \pm 2$	15.5
	cc-pVQZ	$-1.07 \pm 0.01$	$-168 \pm 2$	15.4
	cc-pV5Z	$-1.08 \pm 0.01$	$-174 \pm 2$	15.3
	CBS	$-1.09 \pm 0.01$	$-177 \pm 2$	15.5
<b>Fluorine-19</b> N = 60	cc-pVDZ	$-1.15 \pm 0.02$	$145 \pm 3$	10.3
	cc-pVTZ	$-1.18 \pm 0.02$	$132 \pm 3$	9.6
	cc-pVQZ	$-1.17 \pm 0.02$	$133 \pm 3$	9.1
	cc-pV5Z	$-1.17 \pm 0.02$	$130 \pm 3$	9.6
	CBS	$-1.17 \pm 0.02$	$131 \pm 3$	9.2
<b>Phosphorus-31</b> N = 57	cc-pVDZ	$-0.96 \pm 0.02$	$377 \pm 4$	24.1
	cc-pVTZ	$-1.02 \pm 0.02$	$318 \pm 3$	21.3
	cc-pVQZ	$-0.99 \pm 0.02$	$330 \pm 3$	21.6
	cc-pV5Z	$-1.09 \pm 0.02$	$279 \pm 3$	20.6
	CBS	$-1.09 \pm 0.02$	$269 \pm 3$	21.1

<sup>a</sup>All calculations were performed at the PW91 level. <sup>b</sup>Linear-regression parameters are given for the correlation line  $\sigma_{ii}^{\text{calc}} = m\delta_{ii}^{\text{exp}} + \sigma_{\text{ref}}$ , where  $(\sigma_{ii}^{\text{calc}})$  represents the calculated principal components of magnetic-shielding tensors,  $(\delta_{ii}^{\text{exp}})$  represents experimental principal components of chemical-shift tensors,  $\sigma_{\text{ref}}$  is the shielding of the reference compound, and  $m$  is the slope of a correlation plot of calculated shielding versus experimental shift. <sup>c</sup>The RMSD is defined by  $\text{RMSD} = [(N - 2)^{-1} \sum_{n=1}^N (\delta_{ii}^{\text{calc}} - \delta_{ii}^{\text{exp}})^2]^{1/2}$ . Calculated magnetic shielding is converted to the chemical-shift scale  $(\delta_{ii}^{\text{calc}})$  using the relationship  $\delta_{ii}^{\text{calc}} = (\sigma_{ii}^{\text{calc}} - \sigma_{\text{ref}})/m$ .

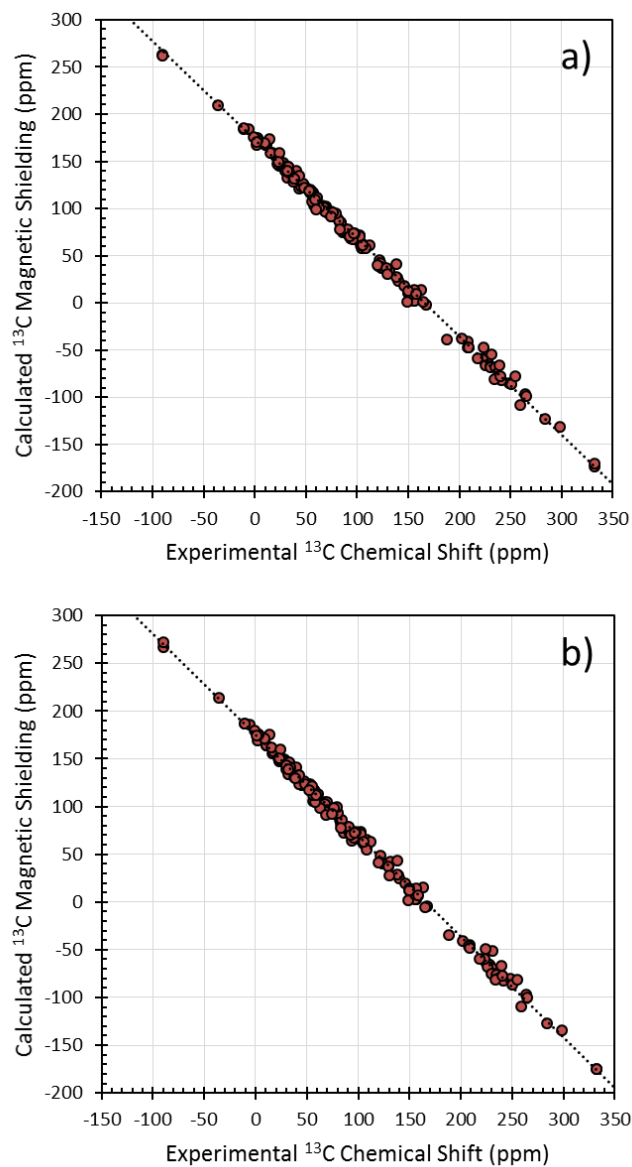


**Figure 4.4.** Calculated principal components of  $^{13}\text{C}$  magnetic-shielding tensors versus experimental principal components of  $^{13}\text{C}$  chemical-shift tensors. (a) GIPAW, (b) Clusters

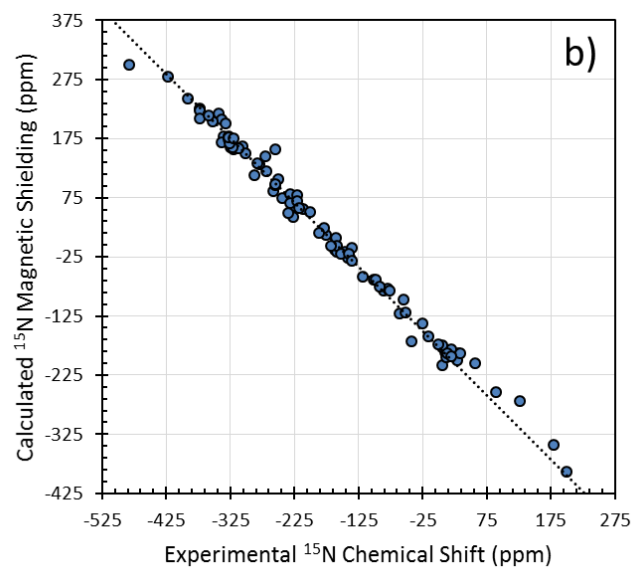
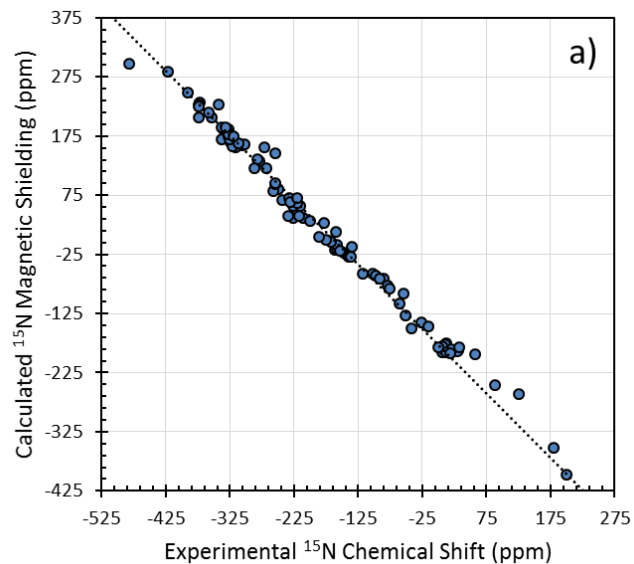


**Figure 4.5.** Calculated principal components of  $^{15}\text{N}$  magnetic-shielding tensors versus experimental principal components of  $^{15}\text{N}$  chemical-shift tensors. (a) GIPAW, (b) Clusters

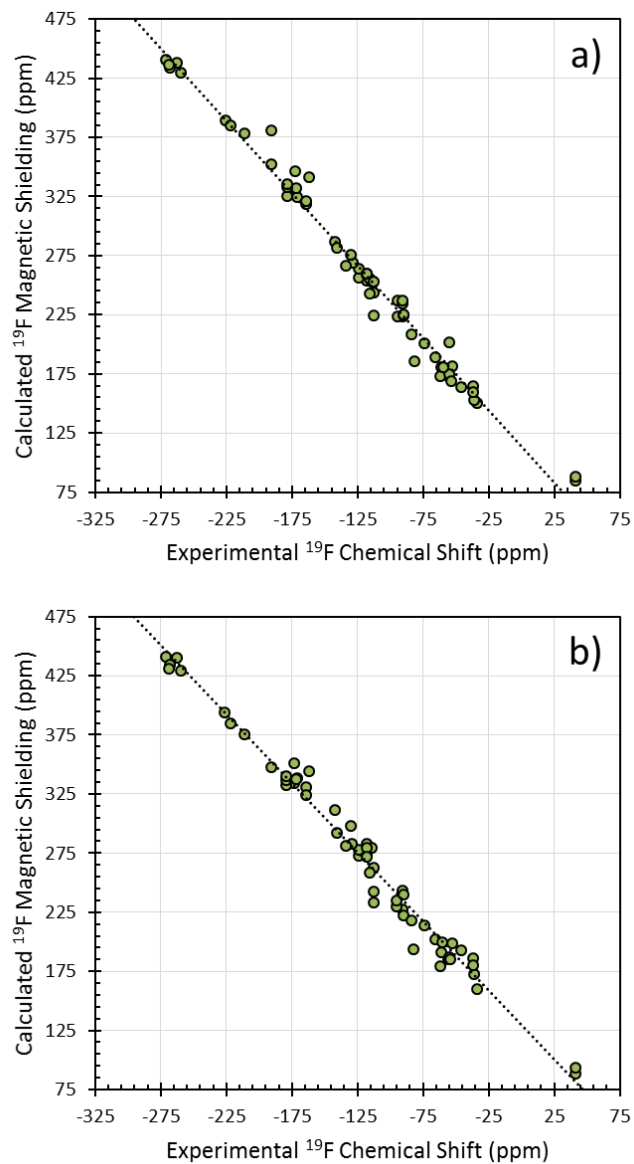


**Figure 4.6.** Calculated principal components of  $^{19}\text{F}$  magnetic-shielding tensors versus experimental principal components of  $^{19}\text{F}$  chemical-shift tensors. (a) GIPAW, (b) Clusters

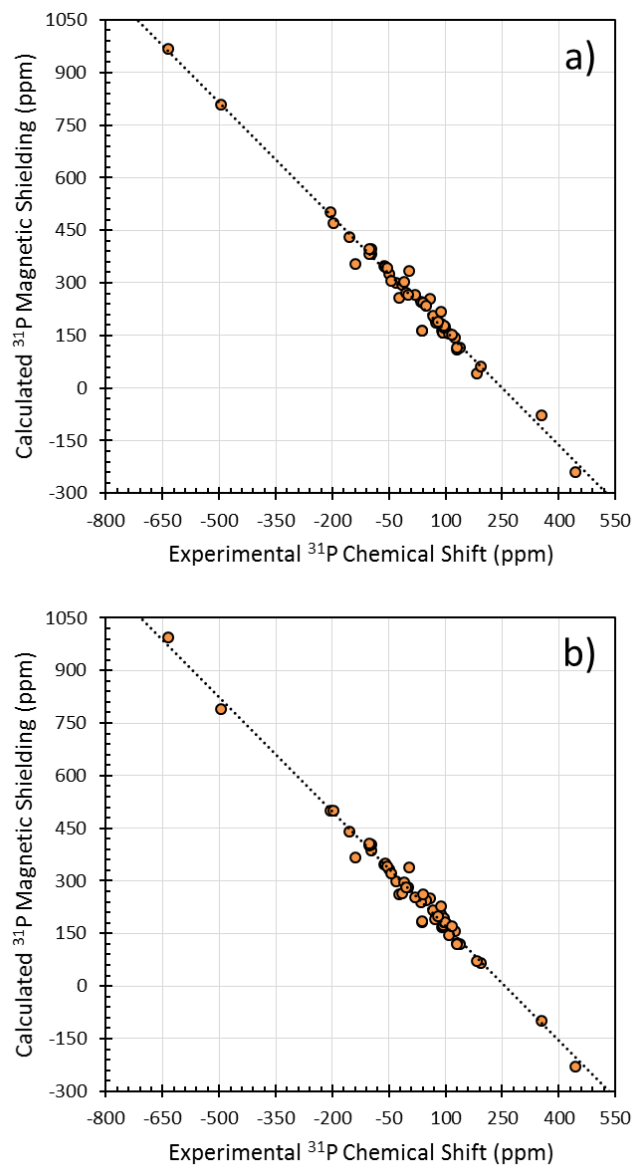


**Figure 4.7.** Calculated principal components of  $^{31}\text{P}$  magnetic-shielding tensors versus experimental principal components of  $^{31}\text{P}$  chemical-shift tensors. (a) GIPAW, (b) Clusters.

**Table 4.8.** T-test statistics for assessing differences between the GIPAW and GIAO/cluster methodologies for computing magnetic-shielding parameters.<sup>a</sup>

Nucleus	N	$\Delta$ RMSD (ppm)	RMSD Cutoff (ppm)
Carbon-13	177	0.08	0.10
Nitrogen-15	99	0.03	0.29
Fluorine-19	60	4.68	2.23
Phosphorus-31	57	0.04	0.47

<sup>a</sup>Differences between the computational methodologies are significant if  $\Delta$ RMSD is greater than the RMSD cutoff.

#### 4.5 Examination of Exchange-Correlation Functionals

Computed NMR parameters display a strong dependence on the model chemistry used in the calculation. The limitation is often a practical one, in which one must trade off accuracy for reasonable computational time. Most studies that have explored level-of-theory effects on NMR parameters have examined the effects on the isotropic shielding of nuclei in gas-phase molecules. Highly accurate benchmark magnetic-shielding constants from coupled-cluster calculations have been presented for the four nuclei in this study (<sup>13</sup>C, <sup>15</sup>N, <sup>19</sup>F, and <sup>31</sup>P) [135-137]. NMR parameters obtained from various DFT methods have been benchmarked against values computed using *ab initio* methods such as Hartree-Fock or MP2 [112, 138, 139] and against other DFT methods [140-146]. Compared to post-Hartree-Fock methods, DFT typically underestimates magnetic-shielding constants [112, 139]. This underestimation is often rationalized in terms of a systematic failure in calculating differences between the Kohn-Sham energy levels, leading to overestimations of the paramagnetic contribution to the

magnetic shielding. In particular, the relative performance of various exchange-correlation functionals in the prediction of magnetic shielding is of considerable interest.

Considering only the isotropic value of the magnetic-shielding tensor ignores the significant role that the choice of functional may have on the computed anisotropy and asymmetry of the magnetic-shielding tensor. Analyses involving comparisons of the principal components of magnetic-shielding tensors are comparatively rare. A study by Sefzik *et al.* correlated computed principal components of  $^{13}\text{C}$  magnetic-shielding tensors obtained from IM models with experimental values obtained in solids [147]. Several studies have used the GIPAW method to compare various GGA functionals [148-152]. None of these studies found a significant difference between the GGA functionals.

Chapter 2 previously explored hybrid DFT functionals for calculating principal components of  $^{13}\text{C}$  magnetic-shielding tensors [153]. Another recent study has also suggested that hybrid functionals improve the agreement with experimental  $^{13}\text{C}$  chemical shift over GGA functionals [154]. This result has not been generalized to other nuclei, although a preliminary analysis has found that hybrid functionals can alleviate certain systematic problems associated with calculations of  $^{207}\text{Pb}$  magnetic shielding [155].

This section demonstrates that the SAC model can be employed in a systematic investigation of differences in computed principal components of magnetic-shielding tensors determined with different classes of DFT functionals. Linear-regression parameters obtained from calculations using six functionals (PW91, B3PW91, PBE, PBE0, TPSS, and TPSSh) are summarized in Table 4.9.

**Table 4.9.** Linear-regression parameters obtained from correlation plots between calculated principal components of magnetic-shielding tensors and experimental principal components of chemical-shift tensors obtained from the symmetry-adapted cluster approach. Calculated values were obtained using the cc-pVTZ basis set.

Nucleus	Method	Slope	$\sigma_{\text{Ref}}$ (ppm)	RMSD (ppm)
<b>Carbon-13</b> N = 177	PW91	$-1.004 \pm 0.005$	$178.2 \pm 0.6$	5.0
	B3PW91	$-1.045 \pm 0.005$	$184.9 \pm 0.6$	4.6
	PBE	$-1.001 \pm 0.005$	$178.9 \pm 0.6$	5.0
	PBE0	$-1.050 \pm 0.005$	$187.3 \pm 0.6$	4.7
	TPSS	$-0.982 \pm 0.005$	$181.2 \pm 0.6$	4.9
	TPSSh	$-1.004 \pm 0.004$	$184.3 \pm 0.6$	4.7
<b>Nitrogen-15</b> N = 99	PW91	$-1.05 \pm 0.01$	$-158 \pm 2$	15.5
	B3PW91	$-1.11 \pm 0.01$	$-168 \pm 2$	16.2
	PBE	$-1.04 \pm 0.01$	$-156 \pm 2$	15.8
	PBE0	$-1.12 \pm 0.01$	$-170 \pm 2$	16.7
	TPSS	$-0.995 \pm 0.007$	$-140 \pm 2$	13.5
	TPSSh	$-1.026 \pm 0.007$	$-145 \pm 2$	13.5
<b>Fluorine-19</b> N = 60	PW91	$-1.18 \pm 0.02$	$132 \pm 3$	9.6
	B3PW91	$-1.11 \pm 0.02$	$158 \pm 3$	10.2
	PBE	$-1.18 \pm 0.02$	$131 \pm 3$	9.6
	PBE0	$-1.10 \pm 0.02$	$162 \pm 3$	10.6
	TPSS	$-1.13 \pm 0.02$	$145 \pm 3$	10.5
	TPSSh	$-1.11 \pm 0.02$	$156 \pm 3$	10.5
<b>Phosphorus-31</b> N = 57	PW91	$-1.02 \pm 0.02$	$318 \pm 3$	21.3
	B3PW91	$-1.03 \pm 0.02$	$331 \pm 3$	20.4
	PBE	$-1.02 \pm 0.02$	$322 \pm 3$	20.9
	PBE0	$-1.03 \pm 0.02$	$339 \pm 3$	21.0
	TPSS	$-0.99 \pm 0.02$	$335 \pm 3$	21.7
	TPSSh	$-0.99 \pm 0.02$	$339 \pm 3$	22.2

<sup>a</sup>All calculations were performed at the PW91 level. <sup>b</sup>Linear-regression parameters are given for the correlation line  $\sigma_{ii}^{calc} = m\delta_{ii}^{exp} + \sigma_{\text{ref}}$ , where  $(\sigma_{ii}^{calc})$  represents the calculated principal components of magnetic-shielding tensors,  $(\delta_{ii}^{exp})$  represents experimental principal components of chemical-shift tensors,  $\sigma_{\text{ref}}$  is the shielding of the reference compound, and  $m$  is the slope of a correlation plot of calculated shielding versus experimental shift. <sup>c</sup>The RMSD is defined by  $RMSD = [(N - 2)^{-1} \sum_{n=1}^N (\delta_{ii}^{calc} - \delta_{ii}^{exp})^2]^{1/2}$ . Calculated magnetic shielding is converted to the chemical-shift scale  $(\delta_{ii}^{calc})$  using the relationship  $\delta_{ii}^{calc} = (\sigma_{ii}^{calc} - \sigma_{\text{ref}})/m$ .

### 4.5.1 Discussion of $^{13}\text{C}$ Results

The  $^{13}\text{C}$  results in Table 4.9 demonstrate that, for this nucleus, the GGA functionals (PW91 and PBE) are outperformed by every other class of functional studied, as indicated by the RMSDs of the various data sets. Using the scatter as the sole criterion for goodness-of-fit, the hybrid functionals seem to outperform the others.

A significant difficulty in the analysis of carbon data arises because different carbon species tend to group into distinct subpopulations on the correlation plot. Several studies have found that the correlation line between calculated magnetic shielding and experimental chemical shift for distinct carbon species can differ by a substantial amount [147, 156]. The differences appear to be more pronounced when the materials under consideration are constrained to a well-defined class of compounds such as carbohydrates or aromatic hydrocarbons [147]. Our previous work has suggested that hybrid functionals remove the systematic differences between carbon subpopulations, resulting in a unique trend line which can successfully model all carbon species. As above, statistical analysis was used to determine if the two classes of carbon species ( $sp^3$  and  $sp^2/sp$ ) represent statistically significant subpopulations at the 95% confidence level (Table 4.10). We find that when using pure DFT functionals (PW91, PBE, TPSS), the two carbon species represent distinct subpopulations, whereas the hybrid functionals (B3PW91, PBE0, TPSSh) do not result in distinct subpopulations.

The two carbon subpopulations can be visualized in the systematic differences between calculated magnetic-shielding parameters using a GGA functional and a hybrid functional. Figure 4.8 shows differences between principal magnetic-shielding values obtained from the PBE and PBE0 functionals for carbons in different hybridization. Carbons at  $sp^3$  sites behave differently from  $sp^2$  and  $sp$  sites. For the  $sp^3$ -hybridized sites, where the electron density is much more homogeneous around the nuclear site,

the added flexibility of the hybrid functional has a lesser effect than for the  $sp^2$ - and  $sp$ -hybridized sites, where the electron density, and therefore the corresponding current density, varies substantially with orientation. In Figure 4.8 one sees that  $\sigma_{11}$  and  $\sigma_{22}$  components for the  $sp^2$ - and  $sp$ -hybridized sites tend to be more affected by the use of the hybrid functionals than the GGA functionals, whereas there is a lesser difference for  $\sigma_{33}$ .

Differences between the experimental value for the shielding of TMS (184.1 ppm) [157] and the extrapolated values (as reported in Table 4.8) are shown in Figure 4.9(a) for the six functionals considered in the present work. Because the absolute shielding for TMS is predicted to be more deshielded when increasing the number of basis functions, we have applied a finite basis-set correction to the reference shieldings of  $-3.8 \pm 0.8$  ppm, based on the difference between the reference values for the cc-pVTZ basis set and the basis-set limit. The results illustrate that the hybrid functionals more closely predict the reference shielding than do the pure DFT functionals. The best results were obtained with PBE0. The meta-GGA functional (TPSS) results in an improvement in the reference value, intermediate between the GGA functionals and the hybrid functionals.

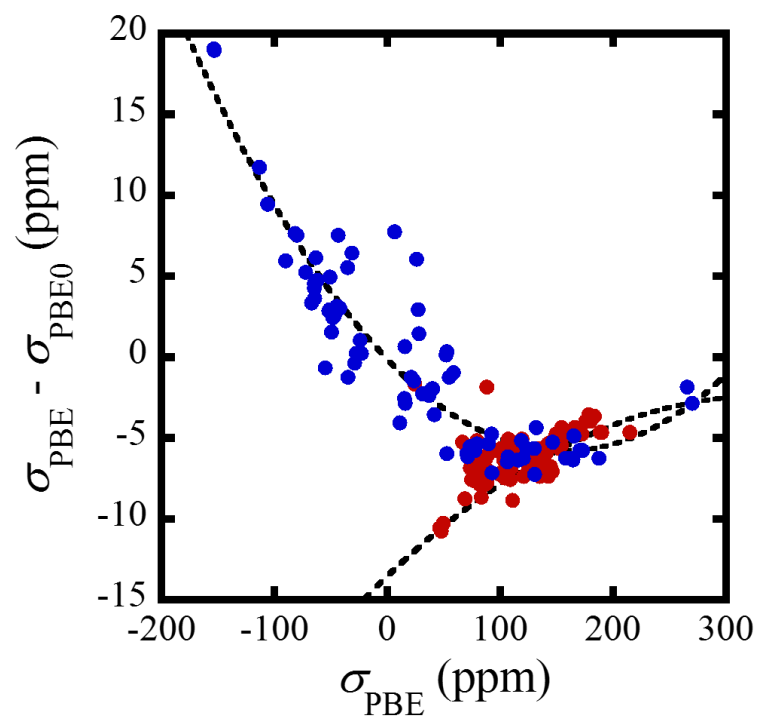


**Figure 4.8.** Difference between GGA-PBE- and PBE0-calculated  $^{13}\text{C}$  principal chemical-shielding values for  $sp^3$ -hybridized (red) and  $sp^2$ - and  $sp$ -hybridized (blue) sites. The trend lines are meant to guide the eye.

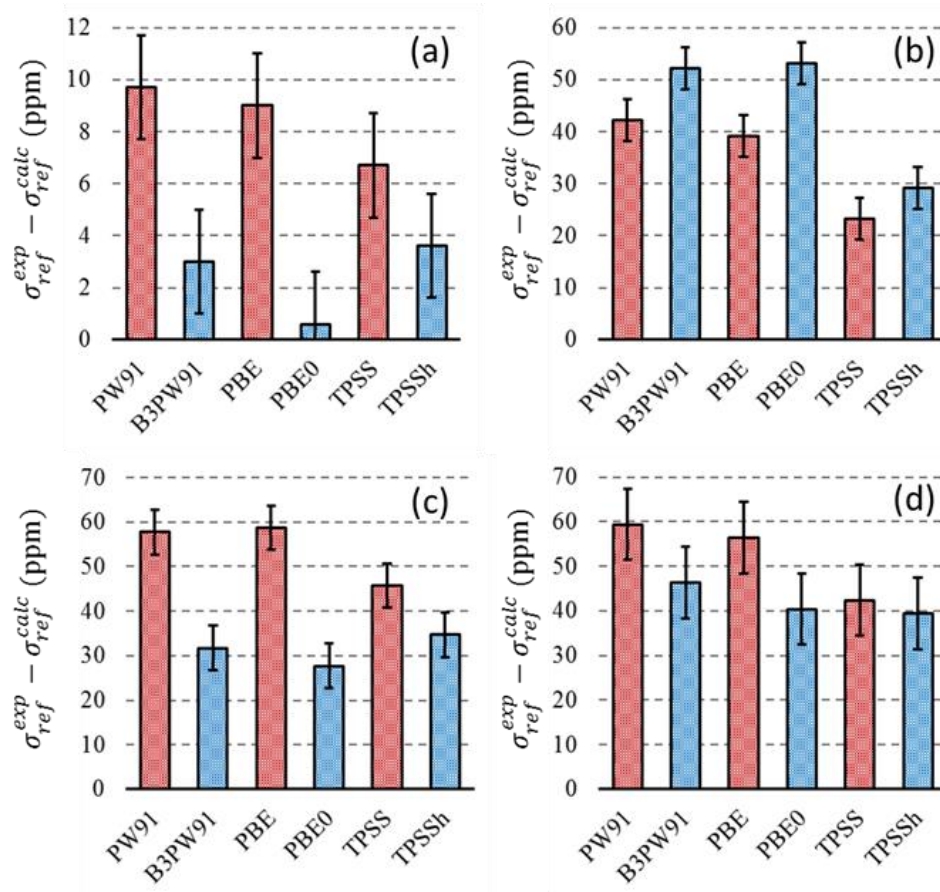


**Figure 4.9** Deviation of the extrapolated magnetic shielding of the reference compound obtained with least-squares analyses for various DFT functionals from the accepted literature value. Results are shown for  $^{13}\text{C}$  (a),  $^{15}\text{N}$  (b),  $^{19}\text{F}$  (c), and  $^{31}\text{P}$  (d). The reference compounds and literature shielding values are TMS at 184.1 ppm ( $^{13}\text{C}$ ) [176],  $\text{CH}_3\text{NO}_2$  at -135.8 ppm ( $^{15}\text{N}$ ) [177],  $\text{CFCl}_3$  at 188.7 ppm ( $^{19}\text{F}$ ) [178], and 85%  $\text{H}_3\text{PO}_4$  at 328.4 ppm ( $^{31}\text{P}$ ) [179]. A finite-basis-set corrections was applied to each calculated value by subtracting 3.8 ppm ( $^{13}\text{C}$ ), 19 ppm ( $^{15}\text{N}$ ), 1 ppm ( $^{19}\text{F}$ ), and 48 ppm ( $^{31}\text{P}$ ) from calculated values of  $\sigma_{ref}$ . The error bars represent both the uncertainty in the calculated and experimental values and the basis-set correction. Pure DFT functionals are shown in red and hybrid functionals are shown in blue.

**Table 4.10.** Linear-regression parameters and  $T$ -test statistics for assessing differences between  $sp^3$ - and  $sp^2/sp$ -hybridized carbon subpopulations.<sup>a</sup>

Method	$sp^3$ carbons		$sp^2/sp$ carbons		$\Delta RMSD$ (ppm)
	$ m $	$\sigma_{ref}$ (ppm)	$ m $	$\sigma_{ref}$ (ppm)	
PW91	1.049	180.2	1.005	178.9	0.7
B3PW91	1.031	184	1.046	184.9	0.1
PBE	1.048	181	1.001	179.4	0.7
PBE0	1.025	185.9	1.05	186.9	0.1
TPSS	1.018	182.6	0.985	182.2	0.6
TPSSh	1.012	184.3	1.006	184.9	0.1

<sup>a</sup>Differences in the best-fit lines between  $sp^3$  and  $sp^2$  carbon species are statistically significant if the  $\Delta RMSD$  is greater than 0.2 ppm.

#### 4.5.2 Discussion of $^{15}\text{N}$ Results

In calculation of  $^{15}\text{N}$  shielding, the RMSDs range between 16.8 ppm (PBE0) and 13.6 ppm (TPSSh), as shown in Table 4.9. Using the scatter about the best-fit line as the criterion for judging the functionals, the best class of functionals appears to be the meta-GGAs (TPSS and TPSSh), whereas the worst class of functionals is the hybrid GGAs (B3PW91 and PBE0). The meta-GGA functionals yield slopes closest to unity, ranging between  $-0.995 \pm 0.007$  (TPSS) and  $-1.027 \pm 0.007$  (TPSSh). These values represent an improvement over the predicted slope of  $-1.04 \pm 0.01$  for PBE. The hybrid functionals have slopes ranging between  $-1.11 \pm 0.01$  (B3PW91) and  $-1.12 \pm 0.01$  (PBE0), as compared to the meta-GGA functionals.

The use of GGA and hybrid-GGA functionals in  $^{15}\text{N}$  calculations differs from their use with other nuclei in one significant way: whereas the reference values of the

other nuclei ( $^{13}\text{C}$ ,  $^{19}\text{F}$ ,  $^{31}\text{P}$ ) are predicted to be more *shielded* (relative to the pure DFT functional) when using hybrid functionals, for  $^{15}\text{N}$  the use of hybrid functionals yields reference values that are *deshielded*. In the most significant case, the reference shielding for the PBE functional is  $-156 \pm 2$  ppm and the reference for the PBE0 functional is  $-170 \pm 2$  ppm. Figure 4.9(b) displays differences between the predicted intercept and the literature value of  $-135.8$  ppm for the bare nucleus [158]. As in the case of carbon, a finite-basis-set correction of  $19 \pm 3$  ppm has been introduced. Interestingly, meta-GGA functionals are the closest to the literature value. In each case, using a hybrid functional increases the deviation from the literature value than does the pure DFT value.

Figure 4.10(a) shows the differences in magnetic shielding between the PBE functional and the PBE0 functional versus the PBE shielding. This plot illustrates that the quantity  $\sigma_{\text{PBE}} - \sigma_{\text{PBE0}}$  varies significantly across the range of computed magnetic shieldings. Similarly, Figure 4.10(b) shows the differences in magnetic shielding between the PBE functional and the TPSS functional versus the PBE shielding. The most significant changes are seen in the calculations of  $\sigma_{33}$  for the  $^{15}\text{N}$  nuclei of azide groups, located around  $-900$  ppm at the PBE level. In the PBE0 calculations, the azide  $\sigma_{33}$  is predicted to be *deshielded* relative to the PBE calculations by  $67 - 84$  ppm, whereas the TPSS calculation predicts these sites to be *shielded* relative to the PBE calculation by  $65 - 77$  ppm. As indicated in Figure 4.3, these points deviate from the predicted trend line by a sizeable amount at the GGA level. This deviation is worsened when using hybrid GGA functionals. When using the TPSS functional, the points fall along the same line predicted by the other calculations, suggesting that meta-GGA functionals improve calculations of highly correlated systems such as those containing nitrogen-nitrogen double bonds.

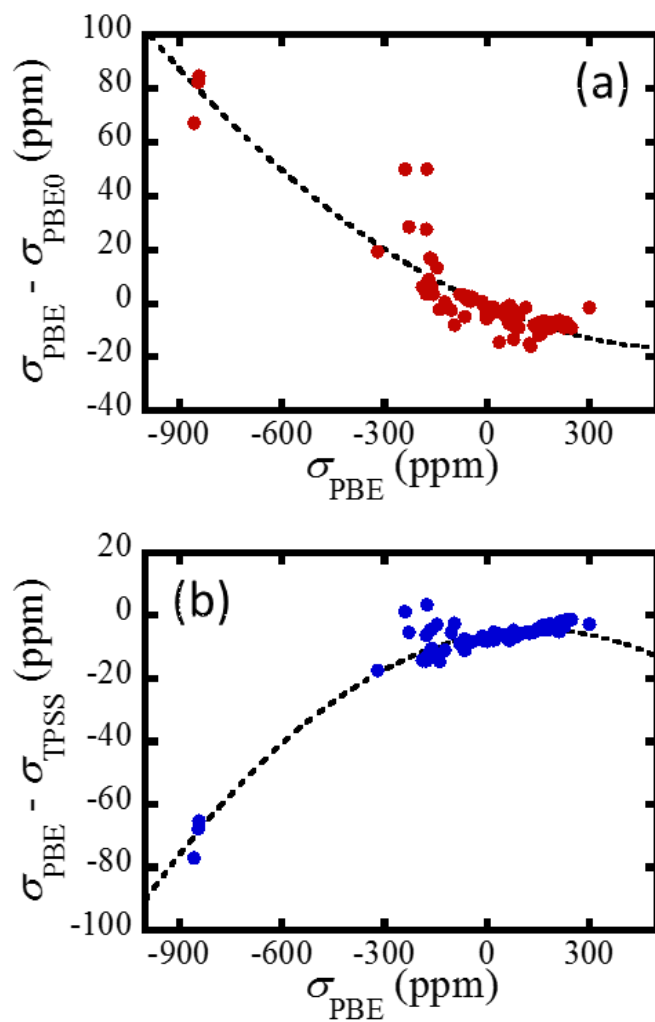


**Figure 4.10.** (a) Differences in computed shielding between the GGA-PBE functional and the hybrid GGA-PBE0 functional. (b) Differences in computed shielding between the GGA-PBE functional and the meta-GGA-TPSS functional.

### 4.5.3 Discussion of $^{19}\text{F}$ Results

A frequent feature of computed  $^{19}\text{F}$  NMR parameters is that they are predicted less reliably than are the NMR parameters of other light nuclei, as is indicated by the substantial deviation in the slope from unity, signifying that the errors arise from a systematic flaw in the calculations. At the basis set limit, the GIPAW method predicts a slope of  $-1.22 \pm 0.02$  at the PW91 level. Comparable systematic errors have been reported in calculations performed at similar levels of theory [140, 159], where it has been shown that altering the computed band gap by applying potentials to certain molecular orbitals corrects systematic flaws in the calculations. Such a correction is empirical and the size of the potential is dependent on the system.

Considering the results in Table 4.9, the GGA and meta-GGA functionals overestimate the slope substantially. Hybrid functionals decrease the slope, with the best result of  $-1.11 \pm 0.02$  obtained from the B3PW91 functional, and reduce the magnitude of the discrepancy so that the slope is within the range of values computed for the other nuclei. This finding suggests that large changes in the magnetic shielding can be induced by the method for calculating the exchange energy. There are two lines of evidence that suggest that the errors in the calculated values are related to the exchange functional. Moving from the PBE functional (0% HF exchange) to the PBE0 functional (25% HF exchange), the slope of the correlation line is changed from  $-1.18 \pm 0.02$  to  $-1.10 \pm 0.02$ , suggesting that increasing the proportion of exact exchange to around 50% would eliminate deviations in the slope. Jameson *et al.* have proposed an absolute reference for  $^{19}\text{F}$  where the shielding of  $\text{CFCl}_3$  is 188.7 ppm [160]. Changing from the PBE functional to the PBE0 functional changes the extrapolated reference shielding from  $131 \pm 3$  ppm at the PBE level to  $162 \pm 3$  at the PBE0 level, consistent with an ideal functional that uses approximately 50% HF exchange. See Figure 4.9(c).

#### 4.5.4 Discussion of $^{31}\text{P}$ Results

The  $^{31}\text{P}$  results in Table 4.9 reveal only small deviations between the different classes of functionals for calculations of  $^{31}\text{P}$  magnetic shielding. In particular, the slopes of the best-fit lines are the same, to within experimental error. The largest deviations between functionals are seen in the reference shieldings. Jameson *et al.* suggest a reference shielding for  $\text{H}_3\text{PO}_4$  of 328.4 ppm [161]. The results, shown in Figure 4.9(d), mirror those obtained for  $^{13}\text{C}$  and  $^{19}\text{F}$ . As with those nuclei, use of a hybrid functional always results in an improvement over the pure DFT functional. In addition, improvement is found for the meta-GGA-TPSS functional over the GGA functionals.

#### 4.6 Conclusion

Consideration of intermolecular effects is essential when calculating NMR parameters for crystalline materials. The periodic GIPAW method, for example, accounts for intermolecular interactions that are not predicted by calculations on isolated molecules (especially in systems containing networks of intermolecular hydrogen bonds). The use of symmetry-adapted-cluster (SAC) models yields similar results to those obtained using GIPAW, showing the importance of inclusion of intermolecular effects in predicting magnetic shielding in solids.

The use of the GIPAW and GIAO/SAC methods for calculating the magnetic shielding of  $^{13}\text{C}$ ,  $^{15}\text{N}$ ,  $^{19}\text{F}$ , and  $^{31}\text{P}$  nuclides in insulating molecular solids demonstrates that one may systematically model a wide variety of solid-state environments with either method, if one uses a sufficiently large basis. This result is demonstrated on a database consisting of 72 crystalline materials with a total of 131 unique NMR-active lattice sites. Computed magnetic shieldings extrapolated to the basis-set limit show that the two methods predict correlation lines that show no statistical difference at the 95% level for

all nuclei except  $^{19}\text{F}$ . In the case of  $^{19}\text{F}$ , the correlation between experimental chemical shifts and calculated magnetic shielding yields a slope closer to unity with the SAC method.

The effects of various model chemistries on computed magnetic shielding have been assessed using the SAC model. Six exchange-correlation functionals have been examined, representing the GGA, hybrid GGA, meta-GGA, and hybrid meta-GGA classes. There is essentially no difference in computed magnetic shielding between GGA functionals (PW91 and PBE) for any of the nuclides studied here. Hybrid GGA functionals yield results that are often quite different from those determined with pure DFT functionals. For  $^{13}\text{C}$ ,  $^{19}\text{F}$ , and  $^{31}\text{P}$ , the additional flexibility of using hybrid functionals leads to improvement of the predicted magnetic shielding with values determined on established absolute scales. In particular, for  $^{19}\text{F}$  magnetic shielding, the use of hybrid functionals substantially decreases the slope of the correlation between calculated shielding and experimental shift from -1.18 when using GGAs to -1.11. For  $^{19}\text{F}$ , we suggest that increasing the proportion of HF exchange beyond the standard 25% may further improve agreement with experiment, although this result needs to be explored in more detail. Calculations of  $^{15}\text{N}$  magnetic shielding, in contrast to the other nuclei, appear to be worsened by the admixture of exact exchange, as indicated by a slope that is further from unity and a reference shielding that differs more substantially from established scales. The use of the meta-GGA TPSS functional lead to improvement over the GGA functionals for all four nuclei, including  $^{15}\text{N}$ .

It is also noteworthy that  $^{13}\text{C}$  magnetic-shielding parameters obtained by pure DFT methods can be grouped into distinct subpopulations based on the hybridization of the carbon site. However, use of hybrid DFT functionals does not lead distinct

subpopulations, allowing all carbon species to be described with a single set of linear-regression parameters.

## REFERENCES

- [1] M.H. Sherwood, J.C. Facelli, D.W. Alderman, D.M. Grant, Carbon-13 chemical shift tensors in polycyclic aromatic compounds. 2. single-crystal study of naphthalene, *J. Am. Chem. Soc.*, 113 (1991) 750-753.
- [2] S.C. Capelli, A. Albinati, S.A. Mason, B.T.M. Willis, Molecular motion in crystalline naphthalene: analysis of multi-temperature X-Ray and neutron diffraction data, *J. Phys. Chem. A*, 110 (2006) 11695-11703.
- [3] S. Pausak, A. Pines, J.S. Waugh, Carbon-13 chemical shielding tensors in single-crystal durene, *J. Chem. Phys.*, 59 (1973) 591-595.
- [4] E. Prince, L.W. Schroeder, J.J. Rush, Constrained refinement of the structure of durene, *Acta Crystallogr., Sect. B*, 29 (1973) 184-191.
- [5] K. Maliňáková, L. Novosadová, M. Lahtinen, E. Kolehmainen, J. Brus, R. Marek, <sup>13</sup>C chemical shift tensors in hypoxanthine and 6-mercaptopurine: effects of substitution, tautomerism, and intermolecular interactions, *J. Phys. Chem. A*, 114 (2010) 1985-1995.
- [6] H.W. Schmalle, G. Hanggi, E. Dubler, Structure of hypoxanthine, *Acta Crystallogr., Sect. C*, 44 (1988) 732-736.
- [7] M.H. Sherwood, D.W. Alderman, D.M. Grant, Assignment of carbon-13 chemical-shift tensors in single-crystal sucrose, *J. Magn. Reson., Ser A*, 104 (1993) 132-145.
- [8] G.M. Brown, H.A. Levy, Further refinement of the structure of sucrose based on neutron-diffraction data, *Acta Crystallogr., Sect. B*, 29 (1973) 790-797.
- [9] R.G. Griffin, A. Pines, S. Pausak, J.S. Waugh, Carbon-13 chemical shielding in oxalic acid, oxalic acid dihydrate, and diammonium oxalate, *J. Chem. Phys.*, 63 (1975) 1267-1271.
- [10] V.R. Thalladi, M. Nüsse, R. Boese, The melting point alternation in alpha, omega-alkanedicarboxylic acids, *J. Am. Chem. Soc.*, 122 (2000) 9227-9236.
- [11] T.M. Sabine, G.W. Cox, B.M. Craven, Neutron-diffraction study of  $\alpha$ -oxalic acid dihydrate, *Acta Crystallogr., Sect. B*, 25 (1969) 2437-2441.

- [12] N. Janes, S. Ganapathy, E. Oldfield, Carbon-13 chemical shielding tensors in L-threonine, *J. Magn. Reson.*, 54 (1983) 111-121.
- [13] M. Ramanadham, S.K. Sikka, R. Chidambaram, Structure determination of L<sub>5</sub>-threonine by neutron diffraction, *Pramana*, 1 (1973) 247-259.
- [14] M. Mehring, J.D. Becker, Observation of electronic structure change at the first-order phase transition in quasi-two-dimensional squaric acid, *Phys. Rev. Lett.*, 47 (1981) 366-370.
- [15] D. Semmingsen, F.J. Hollander, T.F. Koetzle, A neutron diffraction study of squaric acid (3,4-dihydroxy-3-cyclobutene-1,2-dione), *J. Chem. Phys.*, 66 (1977) 4405-4412.
- [16] K.W. Zilm, A.J. Beeler, D.M. Grant, J. Michl, T.C. Chou, E.L. Allred, Carbon-13 magnetic resonance dipolar spectroscopy. orientation of the chemical shift tensor in cyclopropane, *J. Am. Chem. Soc.*, 103 (1981) 2119-2120.
- [17] D. Nijveldt, A. Vos, Single-crystal X-ray geometries and electron-density distributions of cyclopropane, bicyclopropyl and vinylcyclopropane. 3. evidence for conjugation in vinylcyclopropane and bicyclopropyl, *Acta Crystallogr., Sect. B*, 44 (1988) 296-307.
- [18] K.W. Zilm, R.T. Conlin, D.M. Grant, J. Michl, Low-temperature carbon-13 magnetic resonance of solids. 1. alkenes and cycloalkenes, *J. Am. Chem. Soc.*, 102 (1980) 6672-6676.
- [19] G.J.H. van Nes, A. Vos, Single-crystal structures and electron-density distributions of ethane, ethylene and acetylene. 3. single-crystal X-ray structure determination of ethylene at 85K, *Acta Crystallogr., Sect. B*, 35 (1979) 2593-2601.
- [20] M.S. Solum, J.C. Facelli, Z. Gan, D.M. Grant, <sup>13</sup>C dipolar spectroscopy of nitromethane, *Mol. Phys.*, 64 (1988) 1031-1040.
- [21] G.A. Jeffrey, J.R. Ruble, L.M. Wingert, J.H. Yates, R.K. McMullan,  $\pi$ -bond anisotropy and C-D $\cdots$ O hydrogen bonding in the crystal structure of deuterionitromethane, *J. Am. Chem. Soc.*, 107 (1985) 6227-6230.
- [22] A.J. Beeler, A.M. Orendt, D.M. Grant, P.W. Cutts, J. Michl, K.W. Zilm, J.W. Downing, J.C. Facelli, M.S. Schindler, W. Kutzelnigg, Low-temperature <sup>13</sup>C magnetic resonance in solids. 3. linear and pseudolinear molecules, *J. Am. Chem. Soc.*, 106 (1984) 7672-7676.
- [23] R.K. McMullan, A. Kwick, P. Popelier, Structures of the cubic and orthorhombic phases of acetylene by single-crystal neutron diffraction, *Acta Crystallogr., Sect. B*, 48 (1992) 726-731.

- [24] A. Pines, J.S. Waugh, M.G. Gibby, Proton-enhanced nuclear induction spectroscopy.  $^{13}\text{C}$  chemical shielding anisotropy in some organic solids, *Chem. Phys. Lett.*, 15 (1972) 373-&.
- [25] B.M. Powell, G. Dolling, B.H. Torrie, Structure of solid carbon disulfide between 5 and 150 K, *Acta Crystallogr., Sect. B*, 38 (1982) 28-32.
- [26] D.W. Alderman, M.S. Solum, D.M. Grant, Methods for analyzing spectroscopic line shapes. NMR solid powder patterns, *J. Chem. Phys.*, 84 (1986) 3717-3725.
- [27] Y. Yokoyama, Y. Ohashi, Crystal and molecular structures of methoxy and methylthio compounds, *Bull. Chem. Soc. Jpn.*, 72 (1999) 2183-2191.
- [28] F. Liu, A.M. Orendt, D.W. Alderman, D.M. Grant, Carbon-13 chemical shift tensors in pentaerythritol, *J. Am. Chem. Soc.*, 119 (1997) 8981-8984.
- [29] D. Semmingsen, Neutron diffraction refinement of the structure of pentaerythritol, *Acta Chem. Scand.*, A42 (1988) 279-283.
- [30] K. Takegoshi, A. Naito, C.A. McDowell, Intermolecular hydrogen-bonding effects on the  $^{13}\text{C}$  NMR shielding tensor of the carbonyl carbon nucleus in a single crystal of dimedone, *J. Magn. Reson.*, 65 (1985) 34-42.
- [31] M. Bolte, M. Scholtysik, Dimedone at 133K, *Acta Crystallogr., Sect. C*, 53 (1997).
- [32] J.C. Facelli, A.M. Orendt, A.J. Beeler, M.S. Solum, G. Depke, K.D. Malsch, J.W. Downing, P.S. Murthy, D.M. Grant, J. Michl, Low-temperature  $^{13}\text{C}$  magnetic resonance in solids. 5. chemical shielding anisotropy of the  $^{13}\text{CH}_2$  group, *J. Am. Chem. Soc.*, 107 (1985) 6749-6754.
- [33] J. Benet-Buchholz, T. Haumann, R. Boese, How to circumvent plastic phases: The single crystal X-ray analysis of norbornadiene, *Chem. Commun.*, (1998) 2003-2004.
- [34] A.M. Orendt, J.C. Facelli, D.M. Grant, J. Michl, F.H. Walker, W.P. Dailey, S.T. Waddell, K.B. Wiberg, M. Schindler, W. Kutzelnigg, Low temperature  $^{13}\text{C}$  NMR magnetic resonance in solids. 4. Cyclopropane, bicyclo[1.1.0]butane and [1.1.1]propellane, *Theor. Chim. Acta*, 68 (1985) 421-430.
- [35] P. Seiler, The crystal structure of [1.1.1]propellane at 138K, *Helv. Chim. Acta*, 73 (1990) 1574-1585.
- [36] J.Z. Hu, J.C. Facelli, D.W. Alderman, R.J. Pugmire, D.M. Grant,  $^{15}\text{N}$  chemical shift tensors in nucleic acid bases, *J. Am. Chem. Soc.*, 120 (1998) 9863-9869.

- [37] S.M. Tretjak, V.V. Mitkevich, L.F. Sukhodub, Adenine trihydrate: its structure at 295 and 105 K, *Kristallografiya*, 32 (1987) 1268-1271.
- [38] R.J. McClure, B.M. Craven, New investigations of cytosine and its monohydrate, *Acta Crystallogr., Sect. B*, B 29 (1973) 1234-1238.
- [39] U. Thewalt, C.E. Bugg, R.E. Marsh, Crystal structure of guanine monohydrate, *Acta Crystallogr., Sect. B*, B 27 (1971) 2358-&.
- [40] G. Portalone, L. Bencivenni, M. Colapietro, A. Pieretti, F. Ramondo, The effect of hydrogen bonding on the structures of uracil and some methyl derivatives studied by experiment and theory, *Acta Chem. Scand.*, 53 (1999) 57-68.
- [41] R.F. Stewart, Redetermination of the crystal structure of uracil, *Acta Crystallogr.*, 23 (1967) 1102-&.
- [42] M.S. Solum, K.L. Altman, M. Strohmeier, D.A. Berges, Y. Zhang, J.C. Facelli, R.J. Pugmire, D.M. Grant,  $^{15}\text{N}$  chemical shift principal values in nitrogen heterocycles, *J. Am. Chem. Soc.*, 119 (1997) 9804-9809.
- [43] R. Goddard, O. Heinemann, C. Kruger, Pyrrole and a co-crystal of 1H- and 2H-1,2,3-triazole, *Acta Crystallogr., Sect. C*, 53 (1997) 1846-1850.
- [44] B.M. Craven, R.K. McMullan, J.D. Bell, H.C. Freeman, Crystal structure of imidazole by neutron diffraction at 20°C and 150°C, *Acta Crystallogr., Sect. B*, 33 (1977) 2585-2589.
- [45] J.Z. Hu, J.W. Zhou, B.L. Yang, L.Y. Li, J.Q. Qiu, C.H. Ye, M.S. Solum, R.A. Wind, R.J. Pugmire, D.M. Grant, Dynamic nuclear polarization of nitrogen-15 in benzamide, *Solid State Nucl. Magn. Reson.*, 8 (1997) 129-137.
- [46] K. Kobayashi, A. Sato, S. Sakamoto, K. Yamaguchi, Solvent-induced polymorphism of three-dimensional hydrogen-bonded networks of hexakis(4-carbamoylphenyl)benzene, *J. Am. Chem. Soc.*, 125 (2003) 3035-3045.
- [47] A. Escande, J.L. Galigne, Crystalline structure of benzimidazole,  $\text{C}_7\text{N}_2\text{H}_6$ : comparison of results of two independent determinations, *Acta Crystallogr., Sect. B*, 30 (1974) 1647-1648.
- [48] G.H. Penner, G.M. Bernard, R.E. Wasylshen, A. Barrett, R.D. Curtis, A solid-state nitrogen-15 NMR and ab initio study of nitrobenzenes, *J. Org. Chem.*, 68 (2003) 4258-4264.

- [49] R. Boese, D. Blaser, M. Nussbaumer, T.M. Krygowski, Low-temperature crystal and molecular structure of nitrobenzene, *Struct. Chem.*, 3 (1992) 363-368.
- [50] R.E. Wasylishen, G.H. Penner, W.P. Power, R.D. Curtis, Dipolar NMR spectra of the oxime moiety in (E)-acetophenone oxime. carbon and nitrogen chemical shielding anisotropies, *J. Am. Chem. Soc.*, 111 (1989) 6082-6086.
- [51] A. Gieren, T. Hubner, C. Ruizperez, X-ray structure of (E)-acetophenone oxime, *Chem. Zeit.*, 110 (1986) 73-76.
- [52] S. Crawford, M.T. Kirchner, D. Blaser, R. Boese, W.I.F. David, A. Dawson, A. Gehrke, R.M. Ibberson, W.G. Marshall, S. Parsons, O. Yamamuro, Isotopic polymorphism in pyridine, *Angew. Chem. Int. Ed.*, 48 (2009) 755-757.
- [53] R.E. Marsh, M. Kapon, S.Z. Hu, F.H. Herbststein, Some 60 new space-group corrections, *Acta Crystallogr., Sect. B*, 58 (2002) 62-77.
- [54] S. Kaplan, A. Pines, R.G. Griffin, J.S. Waugh, Chemical shielding anisotropy of  $^{13}\text{C}$  and  $^{15}\text{N}$  in acetonitrile, *Chem. Phys. Lett.*, 25 (1974) 78-79.
- [55] R. Enjalbert, J. Galy,  $\text{CH}_3\text{CN}$  : X-ray structural investigation of a unique single crystal.  $\beta \rightarrow \alpha$  phase transition and crystal structure, *Acta Crystallogr., Sect. B*, 58 (2002) 1005-1010.
- [56] M. Sardashti, G.E. Maciel,  $^{13}\text{C}$  and  $^{15}\text{N}$  chemical shift tensors in para-substituted benzonitriles, *J. Phys. Chem.*, 92 (1988) 4620-4632.
- [57] H. Guth, G. Heger, U. Druck, Neutron-diffraction study of the structure of *para*-benzenedicarbonitrile, *Z. Kristallogr.*, 159 (1982) 185-190.
- [58] R.D. Curtis, J.W. Hilborn, G. Wu, M.D. Lumsden, R.E. Wasylishen, J.A. Pincock, A nitrogen-15 NMR study of *cis*-azobenzene in the solid state, *J. Phys. Chem.*, 97 (1993) 1856-1861.
- [59] A. Mostad, C. Romming, Refinement of the crystal structure of *cis*-azobenzene, *Acta Chem. Scand.*, 25 (1971) 3561-&.
- [60] R.E. Wasylishen, W.P. Power, G.H. Penner, R.D. Curtis, Nitrogen-15 shielding in *trans*-azobenzene, *Can. J. Chem.*, 67 (1989) 1219-1224.
- [61] J. Harada, K. Ogawa, S. Tomoda, Molecular motion and conformational interconversion of azobenzenes in crystals as studied by X-ray diffraction, *Acta Crystallogr., Sect. B*, 53 (1997) 662-672.

- [62] G.S. Harbison, Y.-S. Kye, G.H. Penner, M. Grandin, M. Monette,  $^{14}\text{N}$  quadrupolar,  $^{14}\text{N}$  and  $^{15}\text{N}$  chemical shift, and  $^{14}\text{N}$ - $^1\text{H}$  dipolar tensors of sulfamic acid, *J. Phys. Chem. B*, 106 (2002) 10285-10291.
- [63] F.A. Kanda, A.J. King, The crystal structure of sulfamic acid, *J. Am. Chem. Soc.*, 73 (1951) 2315-2319.
- [64] H. Raber, M. Mehring,  $^{19}\text{F}$  chemical shift tensor in fluorobenzene compounds, *Chem. Phys.*, 26 (1977) 123-130.
- [65] V.R. Thalladi, H.C. Weiss, D. Blaser, R. Boese, A. Nangia, G.R. Desiraju, C-H $\cdots$ F interactions in the crystal structures of some fluorobenzenes, *J. Am. Chem. Soc.*, 120 (1998) 8702-8710.
- [66] M.T. Kirchner, D. Blaser, R. Boese, T.S. Thakur, G.R. Desiraju, 1,3-Difluorobenzene, *Acta Crystallogr., Sect. E*, 65 (2009) O2668-U2912.
- [67] M.J. Molski, D. Mollenhauer, S. Gohr, B. Paulus, M.A. Khanfar, H. Shorafa, S.H. Strauss, K. Seppelt, Halogenated benzene cation radicals, *Chem. Eur. J.*, 18 (2012) 6644-6654.
- [68] M. Mehring, R.G. Griffin, J.S. Waugh,  $^{19}\text{F}$  shielding tensors from coherently narrowed NMR powder spectra, *J. Chem. Phys.*, 55 (1971) 746-&.
- [69] H. Shorafa, D. Mollenhauer, B. Paulus, K. Seppelt, The two structures of the hexafluorobenzene radical cation  $\text{C}_6\text{F}_6^{+\bullet}$ , *Angew. Chem. Int. Ed.*, 48 (2009) 5845-5847.
- [70] R.K. Harris, P. Jackson, G.J. Nesbitt, Fluorine-19 CRAMPS and its application to the solid-state spectrum of perfluoronaphthalene, *J. Magn. Reson.*, 85 (1989) 294-302.
- [71] N.A. Akhmed, Study of crystalline structure of octafluoronaphthalene, *Zh. Strukt. Khim.*, 14 (1973) 573-574.
- [72] V.R. Hathwar, T.S. Thakur, R. Dubey, M.S. Pavan, T.N.G. Row, G.R. Desiraju, Extending the supramolecular synthon based fragment approach (SBFA) for transferability of multipole charge density parameters to monofluorobenzoic acids and their cocrystals with isonicotinamide: importance of C-H $\cdots$ O, C-H $\cdots$ F, and F $\cdots$ F intermolecular regions, *J. Phys. Chem. A*, 115 (2011) 12852-12863.
- [73] M. Kubota, S. Ohba, Electron-density distribution in fluorobenzene derivatives, *Acta Crystallogr., Sect. B*, 48 (1992) 849-854.
- [74] T.K. Halstead, H.W. Spiess, U. Haeberlen,  $^{19}\text{F}$  and  $^1\text{H}$  shielding tensors and crystal structure of 4-4'-difluorobiphenyl, *Mol. Phys.*, 31 (1976) 1569-1583.

- [75] M.H. Lemee, L. Toupet, Y. Delugeard, J.C. Messenger, H. Cailleau, Crystal structure and thermal motion analysis of 4,4'-difluorobiphenyl, *Acta Crystallogr., Sect. B*, 43 (1987) 466-470.
- [76] I.D.H. Oswald, D.R. Allan, W.D.S. Motherwell, S. Parsons, Structures of the monofluoro- and monochlorophenols at low temperature and high pressure, *Acta Crystallogr., Sect. B*, 61 (2005) 69-79.
- [77] J. Ridout, M.R. Probert, High-pressure and low-temperature polymorphism in C-H•••F-C hydrogen bonded monofluorotoluenes, *Cryst. Growth Des.*, 13 (2013) 1943-1948.
- [78] K. Hagen, D.G. Nicholson, L.J. Saethre, Structure of tetrafluoro-p-benzoquinone (p-fluoranil) at 120 K, *Acta Crystallogr., Sect. C*, 43 (1987) 1959-1961.
- [79] Q.Z. Guo, R.E.J. Sears, R.D. Campbell,  $^{19}\text{F}$  shielding anisotropy in  $\text{CCl}_3\text{F}$  and  $\text{CBr}_3\text{F}$ , *J. Chem. Phys.*, 81 (1984) 5214-5216.
- [80] J.K. Cockcroft, A.N. Fitch, Structure of solid trichlorofluoromethane,  $\text{CFCl}_3$ , by powder neutron diffraction, *Z. Kristallogr.*, 209 (1994) 488-490.
- [81] J.B. Robert, L. Wiesenfeld,  $^{31}\text{P}$  solid state nuclear magnetic resonance principal values of the chemical shift tensors of phosphane oxides, phosphane sulfides and phosphane selenides, *Mol. Phys.*, 44 (1981) 319-327.
- [82] M.B. Hursthouse, F.A. Hart, J.D.J. Backer-Dirkis, Private Communication (CCDC 679505), 2003.
- [83] C.P. Brock, W.B. Schweizer, J.D. Dunitz, Internal molecular motion of triphenylphosphine oxide: analysis of atomic displacement parameters for orthorhombic and monoclinic crystal modifications at 100K and 150K, *J. Am. Chem. Soc.*, 107 (1985) 6964-6970.
- [84] A.R. Grimmer, D. Muller, Measurement of anisotropy of  $^{31}\text{P}$  shift in solid phosphorus oxide halides, *Z. Chem.*, 16 (1976) 496-497.
- [85] K. Olie, Crystal structure of  $\text{POCl}_3$ , *Acta Crystallogr., Sect. B*, B 27 (1971) 1459-&.
- [86] I.G. Shenderovich, Effect of noncovalent interactions on the  $^{31}\text{P}$  chemical shift tensor of phosphine oxides, phosphinic, phosphonic, and phosphoric acids, and their complexes with lead(II), *J. Phys. Chem. C*, 117 (2013) 26689-26702.
- [87] F. Dornhaus, M. Bolte, H.W. Lerner, M. Wagner, A comparative study of chalcogenated phosphanylborohydrides  $[\text{EPR}_2\text{BH}_3]^-$  (R = Ph, tBu) and

triorganophosphane chalcogenides  $\text{EPPH}_2\text{CH}_3$  (E = O, S, Se, Te), *Eur. J. Inorg. Chem.*, (2006) 5138-5147.

[88] P. Tasker, D. Coventry, S. Parsons, D. Messenger, Private Communication (CCDC 276835), 2005.

[89] M. Gee, R.E. Wasylshen, K. Eichele, J.F. Britten, Phosphorus chemical shift tensors for tetramethyldiphosphine disulfide: a  $^{31}\text{P}$  single-crystal NMR, dipolar-chemical shift NMR, and ab initio molecular orbital study, *J. Phys. Chem. A*, 104 (2000) 4598-4605.

[90] J.D. Lee, G.W. Goodacre, A redetermination of the crystal structure of tetramethyldiphosphine disulfide, *Acta Crystallogr., Sect. B*, B 27 (1971) 302-&.

[91] K. Eichele, G. Wu, R.E. Wasylshen, J.F. Britten, Phosphorus-31 NMR Studies of solid tetraethyldiphosphine disulfide. a reinvestigation of the  $^{31}\text{P}$ ,  $^{31}\text{P}$  spin-spin coupling tensor, *J. Phys. Chem.*, 99 (1995) 1030-1037.

[92] A. Cogne, A. Grand, J. Laugier, J.B. Robert, L. Wiesenfeld, Anisotropy of the  $^1\text{J}(\text{PSE})$  spin-spin coupling. X-ray and liquid crystal NMR study of  $\text{Se}=(\text{CH}_3)_3$ , *J. Am. Chem. Soc.*, 102 (1980) 2238-2242.

[93] J. Herzfeld, R.G. Griffin, R.A. Haberkorn, Phosphorus-31 chemical shift tensors in barium diethyl phosphate and urea-phosphoric acid: model compounds for phospholipid head-group studies, *Biochem.*, 17 (1978) 2711-2718.

[94] C.C. Wilson, K. Shankland, N. Shankland, Single-crystal neutron diffraction of urea-phosphoric acid: evidence for H-atom migration in a short hydrogen bond between 150 K and 350 K, *Z. Kristallogr.*, 216 (2001) 303-306.

[95] H. Reuter, M. Reichelt, Methylphosphonic acid,  $\text{CH}_3\text{PO}(\text{OH})_2$ , *Acta Crystallogr., Sect. E*, 70 (2014) o353.

[96] K. Eichele, R.E. Wasylshen, J.M. Kessler, L. Solujic, J.H. Nelson, Phosphorus chemical shift tensors of phosphole derivatives determined by  $^{31}\text{P}$  NMR spectroscopy of powder samples, *Inorg. Chem.*, 35 (1996) 3904-3912.

[97] A. Decken, Private Communication (CCDC 254271), 2004.

[98] G. Wu, R.E. Wasylshen, Phosphorus chemical shift tensors in dithiadiphosphetane disulfides determined by solid-state  $^{31}\text{P}$  nuclear magnetic resonance, *Solid State Nucl. Magn. Reson.*, 4 (1995) 47-51.

[99] V. Kaiser, F. Menzel, Crystal structure of 2,4-bis(methylthio)-1,3-dithiaphosphetane-2,4-disulfide,  $(\text{CH}_3\text{S})_2(\text{P}_2\text{S}_2)\text{S}_2$ , *Z. Kristallogr.*, 206 (1993) 279-280.

- [100] R. Kempe, J. Sieler, H. Beckmann, G. Ohms, Crystal structure of 2,4-bis(p-methoxyphenyl)-2,4-dithioxo-1,3,2- $\lambda^5$ -,4 $\lambda^5$ -dithiadiphosphetane,  $C_{14}H_{14}P_2S_4$ , Z. Kristallogr., 202 (1992) 159-160.
- [101] D. Gudat, W. Hoffbauer, E. Niecke, W.W. Schoeller, U. Fleischer, W. Kutzelnigg, Phosphorus-31 solid-state NMR study of iminophosphines: influence of electronic structure and configuration of the double bond on phosphorus shielding, J. Am. Chem. Soc., 116 (1994) 7325-7331.
- [102] N. Nieger, C. Cartner-Winkhaus, E. Niecke, Private Communication (CCDC 174707), 2001.
- [103] A.N. Chernega, A.A. Korkin, N.E. Aksinenko, A.V. Ruban, V.D. Romanenko, Spatial and electron structure of P-HALO- $\lambda$ -3-iminophosphines, Zh. Obshch. Khim., 60 (1990) 2462-2469.
- [104] G.H. Penner, R.E. Wasylishen, Phosphorus-31 NMR studies of several phosphines in the solid state, Can. J. Chem., 67 (1989) 1909-1913.
- [105] J.A. Davies, S. Dutremez, A.A. Pinkerton, Solid-state  $^{31}P$  NMR and X-ray crystallographic studies of tertiary phosphines and their derivatives, Inorg. Chem., 30 (1991) 2380-2387.
- [106] A.L. Barra, J.B. Robert, Magnetic shielding tensor components in a highly strained phosphorus molecule: 1,2,3-triphenylphosphirene, Chem. Phys. Lett., 136 (1987) 224-226.
- [107] A. Marinetti, F. Mathey, J. Fischer, A. Mitschler, Synthesis and X-ray crystal structure of 1,2,3-triphenylphosphirene, Chem. Commun., (1984) 45-46.
- [108] A.L. Barra, J.B. Robert,  $^{31}P$  magnetic shielding tensor components of a phosphirane. angular dependence of the  $^{31}P$  magnetic shielding anisotropy, Chem. Phys. Lett., 149 (1988) 363-366.
- [109] R. Appel, T. Gaitzsch, F. Knoch, G. Lenz, Low coordinated phosphorus compounds. 45. mixed substituted bismethylenephosphoranes by the reaction of carbenoids with phosphalkenes, Chem. Ber., 119 (1986) 1977-1985.
- [110] S.J. Clark, M.D. Segall, C.J. Pickard, P.J. Hasnip, M.J. Probert, K. Refson, M.C. Payne, First principles methods using CASTEP, Z. Kristallogr., 220 (2005) 567-570.
- [111] R. Ditchfield, Self-consistent perturbation theory of diamagnetism, Mol. Phys., 27 (1974) 789-807.

- [112] J.R. Cheeseman, G.W. Trucks, T.A. Keith, M.J. Frisch, A comparison of models for calculating nuclear magnetic resonance shielding tensors, *J. Chem. Phys.*, 104 (1996) 5497-5509.
- [113] G. Schreckenbach, T. Ziegler, Calculation of NMR shielding tensors using gauge-including atomic orbitals and modern density functional theory, *J. Phys. Chem.*, 99 (1995) 606-611.
- [114] M.J. Frisch, G.W. Trucks, H.B. Schlegel, G.E. Scuseria, M.A. Robb, J.R. Cheeseman, G. Scalmani, V. Barone, B. Mennucci, G.A. Petersson, H. Nakatsuji, M. Caricato, X. Li, H.P. Hratchian, A.F. Izmaylov, J. Bloino, G. Zheng, J.L. Sonnenberg, M. Hada, M. Ehara, K. Toyota, R. Fukuda, J. Hasegawa, M. Ishida, T. Nakajima, Y. Honda, O. Kitao, H. Nakai, T. Vreven, J.A. Montgomery, J.E. Peralta, F. Ogliaro, M. Bearpark, J.J. Heyd, E. Brothers, K.N. Kudin, V.N. Staroverov, R. Kobayashi, J. Normand, K. Raghavachari, A. Rendell, J.C. Burant, S.S. Iyengar, J. Tomasi, M. Cossi, N. Rega, J.M. Millam, M. Klene, J.E. Knox, J.B. Cross, V. Bakken, C. Adamo, J. Jaramillo, R. Gomperts, R.E. Stratmann, O. Yazyev, A.J. Austin, R. Cammi, C. Pomelli, J.W. Ochterski, R.L. Martin, K. Morokuma, V.G. Zakrzewski, G.A. Voth, P. Salvador, J.J. Dannenberg, S. Dapprich, A.D. Daniels, Farkas, J.B. Foresman, J.V. Ortiz, J. Cioslowski, D.J. Fox, Gaussian 09, Revision B.01, Wallingford CT, 2009.
- [115] T.H. Dunning, Gaussian basis sets for use in correlated molecular calculations. I. the atoms boron through neon and hydrogen, *J. Chem. Phys.*, 90 (1989) 1007-1023.
- [116] D.E. Woon, T.H. Dunning, Gaussian basis sets for use in correlated molecular calculations. III. the atoms aluminum through argon, *J. Chem. Phys.*, 98 (1993) 1358-1371.
- [117] J.P. Perdew, Y. Wang, Accurate and simple analytic representation of the electron-gas correlation energy, *Phys. Rev. B*, 45 (1992) 13244.
- [118] J.P. Perdew, K. Burke, M. Ernzerhof, Generalized gradient approximation made simple, *Phys. Rev. Lett.*, 77 (1996) 3865-3868.
- [119] A.D. Becke, A new mixing of Hartree-Fock and local density-functional theories, *J. Chem. Phys.*, 98 (1993) 1372-1377.
- [120] C. Adamo, V. Barone, Toward reliable density functional methods without adjustable parameters: the PBE0 model, *J. Chem. Phys.*, 110 (1999) 6158-6170.
- [121] J.M. Tao, J.P. Perdew, V.N. Staroverov, G.E. Scuseria, Climbing the density functional ladder: nonempirical meta-generalized gradient approximation designed for molecules and solids, *Phys. Rev. Lett.*, 91 (2003) 146401.

- [122] M. Srebro, J. Autschbach, Computational analysis of  $^{47/49}\text{Ti}$  NMR shifts and electric field gradient tensors of half-titanocene complexes: structure–bonding–property relationships, *Chem. Eur. J.*, 19 (2013) 12018-12033.
- [123] F. Jensen, The basis set convergence of spin-spin coupling constants calculated by density functional methods, *J. Chem. Theory Comput.*, 2 (2006) 1360-1369.
- [124] F. Jensen, Basis set convergence of nuclear magnetic shielding constants calculated by density functional methods, *J. Chem. Theory Comput.*, 4 (2008) 719-727.
- [125] T. Kupka, B. Ruscic, R.E. Botto, Toward Hartree-Fock- and density functional complete basis-set-predicted NMR parameters, *J. Phys. Chem. A*, 106 (2002) 10396-10407.
- [126] T. Kupka, B. Ruscic, R.E. Botto, Hartree-Fock and density functional complete basis-set (CBS) predicted nuclear shielding anisotropy and shielding tensor components, *Solid State Nucl. Magn. Reson.*, 23 (2003) 145-167.
- [127] S. Moon, D.A. Case, A comparison of quantum chemical models for calculating NMR shielding parameters in peptides: mixed basis set and ONIOM methods combined with a complete basis set extrapolation, *J. Comput. Chem.*, 27 (2006) 825-836.
- [128] T.H. Sefzik, J.M. Fidler, R.J. Iulucci, J.C. Facelli, Modeling the  $^{13}\text{C}$  chemical-shift tensor in organic single crystals by quantum mechanical methods: finite basis set effects, *Magn. Reson. Chem.*, 44 (2006) 390-400.
- [129] D.B. Chesnut, K.D. Moore, Locally dense basis sets for chemical shift calculations, *J. Comput. Chem.*, 10 (1989) 648-659.
- [130] D.B. Chesnut, B.E. Rusiloski, K.D. Moore, D.A. Egolf, Use of locally dense basis sets for nuclear magnetic resonance shielding calculations, *J. Comput. Chem.*, 14 (1993) 1364-1375.
- [131] E. Zurek, C.J. Pickard, B. Walczak, J. Autschbach, Density functional study of the  $^{13}\text{C}$  NMR chemical shifts in small-to-medium-diameter infinite single-walled carbon nanotubes, *J. Phys. Chem. A*, 110 (2006) 11995-12004.
- [132] E. Zurek, C.J. Pickard, J. Autschbach, A density functional study of the  $^{13}\text{C}$  NMR chemical shifts in functionalized single-walled carbon nanotubes, *J. Am. Chem. Soc.*, 129 (2007) 4430-4439.
- [133] L.A. O'Dell, R.W. Schurko, K.J. Harris, J. Autschbach, C.I. Ratcliffe, Interaction tensors and local dynamics in common structural motifs of nitrogen: a solid-state  $^{14}\text{N}$  NMR and DFT study, *J. Am. Chem. Soc.*, 133 (2011) 527-546.

- [134] F. Jensen, Segmented contracted basis sets optimized for nuclear magnetic shielding, *J. Chem. Theory Comput.*, 11 (2015) 132-138.
- [135] A.A. Auer, J. Gauss, J.F. Stanton, Quantitative prediction of gas-phase  $^{13}\text{C}$  nuclear magnetic shielding constants, *J. Chem. Phys.*, 118 (2003) 10407-10417.
- [136] M.E. Harding, M. Lenhart, A.A. Auer, J. Gauss, Quantitative prediction of gas-phase  $^{19}\text{F}$  nuclear magnetic shielding constants, *J. Chem. Phys.*, 128 (2008) 244111.
- [137] E. Prochnow, A.A. Auer, Quantitative prediction of gas-phase  $^{15}\text{N}$  and  $^{31}\text{P}$  nuclear magnetic shielding constants, *J. Chem. Phys.*, 132 (2010) 064109.
- [138] G. Rauhut, S. Puyear, K. Wolinski, P. Pulay, Comparison of NMR shieldings calculated from Hartree-Fock and density functional wave functions using gauge-including atomic orbitals, *J. Phys. Chem.*, 100 (1996) 6310-6316.
- [139] A.M. Teale, O.B. Lutnæs, T. Helgaker, D.J. Tozer, J. Gauss, Benchmarking density-functional theory calculations of NMR shielding constants and spin-rotation constants using accurate coupled-cluster calculations, *J. Chem. Phys.*, 138 (2013) 024111.
- [140] R. Laskowski, P. Blaha, F. Tran, Assessment of DFT functionals with NMR chemical shifts, *Phys. Rev. B*, 87 (2013) 195130.
- [141] R. Laskowski, P. Blaha, Understanding of  $^{33}\text{S}$  NMR shielding in inorganic sulfides and sulfates, *J. Phys. Chem. C*, 119 (2015) 731-740.
- [142] D.E. Hill, N. Vasdev, J.P. Holland, Evaluating the accuracy of density functional theory for calculating  $^1\text{H}$  and  $^{13}\text{C}$  NMR chemical shifts in drug molecules, *Comp. Theor. Chem.*, 1051 (2015) 161-172.
- [143] T.W. Keal, D.J. Tozer, T. Helgaker, GIAO shielding constants and indirect spin-spin coupling constants: performance of density functional methods, *Chem. Phys. Lett.*, 391 (2004) 374-379.
- [144] T.W. Keal, T. Helgaker, P. Sałek, D.J. Tozer, Choice of exchange-correlation functional for computing NMR indirect spin-spin coupling constants, *Chem. Phys. Lett.*, 425 (2006) 163-166.
- [145] J. San Fabian, J.M.G. de la Vega, E. San Fabian, Improvements in DFT calculations of spin-spin coupling constants, *J. Chem. Theory Comput.*, 10 (2014) 4938-4949.
- [146] Y. Zhao, D.G. Truhlar, Improved description of nuclear magnetic resonance chemical shielding constants using the M06-L meta-generalized-gradient-approximation density functional, *J. Phys. Chem. A*, 112 (2008) 6794-6799.

- [147] T.H. Sefzik, D. Turco, R.J. Iuliucci, J.C. Facelli, Modeling NMR chemical shift: a survey of density functional theory approaches for calculating tensor properties, *J. Phys. Chem. A*, 109 (2005) 1180-1187.
- [148] A.J. Robbins, W.T.K. Ng, D. Jochym, T.W. Keal, S.J. Clark, D.J. Tozer, P. Hodgkinson, Combining insights from solid-state NMR and first principles calculation: applications to the  $^{19}\text{F}$  NMR of octafluoronaphthalene, *Phys. Chem. Chem. Phys.*, 9 (2007) 2389-2396.
- [149] J.K. Harper, R. Iuliucci, M. Gruber, K. Kalakewich, Refining crystal structures with experimental  $^{13}\text{C}$  NMR shift tensors and lattice-including electronic structure methods, *CrystEngComm*, 15 (2013) 8693-8704.
- [150] J. Czernek, T. Pawlak, M.J. Potrzebowski, Benchmarks for the  $^{13}\text{C}$  NMR chemical shielding tensors in peptides in the solid state, *Chem. Phys. Lett.*, 527 (2012) 31-35.
- [151] J. Czernek, T. Pawlak, M.J. Potrzebowski, J. Brus, The comparison of approaches to the solid-state NMR-based structural refinement of vitamin B-1 hydrochloride and of its monohydrate, *Chem. Phys. Lett.*, 555 (2013) 135-140.
- [152] T. Pawlak, M. Jaworska, M.J. Potrzebowski, NMR crystallography of  $\alpha$ -poly(L-lactide), *Phys. Chem. Chem. Phys.*, 15 (2013) 3137-3145.
- [153] S.T. Holmes, R.J. Iuliucci, K.T. Mueller, C. Dybowski, Density functional investigation of intermolecular effects on  $^{13}\text{C}$  NMR chemical-shielding tensors modeled with molecular clusters, *J. Chem. Phys.*, 141 (2014) 164121.
- [154] J.D. Hartman, S. Monaco, B. Schatschneider, G.J.O. Beran, Fragment-based  $^{13}\text{C}$  nuclear magnetic resonance chemical shift predictions in molecular crystals: an alternative to planewave methods, *J. Chem. Phys.*, 143 (2015) 102809.
- [155] F. Alkan, C. Dybowski, Chemical-shift tensors of heavy nuclei in network solids: a DFT/ZORA investigation of  $^{207}\text{Pb}$  chemical-shift tensors using the bond-valence method, *Phys. Chem. Chem. Phys.*, 17 (2015) 25014-25026.
- [156] J.C. Johnston, R.J. Iuliucci, J.C. Facelli, G. Fitzgerald, K.T. Mueller, Intermolecular shielding contributions studied by modeling the  $^{13}\text{C}$  chemical-shift tensors of organic single crystals with plane waves, *J. Chem. Phys.*, 131 (2009) 144503.
- [157] A.K. Jameson, C.J. Jameson, Gas-phase  $^{13}\text{C}$  chemical shifts in the zero-pressure limit: refinements to the absolute shielding scale for  $^{13}\text{C}$ , *Chem. Phys. Lett.*, 134 (1987) 461-466.

- [158] C.J. Jameson, A.K. Jameson, D. Oppusunggu, S. Wille, P.M. Burrell, J. Mason,  $^{15}\text{N}$  nuclear magnetic shielding scale from gas phase studies, *J. Chem. Phys.*, 74 (1981) 81-88.
- [159] A. Sadoc, M. Body, C. Legein, M. Biswal, F. Fayon, X. Rocquefelte, F. Boucher, NMR parameters in alkali, alkaline earth and rare earth fluorides from first principle calculations, *Phys. Chem. Chem. Phys.*, 13 (2011) 18539-18550.
- [160] C.J. Jameson, A.K. Jameson, P.M. Burrell,  $^{19}\text{F}$  nuclear magnetic shielding scale from gas phase studies, *J. Chem. Phys.*, 73 (1980) 6013-6020.
- [161] C.J. Jameson, A. De Dios, A.K. Jameson, Absolute shielding scale for  $^{31}\text{P}$  from gas-phase NMR studies, *Chem. Phys. Lett.*, 167 (1990) 575-582.

## Chapter 5

### CALCULATIONS OF SOLID-STATE $^{43}\text{Ca}$ NMR PARAMETERS: A COMPARISON OF PERIODIC AND CLUSTER-BASED APPROACHES AND AN EVALUATION OF DFT FUNCTIONALS

#### 5.1 Introduction

Measurements of  $^{43}\text{Ca}$  ( $I = 7/2$ ) solid-state NMR parameters, specifically chemical-shift and quadrupolar-coupling tensors, have grown in popularity over the past decade [1-22]. The difficulties associated with these measurements have, to some extent, been overcome with the advent of ultrahigh-field NMR spectroscopy and the development of radio-frequency pulse sequences that enhance weak signals from nuclides with low natural abundances and low magnetogyric ratios. Two recent accounts of advances in  $^{43}\text{Ca}$  solid-state NMR have been provided by Bryce [5] and by Laurencin and Smith [17].

$^{43}\text{Ca}$  NMR spectroscopy is important in structural characterization and elucidation because of the prevalence of calcium in biological systems and materials. For example,  $^{43}\text{Ca}$  NMR spectroscopy has been used to identify the proper space group of the vaterite phase of  $\text{CaCO}_3$  [7] and to distinguish between the two inequivalent  $^{43}\text{Ca}$  sites of hydroxyapatite [15]. Calcium dibenzoate trihydrate has been studied as a model compound for calcium binding sites in proteins [9]. Methods have been proposed to measure distances between  $^{43}\text{Ca}$  and  $^1\text{H}$  nuclear sites [16]. Solid-state  $^{43}\text{Ca}$  studies have been paired with molecular-dynamics simulations to study the distribution of structural features in amorphous  $\text{CaCO}_3$  [14]. The link between experimental NMR parameters and structure is often aided by advanced computational techniques. Benchmark studies on model compounds are inherently useful as they can gauge the accuracy of NMR

parameters obtained by a computational approach and give insights into the validity of the technique for structural investigations.

Calculated magnetic-shielding tensors depend substantially on the model chemistry used in the analysis, including basis set, pseudopotential, and treatment of the exchange and correlation terms in the Hamiltonian [23]. In principle, better agreement with experimental values can be obtained when the optimal model chemistry is employed. Survey of a wide array of model chemistries for  $^{43}\text{Ca}$  is important because several studies have noted difficulties associated with the prediction of NMR parameters of  $^{43}\text{Ca}$  sites, or of nearby sites in the same material [11, 24] when limited and selected model chemistries were used. For example, the calculations presented in reference [11] suggest a systematic overestimation of  $^{43}\text{Ca}$  chemical shifts associated with the PBE functional and Profeta *et al.* report inability of the PBE functional to predict  $^{17}\text{O}$  quadrupolar coupling in CaO [24].

To the authors' knowledge, no systematic study has been undertaken to investigate model-chemistry effects on computed  $^{43}\text{Ca}$  NMR parameters. This paper presents the results of a series of calculations of  $^{43}\text{Ca}$  magnetic-shielding and quadrupolar-coupling tensors using Hartree-Fock self-consistent field (HF-SCF) theory and seventeen density-functional theory (DFT) methods. The DFT methods are based on the local-density approximation (LDA), the generalized-gradient approximation (GGA), the meta-generalized-gradient approximation (meta-GGA), and hybrid methods. Cluster-based techniques for modeling magnetic-shielding tensors in crystalline solids, which account for extended lattice effects without employing periodic-boundary conditions, have expanded the range of computational methods that can be applied to structural problems [23, 25-33]. Since Hartree-Fock exchange is

difficult to implement in periodic calculations, we also illustrate the use of cluster models for calculating  $^{43}\text{Ca}$  NMR parameters.

## 5.2 Computational Details

### 5.2.1 Materials and Computational Protocols

Benchmark calculations were based on materials that have been characterized previously through X-ray or neutron diffraction and through solid-state  $^{43}\text{Ca}$  NMR spectroscopy. The principal components of the  $^{43}\text{Ca}$  chemical-shift and quadrupolar-coupling tensors have been reported for each of these materials. The materials are calcium formate, calcium acetate monohydrate (two unique calcium sites), calcium tartrate tetrahydrate, calcium dibenzoate trihydrate, the calcite and aragonite phases of  $\text{CaCO}_3$ ,  $\text{Ca}(\text{NO}_3)_2$ ,  $\text{CaSO}_4 \cdot 2\text{H}_2\text{O}$ , and  $\text{CaCl}_2 \cdot 2\text{H}_2\text{O}$  (Table 5.1). Experimental NMR parameters have been reported in references [8, 11]. For  $\text{Ca}(\text{NO}_3)_2$ , the averages of the fractional atomic coordinates and lattice constants of two X-ray structures were used, as no modern structural determination was available. For the hydrates, the positions of the hydrogen atoms were refined through a plane-wave geometry optimization at the PBE level, while the positions of all heavier atoms remained fixed in their experimentally-determined positions (see details on plane-wave DFT calculations below).

**Table 5.1.** Model cluster compositions for the materials used in this study.

Material	Cluster Composition	Space Group	Reference
Ca formate	$[\text{Ca}_4(\text{form})_6(\text{OH})_{12}]^{10-}$	<i>Pbca</i>	[34]
Ca acetate·H <sub>2</sub> O (Ca1)	$[\text{Ca}_4(\text{acet})_6(\text{H}_2\text{O})_4(\text{OH})_8]^{6-}$	$P\bar{1}$	[35]
Ca acetate·H <sub>2</sub> O (Ca2)	$[\text{Ca}_3(\text{acet})_4(\text{H}_2\text{O})_2(\text{OH})_9]^{7-}$		
Ca tartrate·4H <sub>2</sub> O	$[\text{Ca}(\text{tart})_4(\text{H}_2\text{O})_2]^{6-}$	<i>P2<sub>1</sub>2<sub>1</sub>2<sub>1</sub></i>	[36]
Ca dibenzoate·3H <sub>2</sub> O	$[\text{Ca}_3(\text{benz})_3(\text{H}_2\text{O})_{10}(\text{OH})_2]^+$	<i>P2<sub>1</sub>/c</i>	[37]
CaCO <sub>3</sub> (calcite)	$[\text{Ca}_7(\text{CO}_3)_8(\text{H}_2\text{O})_{18}]^{2-}$	<i>R<math>\bar{3}c</math></i>	[38]
CaCO <sub>3</sub> (aragonite)	$[\text{Ca}_{13}(\text{CO}_3)_{12}\text{O}_6(\text{H}_2\text{O})_{33}]^{10-}$	<i>Pnma</i>	[39]
Ca(NO <sub>3</sub> ) <sub>2</sub>	$[\text{Ca}(\text{NO}_3)_6]^{4-}$	<i>Pa<math>\bar{3}</math></i>	[40, 41]
CaSO <sub>4</sub> ·2H <sub>2</sub> O	$[\text{Ca}_3(\text{SO}_4)_4(\text{H}_2\text{O})_6(\text{OH})_6]^{8-}$	<i>C2/c</i>	[42]
CaCl <sub>2</sub> ·2H <sub>2</sub> O	$[\text{Ca}_5\text{Cl}_{16}(\text{H}_2\text{O})_{24}]^{6-}$	<i>Pbcn</i>	[43]

Calculations of <sup>43</sup>Ca NMR parameters were carried out using both periodic and cluster-based approaches. The former set of calculations used the gauge-including-projector-augmented-wave (GIPAW) method of Pickard and Mauri [44] as implemented in the CASTEP module of Accelrys' Materials Studio 7.0 [45]. GIPAW calculations employed ultrasoft pseudopotentials generated *on the fly* to replace core orbitals [46]. Additional considerations include a plane-wave cutoff energy of 600 eV and integration over the Brillouin zone using an ultra-fine *k*-point spacing. Convergence of the computed NMR parameters was verified by additional calculations with higher cutoff energies and finer *k*-point grids for integration. GIPAW calculations employed

the following functionals: CA-PZ [47, 48], PW91 [49], PBE [50], rPBE [51], PBEsol [52], and WC [53].

Cluster-based approaches to model lattice effects for the prediction of NMR parameters have been discussed previously [23, 25-33, 54-58]. In this work, clusters were constructed by expanding to the 3<sup>rd</sup> co-ordination shell of atoms around the central <sup>43</sup>Ca site. For the calcium carboxylates, ligands were not truncated, so that atoms beyond the 3<sup>rd</sup> co-ordination shell were included in the clusters for calcium tartrate tetrahydrate and calcium dibenzoate trihydrate. Hydrogen atoms were attached to the terminal oxygen sites using a standard Ca-O bond length of 0.96 Å and a standard Ca-O-H bond angle of 109.5°, to assure SCF convergence. Coordinates for all atoms in the clusters are provided in the supporting information. A summary of the compositions of all model clusters is given in Table 5.1 and illustrations of several example clusters are shown in Figure 5.1.

Long-range electrostatic effects in the cluster calculations were modeled using the self-consistent-reaction-field (SCRF) polarizable-continuum model (PCM) [59, 60]. Specifically, the integral-equation formalism with atomic radii and non-Coulomb terms computed by the SMD algorithm of Truhlar and co-workers was used [61]. Water was used as the solvent in these calculations. Dunning's correlation-consistent basis sets cc-pVTZ were used for the NMR-active <sup>43</sup>Ca site and the 1<sup>st</sup> co-ordination shell of atoms, whereas all other atoms used the less flexible basis set cc-pVDZ [62, 63]. Magnetic shielding was calculated within the gauge-including-atomic-orbital (GIAO) formalism [64]. Magnetic-shielding and quadrupolar-coupling tensors were computed using Hartree-Fock theory and the following DFT methods: SVWN [65-68], PBE [50], PW91 [49], PKZB [69], TPSS [70], M06-L [71], B3PW91 [72], PBE0 [73], TPSSh [70], BMK

[74], M06 [75], M06-2X [75], and M06-HF [76, 77]. All cluster-based calculations were performed using GAUSSIAN 09 [78].

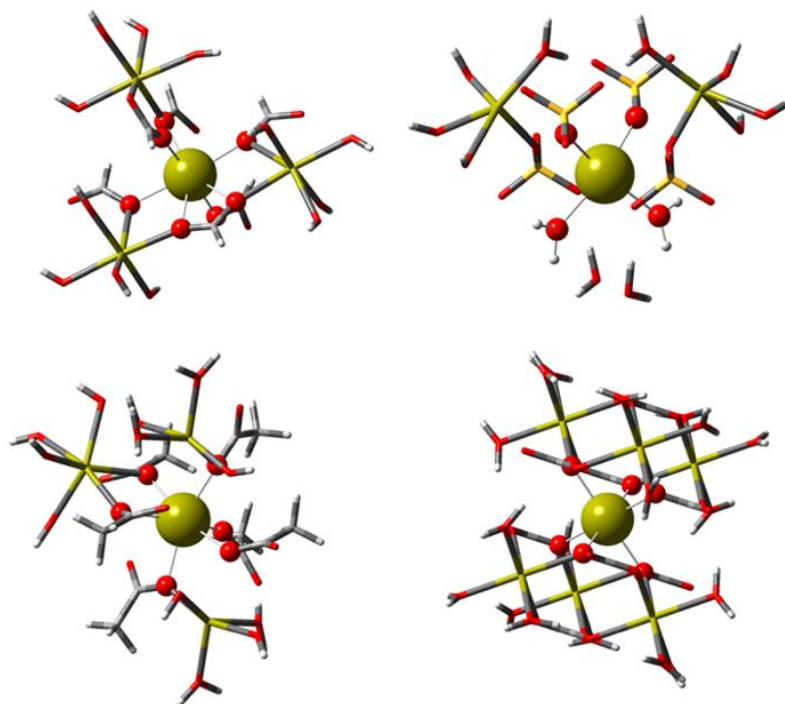


**Figure 5.1.** Schematic drawings showing clusters of calcium formate (upper left), calcium acetate site Ca1 (lower left),  $\text{CaSO}_4 \cdot 2\text{H}_2\text{O}$  (upper right), and calcite (lower right). The cc-pVTZ region is shown in the ball-and-stick representation and the cc-pVDZ region is shown in the wireframe representation.

### 5.2.2 Conventions for Reporting NMR Parameters

The magnetic-shielding interaction is characterized by a second-rank tensor with principal values  $\sigma_{33} \geq \sigma_{22} \geq \sigma_{11}$ . An NMR experiment yields a shift in resonance frequency relative to a reference material rather than the magnetic shielding relative to

the bare nucleus. In this work, calculated  $^{43}\text{Ca}$  magnetic shielding was converted to the  $^{43}\text{Ca}$  chemical-shift scale by the following relationship:

$$\delta_{calc} = \sigma_{ref} - \sigma_{calc}. \quad (\text{Eq. 5.1})$$

In the above equation,  $\sigma_{calc}$  is the calculated magnetic shielding,  $\delta_{calc}$  is the calculated chemical shift, and  $\sigma_{ref}$  is the calculated magnetic shielding of the reference compound (typically, a 1.0 M solution of  $\text{CaCl}_2$  in  $\text{H}_2\text{O}$ ) [5]. In practical analysis, the correlation between calculated  $^{43}\text{Ca}$  magnetic shielding and experimental  $^{43}\text{Ca}$  chemical shift is modeled by the two linear-regression parameters,  $\sigma_{ref}$  and  $|m|$ :

$$\sigma_{calc} = \sigma_{ref} - |m|\delta_{exp}. \quad (\text{Eq. 5.2})$$

In this equation,  $\delta_{exp}$  is the experimental chemical shift,  $|m|$  is the slope of the correlation line, and  $\sigma_{ref}$  is treated as a fitting parameter which varies with the model chemistries. If the value of  $|m|$  is significantly greater than 1, the computational model yields chemical shifts, as defined in Eq. 5.1, that are systematically overestimated relative to experimental chemical shifts.

The electric-field gradient (EFG) at a nucleus is described by a traceless, second-rank tensor with principal values  $|V_{33}| \geq |V_{22}| \geq |V_{11}|$ . Because the tensor is traceless, it can be described by two parameters, namely the quadrupolar-coupling constant,  $C_Q$ , and the asymmetry parameter,  $\eta$ :

$$C_Q = eV_{33}Q/h, \quad (\text{Eq. 5.3})$$

$$\eta = (V_{11} - V_{22})/V_{33}. \quad (\text{Eq. 5.4})$$

In the above expressions,  $e$  is the elementary charge,  $h$  is Planck's constant, and  $Q$  is the  $^{43}\text{Ca}$  quadrupole moment ( $Q = -4.08 \text{ fm}^2$ ). The sign of  $C_Q$  cannot be determined experimentally, so the absolute value of  $C_Q$  is reported. For the purpose of analysis, we have assumed that the sign of the experimental value of  $C_Q$  is the same as the value

predicted by the calculations. Equivalently, the quadrupolar-coupling tensor can be specified by two unique principal values. Residuals between calculated and experimental  $^{43}\text{Ca}$  NMR parameters are based on differences between the principal values of the tensors.

## 5.3 Results and Discussion

### 5.3.1 Comparison of GIPAW and Cluster-Based Calculations

The PBE functional was used in all calculations to compare the results of GIPAW and cluster-based approaches. In addition to the elimination of translational symmetry elements, expansion of a cluster around the central  $^{43}\text{Ca}$  nucleus can also result in the loss of local point-group symmetry. This loss of local symmetry may be reflected strongly in computed magnetic-shielding and quadrupolar-coupling tensors. First, we demonstrate the convergence of computed  $^{43}\text{Ca}$  magnetic-shielding and quadrupolar-coupling tensors as a function of cluster size in  $\text{CaCl}_2 \cdot 2\text{H}_2\text{O}$  and  $\text{Ca}(\text{NO}_3)_2$ . Three clusters of  $\text{CaCl}_2 \cdot 2\text{H}_2\text{O}$  of increasing size are shown in Figure 5.2. Table 5.2 summarizes calculated  $^{43}\text{Ca}$  NMR parameters in the clusters of the two solids. For both the  $^{43}\text{Ca}$  magnetic-shielding and quadrupolar-coupling tensors, there are large differences between computed results for the 1<sup>st</sup>- and 3<sup>rd</sup>-co-ordination-shell clusters, whereas the 3<sup>rd</sup>- and 5<sup>th</sup>-co-ordination-shell clusters yield similar values. The mean-absolute errors (MAEs) between experimental values and those obtained from the two largest clusters (3<sup>rd</sup>- and 5<sup>th</sup>-co-ordination-shell clusters) are substantially smaller than the MAEs for the 1<sup>st</sup>-co-ordination-shell clusters (Table 5.2). This characteristic difference is particularly evident in the chemical-shift span ( $\Omega = \delta_{11} - \delta_{33}$ ) of  $\text{Ca}(\text{NO}_3)_2$ , which is reported as 11.4 ppm experimentally [5], but is predicted to be 675 ppm by

calculation on the 1<sup>st</sup>-co-ordination-shell cluster. The spans obtained with the larger clusters agree better with the experimental span, with the 3<sup>rd</sup>-co-ordination-shell calculation yielding  $\Omega = 10.9$  ppm and the 5<sup>th</sup>-co-ordination-shell calculation yielding  $\Omega = 25.4$  ppm. The span predicted using GIPAW falls between the span of the two large cluster calculations, with  $\Omega = 15.0$  ppm. Based on these observations, and those of earlier work [26, 29-31], we used 3<sup>rd</sup>-co-ordination-shell clusters in all subsequent calculations because clusters of this size appear to conserve sufficiently the local point-group symmetry of the calcium sites.

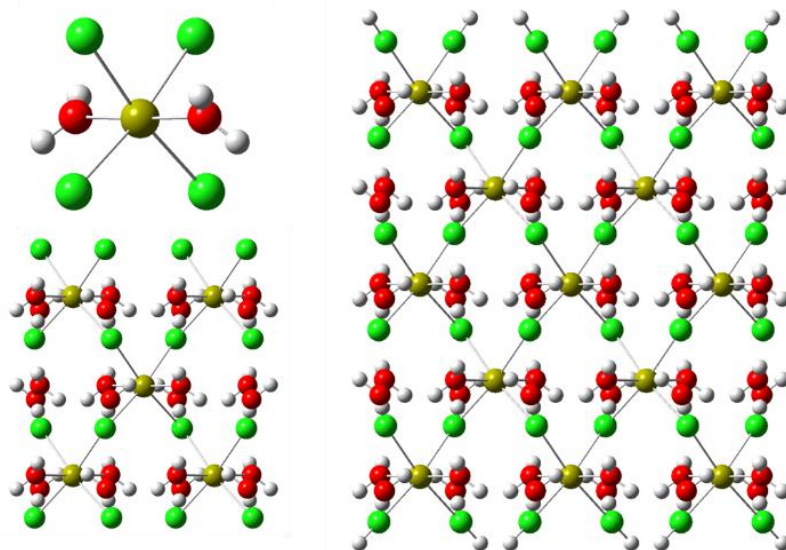


**Figure 5.2.** Illustration of three clusters to represent the local  $^{43}\text{Ca}$  environment in  $\text{CaCl}_2 \cdot 2\text{H}_2\text{O}$ . Upper left: 1<sup>st</sup>-co-ordination shell cluster with composition  $[\text{CaCl}_4(\text{H}_2\text{O})_2]^{2-}$ . Lower left: 3<sup>rd</sup>-co-ordination shell cluster with composition  $[\text{Ca}_5\text{Cl}_{16}(\text{H}_2\text{O})_{24}]^{6-}$ . Right: 5<sup>th</sup>-co-ordination shell cluster with composition  $[\text{Ca}_{13}\text{Cl}_{36}\text{H}_{12}(\text{H}_2\text{O})_{56}]^{2+}$ .

**Table 5.2.** Experimental and calculated  $^{43}\text{Ca}$  NMR parameters using the cluster-based approach, with results obtained from clusters of increasing size, and MAEs<sup>a</sup> from experimental results. All results were obtained at the PBE level.

Model Cluster	Cluster Composition	$\delta_{11}$ (ppm)	$\delta_{22}$ (ppm)	$\delta_{33}$ (ppm)	$\Omega$ (ppm)	MAE (ppm)	$C_Q$ (MHz)	$\eta$	MAE (MHz)
<b>CaCl<sub>2</sub>·2H<sub>2</sub>O</b>									
Exp.	-	63.9	46.1	43.6	20.3	-	2.62	0.22	-
First shell	[CaCl <sub>4</sub> (H <sub>2</sub> O) <sub>2</sub> ] <sup>2-</sup>	133.7	86.1	66.8	66.9	48.3	0.94	0.94	0.85
Third shell	[Ca <sub>5</sub> Cl <sub>16</sub> (H <sub>2</sub> O) <sub>24</sub> ] <sup>6-</sup>	89.2	68.8	60.8	28.4	22.0	2.66	0.19	0.04
Fifth shell	[Ca <sub>13</sub> Cl <sub>36</sub> H <sub>12</sub> (H <sub>2</sub> O) <sub>56</sub> ] <sup>2+</sup>	97.1	70.9	60.4	36.7	25.8	2.59	0.26	0.05
<b>Ca(NO<sub>3</sub>)<sub>2</sub></b>									
Exp.	-	-47.1	-47.1	-58.5	11.4	-	1.57	0.00	-
First shell	[CaO <sub>12</sub> ] <sup>22-</sup>	50.3	-109.2	-624.5	674.8	333.5	2.30	0.04	0.37
Third shell	[Ca(NO <sub>3</sub> ) <sub>6</sub> ] <sup>4+</sup>	-79.7	-79.7	-90.6	10.9	32.4	1.69	0.00	0.06
Fifth shell	[Ca <sub>13</sub> (NO <sub>3</sub> ) <sub>8</sub> O <sub>12</sub> (H <sub>2</sub> O) <sub>42</sub> ] <sup>6-</sup>	-	-	-	-	-	-	-	-
		-65.8	-65.8	-91.2	25.4	24.3	1.51	0.00	0.03

<sup>a</sup>Mean-absolute errors

Figures 5.3a and 5.3b display the relationship between principal components of calculated  $^{43}\text{Ca}$  magnetic-shielding tensors and principal components of experimental  $^{43}\text{Ca}$  chemical-shift tensors for the ten calcium sites listed in Table 5.1. Results were obtained respectively with the GIPAW approach and the cluster-based approach. The data are modeled according to Eq. 5.2 with least-squares linear regression, yielding the following relations:

$$\sigma_{GIPAW} = (1140 \pm 2) \text{ ppm} - (1.35 \pm 0.06)\delta_{exp}, \quad (\text{Eq. 5.5})$$

$$\sigma_{cluster} = (1147 \pm 2) \text{ ppm} - (1.37 \pm 0.07)\delta_{exp}. \quad (\text{Eq. 5.6})$$

The slopes of the correlation lines are essentially identical, and the difference in the reference shielding constants between the two computational methods is consistent with a finite-basis-set effect [23]. The two methods yield MAEs between calculated and experimental chemical shifts of 14 ppm and 15 ppm, respectively. The largest residuals in both computational methods arise from Ca(NO<sub>3</sub>)<sub>2</sub>, an error which has been discussed

elsewhere [11]. The slopes ( $|m| = 1.35 \pm 0.06$  and  $|m| = 1.37 \pm 0.07$  for GIPAW and cluster calculations, respectively) relative to the ideal case (unity) suggests a substantial overestimation of the paramagnetic contribution to the magnetic-shielding tensor by the PBE functional [79]. It has been illustrated for many 1<sup>st</sup>- and 2<sup>nd</sup>-period nuclei that such systematic errors can be partially eliminated by a judicious selection of a more appropriate model chemistry [23, 26]. This consideration is addressed in the following subsections.

Figures 5.3c and 5.3d display the relationship between the calculated and experimental principal components of  $^{43}\text{Ca}$  quadrupolar-coupling tensors for the GIPAW and the cluster-based approaches, respectively. As was the case with the computed magnetic-shielding tensors, both computational approaches yield similar agreement with experiment, with MAEs of 0.14 MHz and 0.16 MHz for the GIPAW and cluster-based methodologies, respectively. One advantage of periodic calculations of quadrupolar-coupling tensors is the ability to model accurately long-range electronic interactions that can potentially contribute to the EFG near the nucleus. The present results indicate that the loss of accuracy in computed quadrupolar-coupling tensors, when modeling the lattice with an appropriately designed cluster and with approximate treatment of long-range interactions (*via* the polarization continuum model), is marginal.

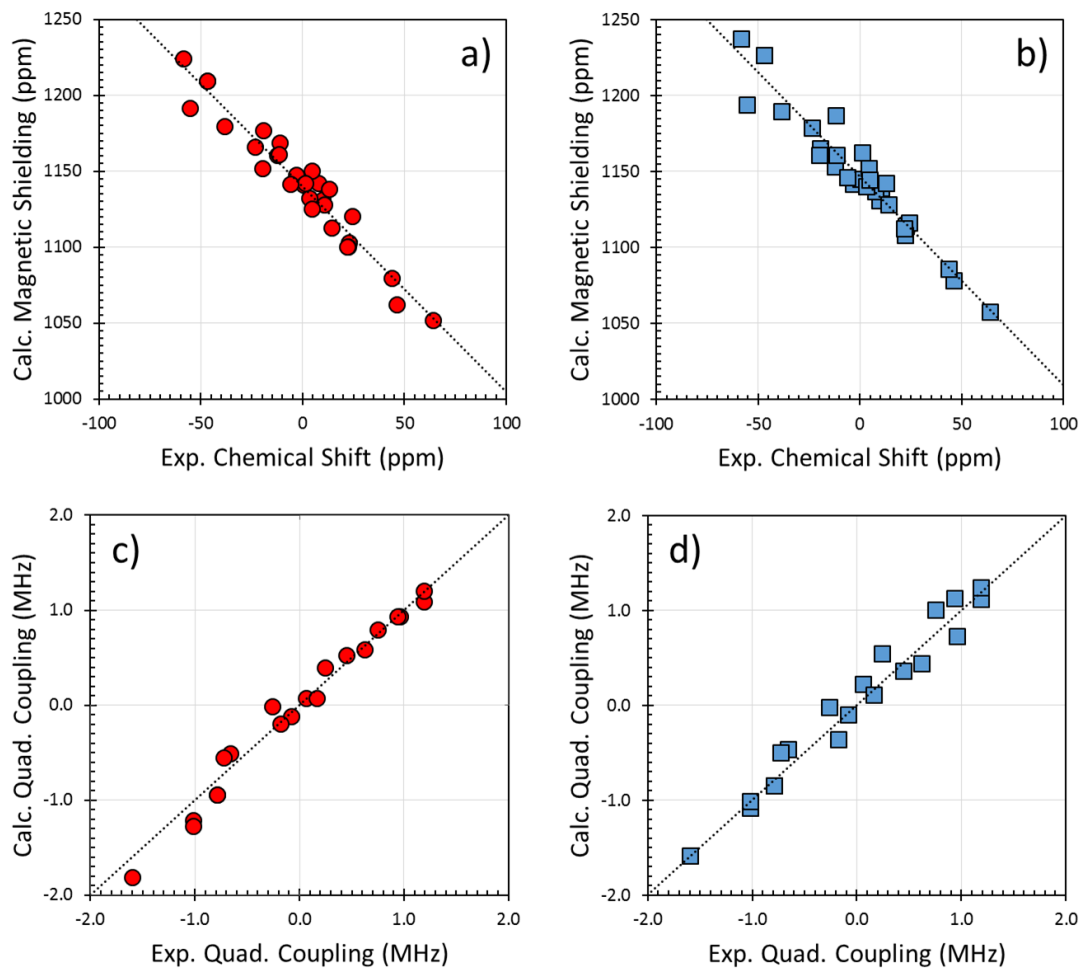


**Figure 5.3.** Plots illustrating the relationship between principal components of calculated  $^{43}\text{Ca}$  magnetic-shielding tensors and experimental chemical-shift tensors obtained using (a) the periodic GIPAW approach and (b) the cluster approach. Plots illustrating the relationship between principal components of calculated and experimental  $^{43}\text{Ca}$  quadrupolar-coupling tensors obtained using (c) the periodic GIPAW approach and (d) the cluster approach. Results were computed at the PBE level of theory with a plane-wave cutoff energy of 600 eV (GIPAW) or with the cc-pVTZ basis set (clusters). Best-fit lines (a,b) and ideal (c,d) relationships are shown as dotted black lines.

### 5.3.2 Discussion of GIPAW Calculations

GIPAW calculations of magnetic shielding are generally restricted to LDA and GGA functionals. Table 5.3 summarizes the results obtained from the LDA functional CA-PZ and the GGA functionals PBE, PW91, rPBE, PBEsol, and WC. MAEs for the computed  $^{43}\text{Ca}$  chemical-shift tensors range between 13 ppm (rPBE) and 20 ppm (CA-PZ). MAEs for quadrupolar-coupling tensors range between 0.10 MHz (rPBE) and 0.15 MHz (CA-PZ). All functionals lead to a substantial overestimation of chemical shifts, as reflected by the value of  $|m|$ . The best results for  $^{43}\text{Ca}$  chemical shifts were obtained by rPBE ( $|m| = 1.30 \pm 0.06$ ) and the worst results were obtained by CA-PZ ( $|m| = 1.50 \pm 0.07$ ). The order of decreasing chemical-shift tensor MAEs is CA-PZ > PBEsol > WC > PW91 > PBE > rPBE. The same ranking of these six functionals has been reported for  $^{29}\text{Si}$  and  $^{31}\text{P}$  chemical-shift tensors, except the order of PBEsol and WC is reversed [26].

**Table 5.3.** Linear-regression parameters ( $\sigma_{ref}$  and  $|m|$ ) and statistical data (MAE,<sup>a</sup> Max.<sup>b</sup>) associated with the correlations of principal values of calculated  $^{43}\text{Ca}$  magnetic-shielding tensors and experimental  $^{43}\text{Ca}$  chemical-shift tensors and of calculated and experimental  $^{43}\text{Ca}$  quadrupolar-coupling tensors obtained from six plane-wave DFT methods.

Method	$\sigma_{ref}$ (ppm)	Magnetic Shielding		$ m $	Quadrupolar Coupling	
		MAE (ppm)	Max. (ppm)		MAE (MHz)	Max. (MHz)
CA-PZ	$1111 \pm 2$	20	43	$1.50 \pm 0.07$	0.15	0.34
PBEsol	$1129 \pm 2$	16	35	$1.41 \pm 0.06$	0.13	0.26
WC	$1130 \pm 2$	16	35	$1.41 \pm 0.07$	0.12	0.26
PW91	$1140 \pm 2$	15	32	$1.36 \pm 0.06$	0.13	0.26
PBE	$1140 \pm 2$	14	32	$1.35 \pm 0.06$	0.14	0.25
rPBE	$1153 \pm 2$	13	27	$1.30 \pm 0.06$	0.10	0.19

<sup>a</sup>Mean absolute error. <sup>b</sup>Maximum error.

### 5.3.3 Discussion of Cluster-Based Calculations

Cluster-based predictions of  $^{43}\text{Ca}$  NMR parameters have been carried out using a variety of DFT functionals, as summarized in Table 5.4. MAEs of computed chemical shifts range between 13 ppm (TPSSh) and 51 ppm (M06-HF), whereas MAEs for the computed quadrupolar coupling range between 0.16 MHz (PBE, PW91, and TPSS) and 0.29 MHz (BMK). As is the case for the GIPAW calculations, all methods systematically overestimate chemical shifts. However, there are cases in which individual chemical shifts have very large errors (up to 141 ppm for the M06-HF functional, for example), as reflected in the large uncertainties in  $|m|$ . For the functionals with poor agreement with experimental  $^{43}\text{Ca}$  chemical-shift tensors (particularly M06-HF), the largest errors are associated with the two polymorphs of  $\text{CaCO}_3$ .

We note three significant trends in the results. First, for the series of closely-related pure DFT functionals SVWN, PBE, and TPSS, which represent the LDA, GGA, and meta-GGA classes of functionals, respectively, there is systematic improvement of agreement of predicted  $^{43}\text{Ca}$  NMR parameters with experiment in the order SVWN < PBE < TPSS. The extrapolated shielding of the reference compound also changes in this series, with the three functionals yielding values for  $\sigma_{ref}$  of  $1124 \pm 2$  ppm,  $1147 \pm 2$  ppm, and  $1159 \pm 2$  ppm, respectively. Second, the hybrid functionals seem to outperform their pure DFT analogs for the prediction of  $^{43}\text{Ca}$  chemical shifts, as is indicated by the functional pairs PBE and PBE0, PW91 and B3PW91, and TPSS and TPSSh. However, this trend is notably absent in the Minnesota functionals, where the best agreement with experiment is obtained with M06-L and the worst agreement with M06-HF. Finally, there is a weak positive correlation between MAEs in the computed chemical shifts and MAEs in the computed quadrupolar couplings. For example, the

functionals M06-HF, M06-2X, and BMK are poor performers for predicting both of these parameters.

**Table 5.4.** Linear-regression parameters ( $\sigma_{ref}$  and  $|m|$ ) and statistical data (MAE,<sup>a</sup> Max.<sup>b</sup>) associated with the correlations of principal values of calculated <sup>43</sup>Ca magnetic-shielding tensors and experimental <sup>43</sup>Ca chemical-shift tensors and of calculated and experimental <sup>43</sup>Ca quadrupolar-coupling tensors obtained from thirteen DFT methods in cluster-based calculations.

Method	$\sigma_{ref}$ (ppm)	Magnetic Shielding		$ m $	Quadrupolar Coupling	
		MAE (ppm)	Max. (ppm)		MAE (MHz)	Max. (MHz)
M06-HF	1191 ± 9	51	141	1.05 ± 0.31	0.25	0.66
BMK	1201 ± 6	30	69	1.12 ± 0.19	0.29	0.65
M06-2X	1182 ± 5	25	67	1.19 ± 0.16	0.26	0.73
PKZB	1184 ± 3	22	58	1.48 ± 0.11	0.17	0.33
SVWN	1124 ± 2	18	41	1.51 ± 0.06	0.21	0.63
M06	1180 ± 2	17	39	1.45 ± 0.07	0.23	0.45
M06-L	1176 ± 3	17	50	1.31 ± 0.09	0.21	0.47
PW91	1145 ± 2	16	34	1.35 ± 0.07	0.16	0.31
PBE	1147 ± 2	15	33	1.37 ± 0.07	0.16	0.31
B3PW91	1178 ± 2	14	32	1.32 ± 0.06	0.17	0.30
PBE0	1184 ± 2	13	30	1.32 ± 0.06	0.20	0.54
TPSS	1159 ± 2	13	27	1.30 ± 0.06	0.16	0.29
TPSSh	1173 ± 2	13	28	1.28 ± 0.06	0.21	0.61

<sup>a</sup>Mean absolute error. <sup>b</sup>Maximum error.

Inspired by the fact that hybrid functionals outperform their pure DFT analogs for the prediction of <sup>43</sup>Ca chemical shifts, the same calculations were carried out at the Hartree-Fock level (Table 5.6). It is apparent that the Hartree-Fock results outperform the DFT methods (Tables 5.3 and 5.4) for the prediction of <sup>43</sup>Ca chemical-shift tensors. A summary of the twenty model chemistries (six plane-wave DFT methods, thirteen

cluster-based DFT methods, and Hartree-Fock theory) for the prediction of  $^{43}\text{Ca}$  chemical shifts is illustrated in Figure 5.4.

Figure 5.5 displays the relationship between principal components of calculated  $^{43}\text{Ca}$  magnetic-shielding tensors and principal components of experimental  $^{43}\text{Ca}$  chemical-shift tensors, with computed results obtained at the PBE and Hartree-Fock levels. Hartree-Fock calculations result in chemical-shift tensors that are more in agreement with experimental values than those obtained at the PBE level. In the former case, the MAE is 9 ppm; in the latter case, the MAE is 14 ppm. In addition, the slopes of the two lines are significantly different, as indicated by the following relations:

$$\sigma_{PBE} = (1147 \pm 2) \text{ ppm} - (1.37 \pm 0.07)\delta_{exp}, \quad (\text{Eq. 5.7})$$

$$\sigma_{HF} = (1244 \pm 1) \text{ ppm} - (1.19 \pm 0.05)\delta_{exp}. \quad (\text{Eq. 5.8})$$

The agreement between calculated and experimental quadrupolar-coupling tensors is similar in the two computation levels, with Hartree-Fock yielding a MAE of 0.20 MHz and the calculation with the PBE functional yielding a MAE of 0.16 MHz.

Calculations performed at the Hartree-Fock level predict magnetic-shielding constants that are systematically shielded relative to DFT values. To explore this relationship further, we provide calculations for the  $^{43}\text{Ca}$  magnetic-shielding tensors in  $\text{Ca}^{2+}$  and the linear ions  $\text{CaF}^+$ ,  $\text{CaOH}^+$ , and  $\text{CaF}^+$  at the HF and PBE levels (Table 5.5). Both computational methods yield the same shielding constant (to within 0.2 ppm) for  $\text{Ca}^{2+}$ . For linear ions, there is no expected paramagnetic contribution to the principal component of the shielding tensor lying along the bonding axis. For the three ions, this principal component differs by no more than 0.8 ppm between the HF and PBE methods, whereas the values predicted for the principal components oriented perpendicular to the bonding axis differ tremendously. This fact suggests that the difference in shielding

constants predicted by the two model chemistries reflect systematic differences in the paramagnetic contributions to the shielding tensors.

**Table 5.5.** HF and PBE calculations of magnetic-shielding tensors in  $\text{Ca}^{2+}$ ,  $\text{CaF}^+$ ,  $\text{CaOH}^+$ , and  $\text{CaH}^+$ .<sup>a</sup>

Ion	Hartree-Fock			PBE		
	$\sigma_{11,22}$ (ppm)	$\sigma_{33}$ (ppm)	$\Omega$ (ppm)	$\sigma_{11,22}$ (ppm)	$\sigma_{33}$ (ppm)	$\Omega$ (ppm)
$\text{Ca}^{2+}$	1413.0	1413.0	0.0	1412.8	1412.8	0.0
$\text{CaF}^+$	1281.0	1419.6	138.6	1135.1	1420.4	285.3
$\text{CaOH}^+$	1277.8	1420.8	143.0	1112.0	1421.6	309.6
$\text{CaH}^+$	1126.8	1417.2	290.4	938.8	1417.4	478.6

<sup>a</sup>Geometries were obtained at the HF/cc-pVTZ level.

Profeta *et al.* have suggested that Ca  $3d^0$  orbitals are able to hybridize with occupied O 2p orbitals [24]. In their study of  $^{17}\text{O}$  quadrupolar-coupling tensors, large errors were seen for O sites in close proximity to a Ca site. The authors demonstrated that the energy gap between these two orbitals can be varied by GGA+U calculations, and that this energy gap has a strong effect on computed NMR parameters. Similar results have been illustrated for materials containing metal-fluorine bonds [80]. Destabilization of the Ca  $3d^0$  orbital leads to a reduction of the covalent nature of the metal-oxygen or metal-fluorine bond. A simple explanation of the variation in the accuracy in computed  $^{43}\text{Ca}$  magnetic-shielding tensors among model chemistries, as noted in the present study, is that these values are linked to the covalent character of the bond. In support of this idea, we note that functionals with an admixture of Hartree-

Fock exchange (PBE0, B3PW91, and TPSSh), which are well known to improve predictions of band gaps, tend to yield superior results relative to pure DFT functionals (PBE, PW91, and TPSS), as illustrated in Table 5.4.

Finite-basis-set effects are necessary considerations for establishing the accuracy of model chemistries. Calculations are presented for the  $^{43}\text{Ca}$  solid-state NMR parameters using the class of correlation-consistent basis sets cc-pVXZ (X = D, T, Q) at the Hartree-Fock level (Table 5.6). The effects of a finite basis set on computed magnetic-shielding parameters for  $^{43}\text{Ca}$  mirror results for other nuclei [23]. MAEs in computed principal values of  $^{43}\text{Ca}$  magnetic-shielding tensors and quadrupolar-coupling tensors do not differ significantly between the cc-pVDZ and cc-pVQZ basis sets.

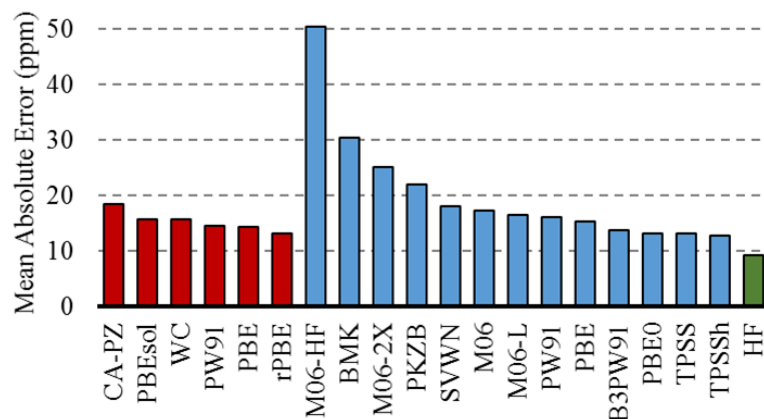


**Figure 5.4.** Mean absolute errors between calculated and experimental  $^{43}\text{Ca}$  chemical-shift tensors. Results obtained using GIPAW are shown in red, DFT results obtained using clusters are shown in blue, and Hartree-Fock results are shown in green.

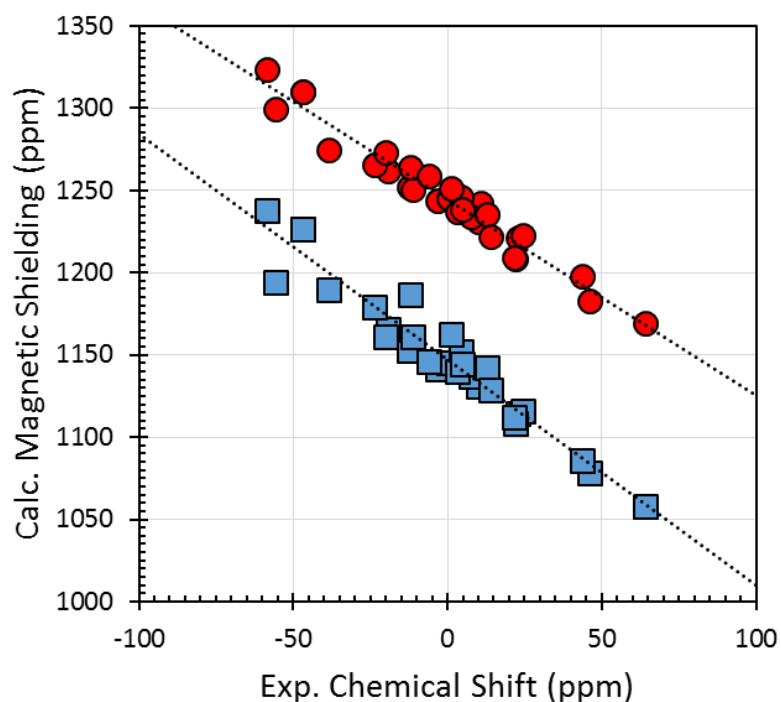


**Figure 5.5.** Relationship between calculated principal values of  $^{43}\text{Ca}$  magnetic-shielding tensors and experimental principal values of  $^{43}\text{Ca}$  chemical-shift tensors obtained at the PBE (blue squares) and Hartree-Fock (red circles) levels.

**Table 5.6.** Linear-regression parameters ( $\sigma_{ref}$  and  $|m|$ ) and statistical data (MAE,<sup>a</sup> Max.<sup>b</sup>) associated with the correlations of principal values of calculated  $^{43}\text{Ca}$  magnetic-shielding tensors and experimental  $^{43}\text{Ca}$  chemical-shift tensors and of calculated and experimental  $^{43}\text{Ca}$  quadrupolar-coupling tensors obtained from Hartree-Fock theory.

Basis set	$\sigma_{ref}$ (ppm)	Magnetic Shielding		$ m $	Quadrupolar Coupling	
		MAE (ppm)	Max. (ppm)		MAE (MHz)	Max. (MHz)
cc-pVDZ	$1250 \pm 2$	9	19	$1.00 \pm 0.06$	0.17	0.31
cc-pVTZ	$1244 \pm 1$	9	21	$1.19 \pm 0.05$	0.20	0.42
cc-pVQZ	$1246 \pm 2$	10	19	$1.11 \pm 0.06$	0.20	0.59

<sup>a</sup>Mean absolute error. <sup>b</sup>Maximum error.

## 5.4 Conclusions

$^{43}\text{Ca}$  magnetic-shielding tensors and quadrupolar-coupling tensors have been calculated for ten calcium sites of calcium-containing materials using periodic and cluster-based computational protocols. Both GIPAW and cluster-based calculations of  $^{43}\text{Ca}$  NMR parameters lead to comparable agreement with experiment when the same functional is employed, demonstrating the cluster approach is applicable to  $^{43}\text{Ca}$  NMR parameter calculations. In addition, since the cluster-based approach allows a wider array of model chemistries to be assessed, a total of twenty-two model chemistries have been studied, including seventeen DFT methods and Hartree-Fock theory. The effects of finite basis sets were also evaluated.

We find that all DFT methods result in either substantial systematic overestimation of chemical shifts for all  $^{43}\text{Ca}$  sites in the database (as characterized by the linear-regression parameter  $|m/|$ ) or in large deviations for individual sites (most often calcite and aragonite). There is also a correlation between errors in computed chemical shifts and computed quadrupolar coupling. For example, the functionals M06-HF, M06-2X, and BMK perform poorly for the prediction of both quantities. In contrast, calculations performed with cluster approach at the Hartree-Fock level yield result in excellent agreement with experiment.

## REFERENCES

- [1] R. Dupree, A.P. Howes, S.C. Kohn, Natural abundance solid state  $^{43}\text{Ca}$  NMR, *Chem. Phys. Lett.*, 276 (1997) 399-404.
- [2] A. Wong, A.P. Howes, R. Dupree, M.E. Smith, Natural abundance  $^{43}\text{Ca}$  NMR study of calcium-containing organic solids: a model study for Ca-binding biomaterials, *Chem. Phys. Lett.*, 427 (2006) 201-205.
- [3] C. Gervais, D. Laurencin, A. Wong, F. Pourpoint, J. Labram, B. Woodward, A.P. Howes, K.J. Pike, R. Dupree, F. Mauri, C. Bonhomme, M.E. Smith, New perspectives on calcium environments in inorganic materials containing calcium–oxygen bonds: a combined computational–experimental  $^{43}\text{Ca}$  NMR approach, *Chem. Phys. Lett.*, 464 (2008) 42-48.
- [4] A. Wong, P.M. Aguiar, T. Charpentier, D. Sakellariou, A low-cost strategy for  $^{43}\text{Ca}$  solid-state NMR spectroscopy, *Chem. Sci.*, 2 (2011) 815-818.
- [5] D.L. Bryce, Calcium binding environments probed by  $^{43}\text{Ca}$  NMR spectroscopy, *J. Chem. Soc., Dalton Trans.*, 39 (2010) 8593-8602.
- [6] D.L. Bryce, E.B. Bultz, D. Aebi, Calcium-43 chemical shift tensors as probes of calcium binding environments. insight into the structure of the vaterite  $\text{CaCO}_3$  polymorph by  $^{43}\text{Ca}$  solid-state NMR spectroscopy, *J. Am. Chem. Soc.*, 130 (2008) 9282-9292.
- [7] K.M.N. Burgess, D.L. Bryce, On the crystal structure of the vaterite polymorph of  $\text{CaCO}_3$ : a calcium-43 solid-state NMR and computational assessment, *Solid State Nucl. Magn. Reson.*, 65 (2015) 75-83.
- [8] K.M.N. Burgess, Y. Xu, M.C. Leclerc, D.L. Bryce, Alkaline-earth metal carboxylates characterized by  $^{43}\text{Ca}$  and  $^{87}\text{Sr}$  solid-state NMR: impact of metal-amine bonding, *Inorg. Chem.*, 53 (2014) 552-561.
- [9] D. Laurencin, C. Gervais, A. Wong, C. Coelho, F. Mauri, D. Massiot, M.E. Smith, C. Bonhomme, Implementation of high resolution  $^{43}\text{Ca}$  solid state NMR spectroscopy: toward the elucidation of calcium sites in biological materials, *J. Am. Chem. Soc.*, 131 (2009) 13430-13440.

- [10] C.M. Widdifield, D.L. Bryce, A multinuclear solid-state magnetic resonance and GIPAW DFT study of anhydrous calcium chloride and its hydrates, *Can. J. Chem.*, 89 (2011) 754-763.
- [11] C.M. Widdifield, I. Moudrakovski, D.L. Bryce, Calcium-43 chemical shift and electric field gradient tensor interplay: a sensitive probe of structure, polymorphism, and hydration, *Phys. Chem. Chem. Phys.*, 16 (2014) 13340-13359.
- [12] A. Trokiner, A. Bessière, R. Thouvenot, D. Hau, J. Marko, V. Nardello, C. Pierlot, J.-M. Aubry, Solid state and solution  $^{43}\text{Ca}$  NMR of calcium peroxides involved in the disproportionation of hydrogen peroxide by calcium hydroxide, *Solid State Nucl. Magn. Reson.*, 25 (2004) 209-215.
- [13] K.J.D. MacKenzie, M.E. Smith, A. Wong, A multinuclear MAS NMR study of calcium-containing aluminosilicate inorganic polymers, *J. Mater. Chem.*, 17 (2007) 5090-5096.
- [14] J.W. Singer, A.Ö. Yazaydin, R.J. Kirkpatrick, G.M. Bowers, Structure and transformation of amorphous calcium carbonate: a solid-state  $^{43}\text{Ca}$  NMR and computational molecular dynamics investigation, *Chem. Mater.*, 24 (2012) 1828-1836.
- [15] D. Laurencin, A. Wong, J.V. Hanna, R. Dupree, M.E. Smith, A high-resolution  $^{43}\text{Ca}$  solid-state NMR study of the calcium sites of hydroxyapatite, *J. Am. Chem. Soc.*, 130 (2008) 2412-2413.
- [16] A. Wong, D. Laurencin, R. Dupree, M.E. Smith, Two-dimensional  $^{43}\text{Ca}$ - $^1\text{H}$  correlation solid-state NMR spectroscopy, *Solid State Nucl. Magn. Reson.*, 35 (2009) 32-36.
- [17] D. Laurencin, M.E. Smith, Development of  $^{43}\text{Ca}$  solid state NMR spectroscopy as a probe of local structure in inorganic and molecular materials, *Prog. Nucl. Magn. Reson. Spectrosc.*, 68 (2013) 1-40.
- [18] K. Shimoda, Y. Tobu, K. Kanehashi, T. Nemoto, K. Saito, Local environments of slags: The first application of Ca-43 3QMAS NMR technique, *Chem. Lett.*, 34 (2005) 1588-1589.
- [19] K. Shimoda, Y. Tobu, K. Kanehashi, T. Nemoto, K. Saito, First evidence of multiple Ca sites in amorphous slag structure: Multiple-quantum MAS NMR spectroscopy on calcium-43 at high magnetic field, *Solid State Nucl. Magn. Reson.*, 30 (2006) 198-202.
- [20] K. Shimoda, Y. Tobu, Y. Shimoikeda, T. Nemoto, K. Saito, Multiple  $\text{Ca}^{2+}$  environments in silicate glasses by high-resolution  $^{43}\text{Ca}$  MQMAS NMR technique at high and ultra-high (21.8 T) magnetic fields, *J. Magn. Reson.*, 186 (2007) 156-159.

- [21] K. Shimoda, Y. Tobu, K. Kanehashi, T. Nemoto, K. Saito, Total understanding of the local structures of an amorphous slag: Perspective from multi-nuclear ( $^{29}\text{Si}$ ,  $^{27}\text{Al}$ ,  $^{17}\text{O}$ ,  $^{25}\text{Mg}$ , and  $^{43}\text{Ca}$ ) solid-state NMR, *J. Non-Cryst. Solids*, 354 (2008) 1036-1043.
- [22] F. Angeli, M. Gaillard, P. Jollivet, T. Charpentier, Contribution of  $^{43}\text{Ca}$  MAS NMR for probing the structural configuration of calcium in glass, *Chem. Phys. Lett.*, 440 (2007) 324-328.
- [23] S.T. Holmes, R.J. Iuliucci, K.T. Mueller, C. Dybowski, Critical analysis of cluster models and exchange-correlation functionals for calculating magnetic shielding in molecular solids, *J. Chem. Theory Comput.*, 11 (2015) 5229-5241.
- [24] M. Profeta, M. Benoit, F. Mauri, C.J. Pickard, First-principles calculation of the  $^{17}\text{O}$  NMR parameters in Ca oxide and Ca aluminosilicates: the partially covalent nature of the Ca–O bond, a challenge for density functional theory, *J. Am. Chem. Soc.*, 126 (2004) 12628-12635.
- [25] S.T. Holmes, R.J. Iuliucci, K.T. Mueller, C. Dybowski, Density functional investigation of intermolecular effects on  $^{13}\text{C}$  NMR chemical-shielding tensors modeled with molecular clusters, *J. Chem. Phys.*, 141 (2014) 164121.
- [26] S.T. Holmes, F. Alkan, R.J. Iuliucci, K.T. Mueller, C. Dybowski, Analysis of the bond-valence method for calculating  $^{29}\text{Si}$  and  $^{31}\text{P}$  magnetic shielding in covalent network solids, *J. Comput. Chem.*, 37 (2016) 1704-1710.
- [27] S.T. Holmes, C. Dybowski, Carbon-13 Chemical-Shift Tensors in Indigo: a Two-Dimensional NMR-ROCSA and DFT Study, *Solid State Nucl. Magn. Reson.*, 72 (2015) 90-95.
- [28] F. Alkan, C. Dybowski, Calculation of chemical-shift tensors of heavy nuclei: a DFT/ZORA investigation of  $^{199}\text{Hg}$  chemical-shift tensors in solids, and the effects of cluster size and electronic-state approximations, *Phys. Chem. Chem. Phys.*, 16 (2014) 14298-14308.
- [29] F. Alkan, C. Dybowski, Chemical-shift tensors of heavy nuclei in network solids: a DFT/ZORA investigation of  $^{207}\text{Pb}$  chemical-shift tensors using the bond-valence method, *Phys. Chem. Chem. Phys.*, 17 (2015) 25014-25026.
- [30] F. Alkan, C. Dybowski, Effect of co-ordination chemistry and oxidation state on  $^{207}\text{Pb}$  magnetic-shielding tensor: a DFT/ZORA investigation. , *J. Phys. Chem. A*, 120 (2016) 161-168.
- [31] F. Alkan, S.T. Holmes, R.J. Iuliucci, K.T. Mueller, C. Dybowski, Spin-orbit effects on the  $^{119}\text{Sn}$  magnetic-shielding tensor in solids: a ZORA/DFT investigation, *Phys. Chem. Chem. Phys.*, 18 (2016) 18914-18922.

- [32] J.D. Hartman, S. Monaco, B. Schatschneider, G.J.O. Beran, Fragment-based  $^{13}\text{C}$  nuclear magnetic resonance chemical shift predictions in molecular crystals: an alternative to planewave methods, *J. Chem. Phys.*, 143 (2015) 102809.
- [33] J.D. Hartman, R.A. Kudla, G.M. Day, L.J. Mueller, G.J.O. Beran, Benchmark fragment-based  $^1\text{H}$ ,  $^{13}\text{C}$ ,  $^{15}\text{N}$  and  $^{17}\text{O}$  chemical shift predictions in molecular crystals, *Phys. Chem. Chem. Phys.*, 18 (2016) 21686-21709.
- [34] M.O. Bargouth, G. Will, Calcium formate  $\text{Ca}(\text{HCOO})_2$  (neutron), *Cryst. Struct. Commun.*, 9 (1980) 605-613.
- [35] E.A. Klop, A. Schouten, P. Vandersluis, A.L. Spek, Structure of calcium acetate monohydrate,  $\text{Ca}(\text{C}_2\text{H}_3\text{O}_2)_2 \cdot \text{H}_2\text{O}$ , *Acta Crystallogr., Sect. C*, 40 (1984) 51-53.
- [36] R. Boese, O. Heinemann, Crystal structure of calcium tartrate tetrahydrate,  $\text{C}_4\text{H}_4\text{O}_6\text{Ca}(\text{H}_2\text{O})_4$ , *Z. Kristallogr.*, 205 (1993) 348-349.
- [37] I. Senkovska, U. Thewalt, Triaquabenzotocalcium(II) monobenzoate: coordination polymer chains linked into a two-dimensional framework by hydrogen bonds, *Acta Crystallogr., Sect. C*, 61 (2005) M448-M449.
- [38] S.A. Markgraf, R.J. Reeder, High-temperature structure refinements of calcite and magnesite, *Am. Mineral.*, 70 (1985) 590-600.
- [39] J.P.R. de Villiers, Crystal structure of aragonite, strontianite, and witherite, *Am. Mineral.*, 56 (1971) 758-766.
- [40] L. Vegard, Struktur der isomorphen gruppe  $\text{Pb}(\text{NO}_3)_2$ ,  $\text{Ba}(\text{NO}_3)_2$ ,  $\text{Sr}(\text{NO}_3)_2$ ,  $\text{Ca}(\text{NO}_3)_2$ , *Z. Phys.*, 9 (1922) 395-410.
- [41] L. Vegard, L. Bilberg, Structure of nitrates in divalent metals, *Skrifter utgitt av det Norske Videnskaps-Akademi i Oslo*, 9 (1932) 1-22.
- [42] B.F. Pedersen, D. Semmingsen, Neutron diffraction refinement of the structure of gypsum,  $\text{CaSO}_4 \cdot 2\text{H}_2\text{O}$ , *Acta Crystallogr., Sect. B*, 38 (1982) 1074-1077.
- [43] B. Leclaire, M.M. Borel, Le dichlorure de calcium dihydrate, *Acta Crystallogr., Sect. B*, 33 (1977) 1608-1610.
- [44] C.J. Pickard, F. Mauri, All-electron magnetic response with pseudopotentials: NMR chemical shifts, *Phys. Rev. B*, 63 (2001) 245101.
- [45] S.J. Clark, M.D. Segall, C.J. Pickard, P.J. Hasnip, M.J. Probert, K. Refson, M.C. Payne, First principles methods using CASTEP, *Z. Kristallogr.*, 220 (2005) 567-570.
- [46] J.R. Yates, C.J. Pickard, F. Mauri, Calculation of NMR chemical shifts for extended systems using ultrasoft pseudopotentials, *Physical Review B*, 76 (2007).

- [47] D.M. Ceperley, B.J. Alder, Ground state of the electron gas by a stochastic method, *Phys. Rev. Lett.*, 45 (1980) 566-569.
- [48] J.P. Perdew, A. Zunger, Self-interaction correction to density-functional approximations for many-electron systems, *Phys. Rev. B*, 23 (1981) 5048-5079.
- [49] J.P. Perdew, Y. Wang, Accurate and simple analytic representation of the electron-gas correlation energy, *Phys. Rev. B*, 45 (1992) 13244.
- [50] J.P. Perdew, K. Burke, M. Ernzerhof, Generalized gradient approximation made simple, *Phys. Rev. Lett.*, 77 (1996) 3865-3868.
- [51] B. Hammer, L.B. Hansen, J.K. Nørskov, Improved adsorption energetics within density-functional theory using revised Perdew-Burke-Ernzerhof functionals, *Phys. Rev. B*, 59 (1999) 7413-7421.
- [52] J.P. Perdew, A. Ruzsinszky, G.I. Csonka, O.A. Vydrov, G.E. Scuseria, L.A. Constantin, X. Zhou, K. Burke, Restoring the density-gradient expansion for exchange in solids and surfaces, *Phys. Rev. Lett.*, 100 (2008) 136406.
- [53] Z. Wu, R.E. Cohen, More accurate generalized gradient approximation for solids, *Phys. Rev. B*, 73 (2006) 235116.
- [54] G. Valerio, A. Goursot, R. Vetrivel, O. Malkina, V. Malkin, D.R. Salahub, Calculation of  $^{29}\text{Si}$  and  $^{27}\text{Al}$  MAS NMR chemical shifts in zeolite- $\beta$  using density functional theory: correlation with lattice structure, *J. Am. Chem. Soc.*, 120 (1998) 11426-11431.
- [55] G. Valerio, A. Goursot, Density functional calculations of the  $^{29}\text{Si}$  and  $^{27}\text{Al}$  MAS NMR spectra of the zeolite mazzite: analysis of geometrical and electronic effects, *J. Phys. Chem. B*, 103 (1999) 51-58.
- [56] J.A. Tossell, Second-nearest-neighbor effects upon N NMR shieldings in models for solid  $\text{Si}_3\text{N}_4$  and  $\text{C}_3\text{N}_4$ , *J. Magn. Reson.*, 127 (1997) 49-53.
- [57] J.A. Tossell, Second-nearest-neighbor effects on the NMR shielding of N in  $\text{P}_3\text{N}_5$  and hexagonal BN, *Chem. Phys. Lett.*, 303 (1999) 435-440.
- [58] J.A. Tossell, Quantum mechanical calculation of  $^{23}\text{Na}$  NMR shieldings in silicates and aluminosilicates, *Phys. Chem. Miner.*, 27 (1999) 70-80.
- [59] R. Improta, V. Barone, G. Scalmani, M.J. Frisch, A state-specific polarizable continuum model time dependent density functional theory method for excited state calculations in solution, *J. Chem. Phys.*, 125 (2006) 054103.
- [60] R. Improta, G. Scalmani, M.J. Frisch, V. Barone, Toward effective and reliable fluorescence energies in solution by a new state specific polarizable continuum model

time dependent density functional theory approach, *J. Chem. Phys.*, 127 (2007) 074504.

[61] A.V. Marenich, C.J. Cramer, D.G. Truhlar, Universal solvation model based on solute electron density and on a continuum model of the solvent defined by the bulk dielectric constant and atomic surface tensions, *J. Phys. Chem. B*, 113 (2009) 6378-6396.

[62] T.H. Dunning, Gaussian basis sets for use in correlated molecular calculations. I. the atoms boron through neon and hydrogen, *J. Chem. Phys.*, 90 (1989) 1007-1023.

[63] D.E. Woon, T.H. Dunning, Gaussian basis sets for use in correlated molecular calculations. III. the atoms aluminum through argon, *J. Chem. Phys.*, 98 (1993) 1358-1371.

[64] J.R. Cheeseman, G.W. Trucks, T.A. Keith, M.J. Frisch, A comparison of models for calculating nuclear magnetic resonance shielding tensors, *J. Chem. Phys.*, 104 (1996) 5497-5509.

[65] P. Hohenberg, W. Kohn, Inhomogeneous electron gas, *Phys. Rev.*, 136 (1964) B864.

[66] W. Kohn, L.J. Sham, Self-consistent equations including exchange and correlation effects, *Phys. Rev.*, 140 (1965) 1133-&.

[67] J.C. Slater, *The Self-Consistent Field for Molecular and Solids, Quantum Theory of Molecular and Solids*, McGraw-Hill, New York, 1974.

[68] S.H. Vosko, L. Wilk, M. Nusair, Accurate spin-dependent electron liquid correlation energies for local spin density calculations: a critical analysis, *Can. J. Phys.*, 58 (1980) 1200-1211.

[69] J.P. Perdew, S. Kurth, A. Zupan, P. Blaha, Accurate density functional with correct formal properties: a step beyond the generalized gradient approximation, *Phys. Rev. Lett.*, 82 (1999) 2544-2547.

[70] J.M. Tao, J.P. Perdew, V.N. Staroverov, G.E. Scuseria, Climbing the density functional ladder: nonempirical meta-generalized gradient approximation designed for molecules and solids, *Phys. Rev. Lett.*, 91 (2003) 146401.

[71] Y. Zhao, D.G. Truhlar, A new local density functional for main-group thermochemistry, transition metal bonding, thermochemical kinetics, and noncovalent interactions, *J. Chem. Phys.*, 125 (2006) 194101.

[72] A.D. Becke, A new mixing of Hartree-Fock and local density-functional theories, *J. Chem. Phys.*, 98 (1993) 1372-1377.

- [73] C. Adamo, V. Barone, Toward reliable density functional methods without adjustable parameters: the PBE0 model, *J. Chem. Phys.*, 110 (1999) 6158-6170.
- [74] A.D. Boese, J.M.L. Martin, Development of density functionals for thermochemical kinetics, *J. Chem. Phys.*, 121 (2004) 3405-3416.
- [75] Y. Zhao, D.G. Truhlar, The M06 suite of density functionals for main group thermochemistry, thermochemical kinetics, noncovalent interactions, excited states, and transition elements: two new functionals and systematic testing of four M06-class functionals and 12 other functionals, *Theor. Chem. Acc.*, 120 (2008) 215-241.
- [76] Y. Zhao, D.G. Truhlar, Comparative DFT study of van der Waals complexes: rare-gas dimers, alkaline-earth dimers, zinc dimer, and zinc-rare-gas dimers, *J. Phys. Chem. A*, 110 (2006) 5121-5129.
- [77] Y. Zhao, D.G. Truhlar, Density functional for spectroscopy: no long-range self-interaction error, good performance for Rydberg and charge-transfer states, and better performance on average than B3LYP for ground states, *J. Phys. Chem. A*, 110 (2006) 13126-13130.
- [78] M.J. Frisch, G.W. Trucks, H.B. Schlegel, G.E. Scuseria, M.A. Robb, J.R. Cheeseman, G. Scalmani, V. Barone, B. Mennucci, G.A. Petersson, H. Nakatsuji, M. Caricato, X. Li, H.P. Hratchian, A.F. Izmaylov, J. Bloino, G. Zheng, J.L. Sonnenberg, M. Hada, M. Ehara, K. Toyota, R. Fukuda, J. Hasegawa, M. Ishida, T. Nakajima, Y. Honda, O. Kitao, H. Nakai, T. Vreven, J.A. Montgomery, J.E. Peralta, F. Ogliaro, M. Bearpark, J.J. Heyd, E. Brothers, K.N. Kudin, V.N. Staroverov, R. Kobayashi, J. Normand, K. Raghavachari, A. Rendell, J.C. Burant, S.S. Iyengar, J. Tomasi, M. Cossi, N. Rega, J.M. Millam, M. Klene, J.E. Knox, J.B. Cross, V. Bakken, C. Adamo, J. Jaramillo, R. Gomperts, R.E. Stratmann, O. Yazyev, A.J. Austin, R. Cammi, C. Pomelli, J.W. Ochterski, R.L. Martin, K. Morokuma, V.G. Zakrzewski, G.A. Voth, P. Salvador, J.J. Dannenberg, S. Dapprich, A.D. Daniels, Farkas, J.B. Foresman, J.V. Ortiz, J. Cioslowski, D.J. Fox, Gaussian 09, Revision B.01, Wallingford CT, 2009.
- [79] G. Schreckenbach, T. Ziegler, Calculation of NMR shielding tensors using gauge-including atomic orbitals and modern density functional theory, *J. Phys. Chem.*, 99 (1995) 606-611.
- [80] R. Laskowski, P. Blaha, F. Tran, Assessment of DFT functionals with NMR chemical shifts, *Phys. Rev. B*, 87 (2013) 195130.

## Chapter 6

### ANALYSIS OF THE BOND-VALENCE METHOD FOR CALCULATING $^{29}\text{Si}$ AND $^{31}\text{P}$ MAGNETIC SHIELDING IN COVALENT NETWORK SOLIDS

#### 6.1 Introduction

This chapter examines several methods for calculating  $^{29}\text{Si}$  and  $^{31}\text{P}$  magnetic-shielding tensors in covalent network solids such as silicates, phosphates, and related minerals. Numerous examples of density-functional calculations of  $^{29}\text{Si}$  and  $^{31}\text{P}$  magnetic shielding are found in the literature [1-6]. As discussed previously, one popular approach for calculating magnetic shieldings in crystalline solids is to expand the wave function in a plane-wave basis, as is done with the gauge-including-projector-augmented-wave (GIPAW) method [7]. This method takes advantage of the periodic nature of the crystalline lattice and is a robust computational technique [8].

On the other hand, there are reasons to model a crystalline lattice without periodic-boundary conditions (PBCs). For example, both PBC and cluster-based calculations scale according to the number of electrons in the model, but the PBC method requires the full unit cell to satisfy translational-symmetry requirements. For systems with large unit cells, an adequately-sized cluster may contain fewer electrons. Another consideration is the model chemistry with which NMR parameters can be computed. Calculations using PBCs are typically restricted to pure DFT exchange-correlation functionals based on the local-density approximation (LDA) or the generalized-gradient approximation (GGA), which excludes higher-level model chemistries. Recent work has illustrated that significant improvement in computed magnetic-shielding tensors is obtainable with more rigorous DFT methods in many types of chemical systems [9].

Sufficient agreement with experiment can be obtained by employing a moderately-sized cluster to represent a local portion of a solid [10-12]. The cluster approximation works well for molecular solids but difficulties arise when modeling network solids such as silicates, phosphates, and other minerals. The major difficulty associated with modeling a local portion of a solid using a cluster-based approach arises from terminating the outermost atoms, as doing so results in dangling bonds and uncompensated charge which increases significantly with increasing cluster size. For charged clusters, SCF convergence is often difficult to achieve due a small HOMO-LUMO gap [11]. When the SCF cycle does converge, the resulting magnetic-shielding tensors may not agree with experimental values.

One approach to deal with excess charge on a cluster is to saturate the dangling bonds with hydrogen atoms [10, 11, 13-18]. There are problems with the hydrogen-addition method, including variation in computed magnetic-shielding tensors depending on the number and placement of hydrogen atoms. There are frequently convergence difficulties, also an indicator of failure to model the electronic structure properly.

A second approach to deal with the charge problem employs the embedded-ion method (EIM) or related formalisms [19-25] to compensate for excess charge by embedding the cluster in an array of classical point charges centered on the crystallographic nuclear origins. This method has been applied to calculations on several magnesium phosphates with success [19]. However, the EIM method has difficulties outlined by Weber [19], typically associated with the quantum-mechanical and electrostatic interface and with charge on the quantum region of the cluster.

A recent approach introduced by Alkan and Dybowski employs pseudoatoms with non-integer nuclear charges for the terminal atoms [11, 12]. Charges are

parameterized using the bond-valence theory of Brown and co-workers [26-30]. This computational approach, referred to as valence modification of terminal atoms using bond-valence theory, or VMTA/BV, has been exploited in calculations of  $^{207}\text{Pb}$  magnetic shielding in network solids [11, 12]. An advantage of the VMTA/BV method is that calculations can be performed on all types of nuclides with model chemistries not available when using the plane-wave approach (hybrid DFT, HF, MP2, etc.).

This chapter presents a series of calculations of  $^{29}\text{Si}$  and  $^{31}\text{P}$  magnetic-shielding tensors in solids. These nuclides were selected because of the wealth of high-quality solid-state NMR measurements of such tensors. Computed magnetic-shielding tensors by the GIPAW procedure and by a cluster-based approach that incorporates bond-valence theory are compared for twenty-seven materials and eight model chemistries.

## 6.2 Computational Details and Theory

The solids selected for inclusion in this study were chosen by the following criteria: (1) the structure of the material had to be known through high-quality diffraction studies; (2) the principal components of the chemical-shift tensors had to have been measured to a high degree of accuracy; and (3) the NMR spectra of materials with more than one unique NMR-active lattice site had to have been assigned unambiguously. For  $^{29}\text{Si}$  calculations, the materials are  $\text{SiO}_2$  [31, 32],  $\text{Li}_2\text{Si}_2\text{O}_5$  [33, 34],  $\text{Na}_2\text{SiO}_3$  [35, 36],  $\text{Na}_2\text{Si}_2\text{O}_5$  [33, 37],  $\text{Mg}_2\text{SiO}_4$  [38, 39],  $\text{MgSiO}_3$  [33, 40],  $\text{CaSiO}_3$  [35, 41],  $\text{Ca}_3\text{Si}_2\text{O}_7$  [35, 42], and  $\text{CaMgSiO}_5$  [33, 43]. For  $^{31}\text{P}$  calculations, the materials are  $\text{Mg}_3(\text{PO}_4)_2$  [19, 44],  $\text{Mg}_2\text{P}_4\text{O}_{12}$  [19, 45],  $\text{Mg}_2\text{P}_2\text{O}_7$  [19, 46],  $\text{MgP}_4\text{O}_{11}$  [19, 47],  $\text{Ca}_4\text{P}_2\text{O}_9$  [48],  $\text{Li}_6\text{O}_6\text{P}_{18}\cdot 3\text{H}_2\text{O}$  [49, 50], and  $\text{SnHPO}_4$  [51, 52]. Altogether, this database consists of thirteen unique  $^{29}\text{Si}$  sites and fourteen unique  $^{31}\text{P}$  sites.

Refinements of the positions of hydrogen atoms in diffraction structures often result in appreciable changes in calculated magnetic shielding, even in cases where the hydrogen atom is located several bonds from the NMR-active nucleus. For hydrates, the lattice positions of hydrogens were optimized while leaving heavy atoms fixed. Optimizations were performed using the GGA functional of Perdew, Burke, and Ernzerhof (PBE) [53] with a plane-wave cutoff energy of 600 eV. Core orbitals were replaced with ultrasoft pseudopotentials (USPPs) generated *on the fly* (OTF) [54].

GIPAW calculations of magnetic shielding were performed using the LDA functional CA-PZ [55, 56], and the GGA functionals PW91 [57], PBE [53], rPBE [58], PBEsol [59], and WC [60] with a plane-wave cutoff energy of 600 eV and ultra-fine SCF convergence criteria, unless indicated otherwise. Core orbitals were replaced by OTF-USPPs [54].

In the cluster-based calculations, which were based on the gauge-including atomic orbital (GIAO) formalism [61, 62], two all-electron (AE) basis sets were employed for different regions of the cluster. The central region of the cluster, which consisted of the central Si or P site and the four directly-adjacent oxygen sites, was given the larger AE TZ2P basis set. The atomic sites located further from the center were given the smaller AE TZP basis set. Charge compensation on the outermost atomic shells was accomplished through the VMTO/BV method [11, 12]. Two example clusters are shown in Figure 6.1. Calculations on clusters were performed using the PBE functional and the hybrid functional PBE0 [63]. The PBE0 functional results from the admixture of 25% Hartree-Fock (HF) exchange with the PBE functional.

Geometry optimizations and magnetic-shielding calculations employing the GIPAW approach were performed using the CASTEP module of MATERIALS STUDIO 7.0

[64]. Magnetic-shielding calculations in the cluster-based approach were performed with the Amsterdam Density Functional (ADF2014) suite of programs [65].

The VMTA/BV model has been discussed previously [11, 12]. Briefly, in the VMTA/BV model, the bond strength of a terminal atom is given by:

$$S = \sum_i \exp\left(\frac{R_{i0} - R_i}{b_i}\right) \quad (\text{Eq. 6.1})$$

In Eq. 6.1,  $S$  is the bond strength of the terminal atom,  $R_i$  is the bond length, and  $R_{i0}$  and  $b_i$  are parameters given in a recent review by Brown [26]. The value of  $R_{i0}$  was adjusted for each system so that the bond strength of a fully-co-ordinated atom was equal to the oxidation state of the atom. The nuclear charges,  $Z_{nuc}$ , on the terminal atoms were modified to counteract the missing co-ordination. The added charge is proportional to the sum of the bond strengths of that atom,

$$Z_{mod} = Z_{nuc} + \Delta S, \quad (\text{Eq. 6.2})$$

where  $Z_{nuc}$  is the unaltered nuclear charge,  $Z_{mod}$  is the modified nuclear charge, and  $\Delta S$  is the difference between the valence of the terminal atom in a periodic solid and the valence of the same atom in a cluster. Using the VMTA/BV method, SCF convergence was achieved for all twenty-seven cluster models without using SCF-convergence aids.

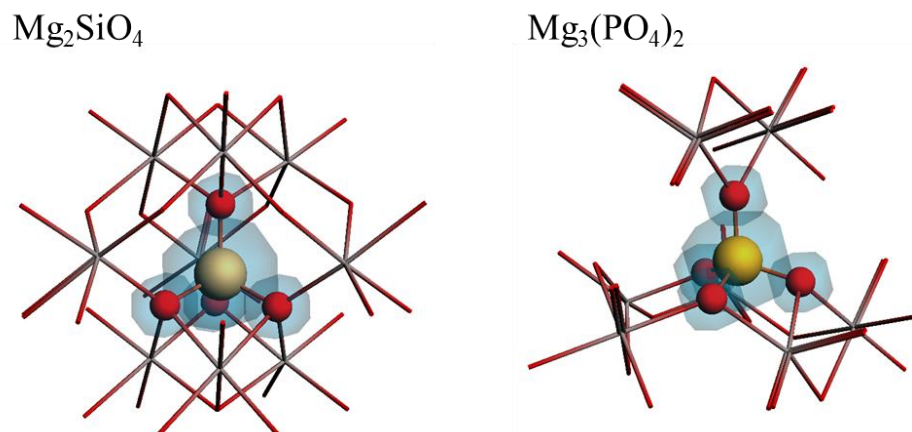


**Figure 6.1.** Illustration of third-co-ordination-shell clusters for  $\text{Mg}_2\text{SiO}_4$  and  $\text{Mg}_3(\text{PO}_4)_2$ . The TZ2P region is shown in ball-and-stick model and the TZP region is shown as a wireframe model.

## 6.3 Results and Discussion

### 6.3.1 Cluster Size

An important step in calculations employing clusters is to verify that the cluster sufficiently models a local portion of the solid-state structure. To maximize computational efficiency, it is desirable to employ the smallest possible cluster capable of accurately representing the environment around the NMR-active nucleus. A series of magnetic-shielding calculations using model clusters of various sizes is summarized in Table 6.1 for  $\text{SiO}_2$ ,  $\text{Na}_2\text{SiO}_3$ ,  $\text{Mg}_2\text{P}_4\text{O}_{12}$  (P1), and  $\text{Mg}_3(\text{PO}_4)_2$ . The clusters are expanded around the NMR-active nucleus ( $^{29}\text{Si}$  or  $^{31}\text{P}$ ) up to the first, third, and fifth co-ordination shells (Figure 6.2).

Experimental chemical shifts (relative to a reference compound) have been converted to the magnetic-shielding scale (relative to the bare nucleus) using a proposed

empirical conversion [66, 67]. The experimental magnetic shielding ( $\sigma^{exp}$ ) is related to the experimental chemical shift ( $\delta^{exp}$ ) by the relation:

$$\sigma^{exp} = \sigma^{ref} - \delta^{exp} \quad (\text{Eq. 6.3})$$

The reference shielding constants ( $\sigma^{ref}$ ) are 368.5 ppm (TMS) and 328.4 ppm (85%  $\text{H}_3\text{PO}_4$ ) for  $^{29}\text{Si}$  and  $^{31}\text{P}$ , respectively. As is displayed in Table 6.1, the computed residuals between calculated and experimental magnetic shielding for the third and fifth co-ordination shells differ from each other in the range of 1 – 2 ppm. However, differences in computed residuals between first- and third-co-ordination-shell clusters are significantly larger, with the highest deviation being around 50 ppm. The similarity in residuals for the third and fifth co-ordination shells suggests that third-co-ordination-shell clusters are sufficiently large to model the magnetic shielding.

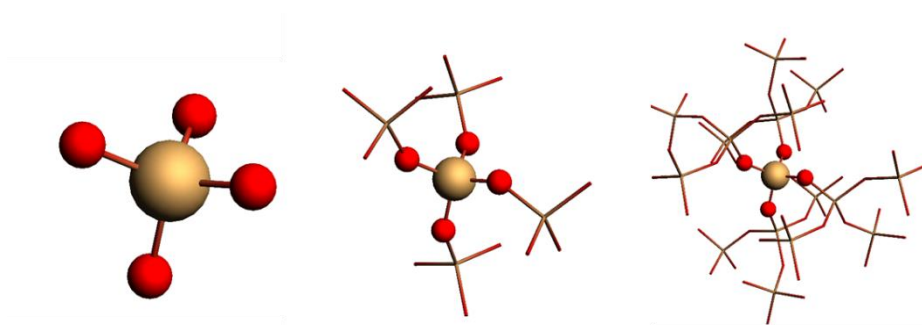


**Figure 6.2.** Clusters of  $\text{SiO}_2$  expanded around the NMR-active  $^{29}\text{Si}$  site to the first (left), third (center) and fifth (right) co-ordination shells. The TZ2P layer is shown in the ball-and-stick representation and the TZP region is shown in the wireframe representation.

**Table 6.1.** Principal components of experimental and computed magnetic-shielding tensors, isotropic magnetic shielding, and span for first, third, and fifth co-ordination-shell clusters of SiO<sub>2</sub>, Na<sub>2</sub>SiO<sub>3</sub>, Mg<sub>2</sub>P<sub>4</sub>O<sub>12</sub> (P1), and Mg<sub>3</sub>(PO<sub>4</sub>)<sub>2</sub><sup>a</sup> determined with VMTA/BV theory.

Model Cluster	$\sigma_{11}$ (ppm)	$\sigma_{22}$ (ppm)	$\sigma_{33}$ (ppm)	$\sigma_{iso}^b$ (ppm)	$\Omega^b$ (ppm)	$R^c$ (ppm)
SiO <sub>2</sub>						
<b>Experimental</b>	<b>471.1</b>	<b>475.5</b>	<b>477.6</b>	<b>474.7</b>	<b>6.5</b>	---
First shell	440.7	441.5	442.5	441.6	1.8	33.2
Third shell	447.0	450.3	456.4	451.2	9.4	23.6
Fifth shell	447.5	449.9	459.2	452.2	11.7	22.7
Na <sub>2</sub> SiO <sub>3</sub>						
<b>Experimental</b>	<b>388.2</b>	<b>429.4</b>	<b>519.1</b>	<b>445.6</b>	<b>130.9</b>	---
First shell	401.4	432.8	483.8	439.3	82.4	21.8
Third shell	357.9	395.9	499.0	417.6	141.1	28.5
Fifth shell	363.9	398.1	495.0	419.0	131.2	26.8
Mg <sub>2</sub> P <sub>4</sub> O <sub>12</sub> (P1)						
<b>Experimental</b>	<b>272.5</b>	<b>329.4</b>	<b>487.0</b>	<b>363.0</b>	<b>214.5</b>	---
First shell	240.8	280.6	403.6	303.8	162.9	58.7
Third shell	262.6	317.3	479.4	353.1	216.8	10.0
Fifth shell	258.7	316.8	489.9	355.1	231.2	10.9
Mg <sub>3</sub> (PO <sub>4</sub> ) <sub>2</sub>						
<b>Experimental</b>	<b>315.7</b>	<b>325.7</b>	<b>344.2</b>	<b>328.5</b>	<b>28.5</b>	---
First shell	293.7	303.7	327.1	308.2	33.4	20.5
Third shell	303.4	317.5	331.3	317.4	27.9	11.3
Fifth shell	305.4	313.5	336.0	318.3	30.6	10.4

<sup>a</sup>Calculations performed at the PBE/TZ2P/AE level of theory.

<sup>b</sup>The isotropic magnetic shielding and span are defined by  $\sigma_{iso} = (\sigma_{11} + \sigma_{22} + \sigma_{33})/3$ , and  $\Omega = \sigma_{33} - \sigma_{11}$ , respectively.

$$^cR = \sqrt{\frac{1}{3} \sum_{ii} (\sigma_{ii}^{exp} - \sigma_{ii}^{calc})^2} .$$

The lowest residuals between calculation and experiment for the three sizes of model clusters examined are generally observed for the third- and fifth-co-ordination-shell clusters. However, for  $\text{Na}_2\text{SiO}_3$ , the lowest value of  $R$  is found for the first co-ordination shell. This deviation from the general trend appears to be the result of accidental cancellation of errors, as indicated by the computed spans ( $\Omega$ ). The experimental span of 130.9 ppm is more in line with the values calculated for the third- and fifth-co-ordination-shell clusters (141.1 ppm and 131.2 ppm, respectively) than with the span calculated for the first-co-ordination shell cluster (82.4 ppm).

### 6.3.2 Basis-Set and Pseudopotential Effects

Calculated magnetic-shielding constants depend strongly on basis sets and electronic-state approximations such as pseudopotentials used in the calculation. Results obtained near the basis-set limit can be used to compare computational methodologies because finite-basis-set effects are minimized. To test the convergence of computed NMR parameters with respect to the basis-set size, plane-wave pseudopotential calculations were run on  $\text{SiO}_2$  and  $\text{Mg}_3(\text{PO}_4)_2$  with cutoff energies of 200 eV, 400 eV, 600 eV, and 800 eV. Similarly, cluster-based calculations were run on the same systems, for which the Slater-type basis set on the central  $\text{SiO}_4$  or  $\text{PO}_4$  tetrahedra was DZ, DZP, TZP, and TZ2P, in increasing order of flexibility. The results of these calculations are presented in Table 6.2.

The difference in the calculated principal components of the magnetic-shielding tensor derived with the TZP basis set, as compared to those determined with the TZ2P basis set (or in going from a cutoff energy of 600 eV to a cutoff energy of 800 eV for the GIPAW calculations), is negligible. For the GIPAW calculations, individual principal components of the computed magnetic-shielding tensor differ by no more than

0.4 ppm between cutoff energies of 600 eV and 800 eV. In the cluster calculations, the largest difference in computed magnetic shielding between TZP and TZ2P is 1.6 ppm. Similarly, the largest difference in calculated spans between 600 eV and 800 eV is 0.2 ppm and the largest difference in spans between TZP and TZ2P is 0.7 ppm.

**Table 6.2.** Calculated  $^{29}\text{Si}$  and  $^{31}\text{P}$  principal components of magnetic shielding tensors for various all-electron Slater-type and pseudopotential plane-wave basis sets.<sup>a</sup>

Basis Set	$\sigma_{11}$ (ppm)	$\sigma_{22}$ (ppm)	$\sigma_{33}$ (ppm)	$\sigma_{iso}$ (ppm)	$\Omega$ (ppm)
<b>SiO<sub>2</sub></b>					
DZ	451.9	463.0	471.8	462.2	19.8
DZP	451.7	454.5	464.4	456.9	12.6
TZP	448.1	451.7	457.7	452.5	9.5
TZ2P	447.0	450.3	456.4	451.2	9.4
200 eV	413.2	424.0	426.7	421.3	13.5
400 eV	427.6	431.4	435.1	431.4	7.5
600 eV	426.8	430.6	434.5	430.6	7.7
800 eV	426.7	430.2	434.2	430.4	7.5
<b>Mg<sub>3</sub>(PO<sub>4</sub>)<sub>2</sub></b>					
DZ	304.9	321.0	335.3	320.4	30.4
DZP	300.8	316.6	330.9	316.1	30.1
TZP	304.2	319.1	332.8	318.7	28.6
TZ2P	303.4	317.5	331.3	317.4	27.9
200 eV	258.3	262.7	284.7	268.6	26.4
400 eV	267.8	273.8	297.2	279.6	29.4
600 eV	268.6	274.4	297.9	280.3	29.3
800 eV	268.6	274.4	297.9	280.3	29.3

<sup>a</sup>Calculations performed at the PBE level of theory.

The periodic and cluster-based computational methodologies yield NMR parameters that differ significantly. At the basis-set limit (600 eV or TZ2P), calculations that used Slater-type basis functions yielded magnetic-shielding parameters that are more shielded than those that were obtained using plane waves. For SiO<sub>2</sub>, the difference in computed isotropic shielding is about 21 ppm; for Mg<sub>3</sub>(PO<sub>4</sub>)<sub>2</sub>, the difference in isotropic shielding is about 37 ppm. However, both methods predict similar values for the spans of the magnetic-shielding tensors of these sites, indicating that the two methods predict similar differences between nuclei in different chemical environments, but different absolute shieldings.

### 6.3.2.1 Comparison of Periodic and Cluster Models

All results presented in this section were obtained with the PBE functional. As suggested in the previous section, magnetic-shielding constants obtained using the cluster-based method are substantially more shielded than those obtained with the PBC method. The mean absolute deviations between the two methodologies for <sup>29</sup>Si and <sup>31</sup>P are 21.4 ppm and 38.0 ppm, respectively. The cluster-based calculations are in closer agreement with experimental magnetic-shielding constants determined from chemical shifts and the absolute reference shieldings of Jameson [66, 67]. For <sup>29</sup>Si, the residuals between calculation and experiment are 51.2 ppm for the GIPAW approach and 25.3 ppm for the VMTA/BV approach. For <sup>31</sup>P, the residuals between calculation and experiment are 57.4 ppm for the GIPAW approach and 13.3 ppm for the VMTA/BV approach.

Plots illustrating the relationship between calculated ( $\sigma_{ii}^{calc}$ ) and experimental ( $\sigma_{ii}^{exp}$ ) principal components of the magnetic-shielding tensors illustrate the relationship between the two computational methodologies and experimental results (Figures 6.3

and 6.4). For  $^{29}\text{Si}$  magnetic shielding, linear regression on the GIPAW and VMTA/BV datasets yields the best-fit relations:

$$\sigma_{ii}^{GIPAW} = (1.05 \pm 0.02) \sigma_{ii}^{exp} - (67 \pm 7) \text{ ppm}, \quad \text{(Eq. 6.4)}$$

$$\sigma_{ii}^{VMTA/BV} = (1.02 \pm 0.02) \sigma_{ii}^{exp} - (33 \pm 9) \text{ ppm}. \quad \text{(Eq. 6.5)}$$

For  $^{31}\text{P}$  magnetic shielding, linear regression on the GIPAW and VMTA/BV datasets yields:

$$\sigma_{ii}^{GIPAW} = (1.10 \pm 0.01) \sigma_{ii}^{exp} - (85 \pm 4) \text{ ppm}, \quad \text{(Eq. 6.6)}$$

$$\sigma_{ii}^{VMTA/BV} = (1.04 \pm 0.01) \sigma_{ii}^{exp} - (24 \pm 5) \text{ ppm}. \quad \text{(Eq. 6.7)}$$

The linear-regression parameters for the GIPAW calculations of  $^{31}\text{P}$  magnetic shieldings are the same (to within experimental uncertainty) as those reported previously for phosphorus-containing molecular solids . Statistical data are presented in Table 6.3.

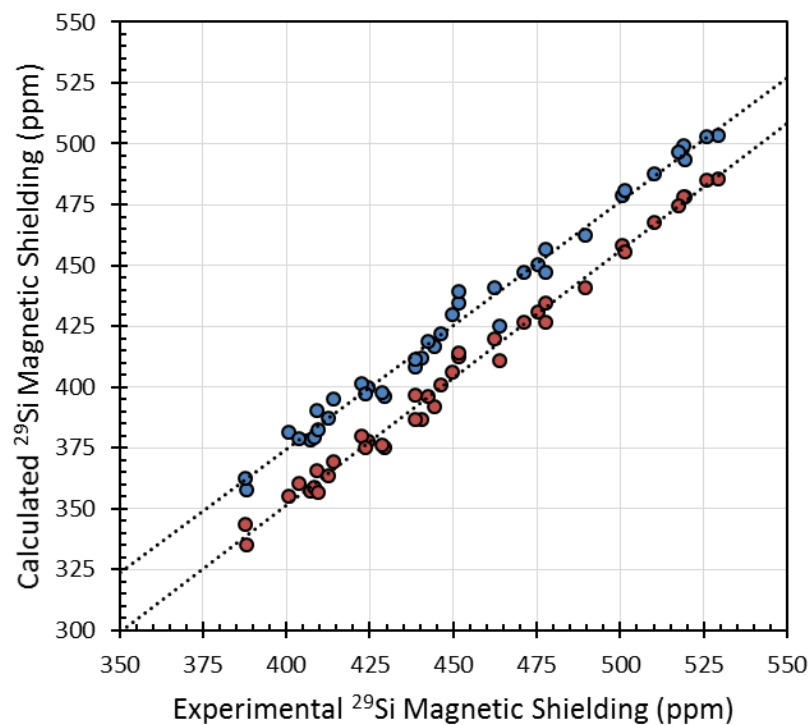


**Figure 6.3.** Plots illustrating the relationship between calculated and experimental principal components of <sup>29</sup>Si magnetic-shielding tensors. Values obtained using the GIPAW approach are shown in red, and results obtained using the cluster-based VMTA/BV approach are shown in blue. Results were computed at the PBE level of theory. The best-fit lines are shown in black.

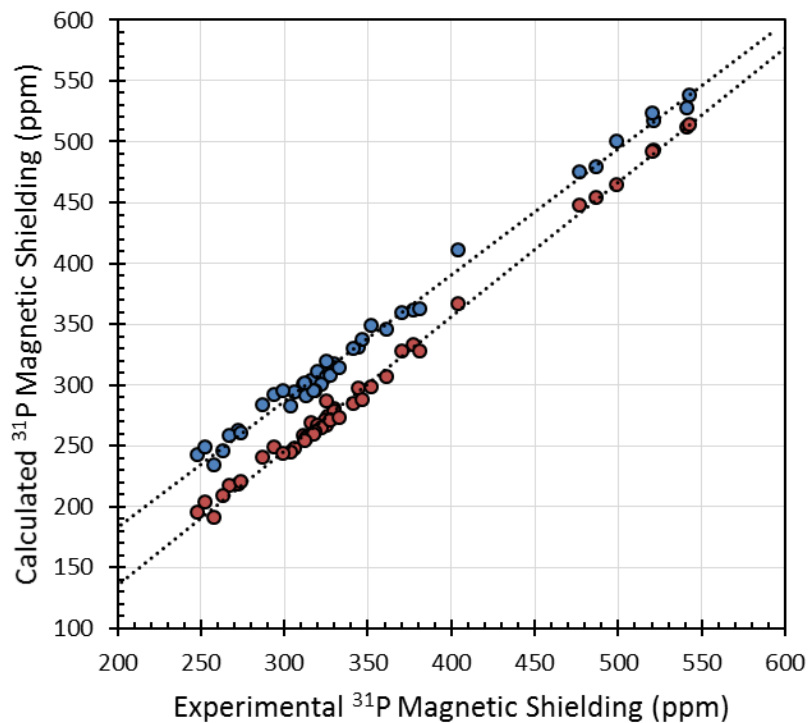


**Figure 6.4.** Plots illustrating the relationship between calculated and experimental principal components of  $^{31}\text{P}$  magnetic-shielding tensors. Values obtained using the GIPAW approach are shown in red, and results obtained using the cluster-based VMTA/BV approach are shown in blue. Results were computed at the PBE level of theory. The best-fit lines are shown in black.

### 6.3.3 Benchmarking DFT Functionals

Magnetic-shielding calculations were also performed using the DFT functionals CA-PZ, PW91, rPBE, PBEsol, WC, and PBE0. Of these calculations, those using the CA-PZ, PW91, rPBE, PBEsol, and WC functionals were performed using the GIPAW method. Calculations with the hybrid PBE0 functional used the cluster-based approach. Statistical data associated with these calculations, as well as the calculations described in the previous section, are summarized in Table 6.3. Five measures are used to quantify agreement between calculation and experiment. The first two are the slope ( $m$ , ideally unity) and intercept ( $b$ , ideally zero) of the best-fit line. In addition, we define the residual  $R_N$  as the standard error between calculated magnetic shielding ( $\sigma_{ii}^{calc}$ ) and experimental magnetic shielding ( $\sigma_{ii}^{exp}$ ), the residual  $R_{N-1}$  as the standard error between  $\sigma_{ii}^{calc}$  and the predicted magnetic shielding ( $\sigma_{ii}^{pred}$ ) obtained using the linear-regression parameter  $b$  for that model chemistry, and the residual  $R_{N-2}$  as the standard error between  $\sigma_{ii}^{calc}$  and the predicted magnetic shielding ( $\hat{\sigma}_{ii}^{pred}$ ) obtained using the linear-regression parameters  $m$  and  $b$  for that model chemistry. Of these metrics,  $R_N$  and  $b$  measure the ability of the model chemistry to calculate magnetic shielding on an absolute scale,  $R_{N-1}$  and  $m$  measure the ability to calculate relative chemical shifts, and  $R_{N-2}$  measures the scatter around the best-fit line.

The GIPAW calculations for each DFT functional result in trend lines with slopes ranging between 1.03 and 1.08 for  $^{29}\text{Si}$  and between 1.09 and 1.14 for  $^{31}\text{P}$ . The computed intercepts range between -52 ppm and -100 ppm for  $^{29}\text{Si}$  and between -70 ppm and -120 ppm for  $^{31}\text{P}$ . As demonstrated in the previous section, PBE calculations employing the TZ2P basis set outperform calculations obtained using plane waves. This result is reflected in the statistical data in Table 6.3. Further improvement over the PBE

model is observed when employing the hybrid PBE0 functional (Figures 6.5 and 6.6).

For  $^{29}\text{Si}$ , the calculations yield:

$$\sigma_{ii}^{PBE0} = (1.00 \pm 0.02) \sigma_{ii}^{exp} - (10 \pm 10) \text{ ppm}, \quad (\text{Eq. 6.8})$$

Similarly, calculations for  $^{31}\text{P}$  yield:

$$\sigma_{ii}^{PBE0} = (1.00 \pm 0.01) \sigma_{ii}^{exp} - (1 \pm 4) \text{ ppm}. \quad (\text{Eq. 6.9})$$

We note that the slopes of the lines obtained at the PBE0/TZ2P level do not differ from unity to within experimental error, whereas the results obtained with the pure PBE method do, and that the intercepts of the lines for PBE0/TZ2P are much closer to zero than are those observed with the PBE method. In the case of  $^{29}\text{Si}$ , the uncertainty in the experimental reference shielding is  $\pm 10$  ppm. Given the uncertainties in  $m$  and  $b$ , deviations in  $R_{N-2}$  are not statistically significant among the computational methodologies.

There is a significant trend in the correlation between errors in  $m$ ,  $b$ ,  $R_N$ , and  $R_{N-1}$ , which follow the scheme CA-PZ/GIPAW > WC/GIPAW > PBEsol/GIPAW > PW91/GIPAW > PBE/GIPAW > rPBE/GIPAW > PBE/VMTA/BV > PBE0/VMTA/BV (Table 6.3). This trend is consistent for both nuclei. The strong correlation between the two linear-regression parameters  $m$  and  $b$  suggests a link between errors in absolute magnetic shielding (evaluated by  $b$ ) and errors in relative chemical shifts (evaluated by  $m$ ) for the eight model chemistries considered here (Figure 6.7).

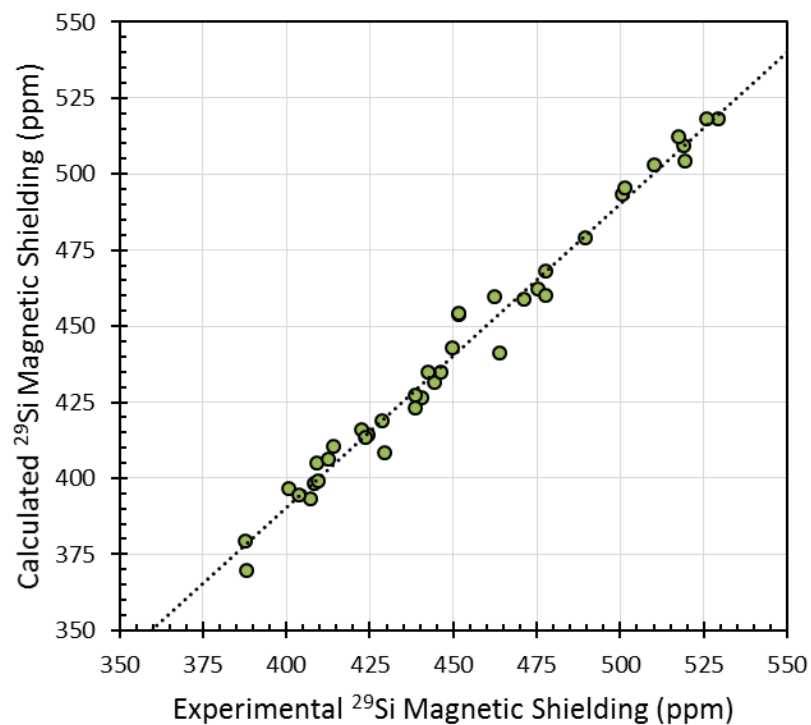


**Figure 6.5.** Plot illustrating the relationship between calculated and experimental principal components of  $^{29}\text{Si}$  magnetic-shielding tensors. Results were computed at the PBE0 level of theory. The best-fit lines are shown in black.

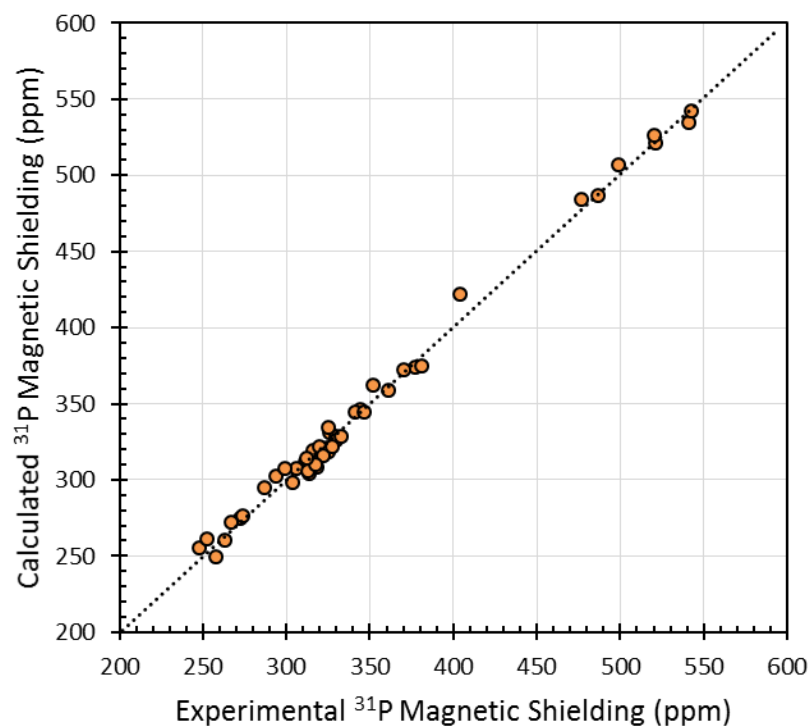


**Figure 6.6.** Plot illustrating the relationship between calculated and experimental principal components of  $^{31}\text{P}$  magnetic-shielding tensors. Results were computed at the PBE0 level of theory. The best-fit lines are shown in black.

**Table 6.3.** Linear-regression parameters ( $m$ ,  $b$ ) for the relationship between experimental and calculated principal components of magnetic-shielding tensors and residuals between experimental and calculated magnetic shielding.

Functional	Method	$m$	$b$ (ppm)	$R_N^a$ (ppm)	$R_{N-1}^b$ (ppm)	$R_{N-2}^c$ (ppm)
<b>Silicon-29</b>						
CA-PZ	GIPAW	$1.08 \pm 0.02$	$-100 \pm 8$	65.6	35.9	4.2
WC	GIPAW	$1.05 \pm 0.02$	$-76 \pm 8$	51.2	26.0	4.0
PBEsol	GIPAW	$1.05 \pm 0.02$	$-74 \pm 8$	50.6	24.6	4.0
PW91	GIPAW	$1.05 \pm 0.02$	$-67 \pm 7$	46.7	21.8	4.1
PBE	GIPAW	$1.04 \pm 0.02$	$-67 \pm 7$	46.4	21.6	4.0
rPBE	GIPAW	$1.03 \pm 0.02$	$-52 \pm 7$	37.9	15.3	3.9
PBE	VMTA/BV	$1.02 \pm 0.02$	$-33 \pm 9$	25.3	10.3	4.9
PBE0	VMTA/BV	$1.00 \pm 0.02$	$-10 \pm 10$	11.1	5.6	5.5
<b>Phosphorus-31</b>						
CA-PZ	GIPAW	$1.14 \pm 0.01$	$-120 \pm 4$	72.7	46.0	5.2
WC	GIPAW	$1.11 \pm 0.01$	$-95 \pm 5$	56.7	37.4	6.2
PBEsol	GIPAW	$1.11 \pm 0.01$	$-92 \pm 4$	54.3	36.7	5.0
PW91	GIPAW	$1.10 \pm 0.01$	$-86 \pm 4$	50.5	34.2	5.1
PBE	GIPAW	$1.10 \pm 0.01$	$-85 \pm 4$	49.9	34.1	5.0
rPBE	GIPAW	$1.09 \pm 0.01$	$-70 \pm 4$	40.2	29.1	4.9
PBE	VMTA/BV	$1.04 \pm 0.01$	$-24 \pm 5$	13.3	13.5	6.6
PBE0	VMTA/BV	$1.00 \pm 0.01$	$-1 \pm 4$	6.3	6.3	6.1

<sup>a</sup>Standard error between calculated magnetic shielding and experimental magnetic

$$\text{shielding, } R_N = \sqrt{\frac{1}{N} \sum_{ii} (\sigma_{ii}^{exp} - \sigma_{ii}^{calc})^2}.$$

<sup>b</sup>Standard error between calculated magnetic shielding and the predicted magnetic shielding obtained using the linear-regression parameter  $b$  for that model chemistry,

$$R_{N-1} = \sqrt{\frac{1}{N-1} \sum_{ii} (\sigma_{ii}^{pred} - \sigma_{ii}^{calc})^2}, \sigma_{ii}^{pred} = \sigma_{ii}^{exp} + b.$$

<sup>c</sup>Standard error between calculated magnetic shielding and the predicted magnetic shielding ( $\hat{\sigma}_{ii}^{pred}$ ) obtained using the linear-regression parameters  $m$  and  $b$  for that

$$\text{model chemistry, } R_{N-2} = \sqrt{\frac{1}{N-2} \sum_{ii} (\hat{\sigma}_{ii}^{pred} - \sigma_{ii}^{calc})^2}, \hat{\sigma}_{ii}^{pred} = (\sigma_{ii}^{exp} + b)/m.$$

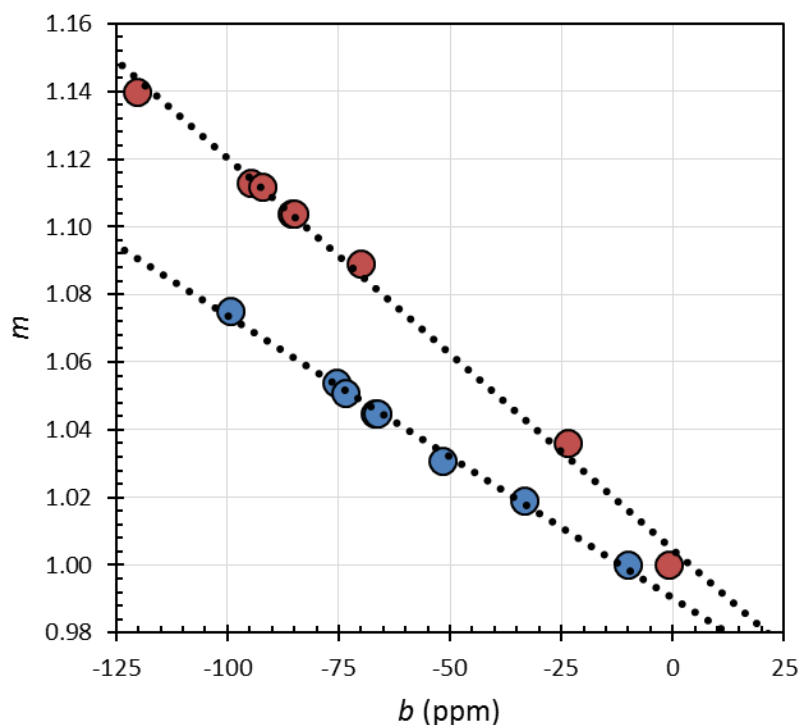


**Figure 6.7.** Correlation between the linear-regression parameters  $m$  and  $b$  for eight DFT model chemistries. Results for  $^{29}\text{Si}$  and  $^{31}\text{P}$  are shown in red and blue, respectively. GIPAW results are shown as circles; cluster-based VMTA/BV results are shown as squares.

## 6.4 Conclusions

We present DFT calculations of  $^{29}\text{Si}$  and  $^{31}\text{P}$  magnetic-shielding constants in crystalline solids obtained using the VMTA/BV method, where the outermost atoms of the cluster are given an effective nuclear charge to reduce the net charge of the cluster. These calculations are compared to values obtained using the GIPAW approach, which treats the materials with periodic boundary conditions. We find that the cluster-based calculations lead to a modest increase in accuracy for relative chemical-shift parameters over those obtained by the GIPAW approach. Furthermore, the cluster-based

calculations lead to a significant increase in accuracy for absolute magnetic-shielding parameters.

Further calculations with the two computational methodologies evaluate differences in eight model chemistries for the prediction of  $^{29}\text{Si}$  and  $^{31}\text{P}$  magnetic shielding. The hybrid functional PBE0 improves upon the GGA-PBE functional for calculations of the principal components of magnetic-shielding tensors of both  $^{29}\text{Si}$  and  $^{31}\text{P}$  sites. The extrapolated shielding of the reference compounds (TMS for  $^{29}\text{Si}$  and  $\text{H}_3\text{PO}_4$  for  $^{31}\text{P}$ ) are predicted to be more shielded when using the PBE0 functional than is observed for the pure DFT functionals. The higher predicted values for the reference shielding are in closer agreement with work on absolute shielding reference scales.[66, 67] The PBE0 model chemistry yields best-fit lines between experimental and calculated magnetic shielding with slopes and intercepts not statistically different from unity and zero, respectively.

## REFERENCES

- [1] X.Y. Xue, M. Kanzaki, An ab initio calculation of  $^{17}\text{O}$  and  $^{29}\text{Si}$  NMR parameters for  $\text{SiO}_2$  polymorphs, *Solid State Nucl. Magn. Reson.*, 16 (2000) 245-259.
- [2] F. Pourpoint, A. Kolassiba, C. Gervais, T. Azais, L. Bonhomme-Coury, C. Bonhomme, F. Mauri, First principles calculations of NMR parameters in biocompatible materials science: the case study of calcium phosphates, b- and g- $\text{Ca}(\text{PO}_3)_2$ . combination with MAS-J experiments, *Chem. Mater.*, 19 (2007) 6367-6369.
- [3] C. van Wullen, A comparison of density functional methods for the calculation of phosphorus-31 NMR chemical shifts, *Phys. Chem. Chem. Phys.*, 2 (2000) 2137-2144.
- [4] T. Heine, A. Goursot, G. Seifert, J. Weber, Performance of DFT for  $^{29}\text{Si}$  NMR chemical shifts of silanes, *J. Phys. Chem. A*, 105 (2001) 620-626.
- [5] E. Brendler, T. Heine, W. Seichter, J. Wagler, R. Witter,  $^{29}\text{Si}$  NMR shielding tensors in triphenylsilanes –  $^{29}\text{Si}$  solid state NMR experiments and DFT-IGLO calculations, *Z. Anorg. Allg. Chem.*, 638 (2012) 935-944.
- [6] D.H. Brouwer, I.L. Moudrakovski, R.J. Darton, R.E. Morris, Comparing quantum-chemical calculation methods for structural investigation of zeolite crystal structures by solid-state NMR spectroscopy, *Magn. Reson. Chem.*, 48 (2010) S113-S121.
- [7] C.J. Pickard, F. Mauri, All-electron magnetic response with pseudopotentials: NMR chemical shifts, *Phys. Rev. B*, 63 (2001) 245101.
- [8] C. Bonhomme, C. Gervais, F. Babonneau, C. Coelho, F. Pourpoint, T. Azais, S.E. Ashbrook, J.M. Griffin, J.R. Yates, F. Mauri, C.J. Pickard, First-principles calculation of NMR parameters using the gauge including projector augmented wave method: a chemist's point of view, *Chem. Rev.*, 112 (2012) 5733-5779.
- [9] S.T. Holmes, R.J. Iulucci, K.T. Mueller, C. Dybowski, Critical analysis of cluster models and exchange-correlation functionals for calculating magnetic shielding in molecular solids, *J. Chem. Theory Comput.*, 11 (2015) 5229-5241.
- [10] F. Alkan, C. Dybowski, Calculation of chemical-shift tensors of heavy nuclei: a DFT/ZORA investigation of  $^{199}\text{Hg}$  chemical-shift tensors in solids, and the effects of cluster size and electronic-state approximations, *Phys. Chem. Chem. Phys.*, 16 (2014) 14298-14308.

- [11] F. Alkan, C. Dybowski, Chemical-shift tensors of heavy nuclei in network solids: a DFT/ZORA investigation of  $^{207}\text{Pb}$  chemical-shift tensors using the bond-valence method, *Phys. Chem. Chem. Phys.*, **17** (2015) 25014-25026.
- [12] F. Alkan, C. Dybowski, Effect of co-ordination chemistry and oxidation state on  $^{207}\text{Pb}$  magnetic-shielding tensor: a DFT/ZORA investigation. , *J. Phys. Chem. A*, **120** (2016) 161-168.
- [13] J.A. Tossell, Second-nearest-neighbor effects upon N NMR shieldings in models for solid  $\text{Si}_3\text{N}_4$  and  $\text{C}_3\text{N}_4$ , *J. Magn. Reson.*, **127** (1997) 49-53.
- [14] J.A. Tossell, Second-nearest-neighbor effects on the NMR shielding of N in  $\text{P}_3\text{N}_5$  and hexagonal BN, *Chem. Phys. Lett.*, **303** (1999) 435-440.
- [15] J.A. Tossell, Quantum mechanical calculation of  $^{23}\text{Na}$  NMR shieldings in silicates and aluminosilicates, *Phys. Chem. Miner.*, **27** (1999) 70-80.
- [16] G. Valerio, A. Goursot, R. Vetrivel, O. Malkina, V. Malkin, D.R. Salahub, Calculation of  $^{29}\text{Si}$  and  $^{27}\text{Al}$  MAS NMR chemical shifts in zeolite- $\beta$  using density functional theory: correlation with lattice structure, *J. Am. Chem. Soc.*, **120** (1998) 11426-11431.
- [17] G. Valerio, A. Goursot, Density functional calculations of the  $^{29}\text{Si}$  and  $^{27}\text{Al}$  MAS NMR spectra of the zeolite mazzite: analysis of geometrical and electronic effects, *J. Phys. Chem. B*, **103** (1999) 51-58.
- [18] D.H. Brouwer, G.D. Enright, Probing local structure in zeolite frameworks: ultrahigh-field NMR measurements and accurate first-principles calculations of zeolite  $^{29}\text{Si}$  magnetic shielding tensors, *J. Am. Chem. Soc.*, **130** (2008) 3095-3105.
- [19] J. Weber, J. Schmedt auf der Gunne, Calculation of NMR parameters in ionic solids by an improved self-consistent embedded cluster method, *Phys. Chem. Chem. Phys.*, **12** (2010) 583-603.
- [20] D. Stueber, F.N. Guenneau, D.M. Grant, The calculation of  $^{13}\text{C}$  chemical shielding tensors in ionic compounds utilizing point charge arrays obtained from Ewald lattice sums, *J. Chem. Phys.*, **114** (2001) 9236-9243.
- [21] D. Stueber, D.M. Grant,  $^{13}\text{C}$  and  $^{15}\text{N}$  chemical shift tensors in adenosine, guanosine dihydrate, 2'-deoxythymidine, and cytidine, *J. Am. Chem. Soc.*, **124** (2002) 10539-10551.
- [22] D. Stueber, The embedded ion method: a new approach to the electrostatic description of crystal lattice effects in chemical shielding calculations, *Concepts Magn. Reson., Part A*, **28A** (2006) 347-368.

- [23] R. Bjornsson, M. Bühl, Modeling molecular crystals by QM/MM: Self-consistent electrostatic embedding for geometry optimizations and molecular property calculations in the solid, *J. Chem. Theory Comput.*, 8 (2012) 498-508.
- [24] M.B. Ferraro, V. Repetto, J.C. Facelli, Modeling NMR chemical shifts: a comparison of charge models for solid state effects on  $^{15}\text{N}$  chemical shift tensors, *Solid State Nucl. Magn. Reson.*, 10 (1998) 185-189.
- [25] D. Solís, M.B. Ferraro, J.C. Facelli, Modeling NMR chemical shifts: surface charge representation of the electrostatic embedding potential modeling of crystalline intermolecular effects in  $^{19}\text{F}$  solid state NMR chemical shifts, *J. Mol. Struct.*, 602–603 (2002) 159-164.
- [26] I.D. Brown, Recent developments in the methods and applications of the bond valence model, *Chem. Rev.*, 109 (2009) 6858-6919.
- [27] I.D. Brown, Bond valences - a simple structural model for inorganic chemistry, *Chem. Soc. Rev.*, 7 (1978) 359-376.
- [28] I.D. Brown, D. Altermatt, Bond-valence parameters obtained from a systematic analysis of the inorganic crystal-structure database, *Acta Crystallogr., Sect. B*, 41 (1985) 244-247.
- [29] I.D. Brown, R.D. Shannon, Empirical bond-strength bond-length curves for oxides, *Acta Crystallogr., Sect. A*, A 29 (1973) 266-282.
- [30] I.D. Brown, K.K. Wu, Empirical parameters for calculating cation-oxygen bond valences, *Acta Crystallogr., Sect. B*, 32 (1976) 1957-1959.
- [31] D.R. Spearing, J.F. Stebbins, The  $^{29}\text{Si}$  NMR shielding tensor in low quartz, *Am. Mineral.*, 74 (1989) 956-959.
- [32] S.M. Antao, I. Hassan, J. Wang, P.L. Lee, B.H. Toby, State-of-the-art high-resolution powder X-ray diffraction (HRXRPD) illustrated with rietveld structure refinement of quartz, sodalite, tremolite, and meionite, *Can. Mineral.*, 46 (2008) 1501-1509.
- [33] K.A. Smith, R.J. Kirkpatrick, E. Oldfield, D.M. Henderson, High-resolution silicon-29 nuclear magnetic resonance spectroscopic study of rock-forming silicates, *Am. Mineral.*, 68 (1983) 1206-1215.
- [34] R.I. Smith, R.A. Howie, A.R. West, A. Aragonpina, M.E. Villafuertecastreion, The structure of metastable lithium disilicate,  $\text{Li}_2\text{Si}_2\text{O}_5$ , *Acta Crystallogr., Sect. C*, 46 (1990) 363-365.

- [35] M.R. Hansen, H.J. Jakobsen, J. Skibsted,  $^{29}\text{Si}$  chemical shift anisotropies in calcium silicates from high-field  $^{29}\text{Si}$  MAS NMR spectroscopy, *Inorg. Chem.*, 42 (2003) 2368-2377.
- [36] F. Liu, S.H. Garofalini, R.D. Kingsmith, D. Vanderbilt, Structural and electronic properties of sodium metasilicate, *Chem. Phys. Lett.*, 215 (1993) 401-404.
- [37] A.K. Pant, D.W.J. Cruickshank, Crystal structure of  $\alpha\text{-Na}_2\text{Si}_2\text{O}_5$ , *Acta Crystallogr., Sect. B*, B 24 (1968) 13-&.
- [38] N. Weiden, H. Rager, The chemical shift of the  $^{29}\text{Si}$  nuclear magnetic resonance in a synthetic single crystal of  $\text{Mg}_2\text{SiO}_4$ , *Z. Naturforsch., A: Phys. Sci.*, 40 (1985) 126-130.
- [39] R.M. Hazen, Effects of temperature and pressure on the crystal structure of forsterite, *Am. Mineral.*, 61 (1976) 1280-1293.
- [40] S. Ghose, V. Schomaker, R.K. McMullan, Enstatite,  $\text{Mg}_2\text{Si}_2\text{O}_6$ : a neutron diffraction refinement of the crystal structure and a rigid-body analysis of the thermal vibration, *Z. Kristallogr.*, 176 (1986) 159-175.
- [41] Y. Ohashi, Polysynthetically-twinned structures of enstatite and wollastonite, *Phys. Chem. Miner.*, 10 (1984) 217-229.
- [42] S. Saburi, I. Kusachi, C. Henmi, A. Kawahara, K. Henmi, I. Kawada, Refinement of the structure of rankinite, *Mineral. J.*, 8 (1976) 240-246.
- [43] Z.D. Sharp, R.M. Hazen, L.W. Finger, High-pressure crystal chemistry of monticellite,  $\text{CaMgSiO}_4$ , *Am. Mineral.*, 72 (1987) 748-755.
- [44] A.G. Nord, Kierkega.P, Crystal structure of  $\text{Mg}_3(\text{PO}_4)_3$ , *Acta Chem. Scand.*, 22 (1968) 1466-&.
- [45] A.G. Nord, K.B. Lindberg, Crystal structure of magnesium tetrametaphosphate,  $\text{Mg}_2\text{P}_4\text{O}_{12}$ , *Acta Chem. Scand.*, A 29 (1975) 1-6.
- [46] C. Calvo, Crystal structure of  $\alpha\text{-Mg}_2\text{P}_2\text{O}_7$ , *Acta Crystallogr.*, 23 (1967) 289-&.
- [47] D. Stachel, H. Paulus, C. Guenter, H. Fuess, Crystal structure of magnesium ultraphosphate,  $\text{MgP}_4\text{O}_{11}$ , *Z. Kristallogr.*, 199 (1992) 275-276.
- [48] F. Pourpoint, C. Gervais, L. Bonhomme-Coury, F. Mauri, B. Alonso, C. Bonhomme, Calcium phosphates: first-principles calculations vs. solid-state NMR experiments, *C. R. Chim.*, 11 (2008) 398-406.
- [49] J. Emery, Y. Lalignat, J.Y. Buzare, L. Smiri, F. Hlel, T. Ben-Chaabane, Correlation between  $^{31}\text{P}$  chemical shift tensor and local structure in lithium cyclohexaphosphates  $\text{Li}_6\text{P}_6\text{O}_{18} \cdot 3\text{H}_2\text{O}$  and  $\text{Li}_6\text{P}_6\text{O}_{18}$ , *Solid State Nucl. Magn. Reson.*, 16 (2000) 291-304.

- [50] M. Toumi, F. Hlel, T. Ben Chaabane, L. Smiri, Y. Laligant, J. Emery, X-Ray powder structure determination of  $\text{Li}_6\text{P}_6\text{O}_{18}\cdot 3\text{H}_2\text{O}$ , *Eur. J. Solid State Inorg. Chem.*, 35 (1998) 689-697.
- [51] P. Amornsakchai, D.C. Apperley, R.K. Harris, P. Hodgkinson, P.C. Waterfield, Solid-state NMR studies of some tin(II) compounds, *Solid State Nucl. Magn. Reson.*, 26 (2004) 160-171.
- [52] R.C. McDonald, K. Eriks, Crystallographic studies of tin(II) compounds. 2. structures of tin(II) hydrogen phosphate and tin(II) phosphite,  $\text{SnHPO}_4$  AND  $\text{SnHPO}_3$ , *Inorg. Chem.*, 19 (1980) 1237-1241.
- [53] J.P. Perdew, K. Burke, M. Ernzerhof, Generalized gradient approximation made simple, *Phys. Rev. Lett.*, 77 (1996) 3865-3868.
- [54] J.R. Yates, C.J. Pickard, F. Mauri, Calculation of NMR chemical shifts for extended systems using ultrasoft pseudopotentials, *Phys. Rev. B*, 76 (2007).
- [55] D.M. Ceperley, B.J. Alder, Ground state of the electron gas by a stochastic method, *Phys. Rev. Lett.*, 45 (1980) 566-569.
- [56] J.P. Perdew, A. Zunger, Self-interaction correction to density-functional approximations for many-electron systems, *Phys. Rev. B*, 23 (1981) 5048-5079.
- [57] J.P. Perdew, Y. Wang, Accurate and simple analytic representation of the electron-gas correlation energy, *Phys. Rev. B*, 45 (1992) 13244.
- [58] B. Hammer, L.B. Hansen, J.K. Nørskov, Improved adsorption energetics within density-functional theory using revised Perdew-Burke-Ernzerhof functionals, *Phys. Rev. B*, 59 (1999) 7413-7421.
- [59] J.P. Perdew, A. Ruzsinszky, G.I. Csonka, O.A. Vydrov, G.E. Scuseria, L.A. Constantin, X. Zhou, K. Burke, Restoring the density-gradient expansion for exchange in solids and surfaces, *Phys. Rev. Lett.*, 100 (2008) 136406.
- [60] Z. Wu, R.E. Cohen, More accurate generalized gradient approximation for solids, *Phys. Rev. B*, 73 (2006) 235116.
- [61] R. Ditchfield, Self-Consistent Perturbation-Theory of Diamagnetism .1. Gauge-Invariant Lcao Method for Nmr Chemical-Shifts, *Mol. Phys.*, 27 (1974) 789-807.
- [62] K. Wolinski, J.F. Hinton, P. Pulay, Efficient Implementation of the Gauge-Independent Atomic Orbital Method for Nmr Chemical-Shift Calculations, *J. Am. Chem. Soc.*, 112 (1990) 8251-8260.

- [63] C. Adamo, V. Barone, Toward reliable density functional methods without adjustable parameters: the PBE0 model, *J. Chem. Phys.*, 110 (1999) 6158-6170.
- [64] S.J. Clark, M.D. Segall, C.J. Pickard, P.J. Hasnip, M.J. Probert, K. Refson, M.C. Payne, First principles methods using CASTEP, *Z. Kristallogr.*, 220 (2005) 567-570.
- [65] ADF2014, SCM, Theoretical Chemistry, Vrije Universiteit, Amsterdam, The Netherlands, <http://www.scm.com>.
- [66] C.J. Jameson, A.K. Jameson, Absolute shielding scale for  $^{29}\text{Si}$ , *Chem. Phys. Lett.*, 149 (1988) 300-305.
- [67] C.J. Jameson, A. De Dios, A.K. Jameson, Absolute shielding scale for  $^{31}\text{P}$  from gas-phase NMR studies, *Chem. Phys. Lett.*, 167 (1990) 575-582.

## Chapter 7

### SEMI-EMPIRICAL REFINEMENTS OF CRYSTAL STRUCTURES USING <sup>17</sup>O QUADRUPOLEAR-COUPLING TENSORS

#### 7.1 Introduction

Solid-state nuclear magnetic resonance (NMR) spectroscopy has emerged as a robust technique for obtaining structural information, leading to suggestions that one may determine crystallographic structures by comparison of experimental NMR parameters to predictions of calculations on theoretical structures [1]. As implemented, NMR crystallography combines solid-state NMR spectroscopy and modern computational methods to verify, refine, or predict crystal structures. One significant advantage that solid-state NMR spectroscopy has long had over X-ray diffraction is the ability to locate the positions of hydrogen atoms with a high degree of precision. The positions of hydrogen atoms in extended hydrogen-bonding networks have been refined in numerous materials using techniques that compare NMR parameters to predictions based on theoretical structures [2-5]. NMR crystallography has also been used to detect distortions in molecular symmetry below the limit of detection of neutron diffraction [6], identify the number of molecules in the asymmetric unit [7], predict stereochemistry [8, 9], refine bond lengths and other ambiguous structural features in disordered systems [10-14], resolve space groups [15], and characterize static disorder in co-crystals [16, 17]. Beyond the ability to refine structures, several studies have illustrated complete, or partial, structural prediction based on constraints derived from NMR spectroscopy in conjunction with calculations of NMR parameters [18-22].

This study focuses on refinements of atomic coordinates in X-ray- or neutron-diffraction-derived crystal structures using parameters obtained by solid-state NMR or nuclear quadrupole resonance (NQR) spectroscopy. To date, several types of NMR data have been used to refine crystal structures. These include isotropic chemical shifts, quadrupolar coupling constants, and homonuclear spin-spin coupling constants [23]. Chemical-shift tensors, which provide more structural detail than isotropic shifts, have been used to assess structural refinements. For example, Harper *et al.* have illustrated that refinement of structures of molecular solids can be evaluated by comparison to computed  $^{13}\text{C}$  magnetic-shielding tensors [24]. Kalakewich *et al.* have performed a similar analysis using computed  $^{15}\text{N}$  magnetic-shielding tensors [23]. Studies by Brouwer and co-workers have discussed refinements of zeolite structures using agreement of  $^{29}\text{Si}$  chemical-shift tensors with predicted values [25-27]. Another study has refined atomic coordinates in sulfates through examination of  $^{33}\text{S}$  chemical-shift tensors [28]. These various studies illustrate how comparison of computed NMR chemical-shift tensors to experimental results provide a barometer of the refinement of atomic positions in crystal structures to a precision that exceeds that of single-crystal X-ray diffraction alone. In some cases, it appears that such a procedure may match or exceed the structural resolution obtainable by neutron diffraction [23, 24, 29].

Although it has been illustrated that structural refinements can be assessed through agreement of computed chemical-shift tensors with experiment, other tensor parameters, such as quadrupolar-coupling tensors, may also prove valuable in this endeavor. The sensitivity of the  $^{17}\text{O}$  quadrupolar-coupling tensor to structure has been established both experimentally [30-35] and computationally [36-42]. Several reviews of techniques and applications of  $^{17}\text{O}$  NMR spectroscopy have been provided [43-45].

One significant application of  $^{17}\text{O}$  NMR crystallography is the evaluation of distributions of structural features in glasses [46-55]. Numerous studies of oxygen-containing molecular solids exist [56-61], including investigations of active pharmaceutical ingredients [62]. A compilation of  $^{17}\text{O}$  quadrupolar-coupling parameters in molecular solids indicates that the range of the principal values of the  $^{17}\text{O}$  quadrupolar-coupling tensor is approximately 18 MHz [43].

The reported uncertainties of  $^{17}\text{O}$  quadrupolar parameters determined by NMR and NQR are different. It is common to determine the quadrupolar-coupling constant,  $C_Q$ , to  $\pm 0.3$  MHz and the asymmetry parameter,  $\eta$ , to within  $\pm 0.05$  by NMR spectroscopy. In contrast, NQR studies are able to specify  $C_Q$  and  $\eta$  to within  $\pm 0.02$  MHz and  $\pm 0.02$ , respectively. The wide range of possible  $^{17}\text{O}$  quadrupolar-coupling tensors suggests comparison of computed quadrupolar parameters to experiment may serve as a sensitive probe of the structure of molecules containing  $^{17}\text{O}$  sites.

In this study, various refinements of crystal structures are assessed by comparison of calculated  $^{17}\text{O}$  quadrupolar-coupling tensors to experimental results. Plane-wave density functional theory (DFT), which inherently accounts for lattice forces during geometry optimization and intermolecular contributions to computed NMR parameters, is used in all calculations. We find that optimizations employing conventional plane-wave DFT are often insufficient to aid in refinement of structures of molecular solids, in a predictable and consistent manner, on the basis of comparison with experimental  $^{17}\text{O}$  quadrupolar-coupling tensors. To overcome this difficulty, we demonstrate a semi-empirical method to perform geometry optimizations with a re-parameterized two-body dispersion force field developed by Grimme [63]. The semi-empirical method is optimized to replicate experimental  $^{17}\text{O}$  quadrupolar-coupling

tensors in a series of model compounds. Subsequently, the optimized method is applied to the prediction of  $^{17}\text{O}$  quadrupolar-coupling tensors for forty-three oxygen sites in twenty-two materials. In addition, we assess structural refinements by this method, using  $^{13}\text{C}$ ,  $^{15}\text{N}$ , and  $^{17}\text{O}$  chemical-shift tensors as well as  $^{35}\text{Cl}$  quadrupolar-coupling tensors. We find that the structures obtained with this methodology give better agreement with experiment than structures obtained by either X-ray diffraction or conventional plane-wave DFT refinement of diffraction structures. Finally, we illustrate that calculations of  $^{17}\text{O}$  quadrupolar-coupling tensors using structures refined with this methodology give closer agreement with experiment than do similar calculations on structures derived from neutron-diffraction experiments.

## 7.2 Computational Details

### 7.2.1 Overview and Computational Strategy

All calculations were performed using crystal structures with atomic coordinates initially determined from X-ray or neutron diffraction studies. We explore several plane-wave DFT strategies for refining atomic coordinates in crystal structures, based on comparing computed  $^{17}\text{O}$  quadrupolar-coupling tensors with experiment. The strategies are based on refinements performed at the PW91 level [64], the PW91-D2 level [63], and the PW91-D2\* level, a semi-empirical method developed in our laboratory. Geometry optimizations and calculations of NMR parameters, including quadrupolar-coupling and magnetic-shielding tensors, used the CASTEP module of Accelrys' Materials Studio 7.0 [65]. Calculations were performed with a plane-wave cutoff energy of 600 eV and with core orbitals replaced by ultrasoft pseudopotentials generated *on the fly* [64]. The Brillouin zone was sampled with a  $k$ -point spacing of

0.07 Å<sup>-1</sup>. Structural refinements employed the energy-minimizing scheme of Broyden, Fletcher, Goldfarb, and Shanno [66]. The thresholds for structural convergence include a maximum change in energy of  $5 \times 10^{-6}$  eV atom<sup>-1</sup>, a maximum displacement of  $5 \times 10^{-4}$  Å atom<sup>-1</sup>, and a maximum Cartesian force of 0.01 eV Å<sup>-1</sup>. Lattice constants remained fixed during the geometry optimizations. Magnetic-shielding tensors were calculated with the GIPAW method of Pickard and Mauri [67].

### 7.2.2 Semi-Empirical Geometry Optimizations

In the proposed semi-empirical approach to geometry optimization, one incorporates a two-body force field into the Hamiltonian, the force field having been optimally parameterized to reflect <sup>17</sup>O quadrupolar-coupling tensors of a calibration set of materials. The structural-refinement strategy employs a re-parameterization of the two-body force field developed by Grimme for the description of long-range correlation interactions (dispersion), commonly referred to as DFT-D2 [63]. The semi-empirical dispersion energy follows the general form of Eq. 7.1:

$$E_{disp}^{D2} = -s_6 \sum_{i,j>1}^N \frac{c_6^{ij}}{R_{ij}^6} f_{damp}(R_{ij}). \quad (\text{Eq. 7.1})$$

In Eq. 7.1,  $E_{disp}^{D2}$  is the two-body dispersion correction to the Kohn-Sham energy ( $E_{KS}$ ).  $s_6$  is a scaling factor, the indices  $i$  and  $j$  denote the  $N$  atoms,  $c_6^{ij}$  is the dispersion coefficient for an atomic pair  $(i, j)$ ,  $R_{ij}$  is the interatomic distance of atomic pairs  $(i, j)$ , and  $f_{damp}(R_{ij})$  is a damping function that determines the effective range and steepness of the dispersion interaction. The total energy ( $E_{tot}$ ) is given by

$$E_{tot} = E_{KS} + E_{disp}^{D2}. \quad (\text{Eq. 7.2})$$

In the empirical D2 model, the damping function has a form similar to that of a Fermi-Dirac distribution function, as shown in Eq. 7.3:

$$f_{damp}(R_{ij}) = \frac{1}{1 + \exp\left[-d\left(\frac{R_{ij}}{R_0} - 1\right)\right]}. \quad (\text{Eq. 7.3})$$

In this expression,  $R_0$  is the sum of the van der Waals' radii of atoms  $i$  and  $j$ , and  $d$  is a damping parameter that specifies how sharply the dispersion interaction tends towards zero.

In Grimme's original work, the values of the adjustable parameters ( $s_6$ ,  $c_6^{ij}$ ,  $R_0$ , and  $d$ ) were obtained by modeling gas-phase thermochemistry [63]. This approach has been applied to periodic systems to predict properties of crystals, such as cohesive energies, lattice constants, bulk moduli, and vibrational lattice modes [68, 69]. Civalleri *et al.* have illustrated that the original parameterization may not be appropriate to molecular solids exhibiting hydrogen bonding, as is evident by the systematic overestimation of cohesive energies in such systems [69]. Jurečka *et al.* have shown that the damping function is “*the most critical point in DFT-D*”, and that rescaling this function often yields superior results [68]. In particular, rescaling the van der Waals' radii can change the effective distance of the dispersion interaction, whereas rescaling the damping parameter,  $d$ , controls the steepness of the onset of the dispersion correction.

In the present chapter, I explore a strategy for re-parameterizing the damping function by systematically varying the value of  $d$  across the range  $2.5 \leq d \leq 20$ . Geometry optimizations employing the various values of  $d$  are performed on a series of model compounds, and the resulting structures are assessed by comparing computed  $^{17}\text{O}$  quadrupolar-coupling tensors, calculated for each structure, to experimental values.

After that calibration step, this strategy is applied to a larger and more varied array of materials to assess the universality of the strategy. When additional types of NMR data, such as chemical-shift tensors, are available, these are also used as additional figures of merit to assess the structural-refinement strategy.

### 7.2.3 Conventions for Reporting NMR Parameters

The nuclear quadrupolar coupling reflects the electric-field gradient (EFG) in the vicinity of the nucleus. The EFG is represented by a traceless, second-rank tensor with principal values  $|V_{33}| \geq |V_{22}| \geq |V_{11}|$ . Because the EFG tensor is traceless, the quadrupolar-coupling tensor can be characterized completely by two parameters. Often, the quadrupolar-coupling tensor is described by the quadrupolar-coupling constant,  $C_Q$ , and the asymmetry parameter,  $\eta$ , given by

$$C_Q = eV_{33}Q/h, \quad \text{and} \quad (\text{Eq. 7.4})$$

$$\eta = \frac{V_{11} - V_{22}}{V_{33}}. \quad (\text{Eq. 7.5})$$

In these expressions,  $e$  is the elementary charge,  $h$  is Planck's constant, and  $Q$  is the  $^{17}\text{O}$  quadrupole moment. Because only the experimental magnitude of  $C_Q$  is typically reported, the analysis assumes that the sign of the experimental value of  $C_Q$  is the same as that predicted by the calculations. Similarly, the quadrupolar-coupling tensor can be characterized by two unique principal values ( $C_{11} = eV_{11}/h$ ,  $C_{22} = eV_{22}/h$ ,  $C_{11} + C_{22} = -C_Q$ ). Errors reported in this study are based on differences between experiment and calculation for the principal values.

The relationship between the principal components of calculated magnetic-shielding tensors ( $\sigma_{ii}^{calc}$ ) and experimental chemical-shift tensors ( $\delta_{ii}^{exp}$ ) is fit to the form

$$\sigma_{ii}^{calc} = \sigma_{ref} - |m|\delta_{ii}^{exp}. \quad (\text{Eq. 7.6})$$

In Eq. 7.6,  $\sigma_{ref}$  is the magnetic shielding of the reference compound, and  $|m|$  is the magnitude of the slope of the best-fit line relating the principal values of  $\sigma_{ii}^{calc}$  and  $\delta_{ii}^{exp}$ . Calculated magnetic shielding is converted to the chemical-shift scale ( $\delta_{ii}^{calc}$ ) for comparison with experimental results by Eq. 7.7.

$$\delta_{ii}^{calc} = \frac{\sigma_{ref} - \sigma_{ii}^{calc}}{|m|}. \quad (\text{Eq. 7.7})$$

A more thorough discussion of the fitting procedure and the effects of different model chemistries on computed magnetic shielding is available in the literature [70]. We have modeled the relationship between principal components of computed magnetic-shielding tensors and experimental chemical-shift tensors with Eq. 7.6. Values for  $\sigma_{ref}$  and  $|m|$  for  $^{13}\text{C}$ ,  $^{15}\text{N}$ , and  $^{17}\text{O}$  sites, obtained by modeling the results with Eq. 7.6, are summarized in Table 7.1.

**Table 7.1.** Summary of linear-regression parameters describing the relationship between the principal components of calculated magnetic-shielding tensors and experimental chemical-shift tensors.

Nucleus	Reference compound	$\sigma_{ref}$ (ppm)	$ m $
Carbon-13	TMS	184.8	1.06
Nitrogen-15	$\text{CH}_3\text{NO}_2$	-171.2	1.10
Oxygen-17	$\text{H}_2\text{O}$	291.8	1.10

## 7.3 Results and Discussion

### 7.3.1 Parameterization of Force Field Using Model Compounds

We assess the structural effects due to rescaling of the damping function (Eq. 7.3) through computed  $^{17}\text{O}$  quadrupolar-coupling tensors for a series of model compounds (formic acid [56, 71], acetic acid [56, 72],  $\alpha$ -oxalic acid [56, 73],  $\beta$ -oxalic acid [56, 74], acrylic acid [56, 75], and urea [76, 77]). Geometry optimizations performed at the PW91-D2 level result only in small and inconsistent improvements in computed  $^{17}\text{O}$  quadrupolar-coupling tensors over optimizations performed at the PW91 level. We find that the largest and most systematic variations in  $^{17}\text{O}$  quadrupolar-coupling tensors result from structural refinements following rescaling of the damping parameter. Geometry optimizations performed on the model compounds for values of the damping parameter over the range  $2.5 \leq d \leq 20$ , with a fixed value of the scaling factor,  $s_6$ , of 1.00, demonstrate that the value of  $d$  affects both intramolecular bond lengths and intermolecular arrangements after geometry optimization.

The results of these calculations are summarized in Figure 7.1. Mean-absolute errors (MAEs) between experimental and computed principal components of  $^{17}\text{O}$  quadrupolar-coupling tensors vary significantly over the range of values of  $d$ . However, increased agreement with experiment is observed only when the steepness of the damping function is decreased, i.e., when the dispersion correction is active at short ranges, where the correlation is already partially described by the PW91 functional. Optimizations performed with this method for  $d \geq 8$  have little effect on computed  $^{17}\text{O}$  quadrupolar-coupling parameters, relative to values predicted at the PW91 level. An important feature of the results in Figure 7.1 is that a value of  $d$  that minimizes  $^{17}\text{O}$  MAEs is  $d = 3.5$ , suggesting that this value is optimal for refining structures using

experimental  $^{17}\text{O}$  quadrupolar-coupling tensors. A minimum  $^{17}\text{O}$  MAE near  $d = 3.5$  was observed for all  $^{17}\text{O}$  sites, regardless of the functional group. In the subsequent text, structural refinement employing the PW91-D2 functional with  $d = 3.5$  is referred to as the PW91-D2\* method, to differentiate the re-parameterized form of the dispersion function from the more common form with  $d = 20$ .

$^{17}\text{O}$  quadrupolar-coupling tensors have been computed for the six model compounds using unrefined X-ray diffraction structures, using X-ray diffraction structures refined at the PW91 level, using structures refined at the PW91-D2 level, and using structures refined at the PW91-D2\* level. Table 7.2 is a summary of the  $^{17}\text{O}$  quadrupolar-coupling tensors and associated statistical data for these four sets of calculations. Structures refined at the PW91-D2\* level result in significantly closer agreement with experimental values than do the results obtained using X-ray diffraction structures, as is evident by the root-mean-square deviations (RMSDs) of 0.20 MHz and 0.42 MHz, respectively. Results obtained by refinement at the PW91 and PW91-D2 levels have RMSDs of 0.55 MHz and 0.52 MHz, respectively. Because of the similarity between values obtained from structures refined at the PW91 and PW91-D2 levels, only PW91 refinements are reported subsequently.

Dispersion correction plays an indirect role in modeling NMR parameters. Calculations of  $^{17}\text{O}$  NMR parameters *on the same structure* using the PW91 and PW91-D2\* methods yield essentially the same results by construction. Computed  $^{17}\text{O}$  quadrupolar couplings differ by  $\sim 0.001$  MHz, whereas computed  $^{17}\text{O}$  magnetic shieldings differ by  $\sim 0.1$  ppm, reflecting the level of convergence in the calculations. Thus, differences in computed NMR parameters in Table II reflect differences in

structures, rather than differences in the model chemistry used to predict the NMR parameters.

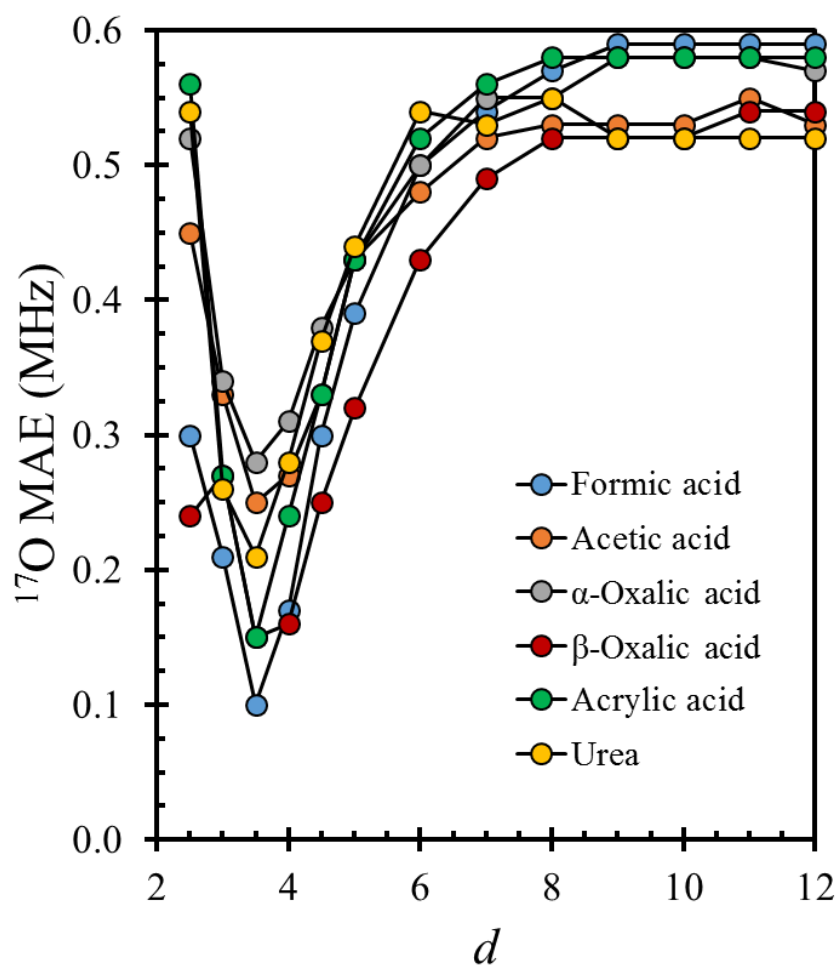


**Figure 7.1.** Mean-absolute errors (MAEs) in computed  $^{17}\text{O}$  quadrupolar-coupling tensors as a function of the value of the damping parameter ( $2.5 \leq d \leq 12$ ) used in the structural refinement using PW91-D2. The minimum MAEs for the materials cluster around a value of  $d = 3.5$ .

**Table 7.2.** Experimental and computed  $^{17}\text{O}$  quadrupolar-coupling tensors obtained from X-ray diffraction structures or from structures refined at the PW91, PW91-D2<sup>a</sup>, or PW91-D2\*<sup>b</sup> levels, and root-mean-square deviations of the sets.

Oxygen Site	Experimental		X-ray		PW91		PW91-D2		PW91-D2*	
	$C_Q$ (MHz)	$\eta$								
Formic acid (O1)	7.82	0.07	8.97	0.05	7.68	0.28	7.75	0.26	8.09	0.06
Formic acid (O2)	-6.90	0.08	-6.78	0.06	-6.77	0.15	-6.86	0.11	-6.88	0.09
Acetic acid (O1)	8.11	0.15	8.84	0.04	8.20	0.31	8.23	0.31	8.40	0.14
Acetic acid (O2)	-7.28	0.19	-6.97	0.35	-7.41	0.10	-7.42	0.10	-7.44	0.10
$\alpha$ -Oxalic acid (O1)	8.46	0.00	8.64	0.03	8.44	0.17	8.47	0.15	8.59	0.01
$\alpha$ -Oxalic acid (O2)	-7.55	0.16	-7.22	0.33	-7.74	0.06	-7.78	0.07	-7.73	0.06
$\beta$ -Oxalic acid (O1)	8.11	0.08	8.50	0.04	7.99	0.25	8.00	0.25	8.29	0.06
$\beta$ -Oxalic acid (O2)	-7.35	0.14	-7.39	0.19	-7.40	0.06	-7.41	0.06	-7.53	0.09
Acrylic acid (O1)	7.57	0.31	8.54	0.20	7.45	0.52	7.44	0.51	7.72	0.30
Acrylic acid (O2)	-7.20	0.17	-7.44	0.13	-7.22	0.09	-7.25	0.10	-7.29	0.11
Urea <sup>c</sup>	7.24	0.92	7.58	0.94	-7.74	0.98	-7.74	0.98	7.64	0.89
RMSD (MHz)			0.42		0.55		0.52		0.20	
Max. (MHz)			0.81		0.87		0.79		0.46	

<sup>a</sup>Calculations employed Grimme's dispersion function with  $d = 20$ .

<sup>b</sup>Calculations employed a re-parameterization of Grimme's dispersion function with  $d = 3.5$ .

<sup>c</sup>The sign of the computed value of  $C_Q$  for urea differs among the various structures.

### 7.3.2 Changes in Bond Lengths

The bond lengths determined by structural refinement at the PW91 level differ from those determined at the PW91-D2\* level for the set of model compounds (formic acid, acetic acid,  $\alpha$ -oxalic acid,  $\beta$ -oxalic acid, acrylic acid, and urea). For refinement at the PW91 level, bonds containing only non-hydrogen atoms are lengthened by an average of 0.009 Å, relative to the X-ray structures. Single bonds ( $C-C$ ,  $C-N$ , and  $C-O$ )

are lengthened by an average of 0.005 Å, whereas double bonds ( $C=C$  and  $C=O$ ) are lengthened by 0.015 Å, on average. The largest changes following refinement are seen for  $C-H$ ,  $N-H$ , and  $O-H$  bond lengths, with an average lengthening of 0.110 Å, relative to bond lengths derived from X-ray diffraction. For refinement at the PW91-D2\* level, lengths of bonds between non-hydrogen atoms decrease by an average of 0.013 Å, relative to the X-ray structures; specifically, single bonds decrease by 0.014 Å, on average, and double bonds decrease by 0.012 Å, on average.  $C-H$  and  $O-H$  bonds are lengthened upon refinement by an average of 0.092 Å whereas the  $N-H$  bond is shortened by 0.041 Å (Figure 7.2.)

Two trends are notable in these results. First, structural refinement at the PW91 level results in lengthening of bonds of all types, whereas refinement at the PW91-D2\* level results in the shortening of all types of bonds except for  $C-H$  and  $O-H$  bonds, which are lengthened. Second, refinement at the PW91 level results in significantly larger changes to the lengths of highly correlated double bonds (0.0146 Å) than to single bonds containing only non-hydrogen atoms (0.005 Å). In contrast, refinement at the PW91-D2\* level affects both bond types similarly.

An important consideration is whether the refined structures are distinguishable from structures derived from X-ray diffraction, within experimental uncertainty. For example, for acetic acid there are four separate determinations of the crystal structure by X-ray diffraction reported in the Cambridge Structural Database. The range of bond lengths reported for these structures give an estimate of the uncertainty in the reported X-ray-determined bond lengths ( $\alpha = 0.05$ ). From these data, one finds that the X-ray-determined  $C-O$ ,  $C=O$ , and  $C-C$  bond lengths are  $1.312 \pm 0.014$  Å,  $1.223 \pm 0.013$  Å, and  $1.492 \pm 0.029$  Å, respectively. The PW91-D2\*-refined bond lengths are 1.310 Å,

1.211 Å, and 1.467 Å, respectively. In all cases, those bond lengths derived for the PW91-D2\* refinement are within the uncertainty of the X-ray-determination.

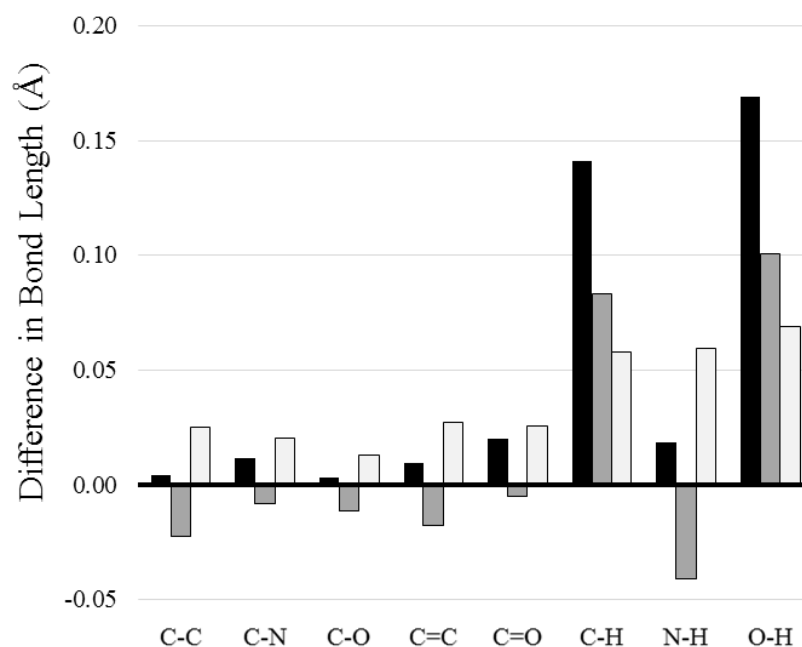


**Figure 7.2.** Changes in bond lengths in model compounds between X-ray diffraction and refined crystal structures. Black: PW91 v. X-ray; dark grey: PW91-D2\* v. X-ray; light grey: PW91 v. PW91-D2\*.

### 7.3.3 Assessment of Structural Refinements by Agreement of Calculated $^{17}\text{O}$ Quadrupolar-Coupling Tensors with Experiment

Figure 7.3 shows the relationship between calculated and experimental principal components of  $^{17}\text{O}$  quadrupolar-coupling tensors for forty-three  $^{17}\text{O}$  sites. These include the  $^{17}\text{O}$  sites of twenty-two materials: formic acid [56, 71], acetic acid [56, 72],  $\alpha$ -oxalic acid [56, 73],  $\beta$ -oxalic acid [56, 74], acrylic acid [56, 75], urea [76, 77], oxalic acid·2H<sub>2</sub>O [78, 79], L-alanine [58, 80], benzophenone [57, 81], thymine [61, 82], uracil

[61, 83], cytosine [61, 84], benzamide [85, 86], taurine [87, 88], salicylic acid [59, 89], phthalic acid [59, 90], maleic acid [56, 91], cyanoacetic acid [56, 92], glycine·HCl [58, 93], L-alanine·HCl [58, 93], L-valine·HCl [58, 94], and L-cysteine·HCl·H<sub>2</sub>O [58, 95]. Calculations of <sup>17</sup>O quadrupolar-coupling tensors were performed on structures obtained by single-crystal X-ray diffraction (Figure 7.3a), on structures obtained by PW91 refinement of diffraction structures (Figure 7.3b), and on structures obtained by PW91-D2\* refinement of diffraction structures (Figure 7.3c). The three datasets in Figure 7.3 differ significantly in the distribution of RMSDs. For unrefined X-ray structures, the RMSD is 0.58 MHz. For PW91 and PW91-D2\* refinement of X-ray structures, the RMSDs are 0.53 MHz and 0.28 MHz, respectively. In almost all cases, the errors associated with the prediction of <sup>17</sup>O quadrupolar-coupling tensors for the X-ray structures and the PW91-refined structures are larger than the expected uncertainties in the experimental values [43]. In contrast, with the values determined with the PW91-D2\*-refined structures are often within the uncertainty of the experimental values.

Relative to values predicted from diffraction structures, PW91-D2\* refinement brings sixty-two of the eighty-six principal values into closer agreement with experiment. Refinement at the PW91 level brings only thirty-three of the eighty-four principal values into closer agreement with experiment. The largest error in any principal component of a <sup>17</sup>O quadrupolar-coupling tensor arises from the unrefined X-ray structure of oxalic acid·2H<sub>2</sub>O. Specifically, this value is associated with the <sup>17</sup>O site in the water molecule, suggesting that one of the largest sources of error in the prediction of <sup>17</sup>O quadrupolar-coupling tensors is associated with the positioning of hydrogen atoms in the hydrogen-bonding network. The prediction of this principal component is

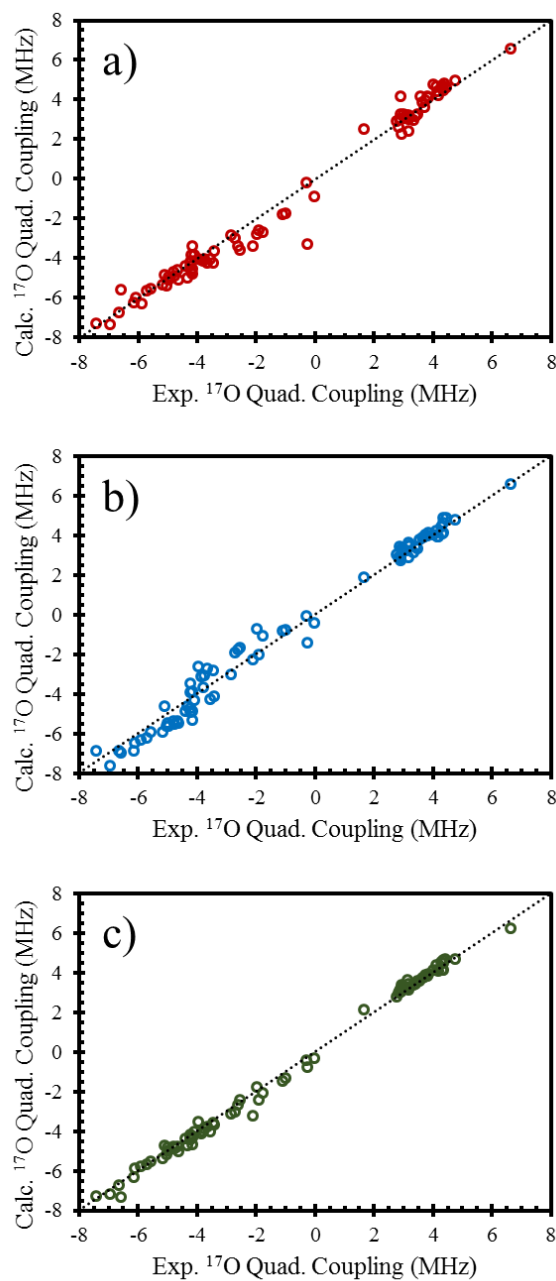


**Figure 7.3.** Relationship between principal components of calculated  $^{17}\text{O}$  quadrupolar-coupling tensors and experimental principal components of  $^{17}\text{O}$  quadrupolar-coupling tensors. Computed results were obtained from (a) X-ray diffraction structures, (b) structures obtained with refinement using PW91, and (c) structures obtained with refinement using PW91-D2\*. The dashed lines represent perfect agreement between calculated and experimental values.

improved by 3.01 MHz following refinement at the PW91-D2\* level. In contrast, the largest increase in error following PW91-D2\* refinement for any of the eighty-four principal components is 0.32 MHz.

#### 7.3.4 Additional Figures of Merit for Assessing Structural Refinements

Although structures optimized at the PW91-D2\* level have superior agreement with experimental  $^{17}\text{O}$  quadrupolar-coupling tensors compared to structures obtained by either X-ray diffraction or PW91 refinements of diffraction structures, it is important to include additional figures of merit to assess the quality of these structural refinements. Further assessment of the quality of structural refinement on these  $^{17}\text{O}$ -containing materials is provided by calculations of the forces on the atoms and by calculated NMR parameters of other nuclear sites in the material. A summary of forces and errors associated with computed NMR parameters of the materials in these materials is provided in Table 7.3.

Plane-wave geometry optimization at either the PW91 or PW91-D2\* level reduces the mean forces experienced by the individual atoms in the lattice by three orders of magnitude in all cases, indicating that the diffraction structures are different from the energy-minimized structures. There does not appear to be a direct correlation between the reduction in forces and the amount of improvement in  $^{17}\text{O}$  quadrupolar-coupling tensors. Differences in forces between the two energy-minimized structures (PW91 and PW91-D2\*) are under  $0.003 \text{ eV } \text{\AA}^{-1}$  for all materials.

Formic acid [96], acetic acid [97],  $\alpha$ -oxalic acid [98], and oxalic acid·2H<sub>2</sub>O [98], have been characterized by the  $^{13}\text{C}$  chemical-shift tensors of carboxyl carbon sites, and L-alanine[99] has been characterized by the  $^{13}\text{C}$  chemical-shift tensor of each carbon site in the material. Refinement at the PW91 level results in improvement of the

prediction of  $^{13}\text{C}$  chemical-shift tensors for two materials (acetic acid and L-alanine) and in poorer agreement with experiment for three materials. Refinement at the PW91-D2\* level results in improvement of the prediction of  $^{13}\text{C}$  chemical-shift tensors for all five materials.

Thymine, uracil, cytosine, and benzamide have been characterized by the  $^{15}\text{N}$  chemical-shift tensor for each nitrogen site [100]. For the prediction of  $^{15}\text{N}$  chemical-shift tensors, refinement at the PW91 level results in improvement for one material (benzamide), whereas refinement at the PW91-D2\* level results in improvement of agreement with experiment for all four materials.

Taurine [88], salicylic acid [60],  $\alpha$ -oxalic acid [101], thymine [61], uracil [61], cytosine [61], and benzamide [85] have been characterized by the  $^{17}\text{O}$  chemical-shift tensor for each unique oxygen site. Refinement at the PW91 level results in improvement of the prediction of  $^{17}\text{O}$  chemical-shift tensors for five materials (all except taurine and salicylic acid), whereas refinement at the PW91-D2\* level results in improvement for all seven materials.

The experimental  $^{35}\text{Cl}$  quadrupolar couplings for glycine·HCl [102], L-alanine·HCl [95], L-valine·HCl [102], and L-cysteine·HCl·H<sub>2</sub>O [95] have been reported. Refinement at the PW91 level results in improvement of the prediction of the  $^{35}\text{Cl}$  quadrupolar coupling for one material (L-cysteine·HCl·H<sub>2</sub>O), whereas refinement at the PW91-D2\* level results in improvement of the prediction of  $^{35}\text{Cl}$  quadrupolar parameters for all seven materials. A summary of experimental and calculated  $^{35}\text{Cl}$  quadrupolar tensors for the four amino acid hydrochlorides is provide in Table 7.4. The RMSDs for the X-ray, PW91-refined, and PW91-D2\*-refined structures are 1.45 MHz, 1.62 MHz, and 0.59 MHz, respectively. The measurement of  $^{35}\text{Cl}$  quadrupolar

parameters has become an important tool for assessing the crystal structures of pharmaceuticals and related HCl salts [95, 103, 104], as many pharmaceuticals are marketed as HCl salts. As these results indicate, computed  $^{35}\text{Cl}$  quadrupolar-coupling tensors are very sensitive to structural refinements.

Overall, we have found that of the twenty sets of  $^{13}\text{C}$ ,  $^{15}\text{N}$ , and  $^{17}\text{O}$  chemical-shift tensors and  $^{35}\text{Cl}$  quadrupolar-coupling tensors listed in Table 7.3, agreement with experiment is lowered for eleven parameters following pure plane-wave DFT structural refinements (relative to the original X-ray structure), and agreement with experiment is improved for nine values. In contrast, refinement at the PW91-D2\* level led to improvement of all twenty parameters. Furthermore, seventeen parameters are improved by PW91-D2\* refinement, relative to PW91 refinement.

### 7.3.5 Discussion of Chemical Shifts

The relationship between computed magnetic-shielding tensors and experimental chemical-shift tensors for  $^{13}\text{C}$ ,  $^{15}\text{N}$ , and  $^{17}\text{O}$  sites is provided in Figure 7.4, which illustrates the superior agreement with experiment for prediction that uses PW91-D2\*-refined structures over X-ray diffraction structures. Table 7.5 shows statistical data associated with the prediction of chemical-shift tensors. RMSDs for the  $^{13}\text{C}$  and  $^{15}\text{N}$  chemical-shift tensors are within the ranges established in previous benchmark studies [29, 70, 105, 106]. Hartman *et al.* have reported a survey of several calculated  $^{17}\text{O}$  isotropic chemical shifts in crystals with a RMSD of 9.8 ppm [107]. We report a RMSD of 18.3 ppm for calculations of principal components of  $^{17}\text{O}$  chemical-shift tensors for structures refined at the PW91-D2\*.

**Table 7.3.** Summary of structural information and statistical data associated with the relationship between experimental and calculated NMR parameters.

Material	Data Type	Forces (eV Å <sup>-1</sup> )	<sup>13</sup> C MAE (ppm)	Chemical Shift		Quadrupolar Coupling	
				<sup>15</sup> N MAE (ppm)	<sup>17</sup> O MAE (ppm)	<sup>17</sup> O MAE (MHz)	<sup>35</sup> Cl MAE (MHz)
Formic acid	X-ray	7.290	9.0	-	-	0.41	-
	PW91	0.005	12.0	-	-	0.60	-
	PW91-D2*	0.005	3.7	-	-	0.10	-
Acetic acid	X-ray	7.310	7.9	-	-	0.56	-
	PW91	0.006	3.7	-	-	0.52	-
	PW91-D2*	0.004	5.8	-	-	0.25	-
α-Oxalic acid	X-ray	2.336	4.8	-	22.5	0.44	-
	PW91	0.006	7.6	-	13.2	0.57	-
	PW91-D2*	0.003	1.9	-	17.0	0.28	-
Oxalic acid·2H <sub>2</sub> O	X-ray	1.035	5.4	-	-	2.26	-
	PW91	0.005	8.9	-	-	0.89	-
	PW91-D2*	0.007	2.6	-	-	0.68	-
L-Alanine	X-ray	5.831	11.0	-	-	0.44	-
	PW91	0.004	9.4	-	-	0.39	-
	PW91-D2*	0.002	3.0	-	-	0.25	-
Taurine	X-ray	8.997	-	-	14.9	0.30	-
	PW91	0.005	-	-	22.6	0.30	-
	PW91-D2*	0.004	-	-	10.9	0.08	-
Salicylic acid	X-ray	6.366	-	-	24.9	0.52	-
	PW91	0.004	-	-	29.5	0.60	-
	PW91-D2*	0.004	-	-	17.3	0.30	-
Thymine	X-ray	6.057	-	8.7	46.9	0.56	-
	PW91	0.004	-	16.8	31.6	0.51	-
	PW91-D2*	0.005	-	4.9	30.6	0.32	-
Uracil	X-ray	6.831	-	9.3	26.2	0.59	-
	PW91	0.005	-	19.5	15.4	0.47	-
	PW91-D2*	0.005	-	4.6	4.5	0.33	-
Cytosine	X-ray	4.054	-	14.9	26.2	0.53	-
	PW91	0.005	-	14.2	17.5	0.58	-
	PW91-D2*	0.006	-	8.2	10.6	0.33	-
Benzamide	X-ray	5.350	-	10.3	102.1	0.85	-
	PW91	0.004	-	19.7	25.5	0.68	-
	PW91-D2*	0.006	-	2.3	24.6	0.09	-
Glycine·HCl	X-ray	2.688	-	-	-	0.24	2.36
	PW91	0.005	-	-	-	0.30	2.57
	PW91-D2*	0.004	-	-	-	0.14	1.08
L-Alanine·HCl	X-ray	2.902	-	-	-	0.80	0.61
	PW91	0.003	-	-	-	0.40	1.12
	PW91-D2*	0.004	-	-	-	0.19	0.17
L-Valine·HCl	X-ray	5.994	-	-	-	0.37	0.95

	PW91	0.003	-	-	-	0.30	1.17
	PW91-D2*	0.004	-	-	-	0.25	0.39
<hr/>							
L-							
Cysteine·HCl·H <sub>2</sub> O	X-ray	7.326	-	-	-	0.33	1.12
	PW91	0.004	-	-	-	0.51	0.15
	PW91-D2*	0.004	-	-	-	0.33	0.19

Because accurate modeling of chemical shifts requires refinement of atomic positions in crystal structures, a common concern in calculations of magnetic shielding is the possible cancellation of errors due to flaws in the structure, such as systematic over- or underestimation of bond lengths, and errors in the model chemistry used to calculate the shielding. It is well-established that calculated magnetic-shielding tensors vary significantly among model chemistries [70, 105, 108]. Similarly, GGA functionals such as PW91 tend to overestimate bond lengths [109], an effect consistent with the results obtained in the present study. A structural-refinement technique that systematically overestimates bond lengths, paired with a method that overestimates magnetic shieldings, or vice versa, could lead to artificial agreement with experiment due to error cancellation [110]. To account for systematic errors in computed magnetic shielding due to the model chemistry, and systematic errors in structures, it is common to model the relationship between computed magnetic shielding and experimental chemical shift with linear regression to account for non-random sources of error (Eq. 7.6). When computed magnetic shieldings are converted to chemical shifts using least-squares linear-regression parameters (Eq. 7.7), systematic errors associated with the structure and the magnetic shielding are partially removed, since these can be accounted for by fitting the values of  $\sigma_{ref}$  and  $|m|$ .

**Table 7.4.** Summary of experimental and calculated  $^{35}\text{Cl}$  quadrupolar-coupling tensors.

Material	Data Type	$C_Q$ (MHz)	$\eta$	MAE (MHz)
<b>Glycine·HCl</b>	<b>Exp.</b>	<b>-6.42</b>	<b>0.61</b>	<b>-</b>
	X-ray	-11.00	0.46	2.36
	PW91	-9.11	0.91	2.57
	PW91-D2*	-6.91	0.87	1.08
<b>L-Alanine·HCl</b>	<b>Exp.</b>	<b>-6.4</b>	<b>0.75</b>	<b>-</b>
	X-ray	-8.11	0.57	0.61
	PW91	-8.97	0.74	1.12
	PW91-D2*	-6.74	0.71	0.17
<b>L-Valine·HCl</b>	<b>Exp.</b>	<b>-5.89</b>	<b>0.51</b>	<b>-</b>
	X-ray	-4.02	0.68	0.95
	PW91	-7.63	0.60	1.17
	PW91-D2*	-5.91	0.64	0.39
<b>L-Cysteine·HCl·H<sub>2</sub>O</b>	<b>Exp</b>	<b>-3.97</b>	<b>0.47</b>	<b>-</b>
	X-ray	-1.90	0.53	1.12
	PW91	-4.06	0.39	0.15
	PW91-D2*	-4.05	0.37	0.19

In contrast to the results of other studies [23, 24], we find that plane-wave DFT structural refinements (without the D2\* correction) sometimes result in poorer prediction of chemical-shift tensors than do unrefined X-ray diffraction structures. As discussed above, the origins of errors in calculated magnetic shieldings are sometimes difficult to pinpoint. However, the PW91-D2\* structural-refinement strategy may provide a method for decoupling errors associated with systematic over- or underestimations of bond lengths from errors associated with over- or underestimations

of chemical shifts. Rather than refining structures by searching for a global energy minimum, the PW91-D2\* structural-refinement method selects structures based on their ability to predict experimental EFGs at the nuclear sites, parameters that are strongly correlated with local electronic structure. Furthermore, EFG tensors are generally simpler to calculate than magnetic-shielding tensors, as the former result from integrals over the ground electronic state only, whereas the latter result from a summation of integrals over the ground and excited electronic states. Thus, the semi-empirical structural-refinement methodology, where structures are selected by their ability to yield  $^{17}\text{O}$  quadrupolar-coupling tensors in significant agreement with experiment, may separate errors associated with the structure from errors associated with the model chemistry used to calculate magnetic-shielding tensors, and provide insights that would otherwise go unnoticed.

**Table 7.5.** Statistical data associated with the prediction of  $^{13}\text{C}$  ( $N = 21$ ),  $^{15}\text{N}$  ( $N = 24$ ), and  $^{17}\text{O}$  ( $N = 42$ ) chemical-shift tensors using structures obtained by X-ray diffraction, by PW91 refinement, and by PW91-D2\* refinement of diffraction structures.

Method	$^{13}\text{C}$ RMSD (ppm)	$^{15}\text{N}$ RMSD (ppm)	$^{17}\text{O}$ RMSD (ppm)
X-ray	9.4	11.1	39.6
PW91	9.4	14.5	24.3
PW91-D2*	3.7	5.8	18.3

The sensitivity of NMR parameters to structural changes due to refinement depends on many factors, including the set of materials examined. For this particular set of materials, one may compare the results on X-ray-determined structures with the

results for PW91-D2\*-refined structures. The RMSDs of PW91-D2\*-derived chemical-shift tensors all improve by factors of around 2 relative to the X-ray-structure-determined chemical-shift tensors:  $^{13}\text{C}$  by 2.5,  $^{15}\text{N}$  by 1.9, and  $^{17}\text{O}$  by 2.2. For prediction of quadrupolar-coupling tensors, a similar improvement is seen when the PW91-D2\*-derived structures are used: the RMSD of  $^{17}\text{O}$  quadrupolar-coupling tensors decreases by a factor of 2.1; and the  $^{35}\text{Cl}$  quadrupolar-coupling tensors by a factor of 3.5.

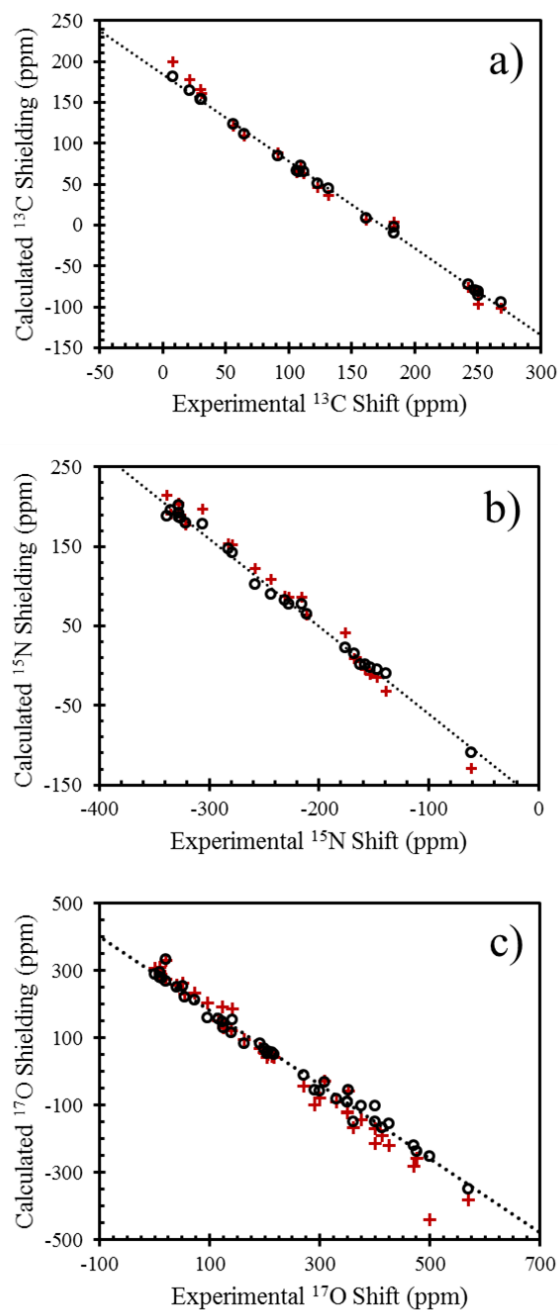


**Figure 7.4.** Correlation between experimental chemical-shift tensors and calculated magnetic-shielding tensors for (a)  $^{13}\text{C}$  sites, (b)  $^{15}\text{N}$  sites, and (c)  $^{17}\text{O}$  sites. Computed magnetic-shielding constants were obtained from either unrefined X-ray diffraction structures (red crosses) or PW91-D2\* refinements of diffraction structures (black circles).

### 7.3.6 Comparison to Neutron-Diffraction Structures

Crystal structures obtained from neutron diffraction are often considered to be more accurate than those derived from X-ray diffraction due to the ability to locate hydrogen atoms with greater accuracy. Neutron structures have been reported for ten systems in the present study (formic acid [111], acetic acid [112], oxalic acid·2H<sub>2</sub>O [113], urea [114], benzamide [115], L-alanine [116], taurine [117], salicylic acid [118], glycine·HCl [119], and valine·HCl [120]). As a final figure of merit, a comparison is made between computed <sup>17</sup>O quadrupolar-coupling tensors obtained from X-ray diffraction structures, neutron-diffraction structures, and PW91-D2\*-refined X-ray diffraction structures (Figure 7.5).

As is evident in Figure 7.5, calculations performed on PW91-D2\*-refined structures yield <sup>17</sup>O quadrupolar-coupling tensors in closer agreement with experimental values than those calculated using X-ray diffraction structures. In addition, calculations on the PW91-D2\*-refined structures provide more accurate results than calculations on the neutron-diffraction-derived structures for seven of the ten materials. The largest difference in computed <sup>17</sup>O quadrupolar coupling between neutron-diffraction-derived and PW91-D2\*-refined structures is observed for acetic acid (0.27 MHz), whereas the smallest differences are found for urea and L-alanine (0.05 MHz). <sup>13</sup>C and <sup>15</sup>N chemical-shift tensors are the only NMR-derived parameters that have been used to provide crystal structures that are more refined than those obtained with neutron diffraction [6, 23, 24, 29]. The present results suggest that <sup>17</sup>O quadrupolar-coupling tensors may also provide another means to refine crystal structures beyond the refinement provided by neutron diffraction.

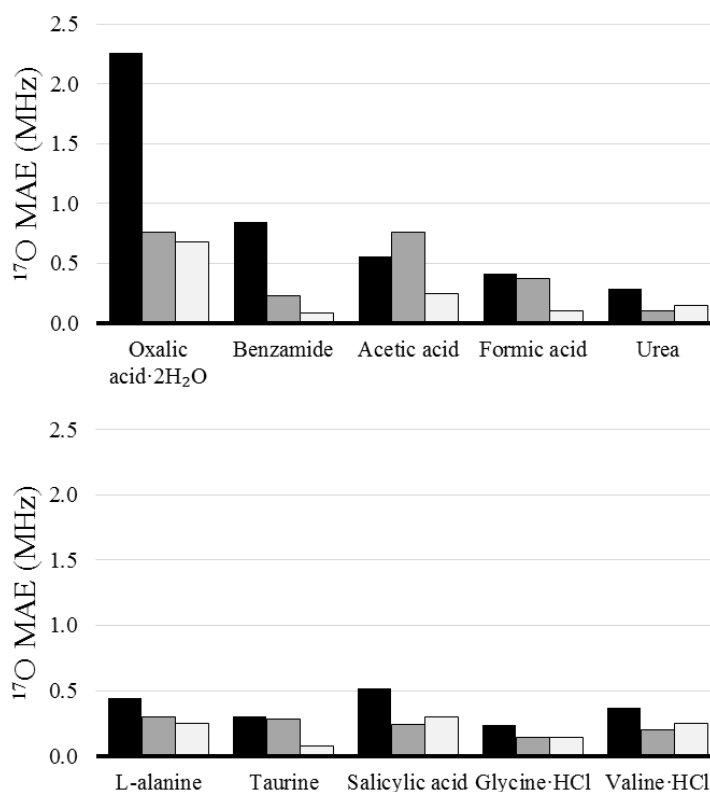


**Figure 7.5.** Mean-absolute errors between calculated and experimental  $^{17}\text{O}$  quadrupolar coupling tensors in formic acid, acetic acid, oxalic acid·2H<sub>2</sub>O, urea, benzamide, L-alanine, taurine, salicylic acid, glycine·HCl, and valine·HCl. Calculated values were obtained using X-ray diffraction structures (black), neutron-diffraction structures (dark grey) or PW91-D2\*-refined X-ray diffraction structures (light grey).

#### 7.4 Conclusion

Calculations of  $^{17}\text{O}$  quadrupolar-coupling tensors have been used to assess refinement of crystal structures. In particular, refinement used plane-wave DFT at the PW91 level, the PW91-D2 level, and a re-parameterization of the latter method termed PW91-D2\*. The PW91-D2\* method originated from the re-parameterization of the Grimme damping function to yield structures that result in accurate predictions of experimental  $^{17}\text{O}$  quadrupolar-coupling tensors. The use of the PW91-D2\* method

produces structures that differ significantly from both X-ray diffraction structures and structures found with PW91 refinement of diffraction structures. Bond lengths involving non-hydrogen atoms in the PW91-D2\* structures are, on average, 0.013 Å shorter than in the X-ray structures, whereas other optimization strategies tend to result in longer bonds. We find a RMSD for  $^{17}\text{O}$  quadrupolar-coupling tensors calculated with PW91-D2\*-refined structures in six model compounds of 0.20 MHz. In contrast, X-ray structures, and PW91 or PW91-D2 refinements of X-ray structures, yield substantially larger errors, with RMSDs of 0.42 MHz, 0.55 MHz, and 0.52 MHz, respectively.

Refinements at the PW91-D2\* level were applied to a larger database containing forty-three oxygen sites. For this larger database, PW91-D2\* refinements led to structures with a RMSD of 0.28 MHz for  $^{17}\text{O}$  quadrupolar-coupling tensors. For comparison, X-ray or PW91-refined structures yielded RMSDs of 0.58 MHz and 0.53 MHz, respectively. Many materials in this database have been characterized by heteronuclear NMR studies. We have calculated the  $^{13}\text{C}$ ,  $^{15}\text{N}$ , and  $^{17}\text{O}$  chemical-shift tensors and  $^{35}\text{Cl}$  quadrupolar-coupling tensors. In every case, structures refined at the PW91-D2\* level yield better agreement with experimental NMR parameters than do unrefined X-ray structures.

## REFERENCES

- [1] R.K. Harris, R.E. Wasylshen, M.J. Duer, *NMR Crystallography*, John Wiley & Sons Ltd, Singapore, 2009.
- [2] J. Powell, K. Kalakewich, F.J. Uribe-Romo, J.K. Harper, Solid-state NMR and DFT predictions of differences in COOH hydrogen bonding in odd and even numbered n-alkyl fatty acids, *Phys. Chem. Chem. Phys.*, 18 (2016) 12541-12549.
- [3] D.L. Bryce, G.D. Sward, Chlorine-35/37 NMR spectroscopy of solid amino acid hydrochlorides: refinement of hydrogen-bonded proton positions using experiment and theory, *J. Phys. Chem. B*, 110 (2006) 26461-26470.
- [4] Y. Nishiyama, J. Sugiyama, H. Chanzy, P. Langan, Crystal structure and hydrogen bonding system in cellulose I $\alpha$  from synchrotron X-ray and neutron fiber diffraction, *J. Am. Chem. Soc.*, 125 (2003) 14300-14306.
- [5] J. Gajda, S. Olejniczak, I. Bryndal, M.J. Potrzebowski, Elucidation of structural restraints for phosphate residues with different hydrogen bonding and ionization states, *J. Phys. Chem. B*, 112 (2008) 14036-14044.
- [6] J.C. Facelli, D.M. Grant, Determination of molecular symmetry in crystalline naphthalene using solid-state NMR, *Nature*, 365 (1993) 325-327.
- [7] M. Edgar, V.J. Carter, D.P. Tunstall, P. Grewal, V. Favre-Nicolin, P.A. Cox, P. Lightfoot, P.A. Wright, Structure solution of a novel aluminium methylphosphonate using a new simulated annealing program and powder X-ray diffraction data, *Chem. Commun.*, (2002) 808-809.
- [8] J.K. Harper, A.E. Mulgrew, J.Y. Li, D.H. Barich, G.A. Strobel, D.M. Grant, Characterization of stereochemistry and molecular conformation using solid-state NMR tensors, *J. Am. Chem. Soc.*, 123 (2001) 9837-9842.
- [9] J.K. Harper, D.H. Barich, J.Z. Hu, G.A. Strobel, D.M. Grant, Stereochemical Analysis by Solid-State NMR: Structural Predictions in Ambuic Acid, *J. Org. Chem.*, 68 (2003) 4609-4614.
- [10] C.A. Fyfe, K.C. Wong-Moon, Y. Huang, H. Grondey, INEPT experiments in solid-state NMR, *J. Am. Chem. Soc.*, 117 (1995) 10397-10398.

- [11] T. Pawlak, M.J. Potrzebowski, Fine refinement of solid-state molecular structures of leu- and met-enkephalins by NMR crystallography, *J. Phys. Chem. B*, 118 (2014) 3298-3309.
- [12] C.A. Fyfe, D.H. Brouwer, A.R. Lewis, L.A. Villaescusa, R.E. Morris, Combined solid state NMR and X-ray diffraction investigation of the local structure of the five-coordinate silicon in fluoride-containing as-synthesized STF zeolite, *J. Am. Chem. Soc.*, 124 (2002) 7770-7778.
- [13] C.A. Fyfe, D.H. Brouwer, A.R. Lewis, J.-M. Chézeau, Location of the fluoride ion in tetrapropylammonium fluoride silicalite-1 determined by  $^1\text{H}/^{19}\text{F}/^{29}\text{Si}$  triple resonance CP, REDOR, and TEDOR NMR experiments, *J. Am. Chem. Soc.*, 123 (2001) 6882-6891.
- [14] D.H. Brouwer, I.L. Moudrakovski, K.A. Udachin, G.D. Enright, J.A. Ripmeester, Guest loading and multiple phases in single crystals of the van der Waals host *p*-*tert*-butylcalix[4]arene, *Cryst. Growth Des.*, 8 (2008) 1878-1885.
- [15] K.M.N. Burgess, D.L. Bryce, On the crystal structure of the vaterite polymorph of  $\text{CaCO}_3$ : a calcium-43 solid-state NMR and computational assessment, *Solid State Nucl. Magn. Reson.*, 65 (2015) 75-83.
- [16] H.E. Kerr, L.K. Softley, K. Suresh, A. Nangia, P. Hodgkinson, I.R. Evans, A furosemide-isonicotinamide cocrystal: an investigation of properties and extensive structural disorder, *CrystEngComm*, 17 (2015) 6707-6715.
- [17] H.E. Kerr, H.E. Mason, H.A. Sparkes, P. Hodgkinson, Testing the limits of NMR crystallography: the case of caffeine-citric acid hydrate, *CrystEngComm*, (2016).
- [18] J.K. Harper, D. Tishler, D. Richardson, J. Lokvam, R. Pendrill, G. Widmalm, Solid-state NMR characterization of the molecular conformation in disordered ethyl  $\alpha$ -l-rhamnofuranoside, *J. Phys. Chem. A*, 117 (2013) 5534-5541.
- [19] W.D. Wang, X.D. Gao, M. Strohmeier, W. Wang, S. Bai, C. Dybowski, Solid-state NMR studies of form I of atorvastatin calcium, *J. Phys. Chem. B*, 116 (2012) 3641-3649.
- [20] C. Yang, L. Zhu, R.A. Kudla, J.D. Hartman, R.O. Al-Kaysi, S. Monaco, B. Schatschneider, A. Magalhaes, G.J.O. Beran, C.J. Bardeen, L.J. Mueller, Crystal structure of the meta-stable intermediate in the photomechanical, crystal-to-crystal reaction of 9-*tert*-butyl anthracene ester, *CrystEngComm*, 18 (2016) 7319-7329.
- [21] J. Leclaire, G. Poisson, F. Ziarelli, G. Pepe, F. Fotiadu, F.M. Paruzzo, A.J. Rossini, J.-N. Dumez, B. Elena-Herrmann, L. Emsley, Structure elucidation of a complex  $\text{CO}_2$ -based organic framework material by NMR crystallography, *Chem. Sci.*, 7 (2016) 4379-4390.

- [22] K. Kalakewich, R. Iulucci, J.K. Harper, Establishing Accurate High-Resolution Crystal Structures in the Absence of Diffraction Data and Single Crystals—An NMR Approach, *Cryst. Growth Des.*, 13 (2013) 5391-5396.
- [23] K. Kalakewich, R. Iulucci, K.T. Mueller, H. Eloranta, J.K. Harper, Monitoring the refinement of crystal structures with  $^{15}\text{N}$  solid-state NMR shift tensor data, *J. Chem. Phys.*, 143 (2015) 194702.
- [24] J.K. Harper, R. Iulucci, M. Gruber, K. Kalakewich, Refining crystal structures with experimental  $^{13}\text{C}$  NMR shift tensors and lattice-including electronic structure methods, *CrystEngComm*, 15 (2013) 8693-8704.
- [25] D.H. Brouwer, G.D. Enright, Probing local structure in zeolite frameworks: ultrahigh-field NMR measurements and accurate first-principles calculations of zeolite  $^{29}\text{Si}$  magnetic shielding tensors, *J. Am. Chem. Soc.*, 130 (2008) 3095-3105.
- [26] D.H. Brouwer, A structure refinement strategy for NMR crystallography: an improved crystal structure of silica-ZSM-12 zeolite from  $^{29}\text{Si}$  chemical shift tensors, *J. Magn. Reson.*, 194 (2008) 136-146.
- [27] D.H. Brouwer, I.L. Moudrakovski, R.J. Darton, R.E. Morris, Comparing quantum-chemical calculation methods for structural investigation of zeolite crystal structures by solid-state NMR spectroscopy, *Magn. Reson. Chem.*, 48 (2010) S113-S121.
- [28] P.J. Pallister, I.L. Moudrakovski, G.D. Enright, J.A. Ripmeester, Structural assessment of anhydrous sulfates with high field  $^{33}\text{S}$  solid state NMR and first principles calculations, *CrystEngComm*, 15 (2013) 8808-8822.
- [29] J.C. Johnston, R.J. Iulucci, J.C. Facelli, G. Fitzgerald, K.T. Mueller, Intermolecular shielding contributions studied by modeling the  $^{13}\text{C}$  chemical-shift tensors of organic single crystals with plane waves, *J. Chem. Phys.*, 131 (2009) 144503.
- [30] K.T. Mueller, B.Q. Sun, G.C. Chingas, J.W. Zwanziger, T. Terao, A. Pines, Dynamic-angle spinning of quadrupolar nuclei, *J. Magn. Reson.*, 86 (1990) 470-487.
- [31] K.T. Mueller, Y. Wu, B.F. Chmelka, J. Stebbins, A. Pines, High-resolution oxygen-17 NMR of solid silicates, *J. Am. Chem. Soc.*, 113 (1991) 32-38.
- [32] B.F. Chmelka, K.T. Mueller, A. Pines, J. Stebbins, Y. Wu, J.W. Zwanziger, Oxygen-17 NMR in solids by dynamic-angle spinning and double rotation, *Nature*, 339 (1989) 42-43.
- [33] K.T. Mueller, J.H. Baltisberger, E.W. Wooten, A. Pines, Isotropic chemical shifts and quadrupolar parameters for oxygen-17 using dynamic angle spinning NMR, *J. Phys. Chem.*, 96 (1992) 7001-7004.

- [34] T.H. Sefzik, J.B. Houseknecht, T.M. Clark, S. Prasad, T.L. Lowary, Z. Gan, P.J. Grandinetti, Solid-state  $^{17}\text{O}$  NMR in carbohydrates, *Chem. Phys. Lett.*, 434 (2007) 312-315.
- [35] P.J. Grandinetti, J.H. Baltisberger, I. Farnan, J.F. Stebbins, U. Werner, A. Pines, Solid-state  $^{17}\text{O}$  magic-angle and dynamic-angle spinning NMR study of the  $\text{SiO}_2$  polymorph coesite, *J. Phys. Chem.*, 99 (1995) 12341-12348.
- [36] T.M. Clark, P.J. Grandinetti, Factors influencing the  $^{17}\text{O}$  quadrupole coupling constant in bridging oxygen environments, *Solid State Nucl. Magn. Reson.*, 16 (2000) 55-62.
- [37] T.M. Clark, P.J. Grandinetti, Calculation of bridging oxygen quadrupolar coupling parameters in alkali silicates: a combined ab initio investigation, *Solid State Nucl. Magn. Reson.*, 27 (2005) 233-241.
- [38] T.H. Sefzik, T.M. Clark, P.J. Grandinetti, A computational investigation of  $^{17}\text{O}$  quadrupolar coupling parameters and structure in  $\beta$ -quartz phase, *Solid State Nucl. Magn. Reson.*, 32 (2007) 16-23.
- [39] T.M. Clark, P.J. Grandinetti, Dependence of bridging oxygen  $^{17}\text{O}$  quadrupolar coupling parameters on Si–O distance and Si–O–Si angle, *J. Phys.: Condens. Matter*, 15 (2003) S2387.
- [40] T.M. Clark, P.J. Grandinetti, P. Florian, J.F. Stebbins, An  $^{17}\text{O}$  NMR investigation of crystalline sodium metasilicate: implications for the determination of local structure in alkali silicates, *J. Phys. Chem. B*, 105 (2001) 12257-12265.
- [41] K.E. Vermillion, P. Florian, P.J. Grandinetti, Relationships between bridging oxygen  $^{17}\text{O}$  quadrupolar coupling parameters and structure in alkali silicates, *J. Chem. Phys.*, 108 (1998) 7274-7285.
- [42] T.M. Clark, P.J. Grandinetti, Relationships between bridging oxygen  $^{17}\text{O}$  quadrupolar coupling parameters and structure in germanates, *J. Non-Cryst. Solids*, 265 (2000) 75-82.
- [43] V. Lemaître, M.E. Smith, A. Watts, A review of oxygen-17 solid-state NMR of organic materials—towards biological applications, *Solid State Nucl. Magn. Reson.*, 26 (2004) 215-235.
- [44] G. Wu, Solid-State  $^{17}\text{O}$  NMR studies of organic and biological molecules: recent advances and future directions, *Solid State Nucl. Magn. Reson.*, 73 (2016) 1-14.
- [45] S.E. Ashbrook, M.E. Smith, Solid state  $^{17}\text{O}$  NMR—an introduction to the background principles and applications to inorganic materials, *Chem. Soc. Rev.*, 35 (2006) 718-735.

- [46] L. Peng, J.F. Stebbins, High resolution  $^{17}\text{O}$  MAS and triple-quantum MAS NMR studies of gallosilicate glasses, *J. Non-Cryst. Solids*, 354 (2008) 3120-3128.
- [47] L. Peng, J.F. Stebbins, Sodium germanate glasses and crystals: NMR constraints on variation in structure with composition, *J. Non-Cryst. Solids*, 353 (2007) 4732-4742.
- [48] L.-S. Du, L. Peng, J.F. Stebbins, Germanosilicate and alkali germanosilicate glass structure: New insights from high-resolution oxygen-17 NMR, *J. Non-Cryst. Solids*, 353 (2007) 2910-2918.
- [49] F.H. Larsen, S. Rossano, I. Farnan, Order and disorder in titanosilicate glass by  $^{17}\text{O}$  MAS, off-MAS, and 3Q-QCPMG-MAS solid-state NMR, *J. Phys. Chem. B*, 111 (2007) 8014-8019.
- [50] L.-S. Du, J.F. Stebbins, Oxygen sites and network coordination in sodium germanate glasses and crystals: high-resolution oxygen-17 and sodium-23 NMR, *J. Phys. Chem. B*, 110 (2006) 12427-12437.
- [51] S.K. Lee, E.J. Kim, Probing metal-bridging oxygen and configurational disorder in amorphous lead silicates: insights from  $^{17}\text{O}$  solid-state nuclear magnetic resonance, *J. Phys. Chem. C*, 119 (2015) 748-756.
- [52] S.K. Lee, G.D. Cody, Y. Fei, B.O. Mysen, The effect of Na/Si on the structure of sodium silicate and aluminosilicate glasses quenched from melts at high pressure: A multi-nuclear (Al-27, Na-23, O-17) 1D and 2D solid-state NMR study, *Chem. Geol.*, 229 (2006) 162-172.
- [53] M. Zeyer-Düsterer, L. Montagne, G. Palavit, C. Jäger, Combined  $^{17}\text{O}$  NMR and  $^{11}\text{B}$ - $^{31}\text{P}$  double resonance NMR studies of sodium borophosphate glasses, *Solid State Nucl. Magn. Reson.*, 27 (2005) 50-64.
- [54] L.-S. Du, J.F. Stebbins, Site connectivities in sodium aluminoborate glasses: multinuclear and multiple quantum NMR results, *Solid State Nucl. Magn. Reson.*, 27 (2005) 37-49.
- [55] D.L. Pechkis, E.J. Walter, H. Krakauer, First-principles calculations of  $^{17}\text{O}$  nuclear magnetic resonance chemical shielding in  $\text{Pb}(\text{Zr}_{1/2}\text{Ti}_{1/2})\text{O}_3$  and  $\text{Pb}(\text{Mg}_{1/3}\text{Nb}_{2/3})\text{O}_3$ : linear dependence on transition-metal/oxygen bond lengths, *J. Chem. Phys.*, 135 (2011) 114507.
- [56] S.G.P. Brosnan, D.T. Edmonds, I.J.F. Poplett, An  $^{17}\text{O}$  nuclear quadrupole resonance study of some carboxylic acids, *J. Magn. Reson.*, 45 (1981) 451-460.
- [57] W. Scheubel, H. Zimmermann, U. Haeberlen,  $^{17}\text{O}$  quadrupole coupling and nuclear magnetic shielding tensors in benzophenone, *J. Magn. Reson.*, 63 (1985) 544-555.

- [58] K.J. Pike, V. Lemaitre, A. Kukol, T. Anupöld, A. Samoson, A.P. Howes, A. Watts, M.E. Smith, R. Dupree, Solid-state  $^{17}\text{O}$  NMR of amino acids, *J. Phys. Chem. B*, 108 (2004) 9256-9263.
- [59] I.J.F. Poplett, J.A.S. Smith,  $^{17}\text{O}$  and  $^2\text{H}$  quadrupole double resonance in some carboxylic acid dimers, *J. Chem. Soc., Faraday Trans.*, 77 (1981) 1473-1485.
- [60] X. Kong, M. Shan, V. Terskikh, I. Hung, Z. Gan, G. Wu, Solid-State  $^{17}\text{O}$  NMR of pharmaceutical compounds: salicylic acid and aspirin, *J. Phys. Chem. B*, 117 (2013) 9643-9654.
- [61] G. Wu, S. Dong, R. Ida, N. Reen, A solid-state  $^{17}\text{O}$  nuclear magnetic resonance study of nucleic acid bases, *J. Am. Chem. Soc.*, 124 (2002) 1768-1777.
- [62] X. Kong, V. Terskikh, A. Toubaei, G. Wu, A solid-state  $^{17}\text{O}$  NMR study of platinum-carboxylate complexes: carboplatin and oxaliplatin, *Can. J. Chem.*, 93 (2015) 945-953.
- [63] S. Grimme, Semiempirical GGA-type density functional constructed with a long-range dispersion correction, *J. Comput. Chem.*, 27 (2006) 1787-1799.
- [64] J.P. Perdew, Y. Wang, Accurate and simple analytic representation of the electron-gas correlation energy, *Phys. Rev. B*, 45 (1992) 13244.
- [65] S.J. Clark, M.D. Segall, C.J. Pickard, P.J. Hasnip, M.J. Probert, K. Refson, M.C. Payne, First principles methods using CASTEP, *Z. Kristallogr.*, 220 (2005) 567-570.
- [66] B.G. Pfrommer, M. Côté, S.G. Louie, M.L. Cohen, Relaxation of crystals with the quasi-Newton method, *J. Comput. Phys.*, 131 (1997) 233-240.
- [67] C.J. Pickard, F. Mauri, All-electron magnetic response with pseudopotentials: NMR chemical shifts, *Phys. Rev. B*, 63 (2001) 245101.
- [68] P. Jurečka, J. Černý, P. Hobza, D.R. Salahub, Density functional theory augmented with an empirical dispersion term. Interaction energies and geometries of 80 noncovalent complexes compared with ab initio quantum mechanics calculations, *J. Comput. Chem.*, 28 (2007) 555-569.
- [69] B. Civalleri, C.M. Zicovich-Wilson, L. Valenzano, P. Ugliengo, B3LYP augmented with an empirical dispersion term (B3LYP-D\*) as applied to molecular crystals, *CrystEngComm*, 10 (2008) 405-410.
- [70] S.T. Holmes, R.J. Iulucci, K.T. Mueller, C. Dybowski, Critical analysis of cluster models and exchange-correlation functionals for calculating magnetic shielding in molecular solids, *J. Chem. Theory Comput.*, 11 (2015) 5229-5241.

- [71] I. Nahrungbauer, A reinvestigation of the structure of formic acid (at 98 K), *Acta Crystallogr., Sect. B*, 34 (1978) 315-318.
- [72] R. Boese, D. Blaser, R. Latz, A. Baumen, Acetic acid at 40 K, *Acta Crystallogr., Sect. C*, 55 (1999) 9900001.
- [73] J.L. Derissen, P.H. Smith, Refinement of the crystal structures of anhydrous  $\alpha$ - and  $\beta$ -oxalic acids, *Acta Crystallogr., Sect. B*, 30 (1974) 2240.
- [74] S. Bhattacharya, V.G. Saraswatula, B.K. Saha, Thermal expansion in alkane diacids - another property showing alternation in an odd-even series, *Cryst. Growth Des.*, 13 (2013) 3651-3656.
- [75] R. Boese, D. Blaser, I. Steller, R. Latz, A. Baumen, Redetermination of 2-propenoic acid at 125 K, *Acta Crystallogr., Sect. C*, 55 (1999) 9900006.
- [76] S. Dong, R. Ida, G. Wu, A combined experimental and theoretical  $^{17}\text{O}$  NMR study of crystalline urea: an example of large hydrogen-bonding effects, *J. Phys. Chem. A*, 104 (2000) 11194-11202.
- [77] H. Birkedal, D. Madsen, R.H. Mathiesen, K. Knudsen, H.-P. Weber, P. Pattison, D. Schwarzenbach, The charge density of urea from synchrotron diffraction data, *Acta Crystallogr., Sect. A*, 60 (2004) 371-381.
- [78] Q.W. Zhang, H.M. Zhang, M.G. Usha, R.J. Wittebort,  $^{17}\text{O}$  NMR and crystalline hydrates, *Solid State Nucl. Magn. Reson.*, 7 (1996) 147-154.
- [79] N. Casati, P. Macchi, A. Sironi, Hydrogen migration in oxalic acid di-hydrate at high pressure?, *Chem. Commun.*, (2009) 2679-2681.
- [80] F. Kimura, W. Oshima, H. Matsumoto, H. Uekusa, K. Aburaya, M. Maeyama, T. Kimura, Single crystal structure analysis via magnetically oriented microcrystal arrays, *CrystEngComm*, 16 (2014) 6630-6634.
- [81] J. Moncol, P. Coppens, CCDC 245188, 2004.
- [82] G. Portalone, L. Bencivenni, M. Colapietro, A. Pieretti, F. Ramondo, The effect of hydrogen bonding on the structures of uracil and some methyl derivatives studied by experiment and theory, *Acta Chem. Scand.*, 53 (1999) 57-68.
- [83] R.F. Stewart, Redetermination of the crystal structure of uracil, *Acta Crystallogr.*, 23 (1967) 1102-&.
- [84] R.J. McClure, B.M. Craven, New investigations of cytosine and its monohydrate, *Acta Crystallogr., Sect. B*, B 29 (1973) 1234-1238.

- [85] S. Dong, K. Yamada, G. Wu, Oxygen-17 nuclear magnetic resonance of organic solids, *Z. Naturforsch.*, 55a (2000) 21-28.
- [86] J. Thun, L. Seyfarth, C. Butterhof, J. Senker, R.E. Dinnebier, J. Brey, Wohler and Liebig revisited: 176 years of polymorphism in benzamide - and the story still continues!, *Cryst. Growth Des.*, 9 (2009) 2435-2441.
- [87] C.H. Gorbitz, K. Prydz, S. Ugland, Taurine, *Acta Crystallogr., Sect. B*, 56 (2000) 23-24.
- [88] L.A. O'Dell, C.I. Ratcliffe, X. Kong, G. Wu, Multinuclear solid-state nuclear magnetic resonance and density functional theory characterization of interaction tensors in taurine, *J. Phys. Chem. A*, 116 (2012) 1008-1014.
- [89] R. Montis, M.B. Hursthouse, Surprisingly complex supramolecular behaviour in the crystal structures of a family of mono-substituted salicylic acids, *CrystEngComm*, 14 (2012) 5242-5254.
- [90] V.V. Zhurov, A.A. Pinkerton, Quantifying the inter- and intramolecular interactions in crystalline phthalic acid, *Cryst. Growth Des.*, 14 (2014) 5685-5691.
- [91] G.M. Day, A.V. Trask, W.D.S. Motherwell, W. Jones, Investigating the latent polymorphism of maleic acid, *Chem. Commun.*, (2006) 54-56.
- [92] J.A. Kanters, G. Roelofsen, L.H. Straver, Hydrogen-bond motifs of carboxylic acids: the  $\beta$  form of cyanoacetic acid, *Acta Crystallogr., Sect. B*, 34 (1978) 1396-1397.
- [93] B. di Blasio, V. Pavone, C. Pedone, *Cryst. Struct. Commun.*, 6 (1977) 745.
- [94] O. Ando, T. Ashida, Y. Sasada, M. Kakudo, The crystal structure of L-valine hydrochloride, *Acta Crystallogr.*, 23 (1967) 172-173.
- [95] R.P. Chapman, D.L. Bryce, A high-field solid-state  $^{35/37}\text{Cl}$  NMR and quantum chemical investigation of the chlorine quadrupolar and chemical shift tensors in amino acid hydrochlorides, *Phys. Chem. Chem. Phys.*, 9 (2007) 6219-6230.
- [96] T.M. Duncan, R.W. Vaughan, The adsorption of formic acid on Y zeolites: A multiple-pulse nuclear magnetic resonance study, *J. Catal.*, 67 (1981) 49-70.
- [97] A. Pines, J.S. Waugh, M.G. Gibby, Proton-enhanced nuclear induction spectroscopy.  $^{13}\text{C}$  chemical shielding anisotropy in some organic solids, *Chem. Phys. Lett.*, 15 (1972) 373-&.
- [98] R.G. Griffin, A. Pines, S. Pausak, J.S. Waugh, Carbon-13 chemical shielding in oxalic acid, oxalic acid dihydrate, and diammonium oxalate, *J. Chem. Phys.*, 63 (1975) 1267-1271.

- [99] A. Naito, S. Ganapathy, K. Akasaka, C.A. McDowell, Chemical shielding tensor and  $^{13}\text{C}$ - $^{14}\text{N}$  dipolar splitting in single crystals of L-alanine, *J. Chem. Phys.*, 74 (1981) 3190-3197.
- [100] J.Z. Hu, J.C. Facelli, D.W. Alderman, R.J. Pugmire, D.M. Grant,  $^{15}\text{N}$  chemical shift tensors in nucleic acid bases, *J. Am. Chem. Soc.*, 120 (1998) 9863-9869.
- [101] Q. Zhang, E.Y. Chekmenev, R.J. Wittebort,  $^{17}\text{O}$  quadrupole coupling and chemical shielding tensors in an H-bonded carboxyl group:  $\alpha$ -oxalic acid, *J. Am. Chem. Soc.*, 125 (2003) 9140-9146.
- [102] C. Gervais, R. Dupree, K.J. Pike, C. Bonhomme, M. Profeta, C.J. Pickard, F. Mauri, Combined first-principles computational and experimental multinuclear solid-state NMR investigation of amino acids, *J. Phys. Chem. A*, 109 (2005) 6960-6969.
- [103] H. Hamaed, J.M. Pawlowski, B.F.T. Cooper, R. Fu, S.H. Eichhorn, R.W. Schurko, Application of solid-state  $^{35}\text{Cl}$  NMR to the structural characterization of hydrochloride pharmaceuticals and their polymorphs, *J. Am. Chem. Soc.*, 130 (2008) 11056-11065.
- [104] M. Hildebrand, H. Hamaed, A.M. Namespetra, J.M. Donohue, R. Fu, I. Hung, Z. Gan, R.W. Schurko,  $^{35}\text{Cl}$  solid-state NMR of HCl salts of active pharmaceutical ingredients: structural prediction, spectral fingerprinting and polymorph recognition, *CrystEngComm*, 16 (2014) 7334-7356.
- [105] S.T. Holmes, R.J. Iulucci, K.T. Mueller, C. Dybowski, Density functional investigation of intermolecular effects on  $^{13}\text{C}$  NMR chemical-shielding tensors modeled with molecular clusters, *J. Chem. Phys.*, 141 (2014) 164121.
- [106] J.D. Hartman, S. Monaco, B. Schatschneider, G.J.O. Beran, Fragment-based  $^{13}\text{C}$  nuclear magnetic resonance chemical shift predictions in molecular crystals: an alternative to planewave methods, *J. Chem. Phys.*, 143 (2015) 102809.
- [107] J.D. Hartman, R.A. Kudla, G.M. Day, L.J. Mueller, G.J.O. Beran, Benchmark fragment-based  $^1\text{H}$ ,  $^{13}\text{C}$ ,  $^{15}\text{N}$  and  $^{17}\text{O}$  chemical shift predictions in molecular crystals, *Phys. Chem. Chem. Phys.*, 18 (2016) 21686-21709.
- [108] S.T. Holmes, F. Alkan, R.J. Iulucci, K.T. Mueller, C. Dybowski, Analysis of the bond-valence method for calculating  $^{29}\text{Si}$  and  $^{31}\text{P}$  magnetic shielding in covalent network solids, *J. Comput. Chem.*, 37 (2016) 1704-1710.
- [109] F. Ortmann, F. Bechstedt, W.G. Schmidt, Semiempirical van der Waals correction to the density functional description of solids and molecular structures, *Phys. Rev. B*, 73 (2006) 205101.

- [110] J.C. Facelli, Modeling NMR Chemical Shifts, in: G.A. Webb (Ed.) Modern Magnetic Resonance, Springer Netherlands, Dordrecht, 2006, pp. 53-62.
- [111] A. Albinati, K.D. Rouse, M.W. Thomas, Neutron powder diffraction analysis of hydrogen-bonded solids. II. structural study of formic acid at 4.5 K, Acta Crystallogr., Sect. B, 34 (1978) 2188-2190.
- [112] A. Albinati, K.D. Rouse, M.W. Thomas, Neutron powder diffraction analysis of hydrogen-bonded solids. I. refinement of deuterated acetic acid at 4.2 and 12.5 K, Acta Crystallogr., Sect. B, 34 (1978) 2184-2187.
- [113] T.M. Sabine, G.W. Cox, B.M. Craven, A neutron diffraction study of  $\alpha$ -oxalic acid dihydrate, Acta Crystallogr., Sect. B, B 25 (1969) 2437-&.
- [114] H. Guth, G. Heger, S. Klein, W. Treutmann, C. Scheringer, Structural refinement of urea with neutron diffraction data at 60, 123 and 293 K and X-N AND X-X(1S2) syntheses at about 100 K, Z. Kristallogr., 153 (1980) 237-254.
- [115] G. Qi, G.A. Jeffrey, J.R. Ruble, R.K. McMullan, A single-crystal neutron-diffraction refinement of benzamide at 15 K and 123 K, Acta Crystallogr., Sect. B, 47 (1991) 742-745.
- [116] N.P. Funnell, A. Dawson, D. Francis, A.R. Lennie, W.G. Marshall, S.A. Moggach, J.E. Warren, S. Parsons, The effect of pressure on the crystal structure of L-alanine, CrystEngComm, 12 (2010) 2573-2583.
- [117] C.E. Briant, D.W. Jones, Neutron refinement of the crystal structure of partially exchanged taurine,  $(\text{ND}_3^+)_{0.65}(\text{NH}_3^+)_{0.35}(\text{CH}_2)_2\text{SO}_3$ , J. Chem. Cryst., 27 (1997) 481-483.
- [118] G.E. Bacon, R.J. Jude, Neutron-diffraction studies of salicylic acid and  $\beta$  resorcinol, Z. Kristallogr., 138 (1973) 19-40.
- [119] A.R. Alkaraghoul, F.E. Cole, M.S. Lehmann, C.F. Miskell, J.J. Verbist, T.F. Koetzle, Precision neutron diffraction structure determination of protein and nucleic acid components.XVII. molecular and crystal structure of the amino acid glycine hydrochlorideLORIDE, J. Chem. Phys., 63 (1975) 1360-1366.
- [120] T.F. Koetzle, L. Golic, M.S. Lehmann, J.J. Verbist, W.C. Hamilton, Precision neutron diffraction structure determination of protein and nucleic acid components.XV. Crystal and molecular structure of the amino acid L-valine hydrochloride, J. Chem. Phys., 60 (1974) 4690-4696.

## Chapter 8

### CONCLUSION

This dissertation discusses several critical aspects of the accurate and efficient calculation of magnetic-shielding and quadrupolar-coupling tensors in crystalline solids. The bulk of the discussion is devoted to exploring the accuracy of cluster-based computational protocols for modeling NMR parameters in solids. The analysis extends from pure molecular solids, such as naphthalene, to covalent network solids, such as quartz. Calculations of NMR parameters are applied to  $^{13}\text{C}$ ,  $^{15}\text{N}$ ,  $^{17}\text{O}$ ,  $^{19}\text{F}$ ,  $^{29}\text{Si}$ ,  $^{31}\text{P}$ ,  $^{35}\text{Cl}$ , and  $^{43}\text{Ca}$  sites. The accuracy of cluster-based calculations are benchmarked against popular periodic computational protocols such as the GIPAW approach. More importantly, the ability to use a wider selection of model chemistries in the cluster-based calculations allows one to specify the effects of choice of hybrid functionals in DFT and other modern electronic-structure methods for the prediction of NMR parameters in solids.

In Chapter 2, a quantum-chemical method for modeling solid-state NMR chemical-shift tensors by calculations on large symmetry-adapted clusters of molecules is demonstrated. Perhaps the most significant result of this chapter is that  $^{13}\text{C}$  chemical-shift tensors in molecular solids can be calculated accurately using clusters of molecules designed to represent a local portion of the lattice structure. NMR parameters are calculated using the hybrid exchange-correlation functional B3PW91, a model chemistry which is difficult to implement efficiently in periodic codes. 465 principal components of the  $^{13}\text{C}$  magnetic-shielding tensors of twenty-four organic materials are analyzed by this method. The comparison of calculations on isolated molecules with

molecules in clusters demonstrates that intermolecular effects can be successfully modeled using a cluster representing a local portion of the lattice structure, without the need to use periodic-boundary conditions (PBCs). The accuracy of calculations that model the solid state using a cluster rivals the accuracy of calculations which model the solid state using PBCs [1], provided the cluster preserves the symmetry properties of the crystalline space group. The size and symmetry conditions that the model cluster must satisfy to obtain significant agreement with experimental chemical-shift values are discussed. In particular, it is illustrated that the chemical-shift skew of the quaternary carbon in pentaerythritol is altered significantly if the proper symmetry of the cluster is not realized. It is illustrated for oxalic acid dihydrate and squaric acid that computed  $^{13}\text{C}$  magnetic-shielding tensors tend to converge smoothly with increasing cluster size. Furthermore, electronic-structure approximations, such as the use of locally dense and locally sparse basis functions, are discussed. The computational protocols described in this chapter provide a systematic route for incorporating intermolecular effects into magnetic-shielding calculations.

In Chapter 3, the principal components of the  $^{13}\text{C}$  chemical-shift tensors for the eight unique carbon sites of crystalline indigo are measured using the ROCSA pulse sequence. The chemical shifts are assigned unambiguously to their respective nuclear sites through comparison of the experimental data to the results of DFT calculations employing a refined X-ray diffraction structure. These measurements expand the database of measured aromatic  $^{13}\text{C}$  chemical-shift tensors to the indole ring. Magnetic shielding calculations for hypoxanthine and adenosine are also reported. The experimental and calculated results reveal that  $^{13}\text{C}$  magnetic-shielding tensors display a significant dependence on the placement of nitrogen atoms in the ring, with  $\sigma_{33}$ , or  $\delta_{33}$ ,

values being most affected. Comparison of calculations that include the effect of the crystalline lattice with calculations that model indigo as an isolated molecule give an estimate of the intermolecular contribution to the magnetic shielding, which can be as large as 20 ppm for particular principal components.

In Chapter 4, I assess periodic (GIPAW) and GIAO/symmetry-adapted cluster (SAC) models for computing magnetic-shielding tensors by calculations on a test set containing 72 molecular solids, with a total of 393 principal components of chemical-shift tensors from  $^{13}\text{C}$ ,  $^{15}\text{N}$ ,  $^{19}\text{F}$ , and  $^{31}\text{P}$  sites. When clusters are carefully designed to represent the local solid-state environment, both methods predict magnetic-shielding tensors that agree well with experimental chemical-shift values, demonstrating the correspondence of the two computational techniques. At the basis-set limit, I find that the linear-regression parameters describing the relationship between experimental chemical shifts and calculated magnetic shieldings are, to within experimental uncertainty, identical for both computational protocols, for three of the four nuclides.

Subsequently, the effects of additional DFT methods available only with the GIAO/cluster approach, particularly the use of hybrid-GGA functionals, meta-GGA functionals, and hybrid meta-GGA functionals that demonstrate improved agreement in calculations on symmetry-adapted clusters, were explored. The results demonstrate that meta-GGA functionals improve computed NMR parameters over those obtained by GGA functionals for all four nuclides, and that hybrid functionals improve computed results over the respective pure DFT functional for all nuclides except  $^{15}\text{N}$ . One of the most significant theoretical insights in this chapter was gained from the systematic analysis of  $^{13}\text{C}$  magnetic-shielding tensors. For this nucleus, the correlation between calculated magnetic shieldings and experimental chemical shifts for  $sp^3$ - and  $sp^2$ -

hybridized carbons were modeled separately. In agreement with earlier work [1], I found that GGA functionals such as PBE and PW91 result in distinct subpopulations that can be modeled with statistically different linear-regression parameters. This result appears to be a general feature of pure DFT functionals, as similar findings were obtained for the meta-GGA functional TPSS. In contrast, the hybrid DFT functionals PBE0, B3PW91, and TPSSh model carbon sites of all types with a single set of linear-regression parameters.

Chapter 5 presents a computational study of magnetic-shielding and quadrupolar-coupling tensors of  $^{43}\text{Ca}$  sites in calcium carboxylates and calcium-containing inorganic solids. Due to the limited experimental  $^{43}\text{Ca}$  NMR data available in the literature [2], the analysis is limited to ten calcium sites. A comparison between periodic and cluster-based approaches for modeling solid-state interactions demonstrates that cluster-based approaches are suitable for predicting  $^{43}\text{Ca}$  NMR parameters. The cluster-based calculations employ a hybrid approach, in which a cluster of atoms or molecules represents the local environment of the  $^{43}\text{Ca}$  site and long-range polarization effects are modeled with electrostatic embedding. At the PBE level, GIPAW and cluster-based calculations yield an RMSD of 14 ppm and 15 ppm for the principal components of the  $^{43}\text{Ca}$  magnetic-shielding tensors, respectively, and 0.14 MHz and 0.16 MHz for the principal components of the quadrupolar-coupling tensors, respectively. Significantly, the slopes of the correlation lines between experimental chemical shifts and calculated quadrupolar couplings are around  $-1.37 \pm 0.08$  for both methods. Several model chemistries, including Hartree-Fock (HF) theory and seventeen DFT approximations (SVWN, CA-PZ, PBE, PBE0, PW91, B3PW91, rPBE, PBEsol, WC, PKZB, BMK, M06-L, M06, M06-2X, M06-HF, TPSS, and TPSSh), are

evaluated for the prediction of  $^{43}\text{Ca}$  NMR parameters. All DFT methods lead to substantial, and frequently systematic, overestimations of experimental chemical shifts. Hartree-Fock calculations outperform all DFT methods for the prediction of  $^{43}\text{Ca}$  chemical-shift tensors. At the HF level, an RMSD for the principal components of the  $^{43}\text{Ca}$  magnetic-shielding tensor is only 9 ppm. Convergence of NMR parameters with respect to basis sets of the form cc-pVXZ ( $X = \text{D, T, Q}$ ) is also evaluated.

In Chapter 6,  $^{29}\text{Si}$  and  $^{31}\text{P}$  magnetic-shielding tensors in covalent network solids, specifically silicates and phosphates, are evaluated using periodic and cluster-based calculations. The cluster-based computational methodology employs pseudoatoms to reduce the net charge (resulting from missing co-ordination on the terminal atoms) through valence modification of terminal atoms using bond-valence theory (VMTA/BV), a computational strategy for modeling NMR parameters in covalent network solids recently proposed by Alkan and Dybowski [3] as an extension of the earlier work of Brown [4]. Although the VMTA/BV model has previously been applied to the prediction of  $^{207}\text{Pb}$  magnetic-shielding tensors, this is the first study in which the magnetic-shielding tensors computed with the VMTA/BV method are compared to magnetic-shielding tensors determined with the periodic GIPAW approach.

The performance of the DFT functionals CA-PZ, PW91, PBE, rPBE, PBEsol, WC, and PBE0 were assessed for the prediction of  $^{29}\text{Si}$  and  $^{31}\text{P}$  magnetic-shielding constants in silicates and phosphates. Consistent with previous calculations, the pure DFT functionals led to systematic overestimations of chemical shifts. Calculations using the hybrid functional PBE0, in combination with the VMTA/BV approach, result in excellent agreement with experiment. Furthermore, proposed absolute shielding scales for  $^{29}\text{Si}$  and  $^{31}\text{P}$  allow another dimension for assessing the accuracy of

calculations [5, 6]. All-electron calculations result in magnetic-shielding constants that agree better with experiment on an absolute scale. At the PBE0 level, the relationship between experimental and calculated magnetic-shielding tensors results in an ideal correlation, with a slope and intercept that are not statistically different from unity and zero, respectively, for both nuclides.

Chapter 7 demonstrates a modification of Grimme's two-parameter empirical dispersion force field (referred to as the PW91-D2\* method), in which the damping function is optimized to yield geometries that result in predictions of the principal values of  $^{17}\text{O}$  quadrupolar-coupling tensors that are in close agreement with experiment. The predictions of  $^{17}\text{O}$  quadrupolar-coupling tensors using PW91-D2\*-refined structures yields a RMSD (0.28 MHz) for twenty-two crystalline systems that is smaller than the RMSD for predictions based on X-ray diffraction structures (0.58 MHz) or on structures refined with PW91 (0.53 MHz). In addition,  $^{13}\text{C}$ ,  $^{15}\text{N}$  and  $^{17}\text{O}$  chemical-shift tensors and  $^{35}\text{Cl}$  quadrupolar-coupling tensors determined with PW91-D2\*-refined structures are compared to experiment. Errors in the prediction of chemical-shift tensors and quadrupolar-coupling tensors are, in these cases, substantially lower than predictions based on PW91-refined structures. With this PW91-D2\*-based method, analysis of 42  $^{17}\text{O}$  chemical-shift-tensor principal components gives a RMSD of only 18.3 ppm, whereas calculations on unrefined X-ray structures give a RMSD of 39.6 ppm. A similar analysis of  $^{35}\text{Cl}$  quadrupolar-coupling tensor principal components gives a RMSD of 1.45 MHz for the unrefined X-ray structures, and 0.59 MHz for the PW91-D2\*-refined structures. The results in this chapter have the potential to serve as the groundwork for future studies on NMR crystallography.

This dissertation provides a practical route to the prediction of magnetic-shielding and quadrupolar-coupling tensors in ordered solids. The results illustrate that cluster-based approaches can be applied successfully to model NMR parameters in solids. Theoretical considerations, related to the selection of model chemistry, are assessed for the prediction of NMR parameters. Finally, it is demonstrated that accurate predictions of solid-state NMR parameters can be used for semi-empirical refinements of the coordinates of atoms in crystal structures.

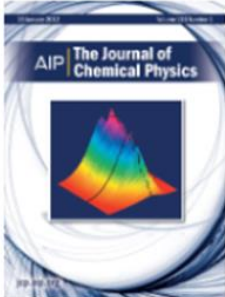
## REFERENCES

- [1] J.C. Johnston, R.J. Iulucci, J.C. Facelli, G. Fitzgerald, K.T. Mueller, Intermolecular shielding contributions studied by modeling the  $^{13}\text{C}$  chemical-shift tensors of organic single crystals with plane waves, *J. Chem. Phys.*, 131 (2009) 144503.
- [2] D.L. Bryce, Calcium binding environments probed by Ca-43 NMR spectroscopy, *Dalton Trans.*, 39 (2010) 8593-8602.
- [3] F. Alkan, C. Dybowski, Chemical-shift tensors of heavy nuclei in network solids: a DFT/ZORA investigation of  $^{207}\text{Pb}$  chemical-shift tensors using the bond-valence method, *Phys. Chem. Chem. Phys.*, 17 (2015) 25014-25026.
- [4] I.D. Brown, Recent developments in the methods and applications of the bond valence model, *Chem. Rev.*, 109 (2009) 6858-6919.
- [5] C.J. Jameson, A.K. Jameson, Absolute shielding scale for  $^{29}\text{Si}$ , *Chem. Phys. Lett.*, 149 (1988) 300-305.
- [6] C.J. Jameson, A. De Dios, A.K. Jameson, Absolute shielding scale for  $^{31}\text{P}$  from gas-phase NMR studies, *Chem. Phys. Lett.*, 167 (1990) 575-582.

## Appendix

### PERMISSION AND COPYRIGHT

 [Home](#) [Account Info](#) [Help](#) 

 **Title:** Density functional investigation of intermolecular effects on  $^{13}\text{C}$  NMR chemical-shielding tensors modeled with molecular clusters

**Author:** Sean T. Holmes, Robbie J. Iuliucci, Karl T. Mueller, et al

**Publication:** Journal of Chemical Physics

**Volume/Issue:** 141/16

**Publisher:** AIP Publishing LLC

**Date:** Oct 28, 2014

**Page Count:** 12

Rights managed by AIP Publishing LLC.

Logged in as:  
Sean Holmes  
[LOGOUT](#)

#### Order Completed

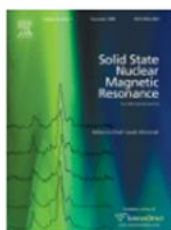
Thank you for your order.

This Agreement between Sean Holmes ("You") and AIP Publishing LLC ("AIP Publishing LLC") consists of your license details and the terms and conditions provided by AIP Publishing LLC and Copyright Clearance Center.

Your confirmation email will contain your order number for future reference.

#### [Printable details.](#)

License Number	4030330154092
License date	Jan 15, 2017
Licensed Content Publisher	AIP Publishing LLC
Licensed Content Publication	Journal of Chemical Physics
Licensed Content Title	Density functional investigation of intermolecular effects on $^{13}\text{C}$ NMR chemical-shielding tensors modeled with molecular clusters
Licensed Content Author	Sean T. Holmes, Robbie J. Iuliucci, Karl T. Mueller, et al
Licensed Content Date	Oct 28, 2014
Licensed Content Volume	141
Licensed Content Issue	16
Requestor type	Author (original article)
Format	Print and electronic
Portion	Excerpt (> 800 words)



**Title:** Carbon-13 chemical-shift tensors in indigo: A two-dimensional NMR-ROCSA and DFT Study  
**Author:** Sean T. Holmes,Cecil Dybowski  
**Publication:** Solid State Nuclear Magnetic Resonance  
**Publisher:** Elsevier  
**Date:** November 2015  
 Copyright © 2015 Elsevier Inc. All rights reserved.

Logged in as:  
Sean Holmes

LOGOUT

### Order Completed

Thank you for your order.

This Agreement between Sean Holmes ("You") and Elsevier ("Elsevier") consists of your license details and the terms and conditions provided by Elsevier and Copyright Clearance Center.

Your confirmation email will contain your order number for future reference.

### [Printable details.](#)

License Number	4030330893416
License date	Jan 15, 2017
Licensed Content Publisher	Elsevier
Licensed Content Publication	Solid State Nuclear Magnetic Resonance
Licensed Content Title	Carbon-13 chemical-shift tensors in indigo: A two-dimensional NMR-ROCSA and DFT Study
Licensed Content Author	Sean T. Holmes,Cecil Dybowski
Licensed Content Date	November 2015
Licensed Content Volume	72
Licensed Content Issue	n/a
Licensed Content Pages	6
Type of Use	reuse in a thesis/dissertation
Portion	full article
Format	both print and electronic
Are you the author of this Elsevier article?	Yes
Will you be translating?	No
Order reference number	
Title of your thesis/dissertation	DFT CALCULATIONS OF MAGNETIC SHIELDING AND QUADRUPOLEAR COUPLING IN ORDERED SYSTEMS: METHODS AND APPLICATIONS TO NMR. CRYSTALLOGRAPHY
Expected completion date	Jan 2017
Estimated size (number of pages)	250
Elsevier VAT number	GB 494 6272 12



**Title:** Critical Analysis of Cluster Models and Exchange-Correlation Functionals for Calculating Magnetic Shielding in Molecular Solids

**Author:** Sean T. Holmes, Robbie J. Iuliucci, Karl T. Mueller, et al

**Publication:** Journal of Chemical Theory and Computation

**Publisher:** American Chemical Society

**Date:** Nov 1, 2015

Copyright © 2015, American Chemical Society

LOGIN

If you're a [copyright.com user](#), you can login to RightsLink using your [copyright.com](#) credentials. Already a [RightsLink user](#) or want to [learn more?](#)

#### PERMISSION/LICENSE IS GRANTED FOR YOUR ORDER AT NO CHARGE

This type of permission/license, instead of the standard Terms & Conditions, is sent to you because no fee is being charged for your order. Please note the following:

- Permission is granted for your request in both print and electronic formats, and translations.
- If figures and/or tables were requested, they may be adapted or used in part.
- Please print this page for your records and send a copy of it to your publisher/graduate school.
- Appropriate credit for the requested material should be given as follows: "Reprinted (adapted) with permission from (COMPLETE REFERENCE CITATION). Copyright (YEAR) American Chemical Society." Insert appropriate information in place of the capitalized words.
- One-time permission is granted only for the use specified in your request. No additional uses are granted (such as derivative works or other editions). For any other uses, please submit a new request.



**Title:** Analysis of the bond-valence method for calculating  $^{29}\text{Si}$  and  $^{31}\text{P}$  magnetic shielding in covalent network solids

**Author:** Sean T. Holmes, Fahri Alkan, Robbie J. Iulucci, Karl T. Mueller, Cecil Dybowski

**Publication:** Journal of Computational Chemistry

**Publisher:** John Wiley and Sons

**Date:** Apr 26, 2016

© 2016 Wiley Periodicals, Inc.

Logged in as:  
Sean Holmes

[LOGOUT](#)

## Order Completed

Thank you for your order.

This Agreement between Sean Holmes ("You") and John Wiley and Sons ("John Wiley and Sons") consists of your license details and the terms and conditions provided by John Wiley and Sons and Copyright Clearance Center.

Your confirmation email will contain your order number for future reference.

### [Printable details.](#)

License Number	4030330585549
License date	Jan 15, 2017
Licensed Content Publisher	John Wiley and Sons
Licensed Content Publication	Journal of Computational Chemistry
Licensed Content Title	Analysis of the bond-valence method for calculating $^{29}\text{Si}$ and $^{31}\text{P}$ magnetic shielding in covalent network solids
Licensed Content Author	Sean T. Holmes, Fahri Alkan, Robbie J. Iulucci, Karl T. Mueller, Cecil Dybowski
Licensed Content Date	Apr 26, 2016
Licensed Content Pages	7
Type of use	Dissertation/Thesis
Requestor type	Author of this Wiley article
Format	Print and electronic
Portion	Full article
Will you be translating?	No
Title of your thesis / dissertation	DFT CALCULATIONS OF MAGNETIC SHIELDING AND QUADRUPOLEAR COUPLING IN ORDERED SYSTEMS: METHODS AND APPLICATIONS TO NMR. CRYSTALLOGRAPHY
Expected completion date	Jan 2017
Expected size (number of pages)	250